Investigation of Composite Structures

Grant Number NAG-1-1895

NASA-Langley Research Center

Mechanics and Durability Branch

Final Report

November 2000

submitted
by
M.W. Hyer
Principal Investigator

This final report consists of a compilation of four separate written documents, three dealing with the response and failure of elliptical composite cylinders to an internal pressure load, and the fourth dealing with the influence of manufacturing imperfections in curved composite panels. The three focused on elliptical cylinders consist of the following:

1 - A paper entitled "Progressive Failure Analysis of Internally Pressurized Elliptical Composite Cylinders," which is included in the Proceedings of the 15th Annual Technical Meeting of the American Society for Composites held in September 2000.

2 - A paper entitled "Influence of Geometric Nonlinearities on the Response and Failure of Internally Pressurized Elliptical Composite Cylinders," AIAA paper no. 2000-1516, which is included in the Proceedings of the 41st Structures, Structural Dynamics, and Materials Conference held in April 2000.

3 - A report entitled "Response and Failure of Internally Pressurized Elliptical Composite Cylinders," dated September 1999.

The document which deals with the influence of manufacturing imperfections is a paper entitled "Manufacturing Distortions of Curved Composite Panels" which is included in the Proceedings of the 14th Annual Technical Meeting of the American Society for Composites held in September 1999.

PROGRESSIVE FAILURE ANALYSIS OF INTERNALLY PRESSURIZED ELLIPTICAL COMPOSITE CYLINDERS

Jennifer M. McMurray
Michael W. Hyer

Department of Engineering Science and Mechanics
Virginia Polytechnic Institute and State University
Blacksburg VA 24061

ABSTRACT

Presented is a brief overview of a study which focuses on the use of a progressive failure analysis to predict the failure pressure, mode, and location of internally pressurized composite cylinders with elliptical cross sections. The analysis is based on a STAGS finite-element analysis, the maximum stress failure criterion, and a material degradation scheme and the associated redistribution of stresses. A small-scale clamped quasi-isotropic cylinder with a ratio of minor to major diameters of 0.7 is used as an example. A classic first ply failure analysis is also considered for comparison.

INTRODUCTION

Cylinders are often used as the idealized model for a number of important structures. Aircraft fuselages, missile cases, submarine hulls, and tankage for storing and transporting various liquids and gases are but a few example structures. Of interest are deflections, buckling loads, vibration frequencies, stress levels, and interactions with endfittings or supports. Cylinders with circular cross sections are generally used as the basis for many of the models, and much has been written regarding the analysis of circular cylinders. However, next generation civil transports may well utilize fuselage designs that depart from the normal circular cross section, and future reusable launch vehicles may use fuel tanks that are noncircular. Aerodynamic, structural, or payload considerations may dictate the noncircular designs. These aerospace structures can also be idealized as cylinders, but with noncircular cross sections. Since fiber-reinforced composite materials are often the material of choice for aerospace applications, due to weight and design flexibility, it is logical to consider composite materials for these two applications. Furthermore, for both fuselages and fuel tanks for reusable launch vehicles, internal pressure is an important loading. For a fuselage, an elevated internal pressure is necessary for the passenger. For fuel tanks, liquification of a gaseous component of the fuel at cryo-

---

Jennifer M. McMurray and Michael W. Hyer, Campus Code 0219, Department of Engineering Science and Mechanics, Virginia Polytechnic Institute and State University, Blacksburg, VA 24061.

genic temperatures leads to internal pressure. In both cases, failure in the sense of catastrophic material failure is important, but also, failure in the sense of leakage of the cylinder wall can be important. This paper examines the failure of internally pressurized noncircular cylinders by considering cylinders of elliptical cross section. Failure is addressed both by a first ply failure analysis and by a progressive failure analysis. With the latter, rather than stop the analysis when the pressure reaches the level to cause failure, as predicted by some failure criterion, material properties are degraded as failure occurs, the pressure is increased, and the analysis continues. A finite-element analysis is used. Elliptical cross sections are considered because analytical expressions can be written to represent the geometry of the cross section. However, it is felt that many of the conclusions reached for the case of elliptical cross sections also hold for more general noncircular cross sections.

The sections that follow define the specific problem being addressed. The geometry, boundary conditions, and general nomenclature are introduced. The finite-element model used to compute the stresses, and hence the failure characteristics, is discussed. The failure criterion is described, particularly the scheme for introducing material degradation. Results for a quasi-isotropic cylinder are presented and discussed.

PROBLEM DEFINITION

The particular problem being discussed is described in fig. 1. The cylinder has a reference surface of length L, the major and minor diameters are $2a$ and $2b$, respectively, and the cylinder wall is of thickness H. The circumference of the cylinder is denoted as C, and here the ellipticity e is defined as the ratio of the minor to major diameters. The crown and keel denote the upper and lower flatter parts of the cylinder, and the sides the more curved portions. Spatial positions axially are

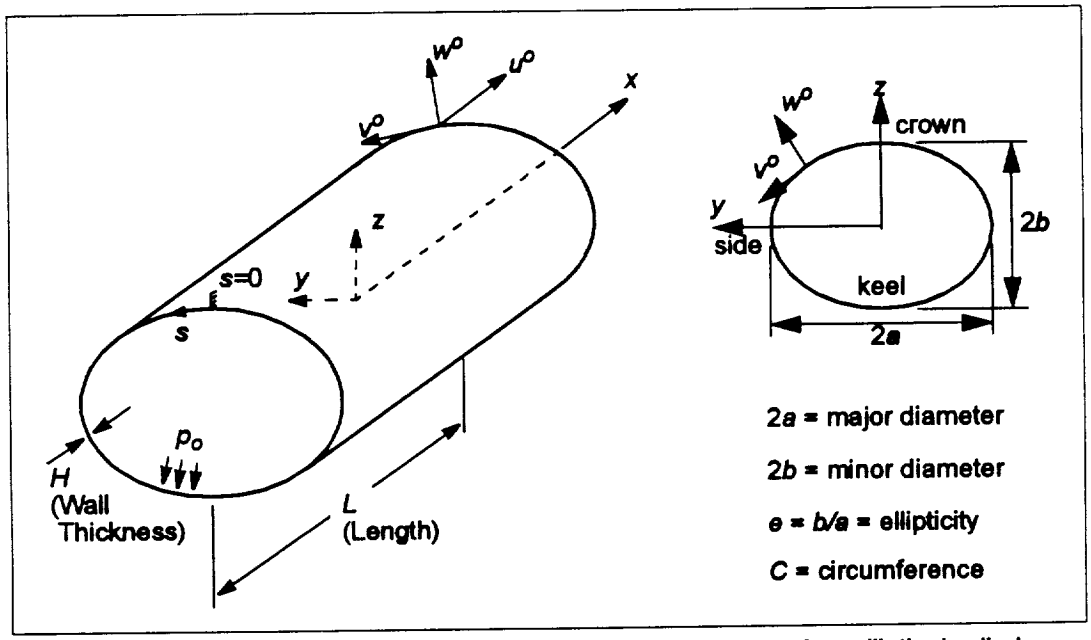

FIGURE 1. Problem description, nomenclature, and geometry of an elliptical cylinder.

denoted by x, with $x = 0$ at the cylinder midspan, i.e., $-L/2 \le x \le +L/2$. The circumferential coordinate is s, where $s = 0$ at the top of the cylinder and $-C/2 \le s \le +C/2$. While they will not be discussed specifically, the axial, circumferential, and normal components of displacement of the reference surface are given by u^o, v^o, and w^o, respectively. The internal pressure is denoted p_o. Compared to a circular cylinder, the behavior of the elliptical cylinder displacements due to internal pressure is significantly different and is characterized by the cylinder tending to become more circular as the internal pressure increases. This leads to the existence of circumferential displacements and inward normal displacements at the ends of the major diameter [1-3]. Both ends of the cylinder are assumed to be attached to rigid end caps. Accordingly, the ends are considered fully clamped, except for the fact that the end at $x = +L/2$ can move axially to accommodate the axial motion Δ which is due to the axial strain caused by a combination of internal pressure and Poisson's ratio effects. Specifically, the boundary conditions are given by

$$\begin{aligned} &\text{i) } u^o = 0 \text{ @ } x = -\frac{L}{2},\ u^o = \Delta \text{ @ } x = +\frac{L}{2} \\ &\text{ii) } v^o = 0 \qquad \text{iii) } w^o = 0 \qquad \text{iv) } \frac{\partial w^o}{\partial x} = 0. \end{aligned} \tag{1}$$

The finite-element mesh representing the cylinder is shown in fig. 2. The STAGS finite-element code [4] is used to solve for cylinder response, and it should be noted that the mesh density in the axial direction increases toward the ends of the cylinder. This is due to the high gradients in the displacements near the ends. There are 70 elements in the axial direction and 50 in the circumferential direction. The 410 element from the STAGS element library is used. Geometric nonlinearities are included.

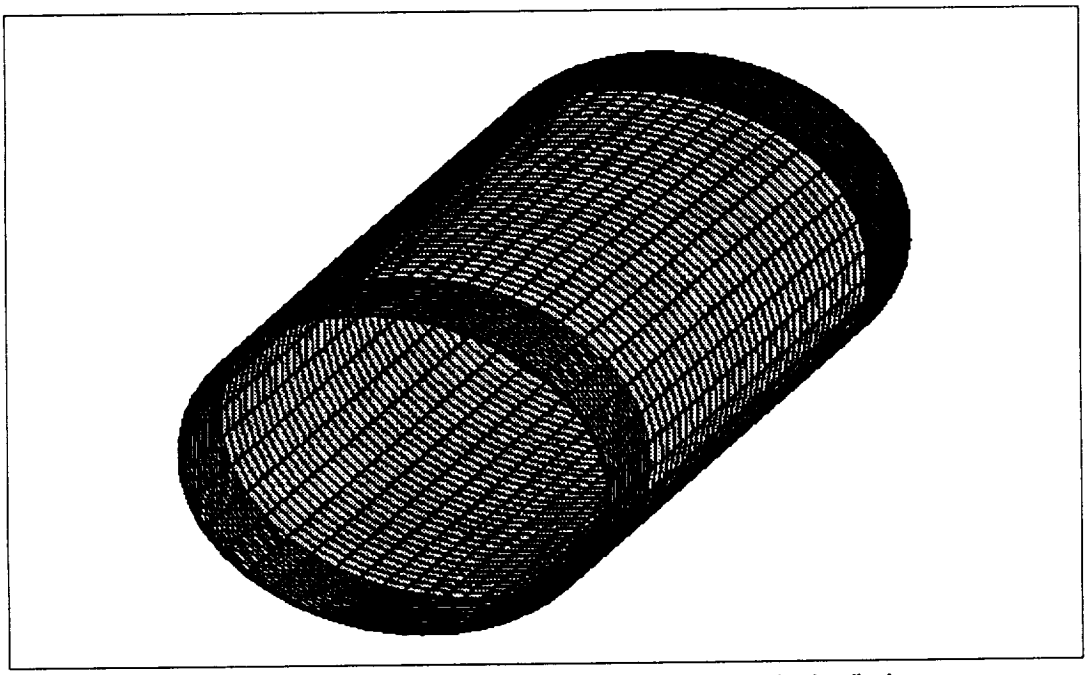

FIGURE 2. STAGS finite element mesh for an elliptical cylinder.

FAILURE CRITERION

For both the first ply, or nonprogressive, failure analysis and the progressive failure analysis, the maximum stress criterion is used to indicate material failure. Previous work [1-3] has shown that interlaminar stresses have minimal contribution to failure and thus are ignored here. The material is assume to have not failed if the following inequalities are all satisfied:

Fiber Modes		Matrix Modes		Shear Mode
$\frac{\sigma_{11}}{\sigma_A^+} < 1$	$\frac{-\sigma_{11}}{\sigma_A^-} < 1$	$\frac{\sigma_{22}}{\sigma_T^+} < 1$	$\frac{-\sigma_{22}}{\sigma_T^-} < 1$	$\frac{\lvert\sigma_{12}\rvert}{\tau_A} < 1$

(2)

These equations are written in the principal material coordinate system and the quantities σ_A^+ and σ_A^- are the tensile and compressive failure stresses in the fiber direction. In like fashion, σ_T^+ and σ_T^- are tensile and compressive failure stresses perpendicular to the fibers, in the plane of a layer, and τ_A is the shear failure stress in the plane of a layer. When any of the five stress ratios equals unity, failure of the material is assumed to have occurred, the failure mode being determined by the particular equation. For the work here, the values of the failure stresses are given by

$$\sigma_A^+ = 200,000 \text{ psi} \qquad \sigma_T^+ = 7250 \text{ psi} \qquad \tau_A = 14,500 \text{ psi}$$
$$\sigma_A^- = 180,000 \text{ psi} \qquad \sigma_T^- = 29,000 \text{ psi} \tag{3}$$

For the nonprogressive failure analysis, the pressure required to cause one of the five equations to be unity is computed. This is done by computing the strains and curvatures at the centroids of all elements and then computing the stresses as a function of cylinder wall thickness location. The result of these calculations is the failure pressure, the element, the location within the wall, and the mode of first failure. For the progressive failure analysis, the same calculations are performed to find the first failure. However, the material properties in the particular layer or layers that fail are then reduced within the finite-element according to the following scheme: If matrix of shear failure occurs then E_2 and G_{12} are degraded by 80%. If fiber failure occurs then E_1, E_2 and G_{12} are degraded by 80%. These reductions reflect the loss of stiffness due to matrix and fiber failures. Following the reductions in properties, the stresses within the cylinder are recomputed using the pressure that caused first failure. Generally other failures result from the localized redistribution of stresses that accompany the local reductions in stiffness. Stiffness are further reduced and the stresses are recomputed at the same pressure. After several iterations, no further failures occur due the redistribution of stresses and the pressure is increased until the next failure is encountered. The material properties are reduced in the appropriate elements and layers and the stresses recomputed with the pressure fixed. Again, after several iterations, no further failures occur at that pressure and the pressure is increased again. This process is continued to any desired pressure level.

NUMERICAL EXAMPLE

As a forerunner to testing full-scale cylinders in the laboratory, small-scale cylinders are being studied. As a result, numerical results here will focus on cylinders with dimensions L = 12.5 in, $2a$ = 10 in., $2b$ = 7 in. made of graphite-epoxy using an eight-layer quasi-isotropic $[\pm 45/0/90]_S$ layup. As a result, the ellipticity e is 0.70. The material properties are assumed to be

$$E_1 = 18.85 \text{ Msi} \qquad E_2 = 1.407 \text{ Msi}$$
$$G_{12} = 0.725 \text{ Msi} \qquad \nu_{12} = 0.300 \qquad h = 0.0055 \text{ in.} \tag{4}$$

and the layer thickness is 0.0055 in.

As might be expected, the first failure to occur is matrix failure, specifically due to a tensile σ_2, and it occurs at a pressure p_f of 140 psi. The first failure occurs at the ends of the cylinder in the inner layer, a +45 deg. layer. Because of the noncircular geometry, the stresses vary with circumferential position and as a result, there are specific circumferential locations where the matrix fails first. The lefthand portion of fig. 3 illustrates the location of this failure. In the figure one quadrant of the cylinder is rendered in somewhat of a three-dimensional fashion. The quadrant extending from $0 \le x \le +L/2$ and $-C/4 \le s \le +C/4$ is shown, but with the through-thickness location, ζ, normalized by the wall thickness H and greatly exaggerated in proportion to x and s, also included in the rendering. There is a dot indicating the location of the first matrix failure, namely the inner layer at s/C = -0.124. There is not another dot at s/C = +0.124 because despite geometric symmetry about s = 0, the material properties are not symmetric about s = 0 - i.e, D_{16} and D_{26} are nonzero - so the cylinder failures there at a slightly higher pressure. There is a companion failure at s/C = +0.376 (not shown), and there are failures at similar locations at the other end of the cylinder (not shown). Since first matrix failure is generally not catastrophic, the pressure to produce the first fiber failure, with no degradation in material properties, is also computed. The first fiber failure is a compressive failure which occurs at the

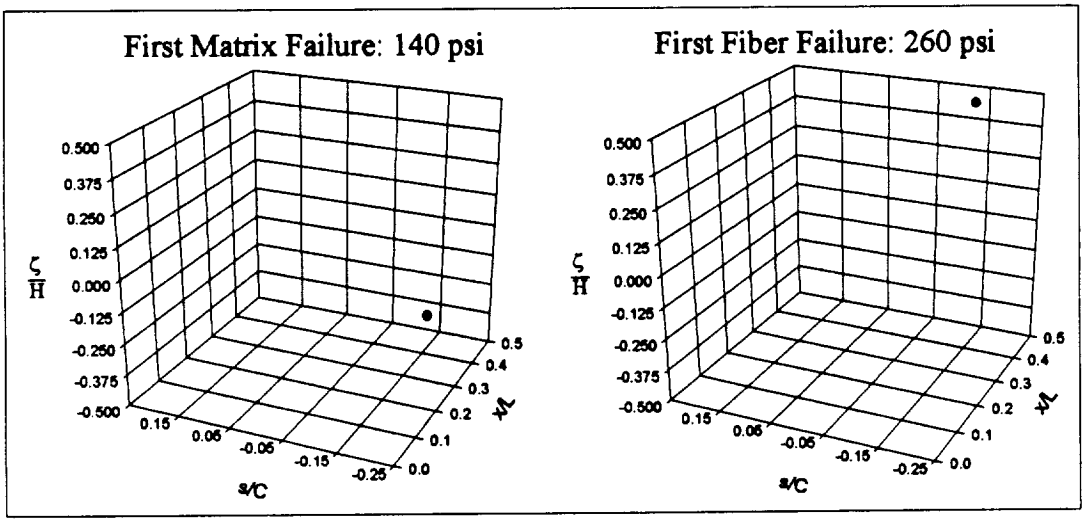

FIGURE 3. Nonprogressive failure of a quasi-isotropic elliptical cylinder.

end of the cylinder in layer no. 8, the outer +45 deg. layer, at a pressure of 260 psi. The location is shown in the righthand portion of fig. 3. These numbers, which are summarized in table 1, agree well with the first matrix and fiber failures computed using a semi-closed form solution [1-3]. The differences that occur are due to the fact that the centroid of the failed element is not at the exact end of the cylinder, whereas with the semi-closed form solution, the failure was predicted to occur exactly at $x = L/2$.

The results of a progressive failure analysis for first matrix and first fiber failures are shown in fig. 4. The first matrix failure, namely, the lefthand side of the figure, is identical to the nonprogressive first matrix failure, namely the lefthand side of fig. 3, because matrix failure is the first to occur in both cases. The righthand side of fig. 4 indicates with dots the locations of all the failures that occur up to and including first fiber failure. The first fiber failure dot is circled in the figure and occurs in the outer layer, again due to compression at $s/C = -0.124$. For the progressive analysis, the pressure to cause first fiber failure is 250 psi, slightly less than the 260 psi of the nonprogressive case. While this is not a large decrease, these results are for one laminate and one cylinder geometry. Furthermore, the results may be sensitive to the material property degradation scheme and the failure criterion used. What is shown in fig. 4 is but a specific example. It is important to point out in fig. 4 that matrix failure begin to occur away from the end of the cylinder. Also, for this example, fiber failure occurs at about twice the pressure of first matrix failure.

Before closing, it is instructive to consider two other issues. Figure 5 provides an indication of why at a given pressure it is important to iterate to determine all the failures when using the material degradation scheme described. The lefthand portion of the figure shows the matrix failures predicted by the first initial iteration of material degradation at 200 psi. The righthand portion shows the matrix failures at the final iteration at 200 psi. Though the details are difficult to discern, the circled regions show where iteration results in additional matrix failures. The need for iteration is an artifact of the numerical scheme employed, but physically the need to iterate is due to the redistribution of stresses that accompanies failure. Finally, fig. 6 compares matrix failures for the nonprogressive and progressive failure analyses.

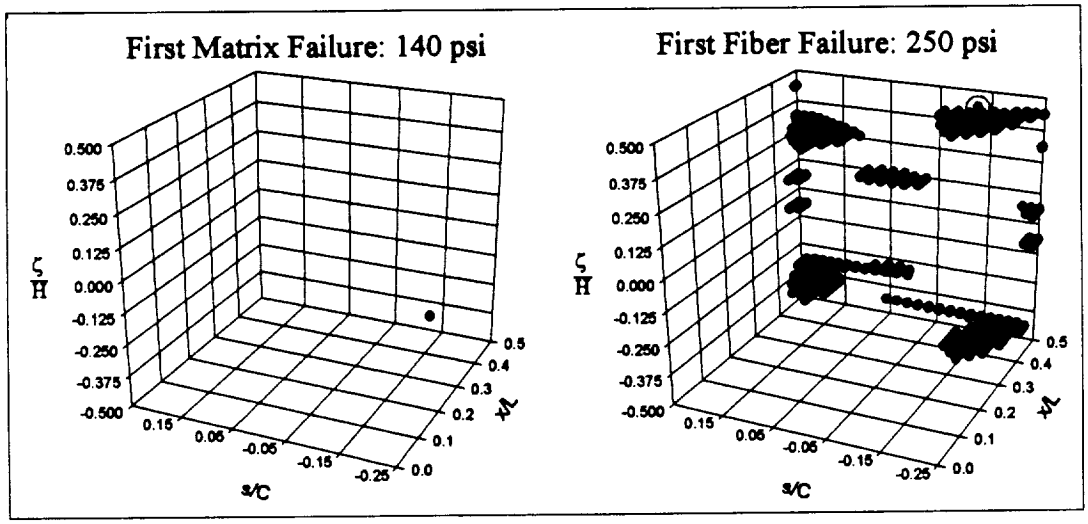

FIGURE 4. Progressive failure of a quasi-isotropic elliptical cylinder.

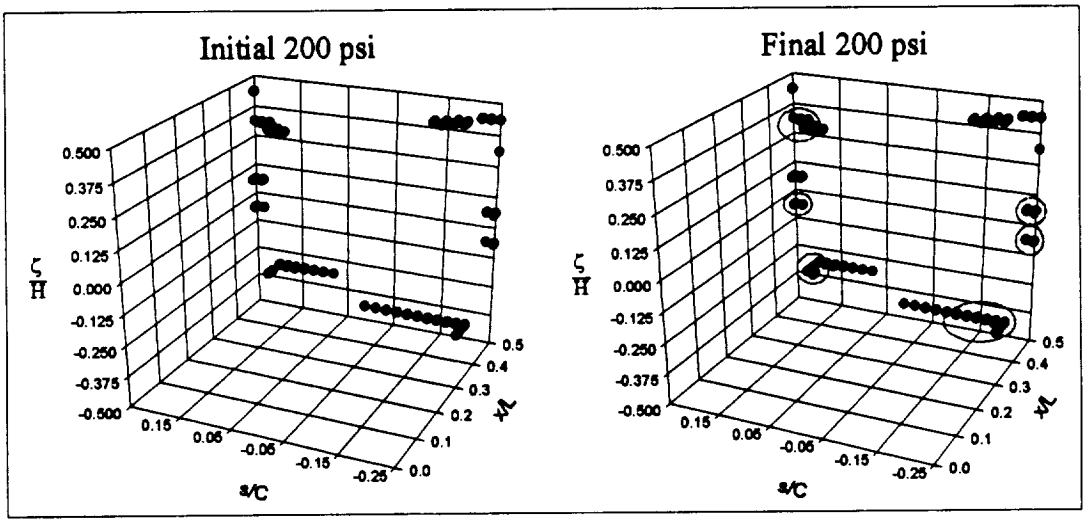

FIGURE 5. Effects of progressive failure for a quasi-isotropic elliptical cylinder at 200 psi.

The lefthand side is somewhat fictitious and shows the matrix failures and one fiber failure (circled) that are predicted to occur at 260 psi using the nonprogressive analysis. The righthand side shows the matrix failures and one fiber failure that occur at 250 psi using the progressive failure analysis. The lefthand side is fictitious because the effects of all the matrix failures on material properties are ignored when computing first fiber failure. The decreased number of matrix failures for the 250 psi progressive case relative to the 260 psi nonprogressive case show the combined effects of a 10 psi pressure increase and stress redistribution caused by material degradation.

Presented has been a discussion of failure of elliptical composite cylinders due to internal pressure. The key points of the discussion are: 1 - Failure occurs at a specific circumferential location due to the varying geometry; 2 - Fiber failure occurs at about twice the pressure of first matrix failure; and 3 - The Progressive failure analysis leads to a slightly lower fiber failure pressure.

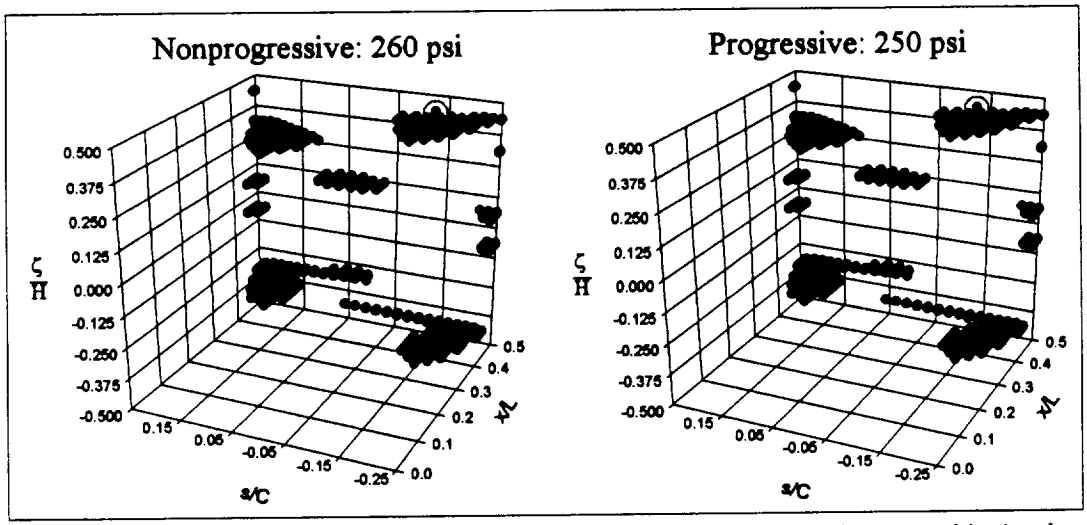

FIGURE 6. Comparison between Nonprogressive failure predictions for a quasi-isotropic elliptical cylinder.

TABLE I. COMPARISON OF MATRIX AND FIRST FIBER FAILURE FOR NONPROGRESSIVE AND PROGRESSIVE FAILURE ANALYSES.

	Matrix	Fiber (Nonprogressive)	Fiber (Progressive)
p_f (psi)	140	260	250
loc	1 (+45)	8 (+45)	8 (+45)
s/C	-0.124	-0.124	-0.124
mode	$+\sigma_2$	$-\sigma_1$	$-\sigma_1$

ACKNOWLEDGEMENTS

The work reported on was supported by grant NAG-1-1895 from the Mechanics and Durability Branch of the NASA Langley Research Center to Virginia Tech. The authors greatly appreciate the grant support.

REFERENCES

1. McMurray, J.M. and Hyer, M.W., "Internally Pressurized Elliptical Composite Cylinders." *Composite Structures* 46 (1999): 17-31.
2. McMurray, J.M. and M.W. Hyer, "Response and Failure of Internally Pressurized Elliptical Composite Cylinders," *Proceedings of the American Society for Composites 14th Technical Conference*, p. 95-105, available Technomic Publishing Co., Inc., 1999.
3. McMurray, J.M. and M.W. Hyer, "Influence of Geometric Nonlinearities on the Response and Failure of Internally Pressurized Elliptical Composite cylinders," AIAA paper no. 2000-1516, presented at 41st AIAA/ASME/ASCE/AHS/ASC Structures, Structural Dynamics, and Materials Conference, Atlanta GA, 2000
4. Rankin, C.C., F.A. Brogan, W.A. Loden, and H.D. Cabiness, "STAGS Users Manual, Version 3.0," Lockheed-Martin Missiles & Space Co., Inc., Report LMSC P032594, March 1999

INFLUENCE OF GEOMETRIC NONLINEARITIES ON THE RESPONSE AND FAILURE OF INTERNALLY PRESSURIZED ELLIPTICAL COMPOSITE CYLINDERS

Jennifer M. McMurray* and Michael W. Hyer†
Engineering Science and Mechanics, Virginia Polytechnic Institute and State University, Blacksburg, VA 24061

Abstract

Discussed are the characteristics of the response of internally pressurized elliptical composite cylinders, including failure. The influence of the elliptical geometry is illustrated by comparison with a circular cylinder. The influence of orthotropy is illustrated by considering axially-stiff, circumferentially-stiff, and quasi-isotropic laminates. The influence of geometric nonlinearities is studied by inclusion of the von Karman terms in the strain-displacement relations. Two failure criteria are considered, the Hashin criterion and the maximum stress criterion. These are used to compute the pressures to cause matrix cracking and fiber failure.

Problem Description

The problem considered consists of the cylinder described in fig. 1, with a, b, and L denoting, respectively, the semi-major diameter, semi-minor diameter, and axial length of the cylinder reference surface. The degree of ellipticity, e, is defined here as the ratio, b/a. The wall thickness of the cylinder is denoted by H and the internal pressure by p_o. The displacement of the reference surface in the axial, x, direction is denoted by $u^o(x,s)$, that in the circumferential, s, direction by $v^o(x,s)$, an that in the direction normal to the reference surface by $w^o(x,s)$. The upper part of the cross-section is referred to as the crown, the lower part the keel, and the sides are referred to as the sides. It will be assumed the cylinder ends are clamped to a rigid end plate or bulkhead which can move axially. Accordingly, clamped boundary conditions are applied to each end of the cylinder, with the exception of allowing the end at $x = +L/2$ to expand uniformly in the axial direction with displacement Δ. The end at $x = -L/2$ cannot move axially in order to restrict axial rigid body translation. Formally, the boundary conditions at the ends of the cylinder ($x = \pm L/2$) are

$$\begin{aligned} &i)\ u^o = 0\ @\ x = -\frac{L}{2},\ u^o = \Delta\ @\ x = +\frac{L}{2} \\ &ii)\ v^o = 0 \qquad iii)\ w^o = 0 \qquad iv)\ \frac{\partial w^o}{\partial x} = 0. \end{aligned} \tag{1}$$

The end displacement Δ is determined by enforcing axial equilibrium of the end enclosure at $x = +L/2$, namely,

$$\int_0^C N_x ds = p_o \pi ab, \tag{2}$$

where N_x is the axial force resultant within the cylinder (to be defined shortly), C is the circumference of the cylinder reference surface, and the cross-sectional area of the ellipse is πab. Physically, eq. 2 states that the net axial force due to the internal pressure times the cross-sectional area of the end enclosure must be balanced by the net axial force due to the axial force resultant.

Solution Approach

The solution procedure begins with the expression for the total potential energy of the cylinder, namely,

$$\pi = \frac{1}{2}\int_0^C \int_0^L N_x \varepsilon_x^o + N_s \varepsilon_s^o + N_{xs}\gamma_{xs}^o + M_x \kappa_x^o + M_s \kappa_s^o + M_{xs}\kappa_{xs}^o]\, dx\, ds. \tag{3}$$

The force and moment resultants in eq. 3 are defined by

$$\begin{aligned} N_x &= \int_{-H/2}^{H/2} \sigma_x d\zeta = A_{11}\varepsilon_x^o + A_{12}\varepsilon_s^o \\ N_s &= \int_{-H/2}^{H/2} \sigma_s d\zeta = A_{12}\varepsilon_x^o + A_{22}\varepsilon_s^o \\ N_{xs} &= \int_{-H/2}^{H/2} \tau_{xs} d\zeta = A_{66}\gamma_{xs}^o \\ M_x &= \int_{-H/2}^{H/2} \sigma_x \zeta d\zeta = D_{11}\kappa_x^o + D_{12}\kappa_s^o + D_{16}\kappa_{xs}^o \\ M_s &= \int_{-H/2}^{H/2} \sigma_s \zeta d\zeta = D_{12}\kappa_x^o + D_{22}\kappa_s^o + D_{26}\kappa_{xs}^o \\ M_{xs} &= \int_{-H/2}^{H/2} \tau_{xs} \zeta d\zeta = D_{16}\kappa_x^o + D_{26}\kappa_s^o + D_{66}\kappa_{xs}^o. \end{aligned} \tag{4}$$

where ζ is the through-thickness coordinate within the cylinder wall. As seen from the form of eq. 4, only symmetric and balanced laminates are being considered. The reference surface strains and curvatures in the energy expression are related to the reference surface displacements by

---

* Graduate Research Associate

† Professor, Associate Fellow, AIAA; Fellow, ASME; President, ASC

$$\varepsilon_x^o = \frac{\partial u^o}{\partial x} + \underline{\frac{1}{2}\left(\frac{\partial w^o}{\partial x}\right)^2} \qquad \kappa_x^o = -\frac{\partial^2 w^o}{\partial x^2}$$

$$\varepsilon_s^o = \frac{\partial v^o}{\partial s} + \frac{w^o}{R(s)} + \underline{\frac{1}{2}\left(\frac{\partial w^o}{\partial s}\right)^2} \qquad \kappa_s^o = -\frac{\partial^2 w^o}{\partial s^2} \qquad (5)$$

$$\gamma_{xs}^o = \frac{\partial u^o}{\partial s} + \frac{\partial v^o}{\partial x} + \underline{\left(\frac{\partial w^o}{\partial x}\right)\left(\frac{\partial w^o}{\partial s}\right)} \qquad \kappa_{xs}^o = -2\frac{\partial^2 w^o}{\partial x \partial s}$$

Note that the radius of curvature being a function of s in ε_s^o is what makes this problem different than that of a circular cylinder. The underlined terms in eq. 5 denote the geometric nonlinearities. These are the von Karman approximations to the fully nonlinear strain-displacement relations.

With the radius of curvature varying circumferentially, a closed-form solution to the problem is not easily found. Accordingly, an approximate solution is sought. To begin the approximate solution, the circumferential variation of the inverse radius of curvature is expanded, in a method suggested by Marguerre [1], in a cosine series, such that

$$\frac{1}{R(s)} \cong \sum_{i=0}^{I} a_{4i} \cos\frac{4i\pi s}{C}, \qquad (6)$$

where the coefficients a_{4i} are constants which depend on the specific cross-sectional geometry (semi-diameters a and b) and I is the number of terms needed to properly represent the variation of the inverse radius of curvature. The dependence of the reference surface displacements on the circumferential coordinate is approximated using the Kantorovich method by a harmonic series in a form inspired by the inverse radius of curvature, namely,

$$\begin{aligned}
u^o(x,s) &= u_o^o(x) + \sum_{n=1}^{N} u_n^o(x)\cos\frac{4n\pi s}{C} + \sum_{m=1}^{M} u_{N+m}^o(x)\sin\frac{4m\pi s}{C} \\
v^o(x,s) &= v_o^o(x) + \sum_{m=1}^{M} v_m^o(x)\cos\frac{4m\pi s}{C} + \sum_{n=1}^{N} v_{M+n}^o(x)\sin\frac{4n\pi s}{C} \\
w^o(x,s) &= w_o^o(x) + \sum_{n=1}^{N} w_n^o(x)\cos\frac{4n\pi s}{C} + \sum_{m=1}^{M} w_{N+m}^o(x)\sin\frac{4m\pi s}{C}.
\end{aligned} \qquad (7)$$

where M and N determine the number of terms in the various series. For an isotropic cylinder, sine terms would not be necessary for $u^o(x,s)$ and $w^o(x,s)$, while cosine terms would not be necessary for $v^o(x,s)$. The presence of the bending stiffness terms D_{16} and D_{26} makes inclusion of these terms necessary.

With eq. 6 and eq. 7, the displacements and the radius of curvature have been explicitly expressed in terms of the circumferential coordinate, s. Substituting the displacements of eq. 7 into the strains and curvatures of eq. 5, and these, in turn, into the stress and moment resultants of eq. 4, integration of the energy expression with respect to s can be performed. The integrand of the energy expression is then dependent on the coefficients in eq. 7, which are only a function of x. As a result, the energy expression can be written symbolically as

$$\begin{aligned}
\pi &= \int_{-\frac{L}{2}}^{+\frac{L}{2}} \left[\int_0^C U(x,s)ds\right]dx \\
&= \int_{-\frac{L}{2}}^{+\frac{L}{2}} F(y_i(x), y'_i(x), y''_i(x))dx, \; (i = 1, 3(N+M+1))
\end{aligned} \qquad (8)$$

In eq. 8 the $y_i(x)$ represent the functional coefficients in eq. 7 and $(\,)'$ represents differentiation with respect to the axial coordinate x. Although the integrand above is also a function of cylinder geometry, material properties, and the pressure, they are constants that are not involved in the variational process. Equating the first variation of the total potential energy to zero results in the Euler-Lagrange equations for the $y_i(x)$ and the associated variationally consistent boundary conditions at $x = \pm L/2$. The boundary conditions of eq. 1 translate into specifying values of $y_i(x)$ and $y_i'(x)$. Defining intermediate variables in order to reduce the system from a third-order to a first-order form, it is possible to obtain a set of coupled nonlinear first-order ordinary differential equations which are integrated by the finite-difference method using the IMSL subroutine DBVPFD, a variable-order, variable-step-size algorithm employing Newton's method. By rendering the governing Euler-Lagrange equations to first-order form, various derivatives of u^o, v^o, and w^o are directly available for computing reference surface strains and curvatures and force and moment resultants. More importantly, stresses as a function of x, s, and ζ can be computed.

Character of the Response

Though ultimate interest with elliptical cylinders is for application to aircraft fuselage structures, initial experimental work will take place with small scale cylinders. The displacement, strain, and stress response of these smaller cylinders must be understood before studies of large-scale cylinders can commence. To that end, in the present study numerical results will be shown

for eight and nine layer graphite-epoxy cylinders with semi-major diameters of 127.0 mm, ellipticities of 0.7, and lengths of 0.318 m. The material and geometric properties of a layer of graphite-epoxy are taken to be

$$E_1 = 130.0\ GPa \qquad E_2 = 9.70\ GPa$$
$$G_{12} = 5.00\ GPa \qquad \upsilon_{12} = 0.300 \qquad h = 0.1400\ mm \tag{9}$$

where h is the thickness of a single layer. The laminates considered are: quasi-isotropic, $[\pm 45/0/90]_S$; axially-stiff, $[\pm 45/0_2/90_{1/2}]_S$; circumferentially-stiff, $[\pm 45/90_2/0_{1/2}]_S$, where 0 deg. is the axial direction. These lay-ups were selected because each has at least one layer with its fibers in the axial direction, at least one layer with its fibers in the circumferential direction, and ±45 degree layers. Eight or nine layers is a reasonable number from the point of view of manufacturing the cylinders by hand on elliptical mandrels.

In order to demonstrate the influence of elliptical geometry, the basic responses of an elliptical cylinder subjected to internal pressure are compared with those of a circular cylinder. For this comparison the quasi-isotropic laminate is chosen and a geometrically linear analysis is used to compare reference surface displacements. Figure 2 illustrates axial, circumferential, and normal displacements as a function of the axial and circumferential coordinates. The displacements have been normalized by the laminate thickness H. An internal pressure of p_o=0.690 MPa is used to compute the results in these figures. The format of the fig. 2 illustrates the response of one-eighth of the cylinder. The coordinate locations have been normalized and, referring to fig. 1, the range of $0 \le x/L \le 0.5$ and $0 \le s/C \le 0.25$ is considered. Due to the presence of D_{16} and D_{26}, the problem does not exhibit octal symmetry. However looking at only one eighth of the cylinder provides a fairly accurate detailing of the response, and simplifies displaying the results. Implementing symmetry and anti-symmetry arguments for various responses, the response for the remainder of the cylinder can be envisioned.

Regarding the axial displacement, for an internally pressurized circular cylinder the axial displacement would be the net result of the pressure forcing the end enclosures apart and the Poisson effect due to circumferential expansion pulling them together. This results in a nearly linear axial displacement with the axial coordinate and, since the problem is axisymmetric, the axial displacement would not vary with s. Recall from the boundary conditions of eq. 1 that the axial displacement is zero at x/L = -0.5. At x/L = 0.5 the axial displacement is determined by eq. 2. Because of the nearly linear variation with x, the axial displacement at x/L = 0.5 would be approximately twice the value at x/L = 0. As seen in fig. 2, for the elliptical cylinder, the axial displacement response is not axisymmetric and is far from being linear with x. Along the crown of the cylinder, s/C=0, the axial displacement is positive, while along the side of the elliptical cylinder the axial displacement is actually negative at certain axial locations. Since the axial displacement changes signs with spatial location, there are some locations besides x=-L/2 where the axial displacement is zero. It should be noted, however, that the axial displacement at x/L=0 is practically independent of s, as it is at x/L=0.5, and the axial displacements at these locations differ by a factor of 2, as they would for the circular case.

For balanced symmetric laminates, an internally pressurized circular cylinder has no circumferential displacement response. However, as shown in fig. 2, the elliptical case shows circumferential movement away from the sides and toward the crown and keel of the cylinder, a response that clearly distinguishes an elliptical cylinder from a circular one and one that has consequences at the ends of the cylinder where displacements are constrained to be zero. Figure 2 illustrates another distinguishing difference between a circular and elliptical cylinder. With internal pressure the normal displacement of a circular cylinder is uniformly outward. In contrast, under internal pressure the elliptical cylinder moves outward at the crown and keel, but moves inward at the sides. The cylinder tends to become more circular. This also has important consequences at the ends of the cylinder.

To demonstrate the influence of orthotropy, or lamination sequence, circumferential strain is considered. As seen in fig. 3, particularly the upper left subfigure, the degree to which the circumferential strain varies with the s coordinate at the midspan is determined to a large degree by the laminate considered. Recall, the circumferential strain for a circular cylinder has no variation with the s coordinate, independent of lamination sequence. As seen in fig. 3, at midspan the circumferentially-stiff laminate mitigates, to a certain degree, the effect of ellipticity, as the strain does not vary much with s there. The circumferential strain for the axially-stiff and quasi-isotropic laminates varies more. Therefore, it appears that unlike a circular cylinder, the percentage of fibers in the circumferential direction in an elliptical cylinder controls the degree of variation with s of the circumferential strain at midspan.

To demonstrate the influence of geometric nonlinearities, circumferential curvature for the quasi-isotropic case is considered. The differences between linear and nonlinear analyses are easily visible in fig. 4. In the midspan region for the nonlinear analysis case there is a significant flattening along the crown of the cylinder.

Failure Analysis

In this section an evaluation of failure using the Hashin and maximum stress failure criteria is presented by considering geometrically linear and nonlinear analyses and axially-stiff, quasi-isotropic, and circumferentially-stiff cylinders. The failure criteria are used to assess the mode of failure (e.g., tensile or compressive fiber or matrix modes), the location of failure, and the pressure at failure.

The Hashin and maximum stress failure criteria are based on one-dimensional uniaxial and shear failure stresses which are denoted as follows:

σ_A^+ = tensile failure stress in the fiber direction

σ_A^- = compressive failure stress in the fiber direction (absolute value)

σ_T^+ = tensile failure stress transverse to the fiber direction

σ_T^- = compressive failure stress transverse to the fiber direction (absolute value)

τ_T = transverse failure shear stress

τ_A = axial failure shear stress

For graphite-epoxy typical values of the failure stresses are:

$$\begin{aligned} \sigma_A^+ &= 1.379\ GPa & \sigma_T^+ &= 50.0\ MPa \\ \sigma_A^- &= 1.241\ GPa & \sigma_T^- &= 200\ MPa \\ \tau_A &= 100.0\ MPa & \tau_T &= 100.0\ MPa \end{aligned} \tag{10}$$

The failure modes of the Hashin criterion can be denoted as follows:

Tensile Fiber Mode: $\sigma_{11} > 0$

$$\left(\frac{\sigma_{11}}{\sigma_A^+}\right)^2 + \frac{1}{\tau_A^2}(\sigma_{12}^2 + \sigma_{13}^2) < 1 \tag{11}$$

Compressive Fiber Mode: $\sigma_{11} < 0$

$$\frac{-\sigma_{11}}{\sigma_A^-} < 1 \tag{12}$$

Tensile Matrix Mode: $\sigma_{22} > 0$

$$\left(\frac{\sigma_{22}}{\sigma_T^+}\right)^2 + \left(\frac{\sigma_{23}}{\tau_T}\right)^2 + \frac{1}{\tau_A^2}(\sigma_{12}^2 + \sigma_{13}^2) < 1 \tag{13}$$

Compressive Matrix Mode: $\sigma_{22} < 0$

$$\frac{\sigma_{22}}{\sigma_T^-}\left[\left(\frac{\sigma_T^-}{2\tau_T}\right)^2 - 1\right] + \left(\frac{\sigma_{22}}{2\tau_T}\right)^2 + \left(\frac{\sigma_{23}}{\tau_T}\right)^2 + \frac{1}{\tau_A^2}(\sigma_{12}^2 + \sigma_{13}^2) < 1 \tag{14}$$

Hence, the cylinder is assumed to be safe from failure if all four left hand sides of eqs. 11-14 are less than unity, and failure is assumed to have occurred if any one of the four left hand sides equals unity. In the above the subscripts 1, 2, and 3 on the stresses denote principle material system stresses, conventional notation. The failure modes of the maximum stress theory can be denoted as follows:

Tensile Modes (σ_{11}, $\sigma_{22} > 0$):

$$\frac{\sigma_{11}}{\sigma_A^+} < 1 \qquad \frac{\sigma_{22}}{\sigma_T^+} < 1 \tag{15}$$

Compressive Modes (σ_{11}, $\sigma_{22} < 0$):

$$\frac{-\sigma_{11}}{\sigma_A^-} < 1 \qquad \frac{-\sigma_{22}}{\sigma_T^-} < 1 \tag{16}$$

Shear Modes:

$$\frac{|\sigma_{23}|}{\tau_T} < 1 \qquad \frac{|\sigma_{13}|}{\tau_A} < 1 \qquad \frac{|\sigma_{12}|}{\tau_A} < 1 \tag{17}$$

With this form of the failure criterion, the cylinder is assumed to be safe from failure if all seven of the left hand sides of eqs. 15-17 are less than unity, and failure is assumed to occur if any one of the seven left hand sides equals unity.

In order to make use of either failure criterion, computation of the inplane and interlaminar shear stresses in the principal material coordinate system are necessary. The computation of the inplane stresses follows the standard approach of the classical lamination theory [2]. Computation of the interlaminar stresses is more complicated. For the geometrically linear case, the equilibrium equations of elasticity were integrated through the thickness of the cylinder wall to obtain expressions for the interlaminar stresses. These stresses were used in the failure analysis and were found to have minimal influence on the failure predictions and could have been ignored without introducing significant error. The equilibrium equations of elasticity for the geometrically nonlinear case are quite complex compared to the linear case. Therefore, as an approximation, the interlaminar stresses for the geometrically nonlinear failure analysis were computed from the geometrically linear equations. In light of the minimal impact of the interlaminar stresses on the failure analysis, this approximation was felt to be justified.

To compute the predicted failure pressure using the geometrically linear theory, the analyses were conducted using an internal pressure p_o of 0.690 MPa. The lefthand sides of the two failure criteria were then

evaluated as a function of axial, circumferential, and through-thickness location within the cylinder wall. For each criteria the left hand side that was closest to unity identified the failure location and failure mode. The pressure to cause failure was then determined by scaling the 0.690 MPa.

Two issues were immediately obvious from the linear failure analysis. First, as mentioned above, the interlaminar stresses did not contribute to failure. The interlaminar stress components were much smaller than the inplane components, and although the interlaminar failure stresses were small, the components contributed little to the polynomials of the Hashin criterion and did not play a role in the maximum stress criterion. Second, both the Hashin and maximum stress criteria predicted failure to be due to inplane matrix failure, i.e., matrix cracking, due primarily to tensile stress perpendicular to the fibers. Since matrix cracking is not generally catastrophic, it was felt important to look at other failure conditions. Therefore, the pressure to cause fiber failure was also computed. Ignored was any degradation in properties due to matrix failure occurring before fiber failure.

The upper quarter of table 1 summarizes the findings of the linear analyses for the three laminates and the Hashin failure criterion. The table shows the failure pressure, p_f, failure location, failure mode, and the ratio of the bending component of the stress at the failure location, σ_b, to the inplane component of stress there, σ_s. Both the matrix and fiber failures are considered. All failures occurred at two circumferential locations and both ends of the cylinder, though only one location is listed in the table. As can be seen from the upper left portion of the table, for the axially-stiff cylinder, matrix failure occurred at 0.896 MPa at the inner interface of the inner layer, i.e., loc=1/1. In this particular instance the term 'inner interface' is somewhat misleading because there is no interface between layers at the inner interface of layer 1, the inner +45° layer. The inner interface of layer 1 is the inner radial location of the cylinder wall. Circumferentially, the failure occurred about one-third of the distance from the crown to the side (s/C = -0.07, see fig. 1). The failure mode was failure due to high stresses perpendicular to the fibers in the plane of the layer, i.e., σ_2. In this particular situation, the component of σ_2 due to bending effects was 3.3 times larger than the component of σ_2 due to inplane effects. Since failure occurred at the ends of the cylinder, large bending effects were to be expected due to the bending boundary layers there. For fiber failure, a stress of almost twice the level was required, 1.669 MPa, and the mode of failure was compression in the fiber direction. The failure occurred in layer 9, the outer layer, at interface 2, the outer interface, i.e., the outer radius of the cylinder. This was a shift from the inside of the cylinder for matrix failure to the outside for fiber failure. The effect of bending was also reduced for the fiber failure. The characteristics of the failure for the quasi-isotropic cylinder were similar to those for the axially-stiff cylinder. The location of failure, the near-doubling of the pressure to produce fiber failure, and the shift from an inner location for matrix failure to an outer location for fiber failure were all similar. The character of failure for the circumferentially-stiff cylinder was somewhat different than the other two. The failure pressure for matrix failure was lower, and the failure locations were different. Matrix failure occurred in a layer outside the reference surface, layer 7, a 90 deg. layer, at the sides of the cylinder, $s/C = \pm 0.25$. At that location bending effects were not as important as inplane effects, as indicated by the ratio of 0.33/1. An examination of the details of the deformations of the ellipse (not shown) reveal that at the crown and keel bending deformations are more pronounced than at the sides, so the reduced role of bending effects at the sides of the cylinder was not surprising. Also, layer 7 was closer to the reference surface, a location where there were less bending effects, than, say, at layer 9. For fiber failure for the circumferentially-stiff cylinder, fiber compressive failure was again the mode, and this occurred at the outer radial location in layer 9, a +45 deg. layer. The circumferential location was about one-quarter of the distance from the crown to the side.

To compute the failure pressure using the geometrically nonlinear analysis, iteration was be used, each iteration using a different internal pressure. The first step in the iteration process followed the failure analysis for the geometrically linear case, namely, the analysis was conducted for a pressure of p_o=0.690 MPa. Then, considering the maximum stress criterion as an example, the seven left-hand sides of the failure criterion were computed, and using p_o=0.690 MPa the failure pressure, p_f, was computed by scaling. The geometrically nonlinear analysis was then conducted using this predicted failure pressure, i.e., now p_o was the failure pressure predicted from the first step. The seven left-hand sides were again computed and were used to compute a new failure pressure. This procedure was repeated until the calculations were considered converged to the failure pressure. A similar iteration procedure was used for the Hashin criterion and the four left-hand sides in that criterion.

The second quarter of table 1 summarizes the findings of the nonlinear analyses for the three laminates and the Hashin failure criterion. Considering the axially-stiff case, it is seen that relative to the geometrically linear analyses, geometric nonlinearities led to

slightly higher failure pressures, e.g., for matrix failure 0.931 MPa vs. 0.896 MPa. As in the linear case, for matrix failure the tensile stress component σ_2 was responsible for failure, and for fiber failure, a compressive σ_1 was responsible. For both matrix and fiber failure the through-thickness locations were identical to the linear case and the circumferential location of failure moved just slightly away from the crown. The ratio of the bending component of stress to the inplane component was slightly lower for the geometrically nonlinear case. This was felt to be due to the flatten effect caused by geometric nonlinearities. The comments for the axially-stiff cylinder apply to the quasi-isotropic cylinder. Regarding the circumferentially-stiff case: although geometric nonlinearities did not appear to significantly influence matrix failure, they did influence fiber failure predictions. The predicted mode changed from fiber compression for the linear analysis to fiber tension for the nonlinear analysis. Additionally, the location for the nonlinear analysis was near the sides as opposed to being in the crown area. The reason that the linear and nonlinear analyses did not agree for the fiber failure condition is that in the Hashin criterion for tensile fiber failure the shear stress τ_{12} is involved. For the nonlinear analysis the value of τ_{12} was greater than for the linear analysis and the values of tensile σ_1 and τ_{12} near the side of the cylinder outweighed the high value of fiber compression stress in the crown region.

The bottom half of table 1 is a summary of using the maximum stress criterion to predict failure. An examination of the maximum stress criterion prediction reveals that many entries are similar, if not identical, to the Hashin criterion prediction. For the matrix failure the stress component σ_2 was so dominant that the Hashin criterion reduced, in effect, to the maximum stress criterion. The additional terms in the Hashin criterion had little influence. For fiber compression failure the Hashin criterion is identical to the maximum stress criterion, so the entries would be identical in those cases. The primary difference occurred with fiber failure for the circumferentially-stiff cylinder. Whereas with the nonlinear analysis the Hashin criterion predicted fiber tensile failure at the outer radial location near the sides, for the reasons discussed above, the maximum stress criterion prediction was similar to the linear analyses for both the Hashin and maximum stress criteria, namely fiber compression at the outer radial location in the crown region.

A comment is in order regarding the failures occurring in the ±45° layers. First, these layers are at the extreme inner and outer locations, so bending effects are most severe at these locations. However, another factor influences the ±45° layers. In fig. 2 it was seen that with the elliptical geometry there is a tendency to have a circumferential displacement component $v°$. However, at the ends $v°$ is restrained to be zero, requiring an inplane shear force resultant N_{xs} to achieve this. The transformation of the shear effect of N_{xs} into the principal material directions of the ±45° layer leads directly to a stress component σ_2. This adds to the magnitude of σ_2 in these off-axis layers. Interestingly, N_{xs} is zero at s/C = 0, 0.25, 0.5, and 0.75, and has extreme values roughly halfway between these circumferential locations.

Alternate View of Failure Predictions

With composite materials there is often scatter in the results of tests designed to determine failure stresses. Considering the failure stress of a composite material to be exactly a certain level is somewhat unrealistic. The scatter is due to small unpredictable irregularities in the microstructure of composites and possible anomalies in the manufacturing process. As a result, the location with the highest stress may not fail first. A slightly lower stress at another location, coupled with a microstructural irregularity, could lead to lower failure stress levels. To that end, the geometrically nonlinear failure analysis was used to compute the locations within the ellipse where the seven left-hand sides in the Hashin failure criterion were within 20% of the failure level, i.e., the left-hand sides of eqs. 11-14 were in the range 0.80 to 1.00, with 1.00 corresponding to the cases discussed in table 1.

Figures 5 through 7 show the locations where the Hashin failure criterion is within 20% of equaling unity for the axially-stiff, quasi-isotropic, and circumferentially-stiff laminates, respectively. The location of first failure, i.e., matrix failure from table 1, is also shown. The stresses were evaluated using nonlinear analysis at the matrix failure pressure, p_f. In each figure a greatly distorted view of the crown section of the cylinder wall through the thickness from $-0.5 \le \zeta/H \le 0.5$ and around the circumference from $-0.25 \le s/C \le 0.25$ provides a visual display of the points within 20% of failure. It is important to note that all these points are at the clamped end of the cylinder, x/L = 0.50.

Referring to fig. 5 and, as indicated in the table, the maximum left-hand side value, or initial failure point, for the axially-stiff case is located at the first layer, a +45° layer, at the inner radial location of the cylinder at s/C=-0.09. Considering points where the left-hand side is less than 1.00, the points are dispersed circumferentially on both sides of the initial failure point in the first layer at the inner radial location. There are also points on both sides of the interface between the first and second layers. An alternative interpretation of the

spatial distribution of the points is that if the pressure is increased beyond the value to predict failure at point 1, then there will be failure at another location. Further increases in pressure would lead to failure at other locations. It is felt that the geometric distribution of points would represent the progression of damage as the pressure increases beyond the value necessary to have the Hashin criteria to equal 1.00. If this interpretation is correct, then, matrix cracking will accumulate in layer 1 at the inner radial location (ζ/H=-0.5) in the range $-0.16 \leq s/C \leq 0$. There will also be cracking in layer 2 at the interface between the 1st and 2nd layers (ζ/H=-0.389). All these failures would be due to high values of σ_2.

Figure 6 shows a very similar interpretation for the quasi-isotropic case, though there are some failures at outer radial locations (+45° layer). The circumferentially-stiff case in fig. 7 is different. Using the 'progression of damage' interpretation of the locations of the points, it is seen failure spreads from the two initial points at the sides and moves toward the crown (s/C=0) along the interfaces between layers 6, 7, and 8, and at the outer radial location. Several issues must be kept in mind when considering figs. 5 through 7. First, it could be that properly accounting for material degradation due to matrix cracking would result in even greater spread of the locations. The reduction of stiffness due to matrix cracking could cause stresses to increase in nearby locations, thereby enhancing failure. Also, as stated, the locations shown in figs. 5 through 7 are at the ends of the cylinder (x/L = ±0.50). At some point failure will progress axially as well as circumferentially. Properly accounting for material degradation may show this happens before there is a significant circumferential progression. Finally, the Hashin criterion or any criterion for that matter, reaches unity at the inner or outer radial location of a particular layer. This is because for every layer the bending strains vary linearly with thickness and thus take on extreme values at the inner and outer radial locations, never at midlayer locations. However, even though the stresses are the highest at the inner or outer radial location and lead to failure there, failure probably propagates through the entire thickness of the layer. Thus, the matrix failure at the locations shown in fig. 5, for example, really represent a crack through the thickness of the layer. For the condition shown in fig. 5, this means there are matrix cracks through the two inner layers. The internal pressure is thus developing a leakage path through the thickness of the wall. Also, crack mechanics may well change because the internal pressure is acting on the crack faces. This may lead to further cracking, such as crack turning at the interfaces. If, however, an internal bladder or sealant is used, the scenario is likely different.

Finally, it is important to take note of the fact that the matrix and fiber failures in table 1, and the scattering of points in figs. 5-7, are associated with particular circumferential locations. This is, of course, because the stresses vary with circumferential position. In effect, there is a stress concentration as the cylinder is traversed in the circumferential direction. As a result, the cylinder will be prone to fail at a particular circumferential location. In contrast, the circumferential location of failure of a circular cylinder would depend totally on the location of material imperfections. So on the one hand an elliptical cylinder is a disadvantage because of the presence of a stress concentration, but on the other hand, it can be determined where strengthening should be applied to increase the failure pressure.

Acknowledgments

The work reported on herein was supported by grant NAG-1-1895 from the Structural Mechanics Branch of the NASA-Langley Research Center to Virginia Tech. The Virginia Space Grant Consortium provided additional support. The authors sincerely appreciate the financial support from both sources. The NASA grant monitor was Dr. James H. Starnes, Jr.

References

1. Marguerre, K., "Stability of the cylindrical shell of variable curvature," NASA TM 1302, 1951.
2. Hyer, M.W., *Stress Analysis of Fiber-Reinforced Composite Materials*. WCB/McGraw-Hill, New York, 1998.

Table 1. Failure pressure, location, and mode for elliptical graphite-epoxy cylinders, geometrically linear and nonlinear analyses, two failure modes, two failure criteria

			Axially-Stiff		Quasi-Isotropic		Circumferentially-Stiff	
			Matrix	Fiber	Matrix	Fiber	Matrix	Fiber
Hashin	linear	p_f MPa	0.896	1.669	0.903	1.579	0.738	1.551
		loc*	1/1 (+45)	9/2 (+45)	1/1 (+45)	8/2 (+45)	7/2 (90)	9/2 (+45)
		s/C**	-0.07	-0.08	-0.07	-0.07	±0.25	-0.06
		mode σ_x/σ_s	$+\sigma_2$ 3.3/1	$-\sigma_1$ 1.25/1	$+\sigma_2$ 4/1	$-\sigma_1$ 1.3/1	$+\sigma_2$ 0.33/1	$-\sigma_1$ 1.25/1
	nonlinear	p_f MPa	0.931	1.862	0.924	1.800	0.724	1.710
		loc*	1/1 (+45)	9/2 (+45)	1/1 (+45)	8/2 (+45)	7/2 (90)	9/2 (+45)
		s/C**	-0.09	-0.11	-0.10	-0.10	±0.25	0.24
		mode σ_x/σ_s	$+\sigma_2$ 2.7/1	$-\sigma_1$ 1.2/1	$+\sigma_2$ 2.2/1	$-\sigma_1$ 1.2/1	$+\sigma_2$ 0.38/1	$+\sigma_1$ 0.59/1
maximum stress	linear	p_f MPa	0.938	1.668	0.938	1.579	0.738	1.572
		loc*	1/1 (+45)	9/2 (+45)	1/1 (+45)	8/2 (+45)	7/2 (90)	9/2 (+45)
		s/C**	-0.07	-0.08	-0.08	-0.07	±0.25	-0.06
		mode σ_x/σ_s	$+\sigma_2$ 3.3/1	$-\sigma_1$ 1.25/1	$+\sigma_2$ 2.86/1	$-\sigma_1$ 1.3/1	$+\sigma_2$ 0.33/1	$-\sigma_1$ 1.25/1
	nonlinear	p_f MPa	0.965	1.862	0.958	1.800	0.724	1.834
		loc*	1/1 +45)	9/2 (+45)	1/1 (+45)	8/2 (+45)	7/2 90)	9/2 (+45)
		s/C**	-0.09	-0.11	-0.10	-0.10	±0.25	-0.09
		mode σ_x/σ_s	$+\sigma_2$ 2.3/1	$-\sigma_1$ 1.2/1	$+\sigma_2$ 2.2/1	$-\sigma_1$ 1.2/1	$+\sigma_2$ 0.38/1	$-\sigma_1$ 1.28/1

* Location is given as layer number/interface, where 1 is the inner-most layer and 1 denotes the inner and 2 the outer interface. The fiber direction of the layer is shown in parenthesis. 0° is the axial direction.

** All failures occur at the ends of the cylinders: s/C=0 is crown, s/C=±0.25 are sides, C=circumference, s=arclength measure

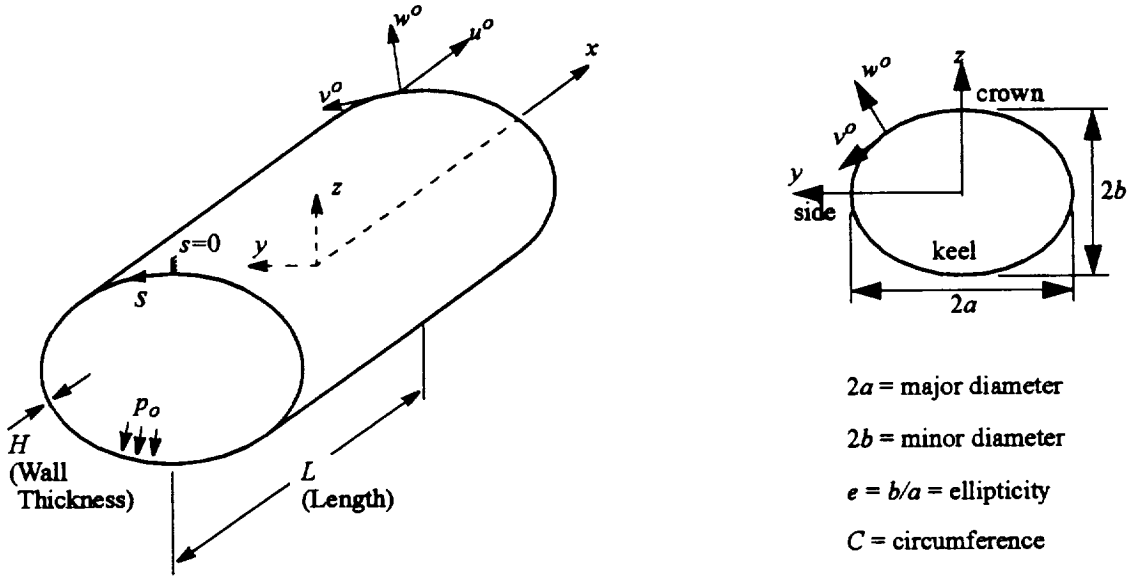

Figure 1. Problem description, nomenclature, and geometry of an elliptical cylinder.

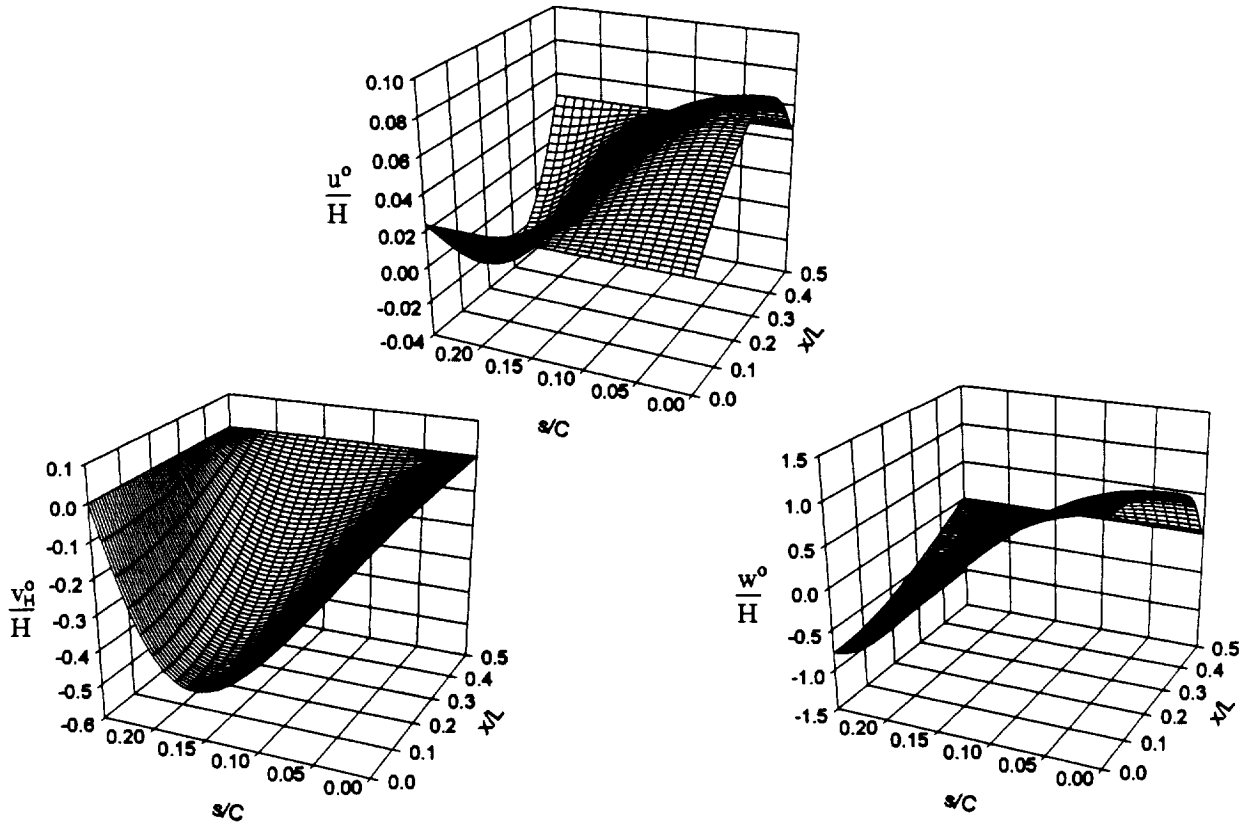

Figure 2. Effect of elliptical geometry on the displacements of an elliptical cylinder.

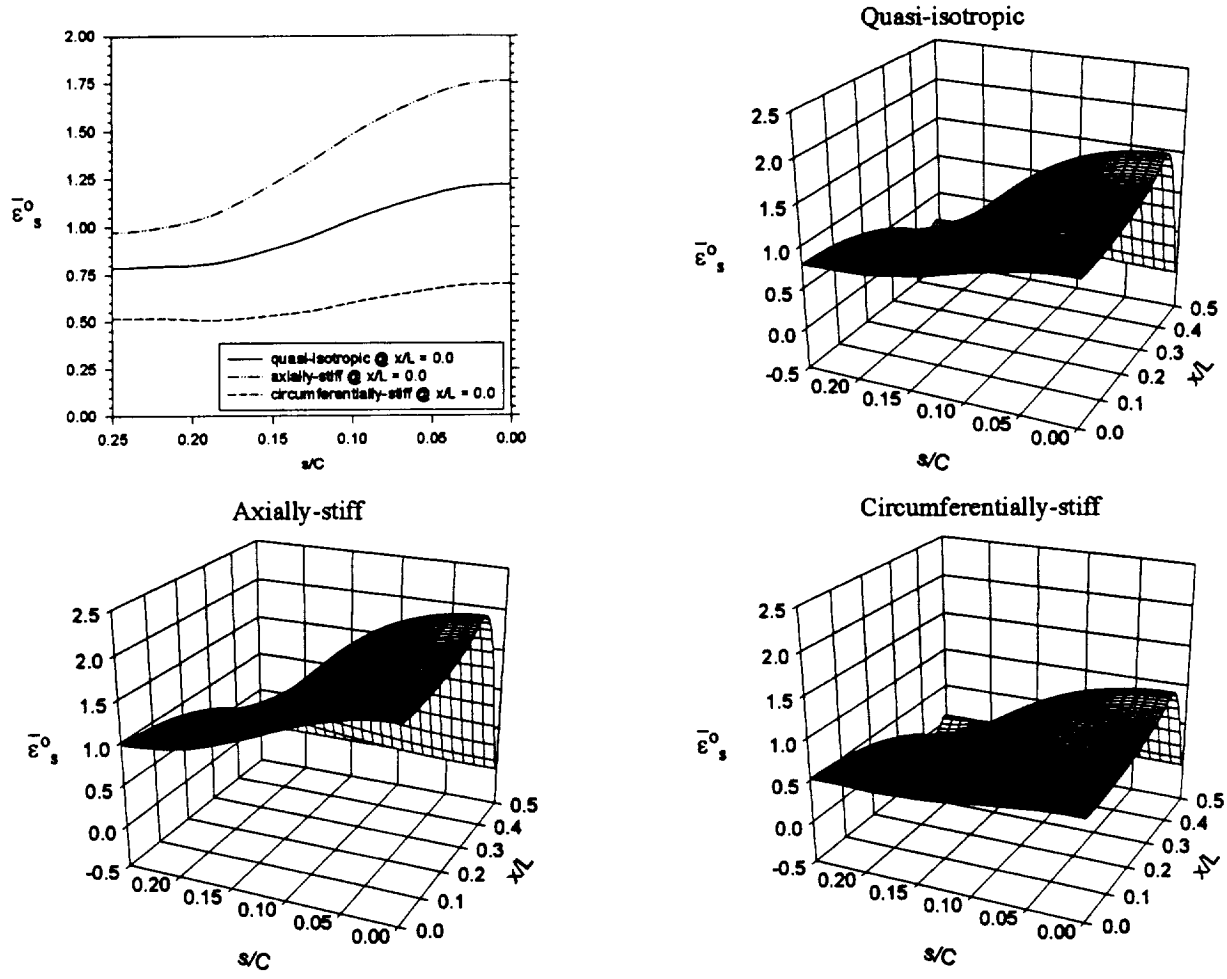

Figure 3. Influence of orthotropy on the circumferential strain.

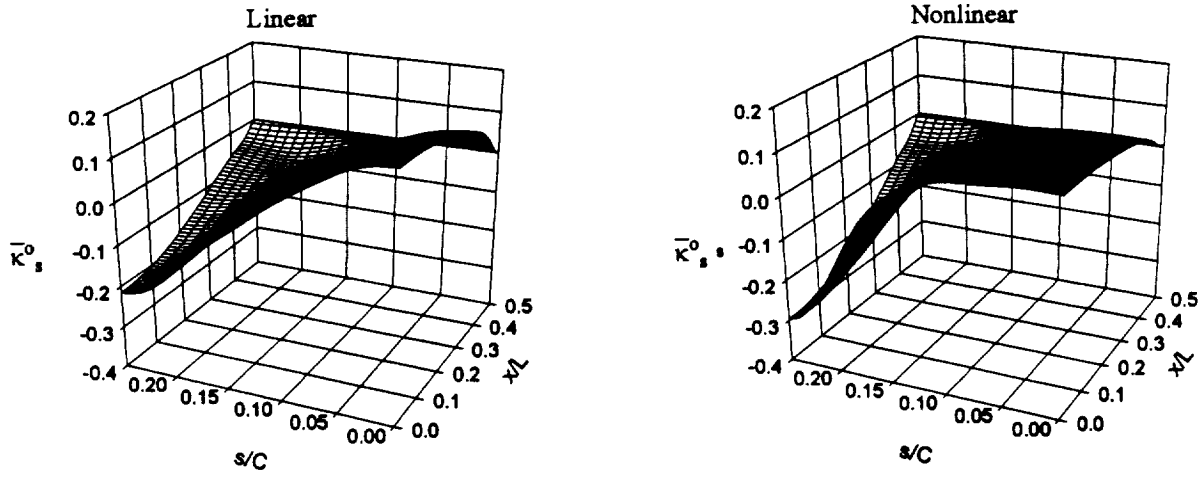

Figure 4. Effect of geometric nonlinearities on the circumferential curvature.

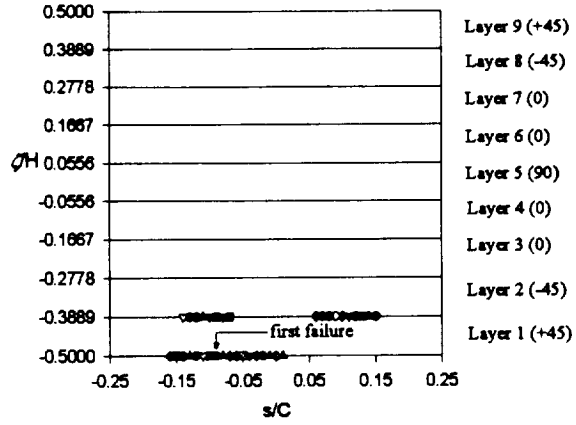

Figure 5. Points within 20% of failure criterion equaling unity, axially-stiff laminate, nonlinear analysis, x/L=0.5, Hashin Criterion

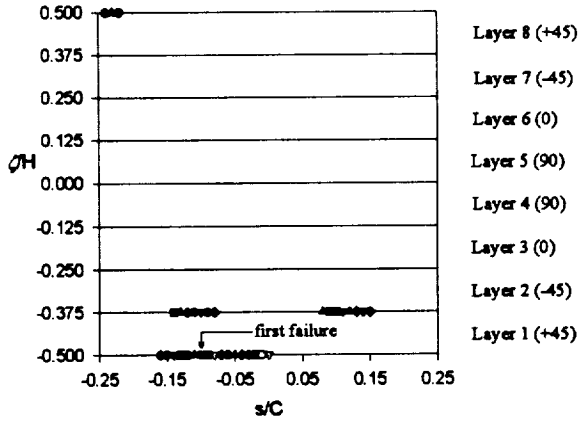

Figure 6. Points within 20% of failure criterion equaling unity, quasi-isotropic laminate, nonlinear analysis, x/L=0.5, Hashin criterion

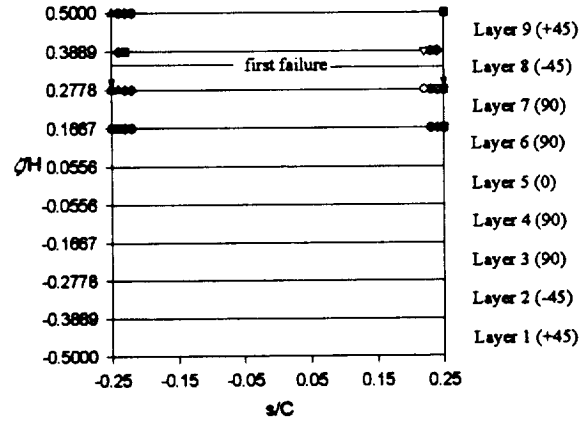

Figure 7. Points within 20% of failure criterion equaling unity, circumferentially-stiff laminate, nonlinear analysis, x/L=0.5, Hashin criterion

CENTER FOR COMPOSITE MATERIALS AND STRUCTURES

CCMS-99-09

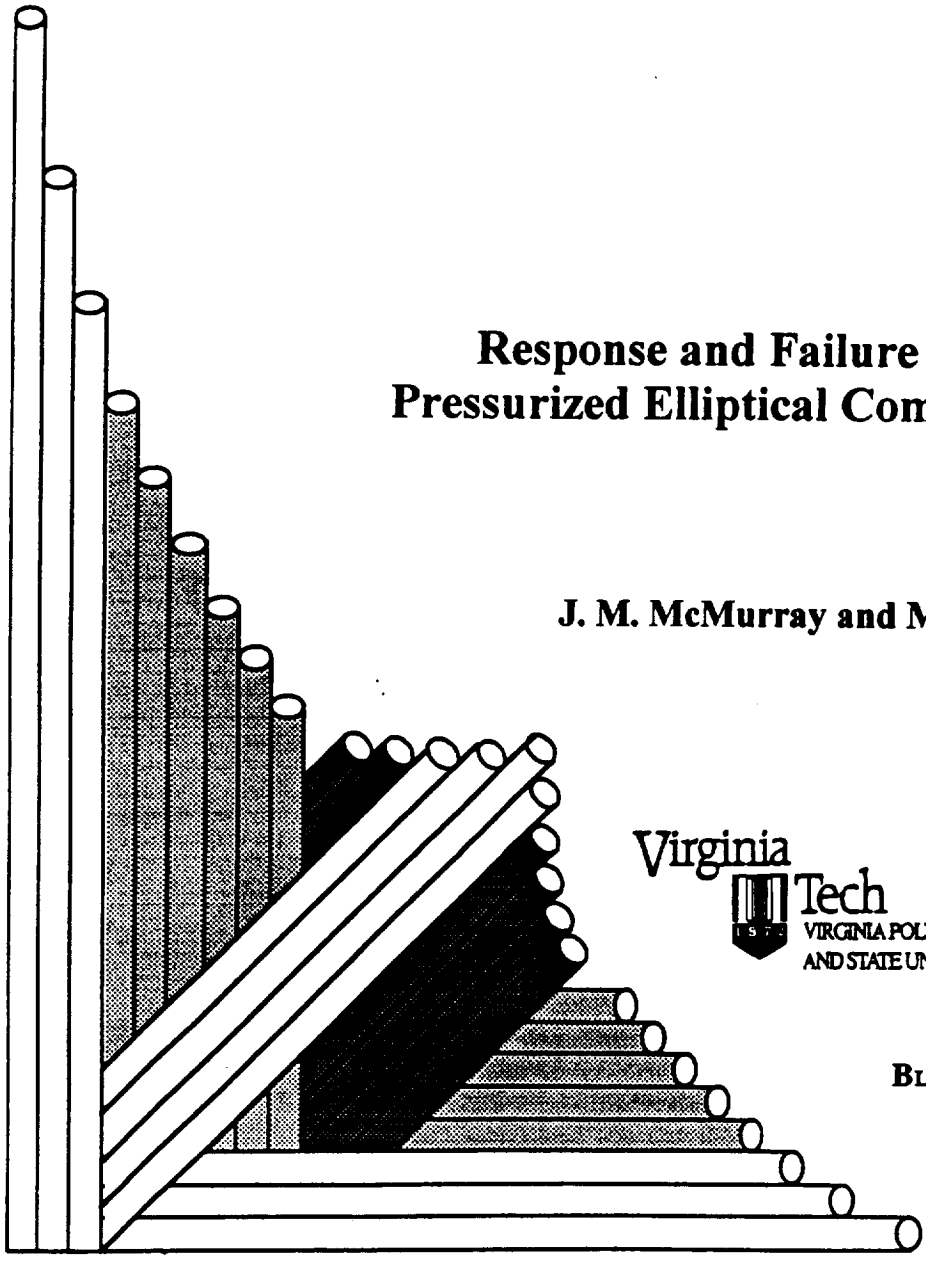

Response and Failure of Internally Pressurized Elliptical Composite Cylinders

J. M. McMurray and M. W. Hyer

Virginia Tech
VIRGINIA POLYTECHNIC INSTITUTE AND STATE UNIVERSITY

BLACKSBURG, VIRGINIA 24061

September 1999

RESPONSE AND FAILURE OF INTERNALLY PRESSURIZED ELLIPTICAL COMPOSITE CYLINDERS

Jennifer M. McMurray
Michael W. Hyer

Department of Engineering Science and Mechanics
Virginia Polytechnic Institute and State University
Blacksburg VA 24061

Sponsoring Agency:
National Aeronautics and Space Administration
Langley Research Center
Structural Mechanics Branch

September 1999

ABSTRACT

Presented is an overview of a semi-analytical solution which was developed to study the response of internally pressurized elliptical composite cylinders with clamped boundaries. Using a geometrically linear analysis and the solution scheme, the response of a quasi-isotropic elliptical cylinder is compared with the response of a quasi-isotropic circular cylinder in order to study the effects of elliptical geometry. The distinguishing features of the response of an elliptical cylinder are the inward normal displacement at the ends of the major diameter that occur despite the outward force of the internal pressure, the presence of circumferential displacements, and the presence of inplane shear strains. These effects lead to spatial variations, including sign reversals, of a number of displacement, strain, and curvature responses. The responses of a quasi-isotropic elliptical cylinder evaluated using a geometrically linear analysis are then compared to the responses evaluated using a geometrically nonlinear analysis. It is shown that geometric nonlinearities tend to flatten certain responses in the crown region, and reduce the magnitude of certain responses in the boundary region. To study the influence of material orthotropy, the responses of axially-stiff and circumferentially-stiff elliptical cylinders evaluated using geometrically nonlinear analyses are examined. It is shown that in some instances material orthotropy can be used to mitigate the influence of the elliptical geometry and make particular responses look like those of a circular cylinder. An evaluation of failure using the maximum stress and Hashin failure criteria and geometrically linear and nonlinear analyses is presented for elliptical cylinders. These failure criteria involve interlaminar shear stresses which are computed by integrating the equilibrium equations of elasticity through the thickness of the cylinder wall. The failure criteria are used to assess the mode of failure (e.g., tensile or compressive fiber or matrix modes), the location of failure, and the pressure at failure. Both criteria predict first failure to occur at the clamped boundaries

because of matrix cracking due to stresses in the plane of the cylinder wall. The predicted failure pressures and circumferential locations are very similar for the two criteria, and the nonlinear analyses predict slightly higher pressures at somewhat different circumferential locations. First fiber failure is also considered. For this failure the two criteria predict similar failure scenarios for the linear analyses, but they differ in their predictions for the nonlinear analyses. Specifically, using the maximum stress criterion, the circumferentially-stiff elliptical cylinder is predicted to fail due to fiber compression, but the Hashin criterion predicts failure to be due to fiber tension, and at a different circumferential location. Also, first fiber failure pressures are at least a factor of two greater than the first matrix failure pressure.

Keywords: geometrically nonlinear effects, influence of orthotropy, influence of elliptical geometry, internal pressure, maximum stress failure theory, Hashin failure theory

ACKNOWLEDGEMENTS

This report constitutes the thesis of Jennifer M. McMurray for the partial fulfillment of the requirements for a Master of Science in Engineering Mechanics at Virginia Polytechnic Institute and State University. Prof. Michael W. Hyer was the thesis advisor. The work was conducted with funding from grant NAG-1-1895 from the Structural Mechanics Branch at the NASA-Langley Research Center. The funding is greatly appreciated by both authors. Also, the helpful discussions with the grant monitor, Dr. James H. Starnes, Jr. are sincerely appreciated.

Table of Contents

List of Figures

List of Tables

Chapter 1 Introduction

Due to their high specific strength and stiffness properties, fiber-reinforced thin-walled composite cylinders have numerous applications in the aerospace industry as structural elements. Although circular cylinders are most commonly used and studied, future transport fuselages could have noncircular cross sections, in particular, oval or elliptical cross sections. A noncircular cross section could be beneficial for blended wing-fuselage structural concepts, improved aerodynamics, and increased payload capacity. A number of issues associated with noncircular cross sections must be addressed. These issues include the effect of noncircular geometry, geometric nonlinearities, boundary conditions, loading, and material orthotropy. This study is concerned with internal pressurization, which is an important loading for fuselage structures, and cylinders with elliptical cross sections. There are a number of fundamental issues with this particular loading. For example, a circular cylinder subjected to internal pressure expands outward, whereas, an elliptical cylinder becomes more circular in shape, as shown in fig. 1-1. For an elliptical cylinder, deflections are actually inward at certain circumferential locations. Additionally, with internal pressure there is a net axial force on each end of the cylinder. Assumptions regarding how this force is reacted by the cylinder have an impact on the assumed conditions at the boundary. These concerns are addressed in the present study by using a semi-analytical approach to obtain numerical results. These results are then used to illustrate the differences between a circular and elliptical cross section cylinders, and geometrically linear and nonlinear effects. Also, the influence of orthotropy is discussed, specifically, quasi-isotropic, axially-stiff, and circumferentially-stiff

graphite-epoxy laminates are considered. Failure is addressed. The semi-analytical approach, developed in a previous study [1], utilizes the Kantorovich and finite-difference techniques to solve the governing equations. A description of the details of the specific problem and of the semi-analytical approach is described in the next two sections. The following section outlines the contents of the remainder of this document.

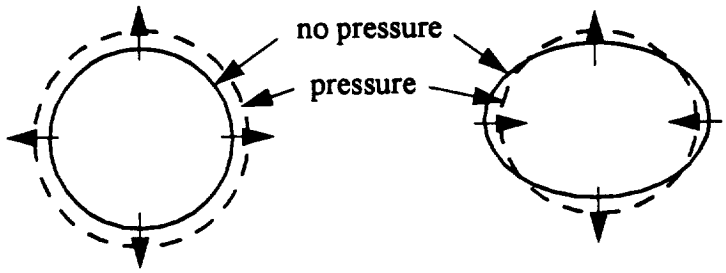

Figure 1-1. Effect of internal pressure on cross-sectional deformation of an ellipse.

1.1 Problem Description

The problem considered consists of a cylinder described in fig. 1-2, with a, b, and L denoting, respectively, the semi-major diameter, semi-minor diameter, and axial length of the cylinder reference surface. The degree of ellipticity, e, is defined here as the ratio of the semi-minor and major diameters, b/a. Alternatively, b/a can be thought of as the cross-sections aspect ratio. The cylinders considered here are symmetrically laminated and have an ellipticity of 0.7 and 1.0, the latter corresponding to a circular cylinder. The wall thickness of the cylinder is denoted by H and the internal pressure by p_o. The upper part of the cross-section is referred to as the crown, the lower part as the keel, and the sides are referred to as the sides.

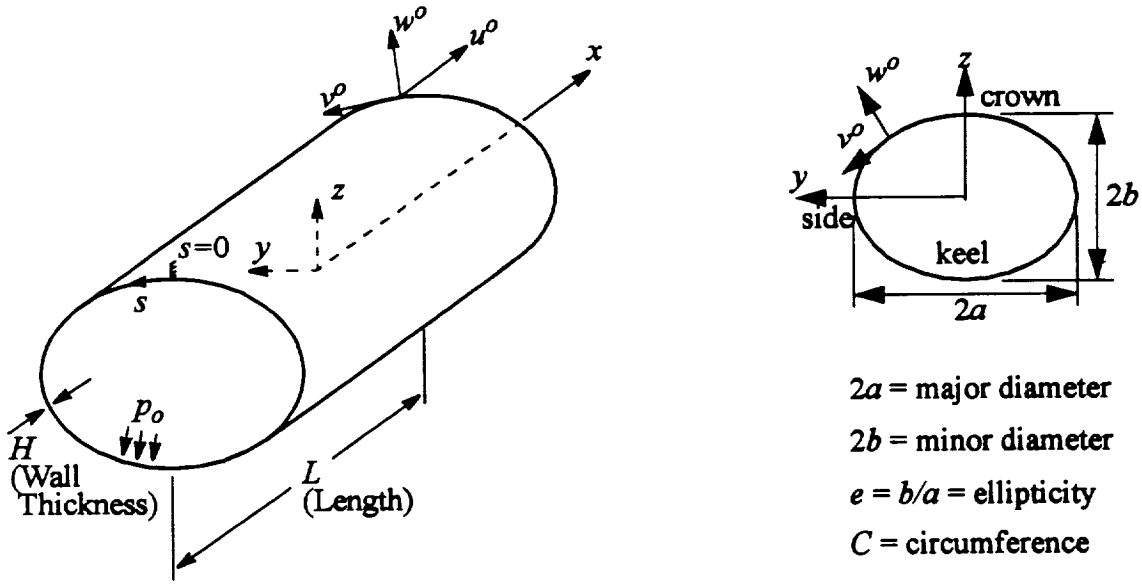

Figure 1-2. Problem description, nomenclature, and geometry of an elliptical cylinder.

The cross sectional shape of the cylinder at the reference surface, or midwall location, is an ellipse lying in the global y-z plane described by

$$\frac{y^2}{a^2} + \frac{z^2}{b^2} = 1. \tag{1.1}$$

The maximum and minimum radii of curvature are

$$R_{MAX} = \frac{a^2}{b} \qquad \text{and} \qquad R_{MIN} = \frac{b^2}{a}, \tag{1.2}$$

which occur at the ends of the semi-minor and -major axes, respectively. Locations on the reference surface are identified by coordinates (x,s), where x is the axial coordinate, measured from the midspan location, and s is the circumferential arc-length coordinate, measured counterclockwise from the top, or crown, of the cylinder. The reference surface displacement in the axial and circumferential directions are denoted as $u^o(x,s)$ and $v^o(x,s)$, respectively, while the normal displace-

ment is denoted by $w^o(x,s)$. Herein, only thin cylinders are discussed, and the orientation of the layers is defined relative to the $+x$ axis in the laminate nomenclature. Here it will be assumed the cylinder ends are clamped to a rigid end plate or bulkhead which can move axially. Accordingly, clamped-clamped boundary conditions are applied to each end of the cylinder, with the exception of allowing the end at $x = +L/2$ end to expand uniformly in the axial direction with displacement Δ. The end at $x = -L/2$ cannot move axially in order to restrict axial rigid body translation. Formally, the boundary conditions at the ends of the cylinder ($x = \pm L/2$) are as follows:

$$\begin{aligned} &\text{i)}\ u^o = 0\ @\ x = -\frac{L}{2},\ u^o = \Delta\ @\ x = +\frac{L}{2} \\ &\text{ii)}\ v^o = 0 \\ &\text{iii)}\ w^o = 0 \\ &\text{iv)}\ \frac{\partial w^o}{\partial x} = 0. \end{aligned} \tag{1.3}$$

The end displacement Δ is determined by enforcing axial equilibrium of the end enclosure at $x = +L/2$, namely,

$$\int_0^C N_x ds = p_o \pi a b, \tag{1.4}$$

where N_x is the axial force resultant within the cylinder (to be defined shortly), C is the circumference of the cylinder reference surface, and the cross-sectional area of the ellipse is πab. Physically, eq. 1.4 states that the net axial force due to the internal pressure times the cross-sectional area of the end enclosure must be balanced by the net axial force due to the axial force resultant.

1.2 Solution Approach

The semi-analytical solution procedure begins with the expression for the total potential energy of the cylinder. The total potential energy is given by

$$\pi = \frac{1}{2}\iiint[\sigma_x\varepsilon_x + \sigma_s\varepsilon_s + \tau_{xs}\gamma_{xs}]dxdsd\zeta - \iint p_o w^o dxds, \tag{1.5}$$

where ζ is the local through-thickness coordinate within the cylinder wall. The coordinate ζ ranges from $-H/2 \le \zeta \le +H/2$ and is zero at the reference surface. Of course the axial coordinate has the limits from $-L/2 \le x \le +L/2$, and the circumferential coordinate has the limits from $0 \le s \le C$. As evidenced by the integrand in eq. 1.5, the plane-stress assumption is being used. The strains in the energy expression are given by

$$\begin{aligned} \varepsilon_x &= \varepsilon_x^o + \zeta\kappa_x^o \\ \varepsilon_s &= \varepsilon_s^o + \zeta\kappa_s^o \\ \gamma_{xs} &= \gamma_{xs}^o + \zeta\kappa_{xs}^o, \end{aligned} \tag{1.6}$$

where the reference surface strains and curvatures are related to the reference surface displacements by

$$\varepsilon_x^o = \frac{\partial u^o}{\partial x} + \underline{\frac{1}{2}\left(\frac{\partial w^o}{\partial x}\right)^2} \tag{a}$$

$$\varepsilon_s^o = \frac{\partial v^o}{\partial s} + \frac{w^o}{R(s)} + \underline{\frac{1}{2}\left(\frac{\partial w^o}{\partial s}\right)^2} \tag{b}$$

$$\gamma_{xs}^o = \frac{\partial u^o}{\partial s} + \frac{\partial v^o}{\partial x} + \underline{\left(\frac{\partial w^o}{\partial x}\right)\left(\frac{\partial w^o}{\partial s}\right)} \tag{c}$$

$$\kappa_x^o = -\frac{\partial^2 w^o}{\partial x^2} \tag{d}$$

$$\kappa_s^o = -\frac{\partial^2 w^o}{\partial s^2} \tag{e}$$

$$\kappa_{xs}^o = -2\frac{\partial^2 w^o}{\partial x \partial s}. \tag{f}$$

(1.7)

Note that the radius of curvature being a function of s in $\varepsilon^o{}_s$ is what makes this problem different than that of a circular cylinder. The underlined terms in eq. 1.7a-c denote the geometric nonlinear-

ities. These are the von Karman approximations to the fully nonlinear strain-displacement relations. Substituting eq. 1.6 into eq. 1.5 and integrating the energy expression through the thickness of the cylinder wall results in

$$\pi = \frac{1}{2}\iint[N_x\varepsilon_x^o + N_s\varepsilon_s^o + N_{xs}\gamma_{xs}^o + M_x\kappa_x^o + M_s\kappa_s^o + M_{xs}\kappa_{xs}^o - p_o w^o]dxds \quad \text{(a)}$$
$$= \iint U(x, s)dxds, \quad \text{(b)} \tag{1.8}$$

where eq. 1.8b serves as the reminder that the integrand is strictly a function of x and s. The force and moment resultants in eq. 1.8 are defined by

$$\begin{aligned}
N_x &= \int\sigma_x d\zeta = A_{11}\varepsilon_x^o + A_{12}\varepsilon_s^o \\
N_s &= \int\sigma_s d\zeta = A_{12}\varepsilon_x^o + A_{22}\varepsilon_s^o \\
N_{xs} &= \int\tau_{xs} d\zeta = A_{66}\gamma_{xs}^o \\
M_x &= \int\sigma_x\zeta d\zeta = D_{11}\kappa_x^o + D_{12}\kappa_s^o + D_{16}\kappa_{xs}^o \\
M_s &= \int\sigma_s\zeta d\zeta = D_{12}\kappa_x^o + D_{22}\kappa_s^o + D_{26}\kappa_{xs}^o \\
M_{xs} &= \int\tau_{xs}\zeta d\zeta = D_{16}\kappa_x^o + D_{26}\kappa_s^o + D_{66}\kappa_{xs}^o.
\end{aligned} \tag{1.9}$$

where, as seen from the form of eq. 1.9, only symmetric and balanced laminates [2] are being considered.

With the radius of curvature varying circumferentially, a closed-form solution to the problem is not easily found. Accordingly, an approximate solution is sought. To begin the approximate solution, the circumferential variation of the radius of curvature is expanded, in a method suggested by Marguerre [3], in a cosine series such that,

$$\frac{1}{R(s)} \cong \sum_{i=0}^{I} a_{4i}\cos(4i\pi s/C), \tag{1.10}$$

where the coefficients a_{4i} are constants which depend on the specific cross-sectional geometry (semi-diameters a and b) and I is the number of terms needed to properly represent the variation of the inverse radius of curvature. The dependence of the reference surface displacements on the circumferential coordinate is approximated using the Kantorovich method by a harmonic series in a form inspired by the inverse radius of curvature, namely,

$$
\begin{aligned}
u^o(x, s) &= u_o^o(x) + \sum_{n=1}^{N} u_n^o(x)\cos(4n\pi s/C) + \sum_{m=1}^{M} u_{N+m}^o(x)\sin(4m\pi s/C) \\
v^o(x, s) &= v_o^o(x) + \sum_{m=1}^{M} v_m^o(x)\cos(4m\pi s/C) + \sum_{n=1}^{N} v_{M+n}^o(x)\sin(4n\pi s/C) \\
w^o(x, s) &= w_o^o(x) + \sum_{n=1}^{N} w_n^o(x)\cos(4n\pi s/C) + \sum_{m=1}^{M} w_{N+m}^o(x)\sin(4m\pi s/C).
\end{aligned}
\tag{1.11}
$$

Both sines and cosines are used to represent all three displacement components, where M and N determine the number of terms of each. For an isotropic cylinder, sine terms would not be necessary for $u^o(x,s)$ and $w^o(x,s)$, while cosine terms would not be necessary for $v^o(x,s)$. The presence of the bending stiffness terms D_{16} and D_{26} makes inclusion of these terms necessary.

With eq. 1.10 and eq. 1.11, the displacements and the radius of curvature have been explicitly expressed in terms of the circumferential coordinate, s. Substituting the displacements of eq. 1.11 into the strains and curvatures of eq. 1.7, and the stress and moment resultants of eq. 1.9 into the energy expression of eq. 1.8, integration of the energy expression can be performed with respect to s. The integrand of the energy expression is then dependent on the coefficients in eq. 1.11, which are only a function of x. As a result, the energy expression can be written symbolically as

$$\pi = \int_{-\frac{L}{2}}^{+\frac{L}{2}} \left[\int_0^C U(x,s)ds \right] dx$$
$$= \int_{-\frac{L}{2}}^{+\frac{L}{2}} F(y_i(x), y'_i(x), y''_i(x))dx; \qquad i = 1, 3(N+M+1) \tag{1.12}$$

In the above the $y_i(x)$ represent the functional coefficients in eq. 1.11 and ( )' represents differentiation with respect to the axial coordinate x. Although the integrand above is also a function of cylinder geometry, material properties, and the pressure, they are constants that are not involved in the variational process. Equating the first variation of the total potential energy to zero results in the Euler-Lagrange equations for the $y_i(x)$ and the associated variationally consistent boundary conditions at $x = \pm L/2$. In general terms, the Euler-Lagrange equations are

$$\frac{d^2}{dx^2}\left(\frac{\partial F}{\partial y_i''}\right) - \frac{d}{dx}\left(\frac{\partial F}{\partial y_i'}\right) + \frac{\partial F}{\partial y_i} = 0 \tag{1.13}$$

and the boundary conditions are

$$\begin{aligned} y_i' \text{ specified} \quad &\text{or} \quad \frac{\partial F}{\partial y_i''} = 0 \\ y_i \text{ specified} \quad &\text{or} \quad \frac{d}{dx}\left(\frac{\partial F}{\partial y_i''}\right) - \frac{\partial F}{\partial y_i'} = 0. \end{aligned} \tag{1.14}$$

The boundary conditions of eq. 1.3 translate into specifying values of $y_i(x)$ and $y_i'(x)$. Defining intermediate variables in order to reduce the system from a third-order to a first-order form, it is possible to obtain a set of coupled nonlinear first-order ordinary differential equations of the form

$$\bar{y}_i'(x) = f_i(\bar{y}_i'(x)); \qquad i,j = 1, 8(N+M+1), \tag{1.15}$$

where

$$\bar{y}_i(x) = \{u_k^o, v_k^o, w_k^o, q_k, r_k, t_k, g_k, h_k\}; \qquad k = 1, 8(N+M+1) \tag{1.16}$$

and

$$q_k = \frac{dw_k^o}{dx}, \quad r_k = \frac{dq_k}{dx}, \quad t_k = \frac{dr_k}{dx}, \quad g_k = \frac{du_k^o}{dx}, \quad h_k = \frac{dv_k^o}{dx}. \tag{1.17}$$

This process has been automated using the symbolic manipulation package *Mathematica*©[4]. The resulting differential equations in x are written into FORTRAN code using the FORTRANASSIGN package within *Mathematica*©. These equations are integrated by the finite-difference method using the IMSL subroutine DBVPFD [5] which is based on a variable-order, variable-step-size algorithm employing Newton's method. By rendering the governing Euler-Lagrange equations to first-order form, as in eq. 1.17, various derivatives of u^o, v^o, and w^o are directly available for computing reference surface strains and curvatures and force and moment resultants. More importantly, stresses as a function of x, s, and ζ can be computed.

1.3 Remainder of Document

In the following chapters, using numerical results, a thorough explanation will be given of the effects of cylinder geometry, specifically circular vs. elliptical cross sections, and geometric nonlinearities on cylinder responses. Also, the effects of orthotropy will be studied using quasi-isotropic, axially-stiff, and circumferentially-stiff graphite-epoxy laminates. Displacements, reference surface strains and curvatures, and force and moment resultants will be used to define cylinder responses. A comparison of these cylinder responses will be made with finite-element analysis to verify the numerical results. These discussions will take place in chapters 2, 3 and 4. In chapters 5 and 6, two failure theories, the Hashin failure theory and the maximum stress theory, will be used to assess the pressure capacity of elliptical composite cylinders. Interlaminar shear stresses are considered by integrating the geometrically linear equilibrium equations of elasticity in polar coordinates through the thickness at the cylinder wall. These interlaminar shear stresses

together with the inplane (intralaminar) stresses are used in the failure theories. Failure pressure levels, failure location, and failure modes are studied. Finally, conclusions of this work will be presented, and future directions discussed.

Chapter 2 Effect of Elliptical Geometry on Cylinder Response

This chapter addresses the influences of ellipticity by using the semi-analytical scheme described in the previous chapter.

2.1 Numerical Values of Problem Parameters

Though ultimate interest with elliptical cylinders is for application to aircraft fuselage structures, initial experimental work will take place with small scale cylinders. The displacement, strain, and stress response of these smaller cylinders must be understood before studies of scaled-up cylinders can commence. To that end, in the present study numerical results will be shown for eight and nine layer graphite-epoxy cylinders with semi-major diameters of 5 in., ellipticities of 0.7, and lengths of 12.5 in. The material and geometric properties of a layer of graphite-epoxy are taken to be

$$\begin{aligned} E_1 &= 18.85 \text{ Msi} \qquad E_2 = 1.407 \text{ Msi} \\ G_{12} &= 0.725 \text{ Msi} \qquad \nu_{12} = 0.300 \qquad h = 0.0055 \text{ in.} \end{aligned} \tag{2.1}$$

where h is the thickness of a single layer. The laminates considered are: quasi-isotropic, $[\pm 45/0/90]_S$; axially-stiff, $[\pm 45/0_2/90_{½}]_S$; circumferentially-stiff, $[\pm 45/90_2/0_{½}]_S$, where 0 degrees is along the axial direction. These lay-ups were selected because each has at least one layer with its fibers in the axial direction, at least one layer with its fibers in the circumferential direction, and ±45 degree layers. Eight or nine layers is a reasonable number from the point of view of manufacturing the cylinders by hand on elliptical mandrels.

The inverse radius of curvature of eq. 1.10 requires I=7 for convergence of the cosine series with the exact solution, as shown in fig. 2-1. In fig. 2-1 the vertical axis represents the error when using the series of eq. 1.10, and it is seen that I=7 results in minimal error at all circumferential locations.

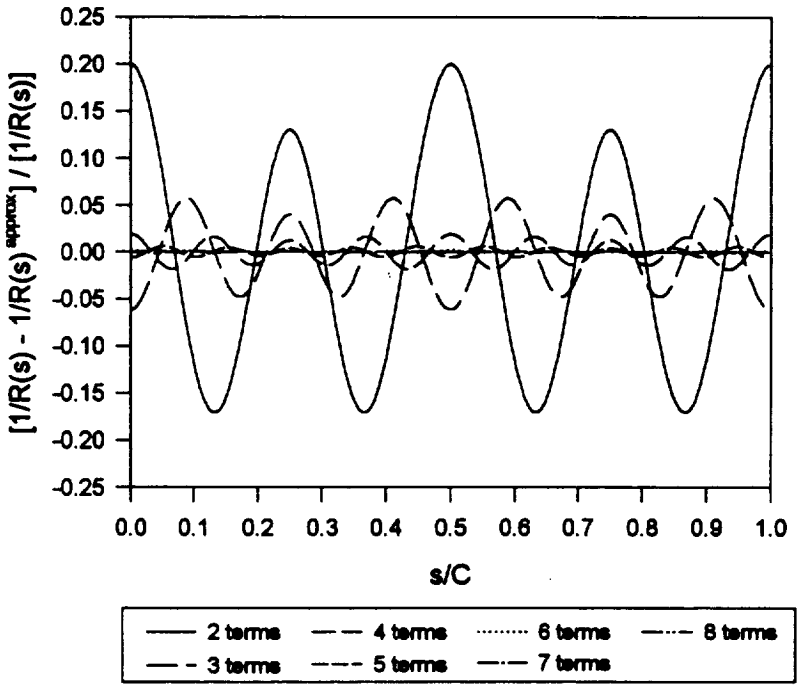

Figure 2-1. Convergence study for the inverse radius of curvature.

Accordingly, the three displacement series of eq. 1.11 require N=7 and M=4 for convergence of the displacements and force resultants. The displacement series is expanded as follows

$$u^o(x,s) = u^o_0(x) + u^o_1(x)cos(4\pi s/C) + u^o_2(x)cos(8\pi s/C) + u^o_3(x)cos(12\pi s/C) + u^o_4(x)cos(16\pi s/C)$$
$$+ u^o_5(x)cos(20\pi s/C) + u^o_6(x)cos(24\pi s/C) + u^o_7(x)cos(28\pi s/C)$$
$$+ u^o_8(x)sin(4\pi s/C) + u^o_9(x)sin(8\pi s/C) + u^o_{10}(x)sin(12\pi s/C) + u^o_{11}(x)sin(16\pi s/C)$$

$$v^o(x,s) = v^o_0(x) + v^o_1(x)cos(4\pi s/C) + v^o_2(x)cos(8\pi s/C) + v^o_3(x)cos(12\pi s/C) + v^o_4(x)cos(16\pi s/C)$$
$$+ v^o_5(x)sin(4\pi s/C) + v^o_6(x)sin(8\pi s/C) + v^o_7(x)sin(12\pi s/C) \qquad (2.2)$$
$$+ v^o_8(x)sin(16\pi s/C) + v^o_9(x)sin(20\pi s/C) + v^o_{10}(x)sin(24\pi s/C) + v^o_{11}(x)sin(28\pi s/C)$$

$$w^o(x,s) = w^o_0(x) + w^o_1(x)cos(4\pi s/C) + w^o_2(x)cos(8\pi s/C) + w^o_3(x)cos(12\pi s/C) + w^o_4(x)cos(16\pi s/C)$$
$$+ w^o_5(x)cos(20\pi s/C) + w^o_6(x)cos(24\pi s/C) + w^o_7(x)cos(28\pi s/C)$$
$$+ w^o_8(x)sin(4\pi s/C) + w^o_9(x)sin(8\pi s/C) + w^o_{10}(x)sin(12\pi s/C) + w^o_{11}(x)sin(16\pi s/C).$$

Further details regarding convergence can be found in ref. 1.

2.2 Displacements

In order to demonstrate the basic responses of an elliptical cylinder subjected to internal pressure, a comparison is made with circular cylinders. For this comparison a quasi-isotropic laminate is chosen and a geometrically linear analysis is used. The basic cylinder responses considered are reference surface displacements, reference surface strains and curvatures, and force and moment resultants. Figure 2-2a-f illustrates axial, circumferential, and normal displacements as a function of the axial and circumferential coordinates. The displacements have been normalized by the laminate thickness H. An internal pressure of p_o=100 psi is used to compute the results in these figures. The format of the fig. 2-2a-f illustrates the response of one-eighth of the cylinder. The coordinate locations have been normalized and, referring to fig. 1-2, the range of $0 \le x/L \le 0.5$ and $0 \le s/C \le 0.25$ is considered. Due to the presence of D_{16} and D_{26}, the problem does not exhibit octal symmetry. However looking at only one eighth of the cylinder provides a fairly accurate detailing of the response, and simplifies displaying the results. Implementing symmetry and

antisymmetry arguments for various responses, the response for the remainder of the cylinder can be envisioned.

Regarding the axial displacement of fig. 2-2a-b, for an internally pressurized cylinder the axial displacement is the net result of the pressure forcing the end enclosures apart and the Poisson effect due to circumferential expansion pulling them together. For a circular cylinder, this results in a nearly linear axial displacement with the axial coordinate. Since the internal pressure problem for a circular cylinder is axisymmetric, the axial displacement does not vary with s. Recall from the boundary conditions of eq. 1.3 that the axial displacement is zero at $x/L = -0.5$, and at $x/L = 0.5$ the axial displacement is determined by eq. 1.4. Because of the nearly linear variation with x, the axial displacement at $x/L = 0.5$ is approximately twice the value at $x/L = 0$. As for the elliptical cylinder, the internal pressure problem is not axisymmetric, and the axial displacement is far from being linear with x. For the elliptical cylinder notice that along the crown of the cylinder, $s/C=0$, the axial displacement is positive, while along the side of the elliptical cylinder the axial displacement is actually negative at certain axial locations. Since the axial displacement changes signs with spatial location, there are some locations besides $x=-L/2$ where the axial displacement is zero. This is not a situation that appears in the circular case. It should be noted, however, that the axial displacement at $x/L=0$ is practically independent of s, as it is at $x/L=0.5$, and the axial displacements at these locations differ by a factor of 2, as they do for the circular case.

Figure 2-2c-d illustrates the circumferential displacement, a response that clearly distinguishes an elliptical cylinder from a circular cylinder. An internally pressurized circular cylinder has no circumferential displacement response for balanced symmetric laminates. However, the elliptical case shows circumferential movement away from the sides and toward the crown and keel of the cylinder. Figure 2-2e-f illustrates another distinguishing difference between a circular

and elliptical cylinder, as was mentioned in connection with fig. 1-1. The normal displacement of a circular cylinder is uniformly outward. In contrast, for the elliptical case the cylinder tends to become more circular. The elliptical cylinder under internal pressure moves outward at the crown and keel, but moves inward at the sides. As will be seen, this has important consequences at the ends of the cylinder.

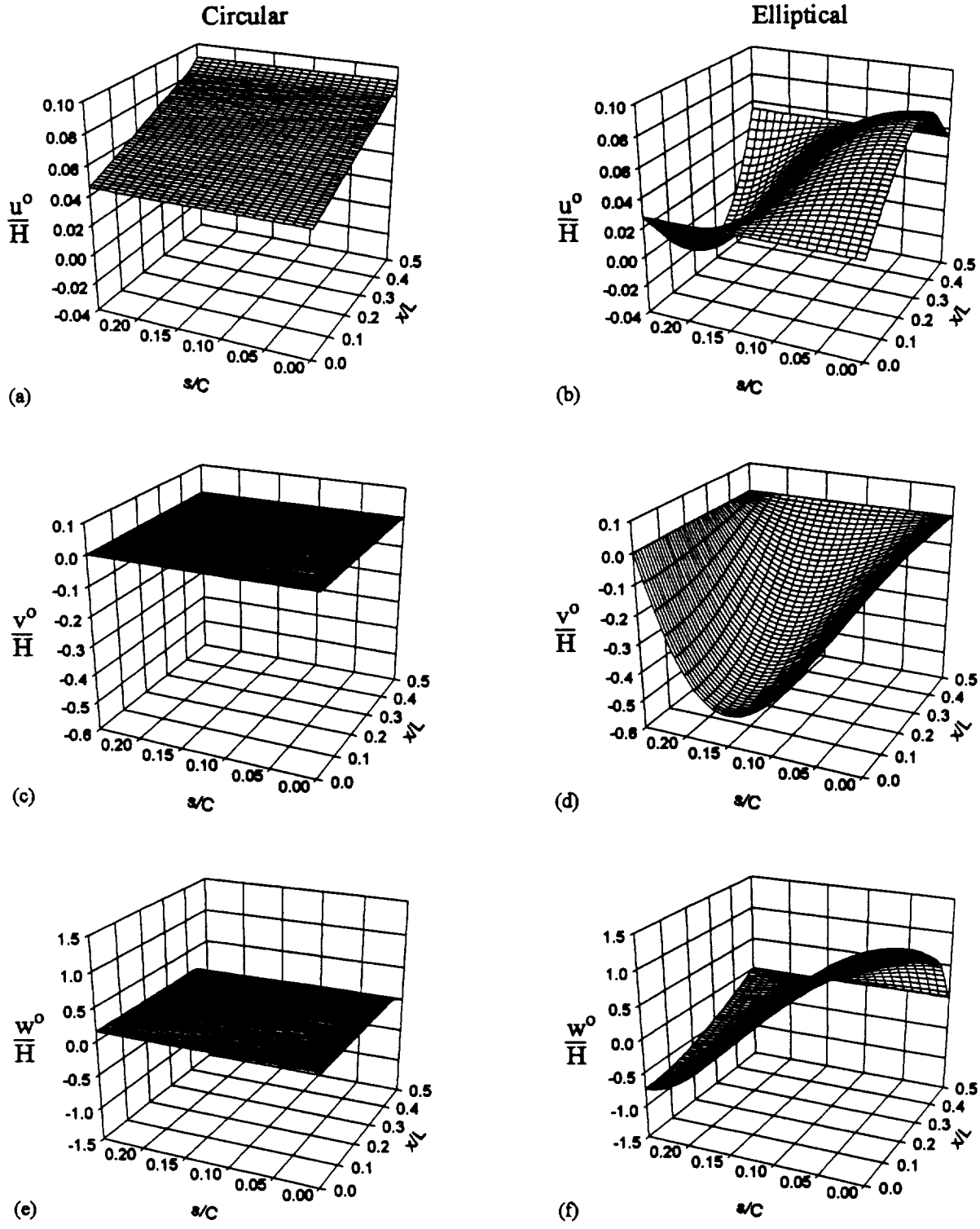

Figure 2-2. Influence of ellipticity on the displacements of a quasi-isotropic cylinder.

2.3 Strains and Curvatures

A comparison of reference surface strains in circular and elliptical cylinders provides a further demonstration on the influence of geometry on responses. In fig. 2-3a-f normalized reference surface strains are compared. Note that from here forward all normalized terms are denoted by an overbar. The normalization factor for the strains is the circumferential reference surface midspan strain in an internally pressurized quasi-isotropic circular cylinder, namely,

$$\left(\frac{A_{11}-\frac{1}{2}A_{12}}{A_{11}A_{22}-A_{12}^2}\right)p_o R, \tag{2.3}$$

where the A_{ij}s for a quasi-isotropic laminate are used. As a result of this normalization, the pressure level used in the calculations does not influence the magnitudes of the responses shown in the figures.

The circumferential strain, ε^o_s, shown in fig. 2-3a-b, varies considerably with both axial and circumferential locations for the elliptical case, whereas, the circumferential strains for the circular cylinder vary only with axial location and only near the ends. This behavior for all ellipses can be explained by studying the relationship between circumferential strain and displacements in eq. 1.7b. As seen in that equation, the inverse radius of curvature and the change in v^o with respect to circumferential location determine the behavior of circumferential strain. In the circular case v^o is zero, and therefore does not change with respect to circumferential or axial location, and the inverse radius of curvature is constant with s. The circumferential strain is determined solely by the inverse radius of curvature term. In the elliptical case, v^o and the inverse radius of curvature change significantly with respect to circumferential location and result in the behavior in fig. 2-3b. For the elliptical case, except for the cylinder ends, there is no location

where the circumferential strain is zero, and it changes sign and magnitude with location The circumferential strain is zero at the ends due to boundary condition on v^o and w^o given in eq. 1.3.

The axial strain, ε^o_x, shown in fig. 2-3c-d, shows behavior similar to the circumferential strain. For instance, in the circular case the midspan regions exhibit uniform strains, and in the elliptical case the strains vary with both axial and circumferential locations, and, in fact, change sign. However, the driving force behind these similar behaviors is due to a different displacement. The relationship between axial strain and displacements is shown in eq. 1.7a as the change in u^o with respect to axial location. In the circular case, u^o does change with respect to axial location, but the change is nearly linear, resulting in a uniform axial strain in the midspan region. For the elliptical case, u^o also changes with respect to axial location, but the change is nowhere near linear and therefore the axial strain, shown in fig. 2-3d, is not uniform.

The shear strain, γ^o_{xs}, shown in fig. 2-3e-f, varies considerably with the axial and circumferential location for the elliptical case, while the shear strain for the circular case is zero. The relationship between shear strain and displacements is shown in eq. 1.7c to be dependent on the change in u^o with respect to circumferential location and the change in v^o with respect to axial location. As a result, the shear strain for elliptical cylinder varies significantly with both circumferential and axial location. The presence of shear strain is another distinguishing feature of the elliptical cylinder. Note also that the shear strain in an ellipse is as large, or larger, than the other two strain components.

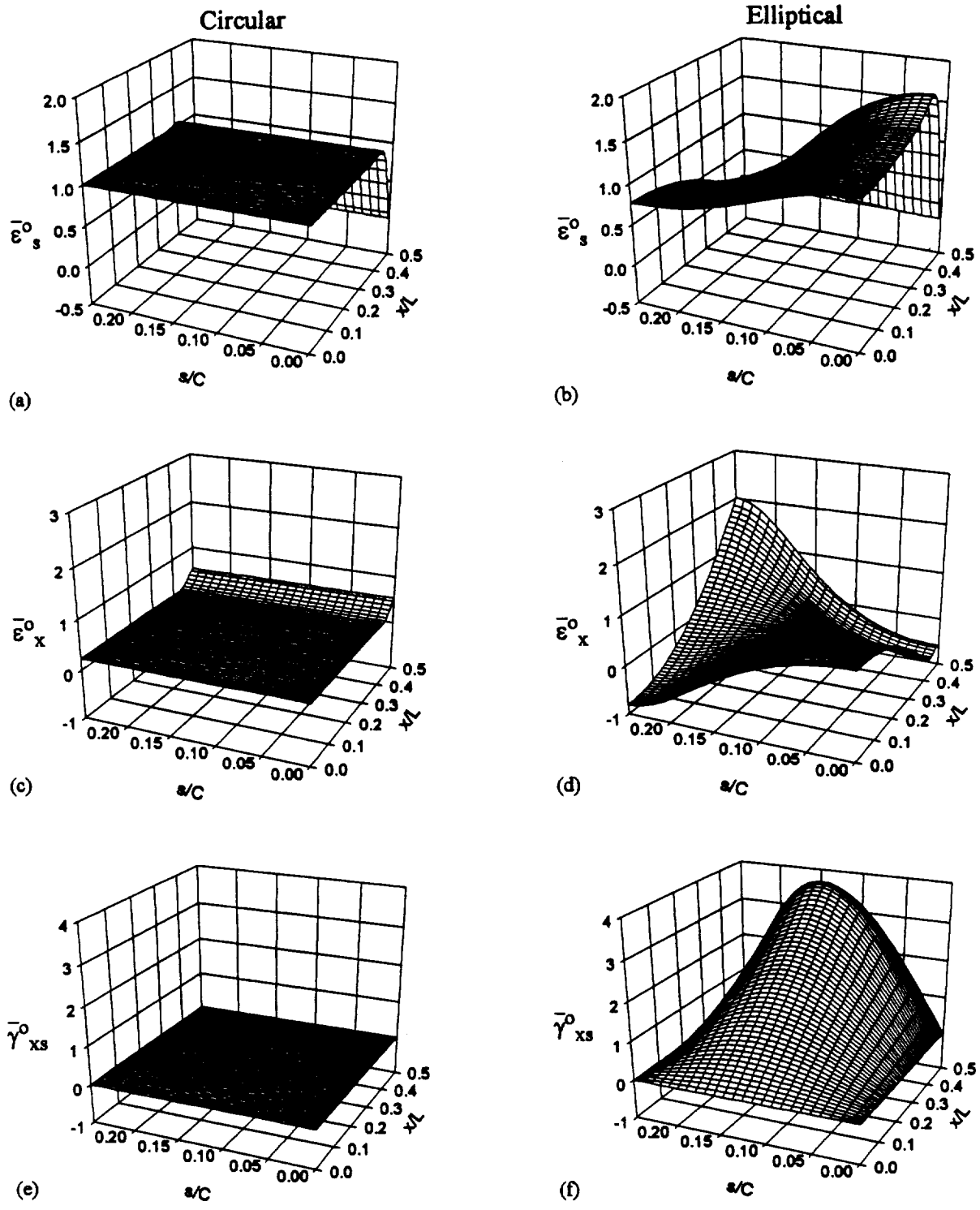

Figure 2-3. Influence of ellipticity on the strains of a quasi-isotropic cylinder.

Comparisons of circumferential, axial, and twist curvatures, $\bar{\kappa}^o_s$, $\bar{\kappa}^o_x$, and $\bar{\kappa}^o_{xs}$ respectively, for circular and elliptical cylinders are also necessary to demonstrate the influence of ellipticity on responses. To make the curvatures comparable to the previous figures involving the strains, the curvatures are converted to normalized strain measures by multiplying them by $H/2$ and then dividing this result by the quantity in eq. 2.3. The result is the normalized strain that would occur at the outer surface of the cylinder due to the curvature. (Note that by multiplying the curvature by $-H/2$, the strain that would occur at the inner surface of the cylinder due to the curvature can be computed.)

The curvatures, shown in fig. 2-4a-f, are strictly a function of normal displacement, w^o, and how it varies with the x and s coordinates, as given by the last three expressions of eq. 1.7. The magnitudes of the curvatures are notable because the axial curvature is an order of magnitude greater than the circumferential or twist curvatures. Due to the uniform outward normal expansion and a lack of variation with the s coordinate, the circular cylinder has zero circumferential and twist curvatures. The boundary conditions on w^o, from eq. 1.3, causes w^o to have a gradient in the x direction. Thus the axial curvature shows a variation with x for the circular cylinder.

In contrast, the elliptical cylinder does not have uniform outward normal expansion, rather it varies both with the x and s coordinates. As a result, the circumferential curvature varies with both x and s in the midspan region, but goes to zero at the boundary. This behavior at the boundary is caused by the boundary conditions which force w^o to be independent of s there. The axial curvature is zero in the midspan region, but varies in the boundary region. Focusing on the behavior at the boundary, recall the normal displacement at the boundary is forced to zero for an elliptical cylinder, while away from the boundary, as shown in fig. 1-1, the normal displacement is outward at the crown and keel and inward at the sides. This situation creates axial curvature which

is positive on the sides and negative on the crown and keel. The twist curvature is due to a variation in w^o with both the x and s coordinates. At the boundary the twist curvature, like the circumferential curvature, is zero. However, beyond the boundary, the twist curvature varies with both x and s.

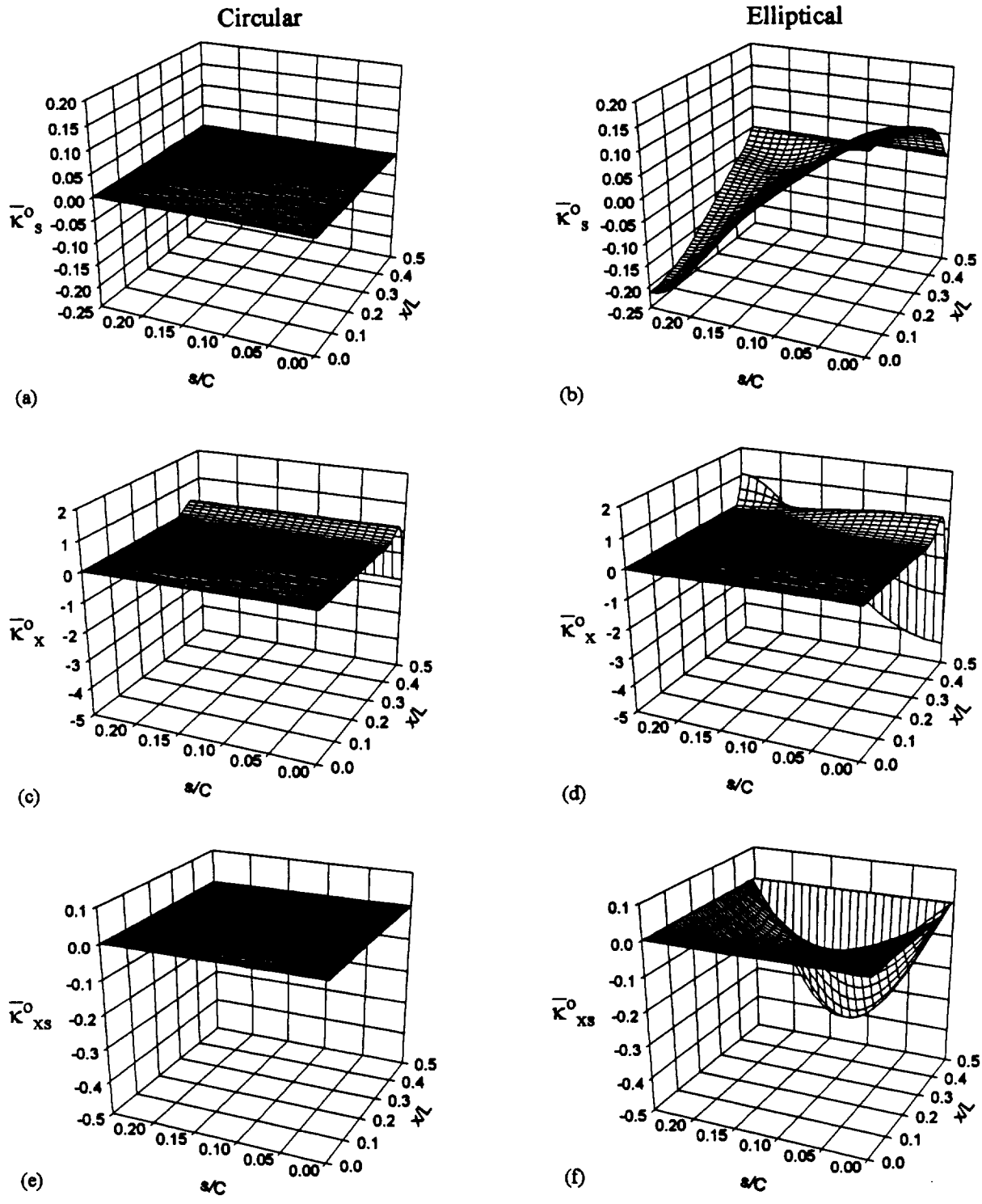

Figure 2-4. Influence of ellipticity on the curvatures of a quasi-isotropic cylinder.

2.4 Force and Moment Resultants

The circumferential, axial, and inplane shear force resultants, $\overline{N}_s$, $\overline{N}_x$, and $\overline{N}_{xs}$, respectively, seen in Figure 2-5a-f, are normalized by the midspan hoop force resultant for a circular cylinder, namely,

$$p_o R. \tag{2.4}$$

The force resultants are based upon a combination of the strains seen in Figure 2-3a-f, each multiplied by a constant, A_{ij}, as given in eq. 1.9a-c. Since A_{16} and A_{26} are zero due to a balanced laminate scheme, the circumferential and axial force resultants are a combination of only the reference surface circumferential and axial strains, and the shear force resultant is proportional only to the reference surface shear strain.

Because of the normalization given in eq. 2.4, the normalized circumferential force resultant for a circular cylinder is unity at the midspan, but deviates from unity at the boundary due to end effects there. The circumferential force resultant for the elliptical case varies with the x and s coordinates, but, for a given s, behaves similarly to the circular cylinder case in the x direction. Of note is that at the midspan the average of the circumferential force resultant for the elliptical cylinder case is approximately equal to the circumferential force resultant for the circular cylinder case, namely unity.

Again because of the normalization given in eq. 2.4, for the circular cylinder case the normalized axial force resultant is 1/2 and is spatially uniform. In contrast, the axial force resultant for the elliptical cylinder case varies with the x and s coordinate. Concentrating on the midspan of the elliptical cylinder, it is seen that the sides of the cylinder are in axial compression and the crown and keel are in tension. Concentrating on the boundary, it is seen that the sides of the cylinder are in tension and the crown and keel are in compression, just the opposite of the midspan. As

with the axial displacement for an elliptical cylinder, the axial force resultant changes signs with spatial location, causing some locations to be zero. This is not a situation that appears in the circular case.

The inplane shear force resultant for the circular case is zero due to the shear strain being zero. For the elliptical case, the shear force resultant is nonzero varies considerably with both x and s, and the magnitude is comparable to that of the circumferential and axial force resultants. Though it cannot be seen in the figure, $\overline{N}_{xs}$ is not zero at x/L=0.5. Since $\frac{\partial v^o}{\partial x}$ is nonzero there, $\overline{N}_{xs}$ is nonzero there.

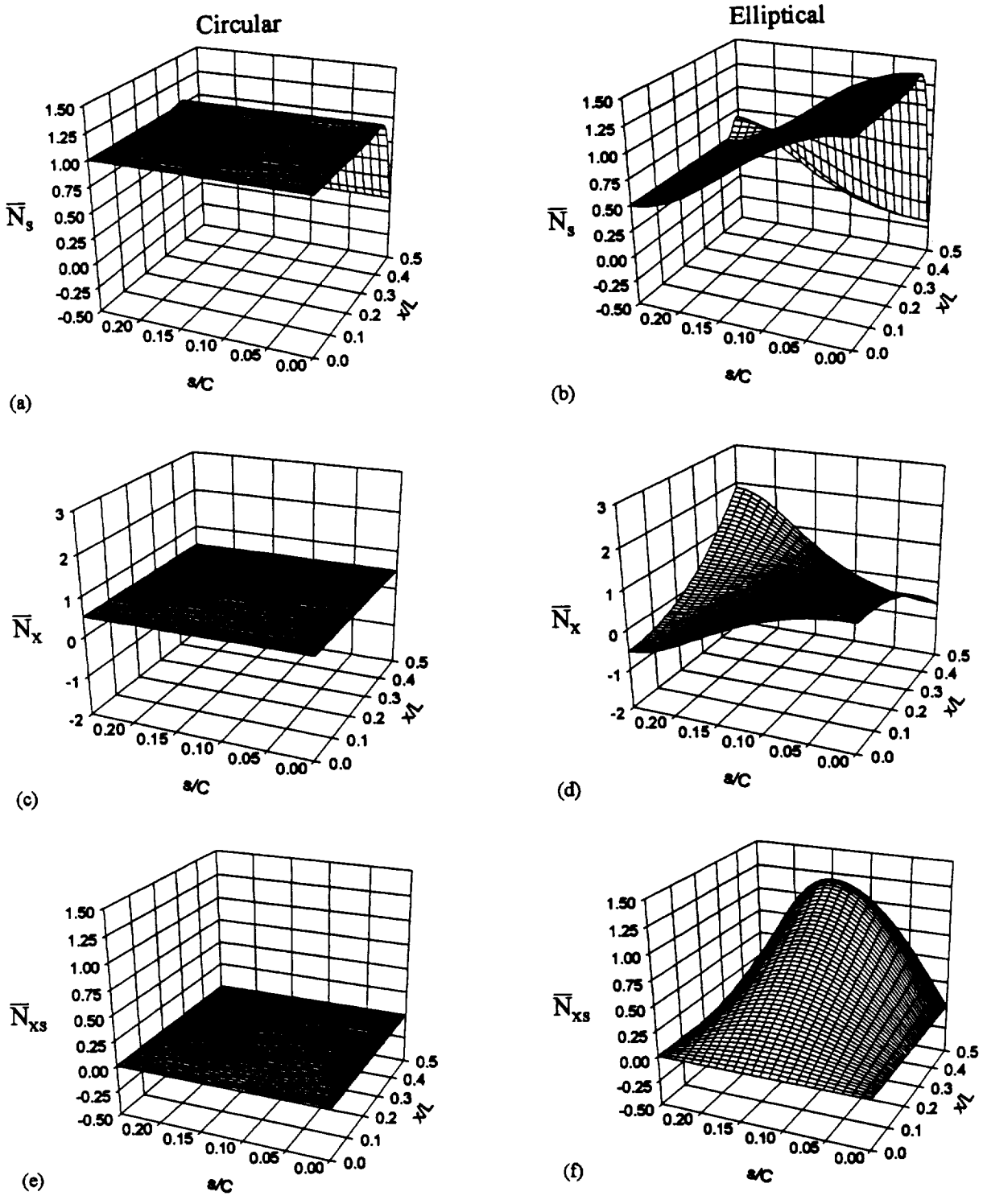

Figure 2-5. Influence of ellipticity on the force resultants of a quasi-isotropic cylinder.

The circumferential, axial, and twist moment resultants, $\overline{M}_s$, $\overline{M}_x$, and $\overline{M}_{xs}$, respectively, are normalized by the factor H/2 times the midspan hoop force resultant in a circular cylinder, namely,

$$p_o R \frac{H}{2} \quad . \tag{2.5}$$

The moment resultants are based upon a combination of the curvatures seen in fig. 2-4a-f, each multiplied by a bending stiffness, D_{ij}, as given in eq. 1.9d-f. Recall from fig. 2-4 that the axial curvature is an order of magnitude greater than the circumferential or twist curvatures. However, the bending stiffnesses, D_{ij}, control the degree to which the curvature influences the moment resultants. For the quasi-isotropic layup used, D_{16} and D_{26} are an order of magnitude smaller than D_{11}, D_{12}, D_{22}, and D_{66}. As a result, the circumferential and axial moment resultants are dominated by $\overline{\kappa}^o_x$, as can be seen by examining the character of $\overline{\kappa}^o_x$ vs. x and s and $\overline{M}_s$ and $\overline{M}_x$ vs. x and s, particularly near the ends. On the other hand, for the twist moment $\overline{M}_{xs}$, $D_{66}\,\overline{\kappa}^o_{xs}$ is similar in magnitude to $D_{16}\,\overline{\kappa}^o_x$ both of which are larger than $D_{26}\,\overline{\kappa}^o_s$. Therefore, $\overline{M}_{xs}$ is controlled by both $\overline{\kappa}^o_{xs}$ and $\overline{\kappa}^o_x$. Note that $\overline{M}_{xs}$ is the smallest of the three moment resultants.

Continuing with the discussion of the moment resultants: the most significant portion of circumferential, axial, and twist moment resultants is at the boundary. There the moment resultants are simply a response to the clamped boundary condition from eq. 1.3. The circular cylinder response to internal pressure is a uniform outward normal expansion which is restricted to be zero at the boundary, independent of s. The moment resultants at the boundary of fig. 2-6a,c,e show a response not dependent on the s coordinate. However, because the elliptical cylinder response to internal pressure is inward normal displacement on the sides and outward normal displacement on the crown and keel, the moment resultants on the boundary are dependent on s. This is reflected in

fig. 2-6b,d,f with a sign reversal in the moment resultants at the boundary between s/C=0 and s/C=0.25.

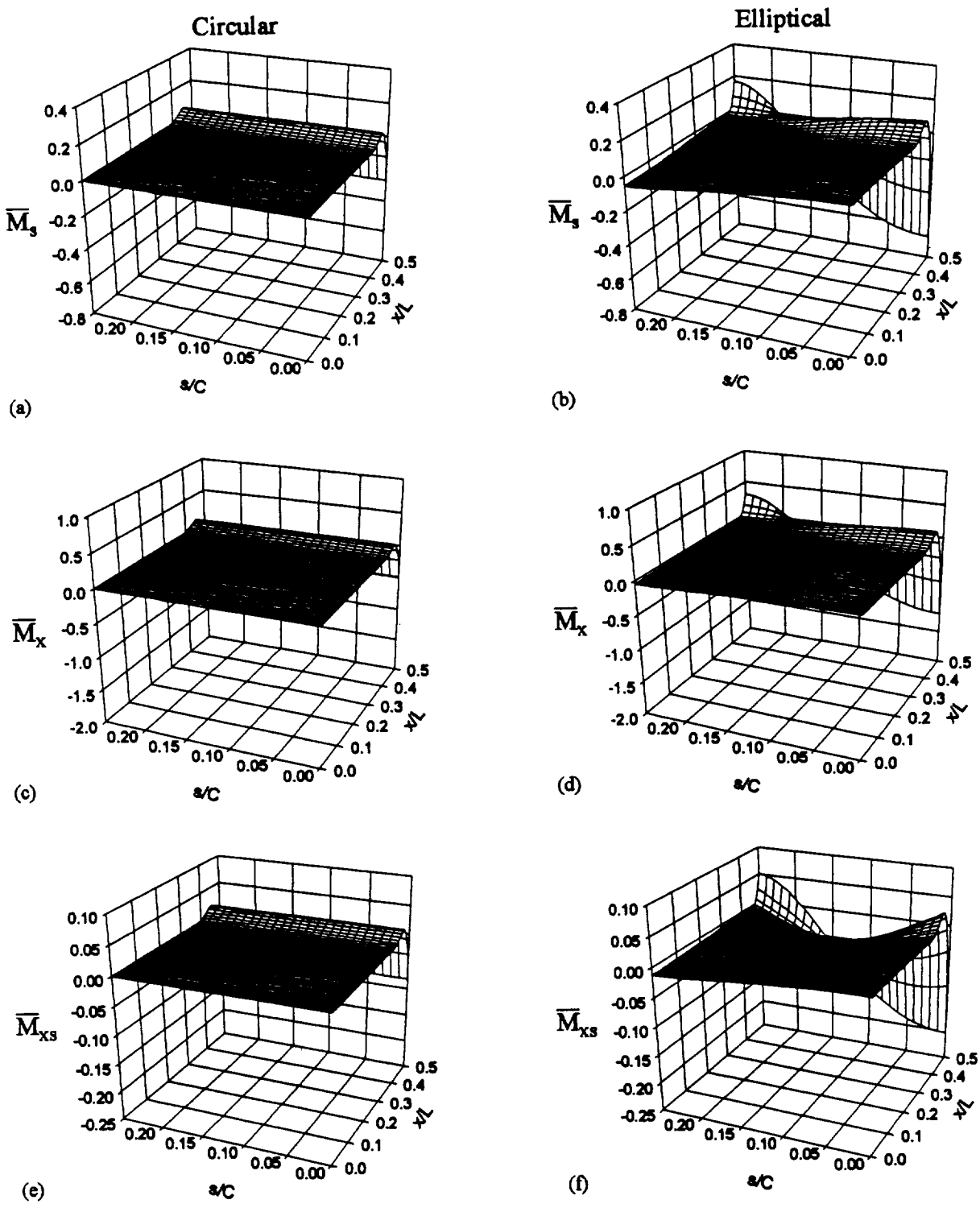

Figure 2-6. Influence of ellipticity on the moment resultants of a quasi-isotropic cylinder.

The transverse shear stresses $\tau_{x\zeta}$ and $\tau_{s\zeta}$ are not directly included in the energy expression of eq. 1.5. Therefore, there are no transverse shear force resultants associated with these stresses in the theory presented. However, Newtonian equilibrium approaches indicate that transverse shear force resultants are necessary for enforcing equilibrium. Moment equilibrium of a differential element of the cylinder wall dictates the following relation between transverse shear force resultants, Q_x and Q_s, and moment resultants:

$$\begin{aligned} Q_x &= \frac{\partial M_x}{\partial x} + \frac{\partial M_{xs}}{\partial s} \\ Q_s &= \frac{\partial M_{xs}}{\partial x} + \frac{\partial M_s}{\partial s}. \end{aligned} \tag{2.6}$$

In terms of transverse shear stresses

$$\begin{aligned} Q_x &= \int_{-\frac{H}{2}}^{+\frac{H}{2}} \tau_{x\zeta} d\zeta \\ Q_s &= \int_{-\frac{H}{2}}^{+\frac{H}{2}} \tau_{s\zeta} d\zeta. \end{aligned} \tag{2.7}$$

Since the present theory involves the moment resultants that appear on the right side of the equations in eq. 2.6 as explicit functions of x and s, Q_x and Q_s can be computed from eq. 2.6.

The circumferential and axial transverse shear force resultants, $\overline{Q}_s$ and $\overline{Q}_x$, respectively, are illustrated in fig. 2-7a-d, and they are normalized by the same factor used for the force resultants, namely eq. 2.4. Similar to the moment responses, the significant transverse shear force resultants are restricted to the boundary. It is essentially these force resultants that enforce the w^o=0 condition at the boundary. The uniformity of the circular case in the s direction results in a reaction at the boundary that is independent of s. However, with the elliptical cylinder, the values of $\overline{Q}_s$ and $\overline{Q}_x$ change sign at the boundary. This is reflected in fig. 2-6b,d with a sign reversal at the

boundary between s/C=0 and s/C=0.25. Note that the magnitudes of the transverse shear force resultants are much less than the magnitudes of the inplane force resultants.

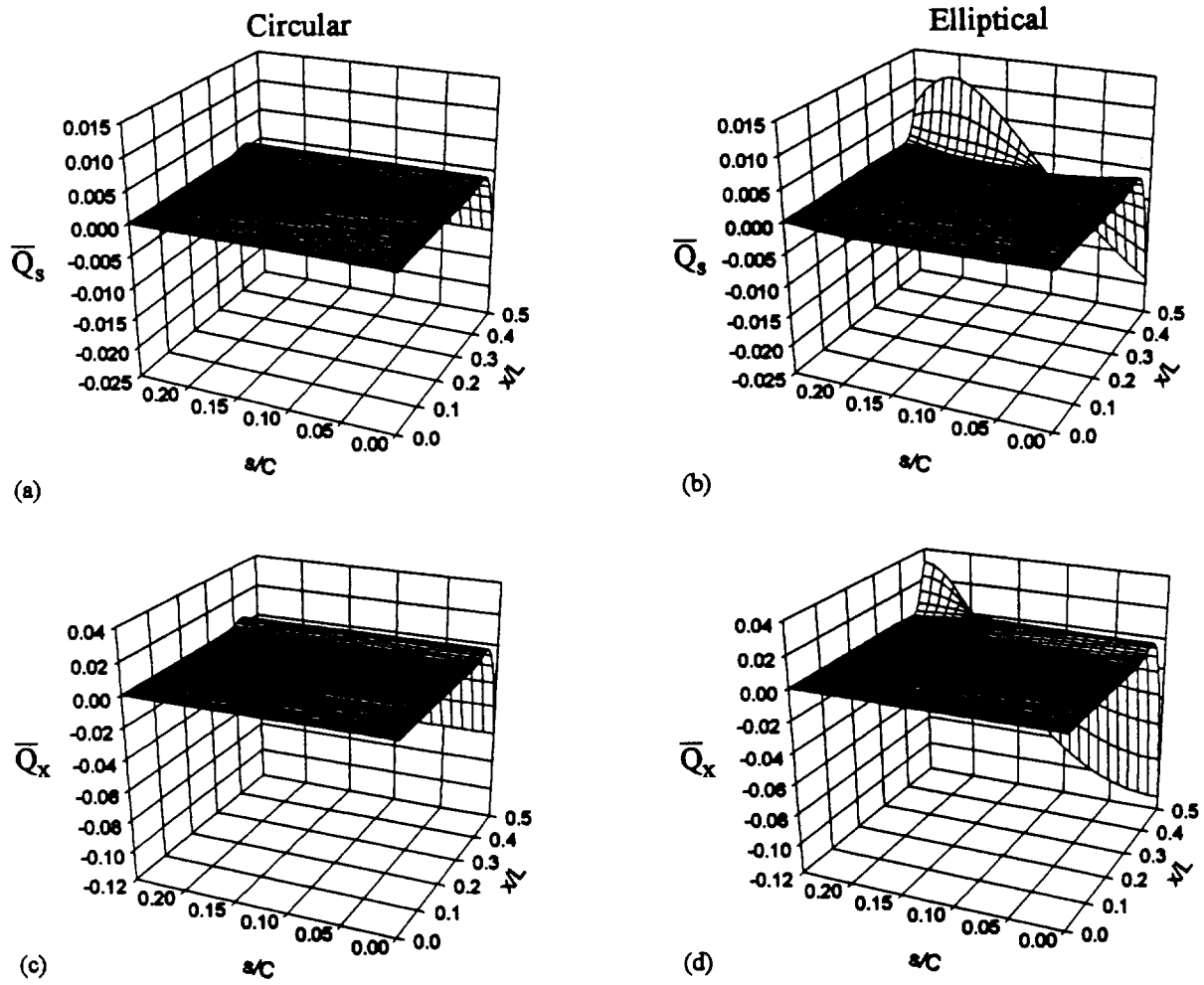

Figure 2-7. Influence of ellipticity on the transverse shear force resultants of a quasi-isotropic cylinder.

2.5 Summary of the Effects of Ellipticity

The effects of ellipticity seen in this chapter included several key issues. For instance, responses for the elliptical case varied with both the x and s coordinate. This variation was seen in every elliptical response, either over the entire domain, or at the boundary. Also, axial responses for the elliptical case were compressive for axial displacement, axial strain, and axial force result-

ant. For the elliptical cylinder, the circumferential displacement and shear force resultant were not zero, whereas, both of these responses were zero for the circular cylinder. Finally, an ellipticity of 0.7 caused a change in sign of the response at the boundary for axial curvature, all moment resultants, and the shear force resultants as s varies from s/C=0 to s/C=0.25. It is felt less severe ellipses, e.g., e=0.90, may not experience these sign reversals. To this point the effects of ellipticity have been evaluated using a geometrically linear analysis for both circular and elliptical cylinders constructed with a quasi-isotropic laminate. In the next chapter the focus will be shifted from comparing the response of elliptical cylinders with circular cylinders to comparing the responses of elliptical cylinders as predicted by the geometrically nonlinear theory with the responses as predicted by the linear theory.

Chapter 3 Effect of Geometric Nonlinearities on Cylinder Response

The differences between linear and nonlinear analyses are strictly due to the nonlinear terms in the strain-displacement equations, as given by the underlined terms in eq. 1.7a-c. This chapter examines the differences between linear and nonlinear analyses created by these nonlinear terms. For this comparison a quasi-isotropic laminate is again chosen, and responses are evaluated using both geometrically linear and geometrically nonlinear analyses, but for just an elliptical cylinder. The effects of geometric nonlinearities are shown using three different types of figures. The first type is a three-dimensional format illustrating the response of one-eighth of the cylinder, as in the previous chapter. The coordinate locations range from $0 \le x/L \le 0.5$ and $0 \le s/C \le 0.25$. The remaining types are two-dimensional in format, with the desired response plotted as a function of x/L *or* s/C. These two-dimensional format graphs show a comparison of linear and nonlinear analyses along a line at a particular s/C or x/L location for the purpose of a closer examination of an issue that may be difficult to discern from a three-dimensional format. A comparison of linear and nonlinear analyses are shown only for responses that display significant differences, not all responses.

3.1 Displacements

Recall from the boundary conditions of eq. 1.3 that the axial displacement is zero at $x/L = -0.5$, and at $x/L = 0.5$ the axial displacement is determined by eq. 1.4. Recall also that for the linear analysis, and as was discussed earlier in connection with fig. 2-2b, the axial displacement at $x/L=0$

is practically independent of s and it is one-half the value of the axial displacement at x/L=0.5. This factor of two also exists for the nonlinear case. However, the magnitude of the axial displacement response differs for the two analyses. As seen in fig. 3-1 and fig. 3-2, the nonlinear analysis requires a slightly smaller axial end displacement, or Δ, to satisfy the axial equilibrium given in eq. 1.4. Figure 3-1 is a three-dimensional format figure and fig. 3-2 is a two-dimensional format figure with the axial displacement given as a function of x/L at two different s/C locations, s/C = 0.0 and 0.25. Though the overall characters of the axial displacement responses are the same for linear and nonlinear analyses, the displacement difference at x/L = 0.5 is evident. The existence of negative axial displacements is also clearly seen in this figure.

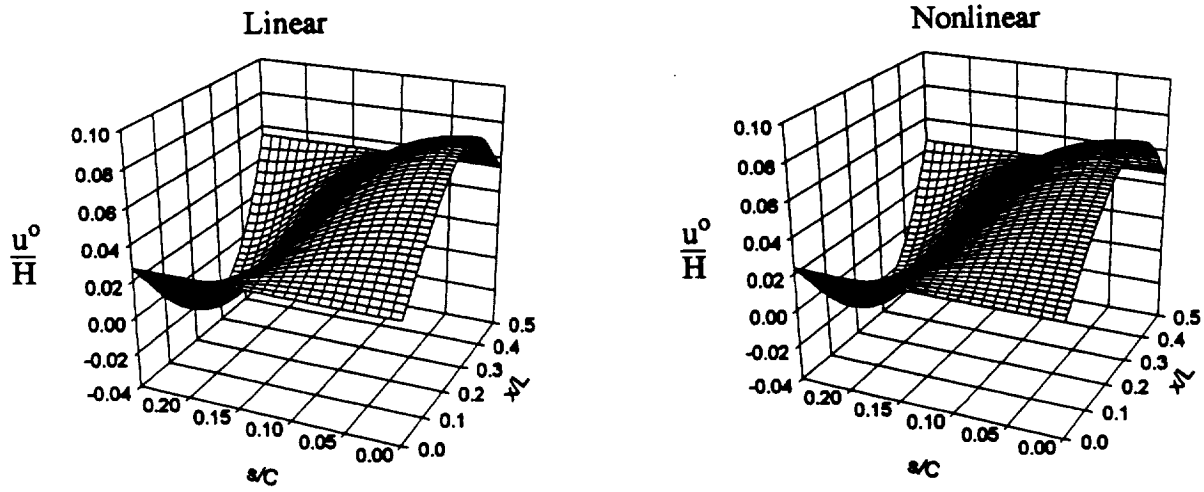

Figure 3-1. Effect of geometric nonlinearities on the axial displacement.

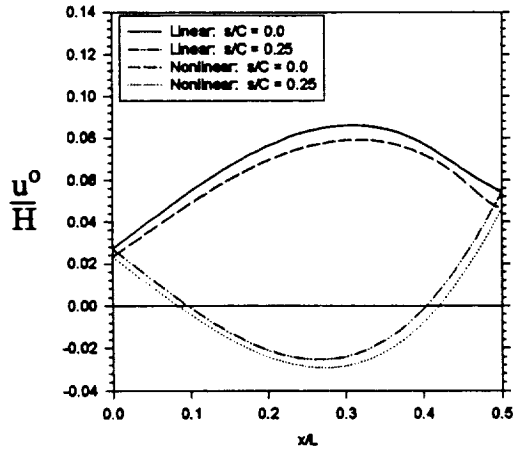

Figure 3-2. Effect of geometric nonlinearities on the axial displacement: linear vs. nonlinear at x/L = 0.

Comparing linear and nonlinear analyses, the circumferential displacements appear almost identical as shown in fig. 3-3. However, when circumferential displacements are plotted as a function of s/C along $x/L = 0$ (midspan), as in fig. 3-4, a difference in the displacement magnitudes is detected. For the linear analysis, the extreme value of v^o/H is -0.4918 and it is located at s/C = 0.1458. For the nonlinear analysis, the extreme value of v^o/H is -0.4633 and it is located at s/C = 0.1563. In short, the extreme circumferential displacement in the nonlinear analysis is smaller in magnitude by approximately 5.8%, and is also shifted approximately 6.7% towards the side of the cylinder.

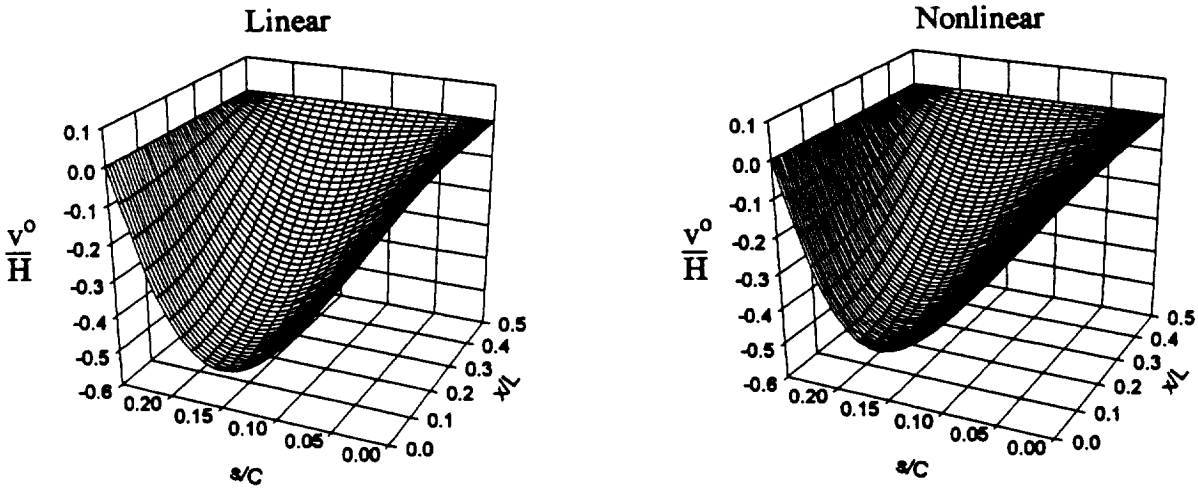

Figure 3-3. Effect of geometric nonlinearities on the circumferential displacement.

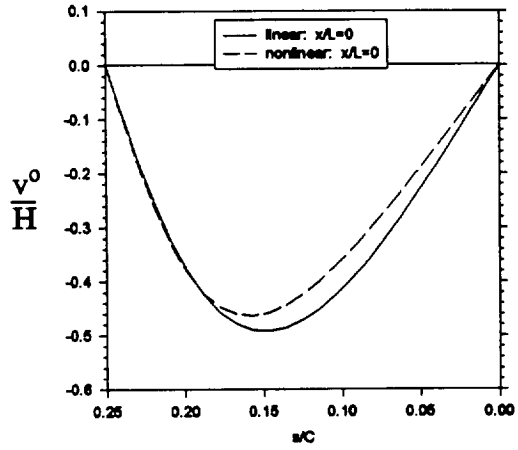

Figure 3-4. Effect of geometric nonlinearities on the circumferential displacement: linear vs. nonlinear at x/L = 0.

The normal displacement, shown in fig. 3-5 and fig. 3-6, tends to 'flatten' relative to the linear analysis when evaluated using a nonlinear analysis. The normal displacement, as seen in fig. 3-6, evaluated using a nonlinear analysis moves outward less in the crown region, represented by $0 \leq s/C \leq 0.10$, than does the normal displacement evaluated using a linear analysis. This is due to the effect of N_s coupling with w^o through geometrically nonlinear effects.

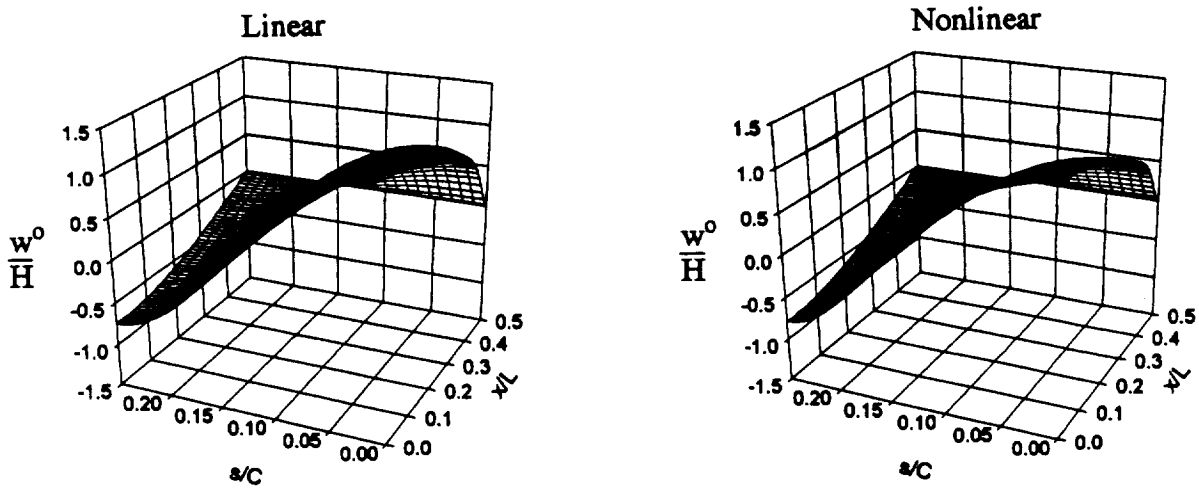

Figure 3-5. Effect of geometric nonlinearities on the normal displacement.

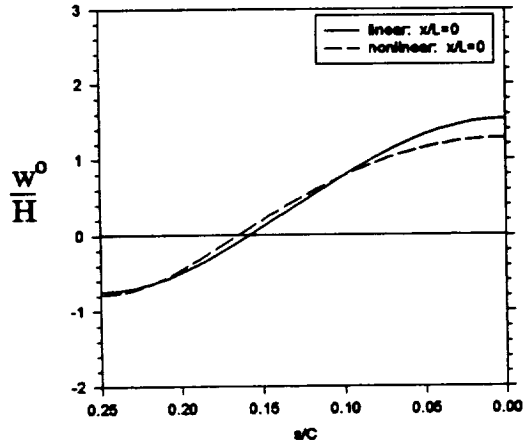

Figure 3-6. Effect of geometric nonlinearities on the normal displacement: linear vs. nonlinear at x/L = 0.

All strain, curvature, and force and moment resultant responses can be expressed in terms of the displacements, and as just shown in fig. 3-1 through fig. 3-6, each of the displacements predicted using a nonlinear analysis varies from the displacements predicted using a linear analysis. Therefore, each of these displacement-dependent responses can be expected to also vary using a

nonlinear analyses. However, some responses show little difference between linear and nonlinear analyses. To follow is a discussion of the responses that do show differences.

3.2 Strains and Curvatures

The circumferential strain for the nonlinear analysis follows the same trend as the circumferential strain for the linear analysis, as seen in fig. 3-7 and fig. 3-8. However, the circumferential strain at the crown of the cylinder using the nonlinear analysis does not reach the same magnitude as the circumferential strain at the crown of the cylinder using the linear analysis. The nonlinear circumferential strain from eq. 1.7a depends on the variation of v^o with s, w^o, the inverse radius of curvature, and an additional nonlinear term which is the square of the variation of w^o with s. As seen earlier, the normal displacement, w^o, experiences a 'flattening' effect, which causes w^o and the variation of w^o with s to be smaller in magnitude at the crown of the cylinder. Also, v^o shows a reduction in magnitude, which lessens the magnitude of the variation of v^o with s. All of these reactions to a nonlinear analysis combine to result in a lower magnitude for $\bar{\varepsilon}^o_s$. The differences between linear and nonlinear analyses for the axial strain and shear strains, from eq. 1.7a and c, appear to be negligible as compared with the difference in the circumferential strains.

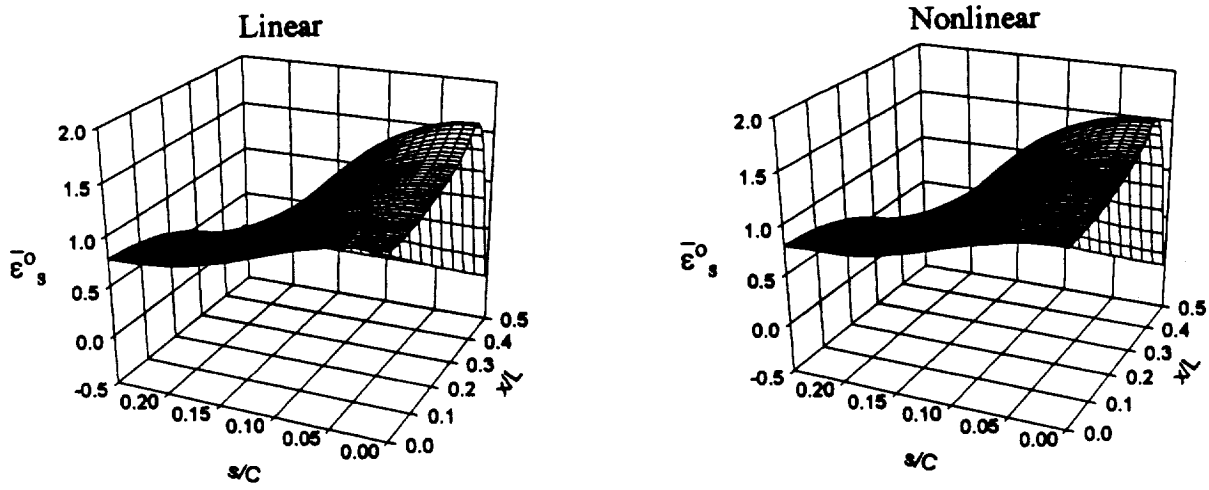

Figure 3-7. Effect of geometric nonlinearities on the circumferential strain.

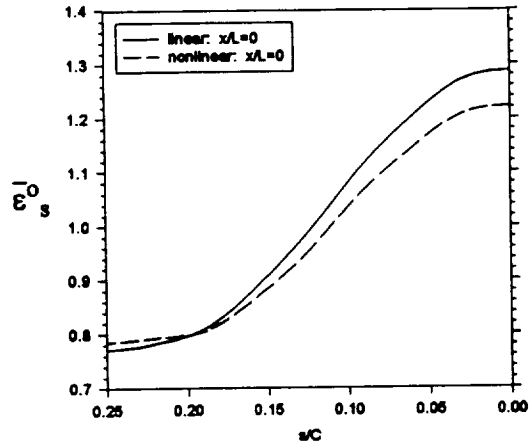

Figure 3-8. Effect of geometric nonlinearities on the circumferential strain: linear vs. nonlinear at x/L = 0.

The differences between linear and nonlinear analyses for circumferential curvature are easily visible in fig. 3-9 and fig. 3-10. In the midspan region for the nonlinear analysis case, there is a significant 'flattening' along the crown of the cylinder. The definition for circumferential curvature, given in eq. 1.7e as the second derivative of w^o with respect to the s coordinate, is the same for both the linear and nonlinear analyses. As the normal displacement experiences a 'flat-

tening' effect at the crown, the circumferential curvature also tends to 'flatten' at the crown of the cylinder.

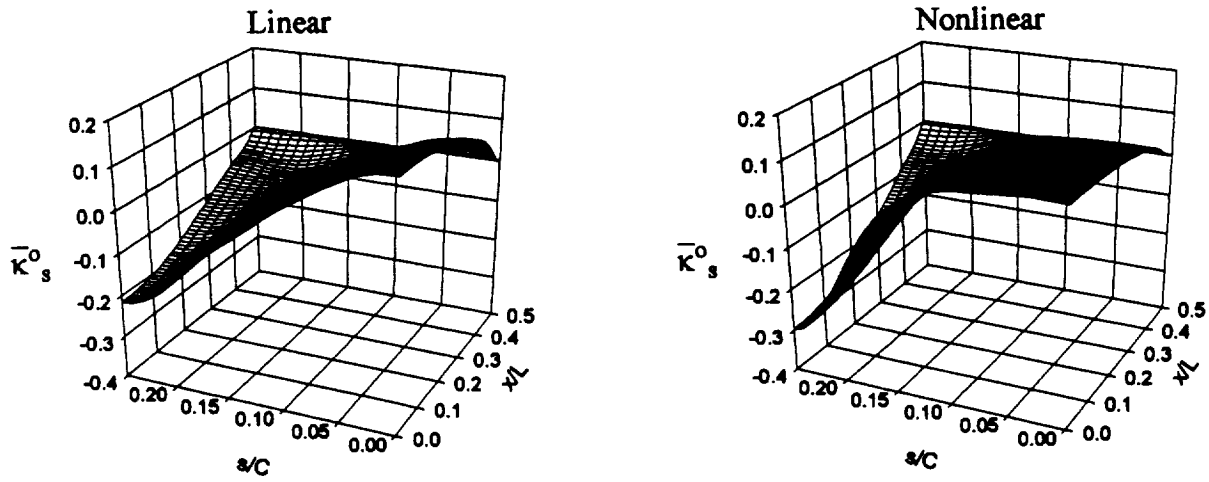

Figure 3-9. Effect of geometric nonlinearities on the circumferential curvature.

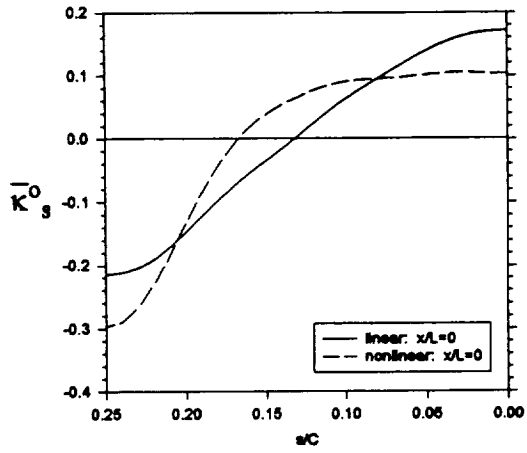

Figure 3-10. Effect of geometric nonlinearities on the circumferential curvature: linear vs. nonlinear at x/L = 0.

The differences between linear and nonlinear analyses for axial curvature, as seen in fig. 3-11 and fig. 3-12, are slight in comparison to differences in the circumferential curvature. In the midspan region there is virtually no difference, both analyses predicting zero axial curvature. The

differences between linear and nonlinear analyses for axial curvature exists almost solely in the boundary region, where the axial curvature experiences a change in sign. For the nonlinear case, at the boundary, fig. 3-12, the magnitude of the positive and negative axial curvatures changes slightly, such that the sides have more curvature and the crown and keel have less, and thus the point where axial curvature changes sign moves circumferentially. The influence of the nonlinearities on the axial curvature is explained as follows: The definition for axial curvature, given in eq. 1.7d as the second derivative of w^o with respect to the x coordinate, is the same for linear and nonlinear analysis. The boundary conditions given in eq. 1.3 require that w^o and $\frac{\partial w^o}{\partial x}$ be zero at the end. Since by fig. 3-6 the magnitude of w^o at the crown is less for the nonlinear case, the axial curvature has less to overcome in order to enforce these boundary conditions at the crown of the cylinder. On the other hand, again referring to fig. 3-6, the magnitude of w^o at the sides of the cylinder is slightly greater for the nonlinear analysis as compared to the linear analysis. Therefore, the axial curvature for the sides is slightly greater for nonlinear case.

The differences between linear and nonlinear analyses for twist curvature is not significant compared to the circumferential and axial curvatures.

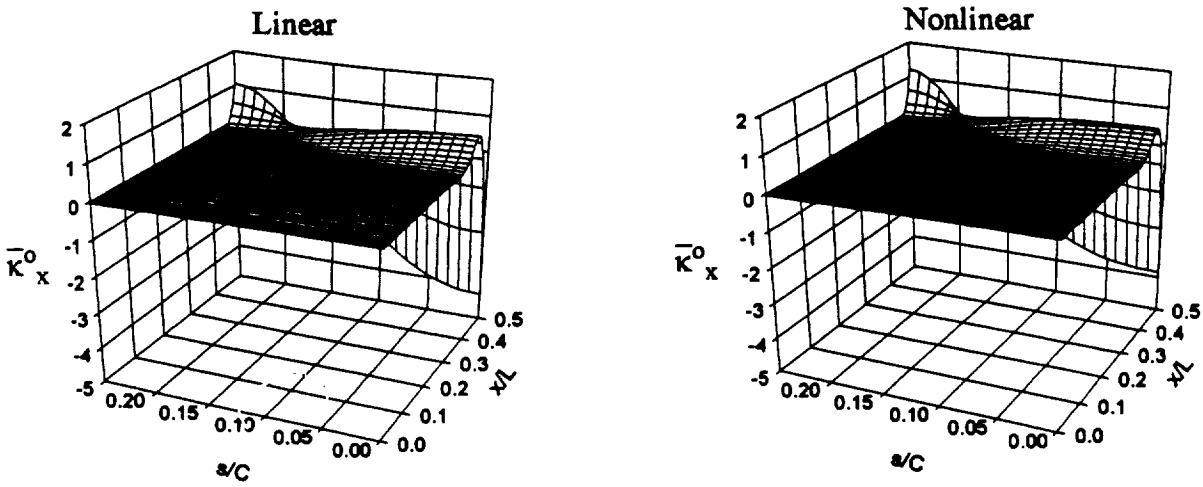

Figure 3-11. Effect of geometric nonlinearities on the axial curvature.

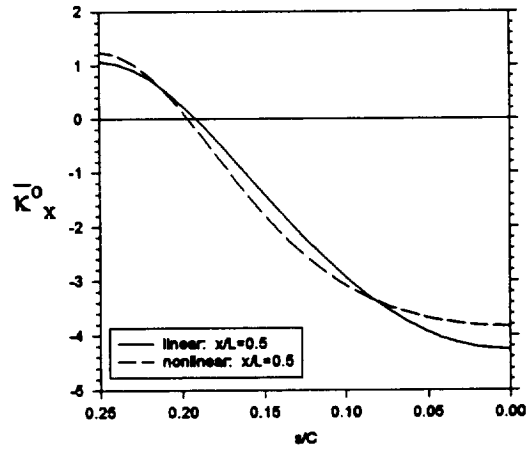

Figure 3-12. Effect of geometric nonlinearities on the axial curvature: linear vs. nonlinear at x/L = 0.5.

3.3 Force and Moment Resultants

The nonlinear circumferential force resultant follows the same trend as the linear circumferential force resultant, as seen in fig. 3-13 and fig. 3-14. However, the circumferential force resultant at the crown of the cylinder using nonlinear analysis does not reach the same magnitude as the circumferential force resultant at the crown of the cylinder using linear analysis. This is the

same behavior as seen for circumferential strain, fig. 3-8, which, as seen in eq. 1.9b, is a part of the circumferential force resultant. The axial force resultant shows this same reduction at the crown of the cylinder, although the reduction is less significant, and it is also due to the differences between linear and nonlinear analyses for the circumferential strain. The differences between linear and nonlinear analyses for the shear force resultant are not significant compared to the differences for the circumferential and axial force resultants.

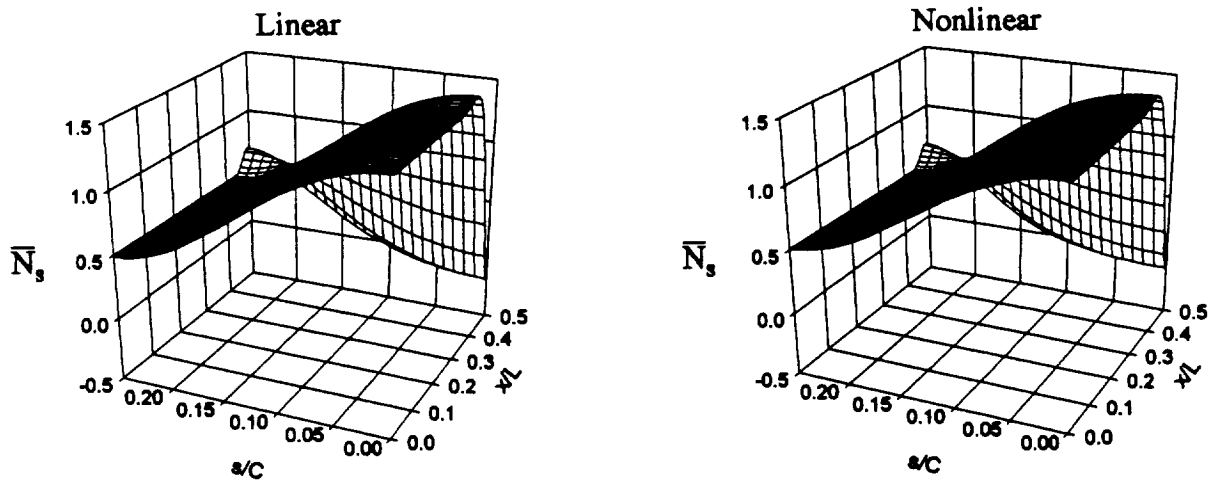

Figure 3-13. Effect of geometric nonlinearities on the circumferential force resultant.

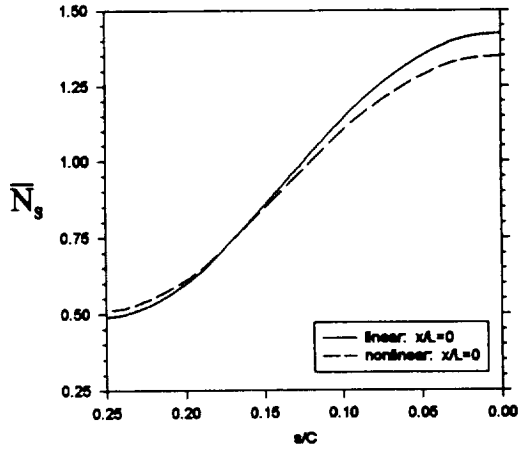

Figure 3-14. Effect of geometric nonlinearities on the circumferential force resultant: linear vs. nonlinear at x/L = 0.

The differences between linear and nonlinear analyses for circumferential moment resultant, as seen in fig. 3-15 and fig. 3-16, are found in both the midspan and boundary regions. In the midspan region for the nonlinear case, there is a reduction in the crown region of the cylinder, and an increase in the side region, as was seen with the circumferential curvature of fig. 3-10. Also, there is a change in the response at the ends due to nonlinear analysis, as was seen with axial curvature. However, the difference in response between linear and nonlinear analyses in the boundary region is significantly less than the difference in response in the midspan region. The definition for circumferential moment resultant, given in eq. 1.9e as a linear combination of $\overline{\kappa}^{o}_{s}$, $\overline{\kappa}^{o}_{x}$, and $\overline{\kappa}^{o}_{xs}$, is the same for linear and nonlinear analysis. Since $\overline{\kappa}^{o}_{s}$ and $\overline{\kappa}^{o}_{x}$ are both a part of the circumferential moment resultant, the differences between linear and nonlinear analyses from each of these curvatures are reflected in the difference for the circumferential moment resultant. Although not shown here since they are small, the same reasoning applies to differences there are in the axial and twist moment resultants.

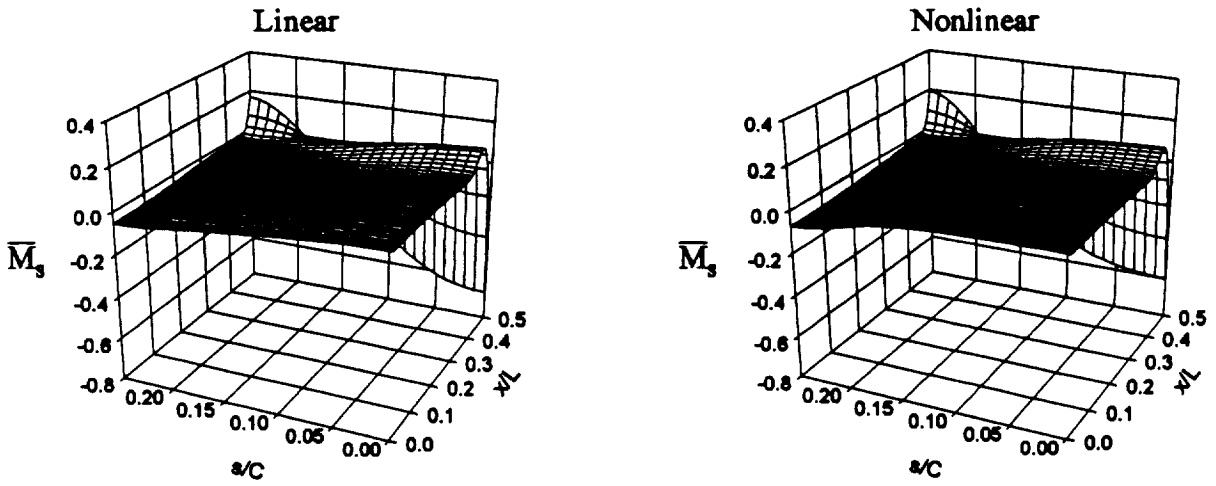

Figure 3-15. Effect of geometric nonlinearities on the circumferential moment resultant.

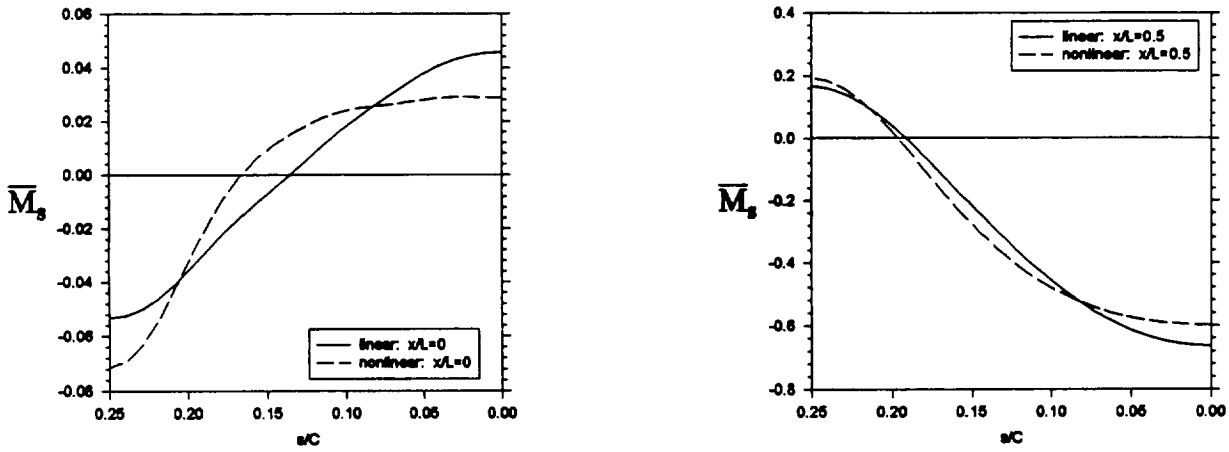

Figure 3-16. Effect of geometric nonlinearities on the circumferential moment resultant: linear vs. nonlinear at x/L = 0 and 0.5.

The transverse shear force resultants, $\overline{Q}_s$ and $\overline{Q}_x$, seen in figs. 3-17 and 3-18, and figs. 3-19 and 3-20, are defined in eq. 2.6 and depend on the moment resultants. As seen with the moment resultants, the difference between linear and nonlinear analyses occurs mostly in the boundary region. The magnitude of the peaks of the transverse shear force resultants at or near the sides are higher for the nonlinear case, while near the crown they are lower. Most noteworthy for $\overline{Q}_s$ is the

change in sign at the boundary, and the point at which the sign changes. The circumferential transverse shear force resultant changes sign at $s/C = 0.1250$ for the linear analysis and at $s/C = 0.1458$ for the nonlinear analysis. However, for $\overline{Q}_x$, the change in sign is at approximately the same s/C location for both analyses.

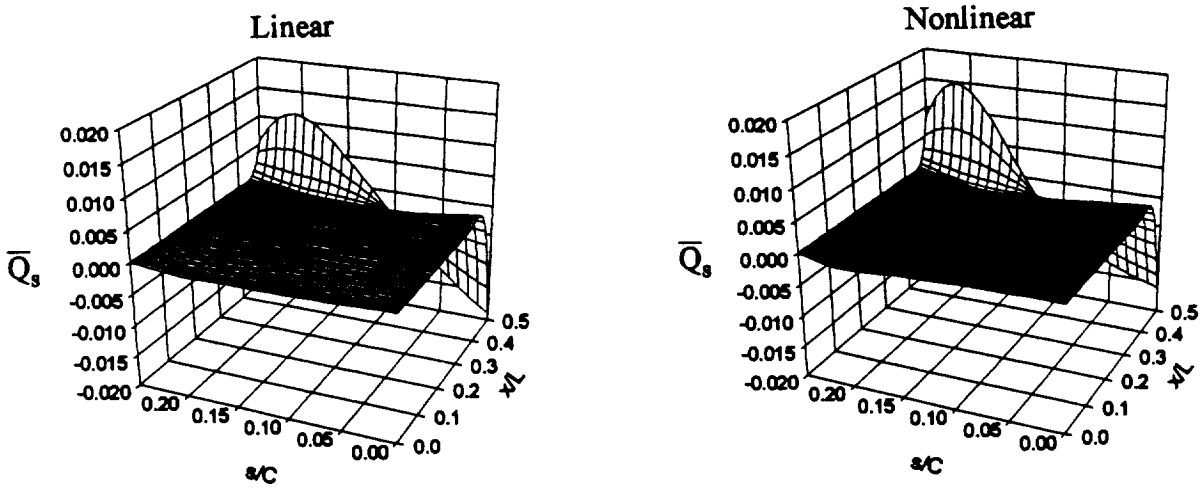

Figure 3-17. Effect of geometric nonlinearities on the circumferential transverse shear force resultant.

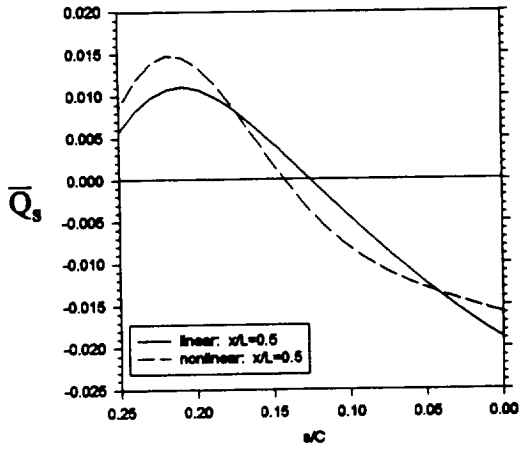

Figure 3-18. Effect of geometric nonlinearities on the circumferential transverse shear force resultant: linear vs. nonlinear at x/L = 0.5.

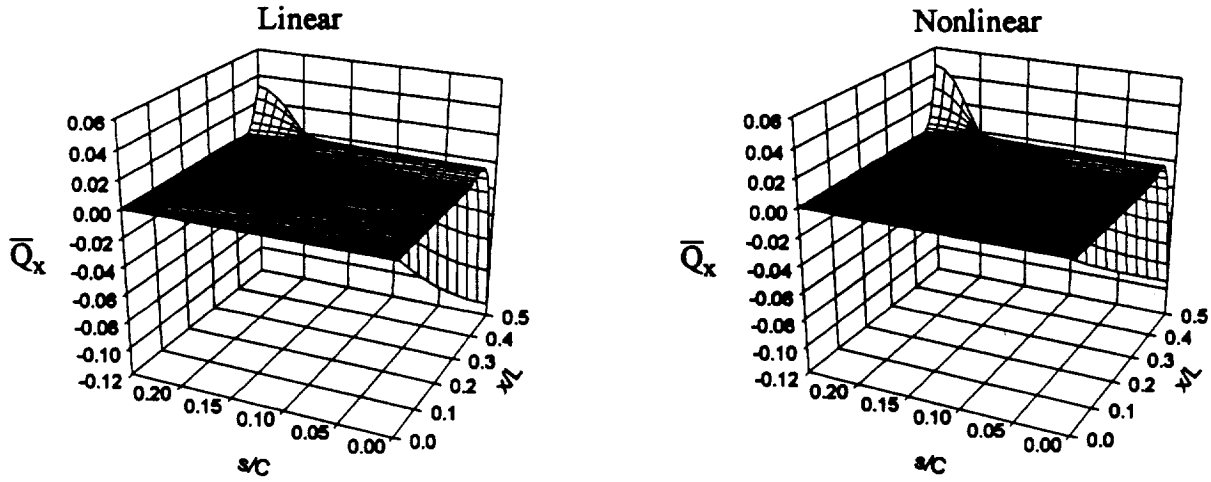

Figure 3-19. Effect of geometric nonlinearities on the axial transverse shear force resultant.

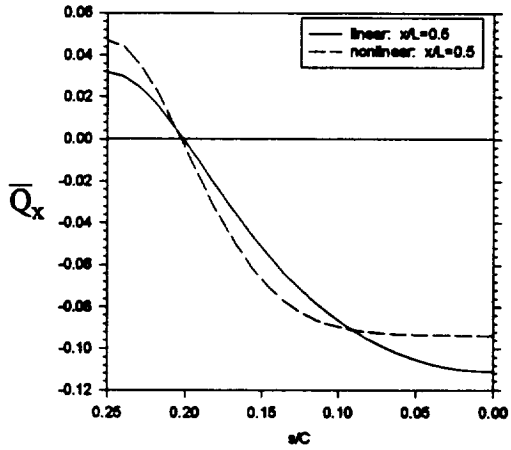

Figure 3-20. Effect of geometric nonlinearities on the axial transverse shear force resultant: linear vs. nonlinear at x/L = 0.5.

While $\overline{Q}_s$ and $\overline{Q}_x$ represent the transverse shear force resultant for the linear analysis, there are other transverse force resultants defined for the nonlinear analysis. The $\overline{Q}_s$ and $\overline{Q}_x$ just shown in fig. 3-17 through fig. 3-20 for the nonlinear case have the same definitions as the linear case and they are given in eq. 2.6. These definitions for $\overline{Q}_s$ and $\overline{Q}_x$ for the nonlinear case still represent

transverse shear force resultants. However, they do not act strictly in the outward or inward normal direction, but are rotated away from the normal direction. The transverse force resultants (note the absence of the word 'shear') in the normal direction for the nonlinear case are denoted here as V_s and V_x, and are given by,

$$V_x = \frac{\partial M_x}{\partial x} + \frac{\partial M_{xs}}{\partial s} + N_x\frac{\partial w^o}{\partial x} + N_{xs}\frac{\partial w^o}{\partial s}$$
$$V_s = \frac{\partial M_{xs}}{\partial x} + \frac{\partial M_s}{\partial s} + N_{xs}\frac{\partial w^o}{\partial x} + N_s\frac{\partial w^o}{\partial s}. \tag{3.1}$$

These definitions of the transverse force resultants are the consequence of enforcing moment equilibrium for a deformed element of cylinder wall. For the nonlinear analysis V_s and V_x are what is needed to enforce w^o=0 at the boundary. As the definition of V_s and V_x include inplane force resultants N_s, N_x, and N_{xs}, and hence σ_s, σ_x, and τ_{xs}, V_s and V_x are not, strictly speaking, shear force resultants in the spirit of eq. 2.7. They are thus referred to as transverse force resultants.

The normalized nonlinear circumferential and axial transverse force resultants, $\overline{V}_s$ and $\overline{V}_x$ respectively, as illustrated in fig. 3-21 and fig. 3-22, are normalized by the same factor used for the force resultants in eq. 2.4. As seen in fig. 3-21, the differences between $\overline{Q}_s$ and $\overline{V}_s$ are significant in all regions. On the other hand, $\overline{Q}_x$ and $\overline{V}_x$, as in fig. 3-22, have similar behaviors in the midspan and boundary regions. However, the surface of $\overline{V}_x$ near the boundary appears smoother than the surface of $\overline{Q}_x$.

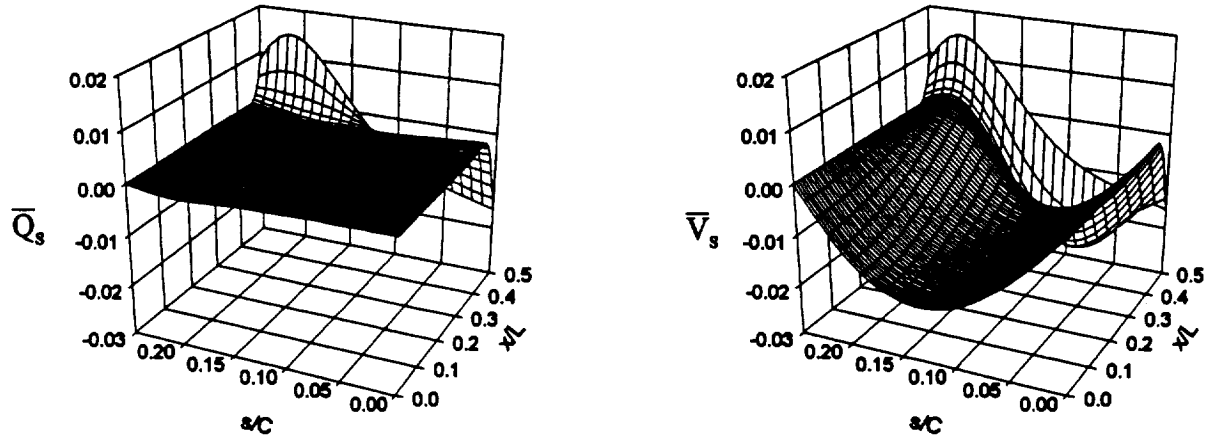

Figure 3-21. Circumferential transverse force resultants.

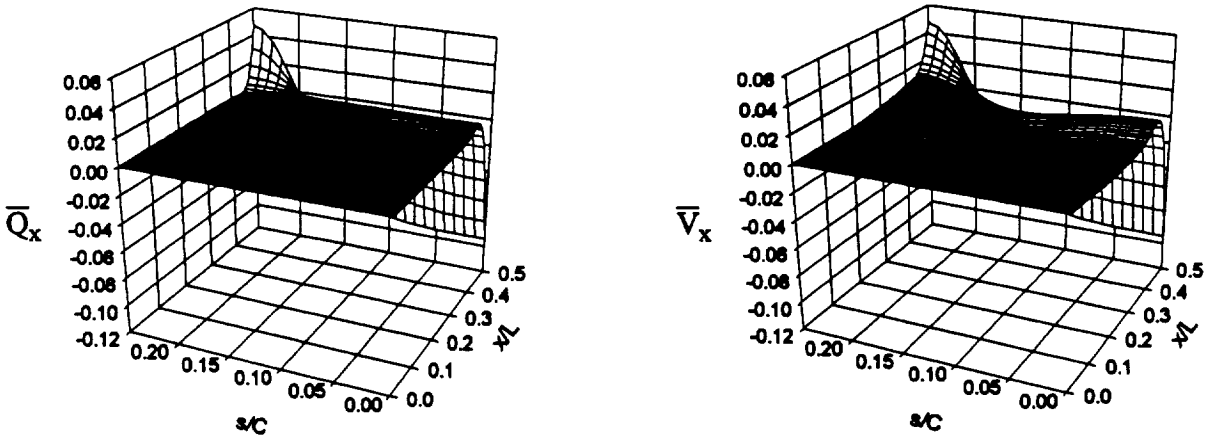

Figure 3-22. Axial transverse force resultants.

3.4 Summary of the Effects of Nonlinearity

The effects of geometric nonlinearities seen in this chapter included several key issues. Between linear and nonlinear analyses, the axial displacement displayed an overall difference in magnitude, the circumferential displacement had a shift in the local minimum, and the normal displacement flattened at the crown of the cylinder. Aside from the displacements, differences between linear and nonlinear analyses, if any exist, seemed to split into two categories, those due

to flattening of the crown of the cylinder, and those involving a change in magnitude of the behavior at the boundary. Flattening of the crown of the cylinder was seen in the circumferential strain, circumferential curvature, and circumferential force resultant. The change of the behavior at the boundary was seen in axial curvature, and axial and circumferential transverse shear force resultants, $\overline{Q}_s$ and $\overline{Q}_x$. The moment resultants showed both behaviors, a flattening in the crown and a change of magnitude at the boundary. Also, two definitions of the transverse force resultants were introduced. There were significant differences between the circumferential transverse shear force resultant, $\overline{Q}_s$, and the circumferential transverse force resultant, $\overline{V}_s$.

The next chapter addresses the consequences of varying the orthotropy of the cylinder. Cylinder responses are compared for axially-stiff, quasi-isotropic, and circumferentially-stiff laminates.

Chapter 4 Effect of Material Orthotropy on Cylinder Response

Thus far, the influences of elliptical geometry have been studied using a linear analysis and a quasi-isotropic cylinder, and the influences of geometric nonlinearities have been studied using a quasi-isotropic cylinder. In this chapter the focus is shifted from the influence of elliptical geometry and geometric nonlinearities to the influence of material othotropy. The quasi-isotropic laminate considered in the previous chapter will be compared with axially-stiff and circumferentially-stiff laminates using a geometrically nonlinear analysis for an elliptical cylinder. Each laminate has a different response to internal pressure due to the percentages of fibers running in the axial and circumferential directions. The axially-stiff laminate has almost 50% of the fibers aligned with the axial direction, the circumferentially-stiff laminate has almost 50% of the fibers aligned with the circumferential direction, and the quasi-isotropic has an equal number of fibers aligned with the axial, circumferential, and $\pm 45^{\circ}$ direction. For this study of the influence of orthotropy, a three-dimensional format figure for each of the three laminates will again be shown, along with two-dimensional format figures along a line at a particular s/C or x/L location for the purpose of a closer examination of an issue that may be difficult to discern from the three-dimensional format figures. Only those responses which show any significant differences due to orthotropy are discussed.

4.1 Displacements

Recall from the boundary conditions of eq. 1.3 that the axial displacement is zero at x/L = -0.5, and at x/L = 0.5 the axial displacement is determined by eq. 1.4. It appears that for all the laminates the axial displacement at x/L = 0.5 is approximately twice the value at x/L = 0. However, the magnitude of the axial displacement response differs for the three laminates. As seen in fig. 4-1, the circumferentially-stiff laminate requires a higher axial end displacement, or Δ, to satisfy the axial equilibrium given in eq. 1.4 than either the quasi-isotropic or axially-stiff laminates. In fact, the axially-stiff elliptical cylinder under internal pressure evaluated using nonlinear analysis requires a *negative* axial displacement to satisfy the axial equilibrium equation. Though the overall characters of the axial displacement responses are the same, the displacement difference at x/L = 0.5 is evident.

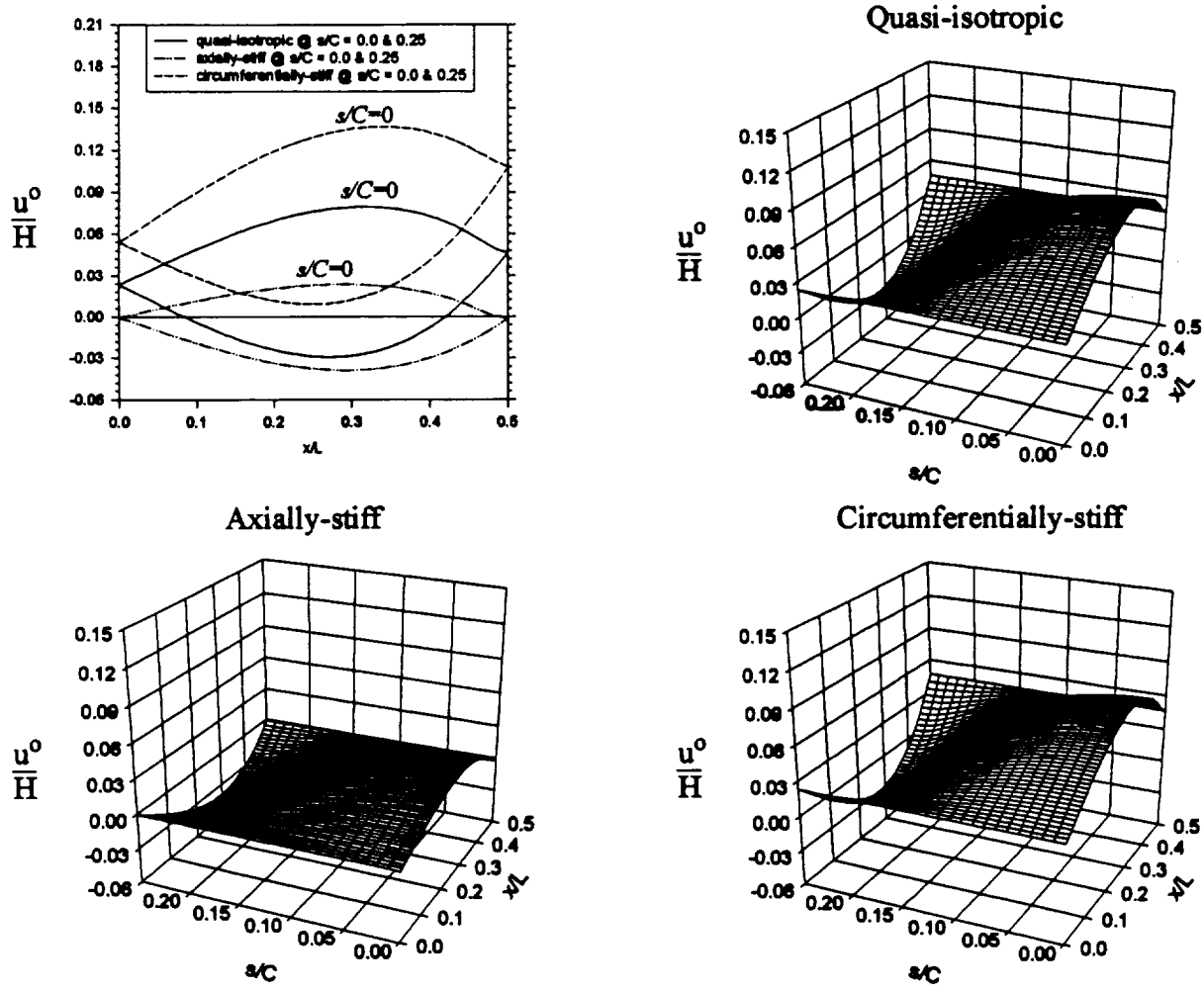

Figure 4-1. Influence of orthotropy on the axial displacement.

The circumferential displacements for the various laminates, as seen in fig. 4-2, have a similar overall behavior. The circumferential displacement is zero at x/L=0.5 due to the boundary conditions given in eq. 1.3, and increases in magnitude to a local extreme at s/C = 0.1563 at the midspan. However, the magnitude of this local extreme varies between the quasi-isotropic, axially-stiff, and circumferentially-stiff laminates. In fig. 4-2a, the three laminates are closely examined along the line at x/L=0. The circumferential displacement for the axially-stiff laminate is the smallest in magnitude, while it is largest in magnitude for the quasi-isotropic laminate.

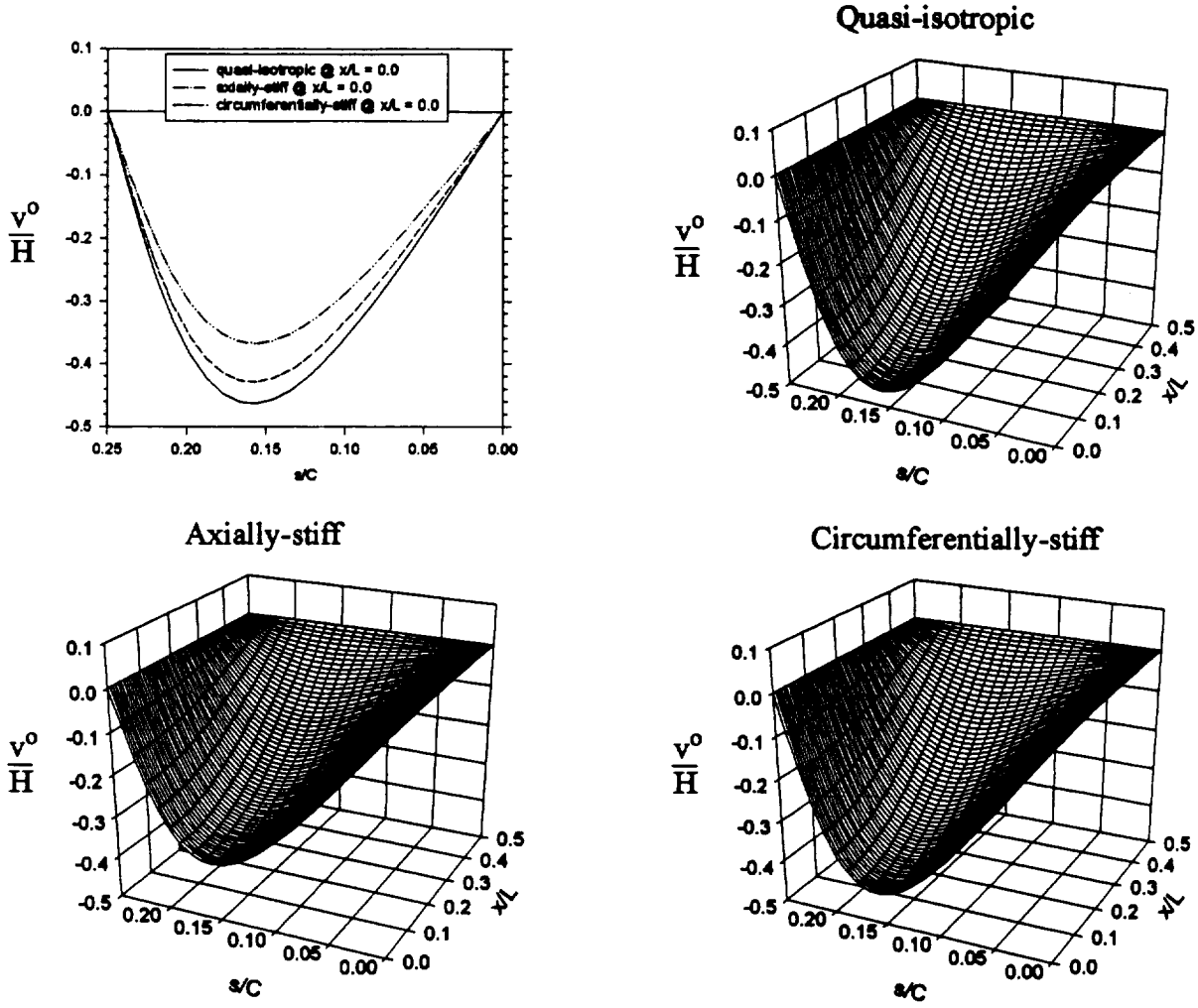

Figure 4-2. Influence of orthotropy on the circumferential displacement.

Although the overall behavior of the normal displacement is unaffected by orthotropy, as seen in fig. 4-3, the magnitude of the normal displacement at the midspan is controlled by the orthotropy. At the crown of the cylinder the normal displacement for the axially-stiff laminate is greater than for the circumferentially-stiff laminate, but less than for the quasi-isotropic laminate. However, at the side of the cylinder the situation is somewhat reversed and the magnitude of the normal displacement for the circumferentially-stiff laminate is greater than for the axially-stiff laminate, but again less than the magnitude of the normal displacement for the quasi-isotropic

laminate. In general, the circumferentially-stiff laminate best controls expansion at the crown of the cylinder and the axially-stiff laminate best controls contraction at the side of the cylinder.

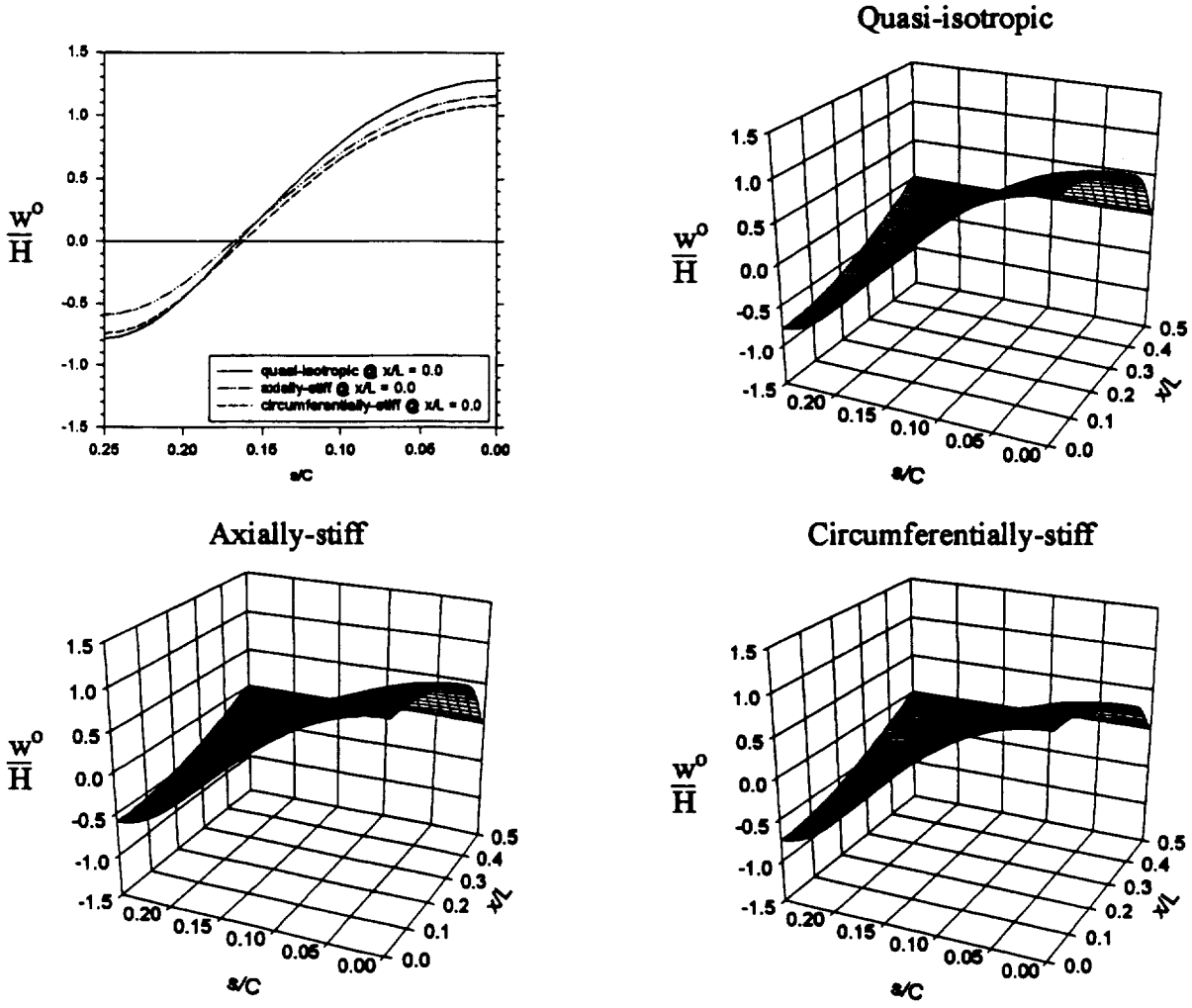

Figure 4-3. Influence of orthotropy on the normal displacement.

4.2 Strains and Curvatures

As seen in fig. 4-4, the degree to which the circumferential strain varies with the *s* coordinate at the midspan is completely affected by the laminate considered. Recall from fig. 2-3a-b, the circumferential strain for a circular cylinder has no variation with the *s* coordinate, while the circumferential strain for the elliptical cylinder varies considerably with the *s* coordinate. As seen in

fig. 4-4, at midspan the circumferentially-stiff laminate mitigates, to a high degree, the effect of ellipticity, as the strain does not vary much with s there. The circumferential strain for the axially-stiff and quasi-isotropic laminates varies more with the s coordinate at the midspan. Therefore, it appears that the percentage of fibers in the circumferential direction controls the degree of variation of the circumferential strain with the s coordinate at the midspan.

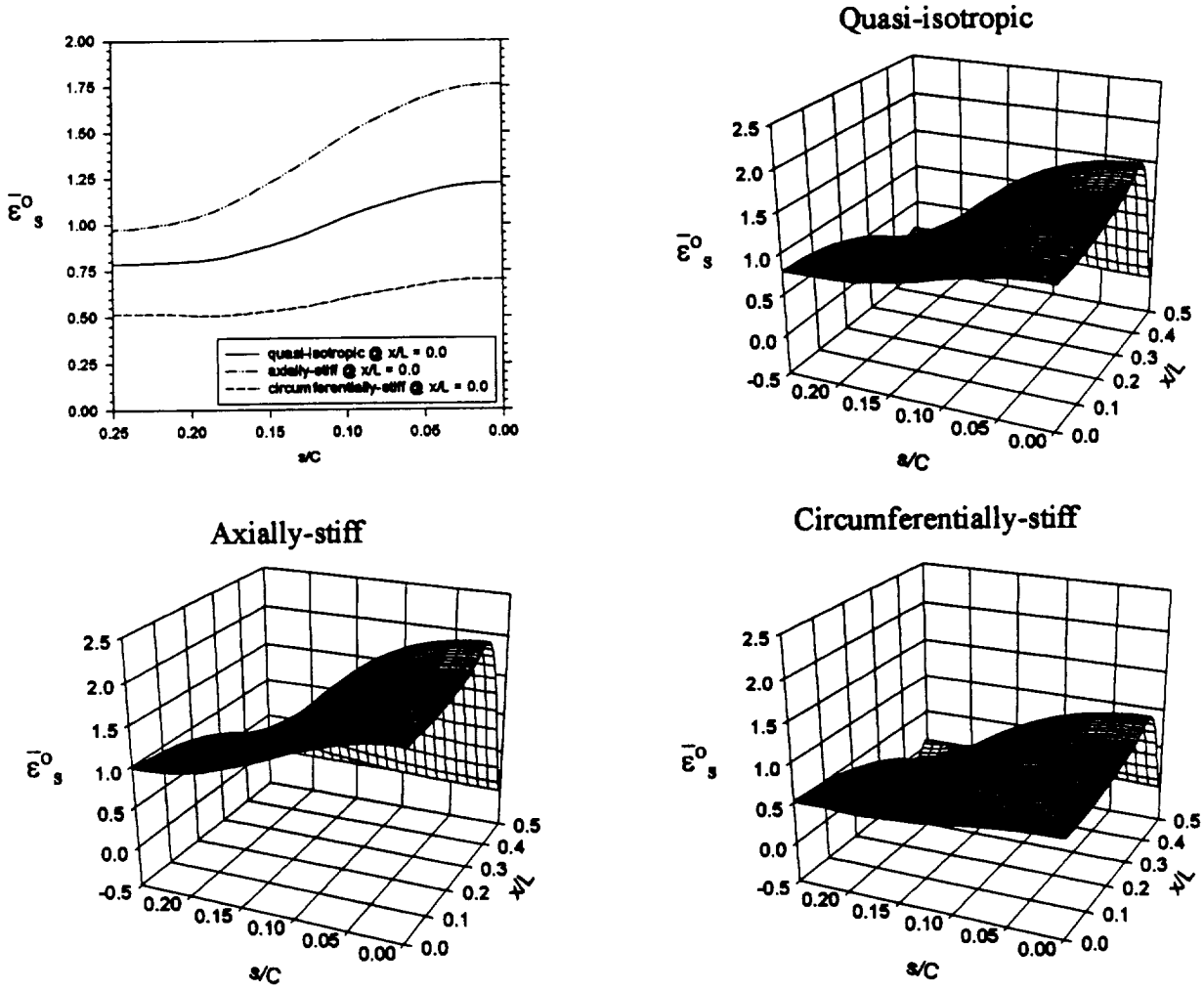

Figure 4-4. Influence of orthotropy on the circumferential strain.

As seen in fig. 4-5, the degree to which the axial strain varies with spatial location is also affected by the laminate considered. Comparatively, the axial strain for the axially-stiff laminate

varies least with both the x and s coordinates and it varies the most for the circumferentially-stiff laminate. Recall from fig. 2-3c-d, the axial strain for a circular cylinder has no variation with the s coordinate, while for the elliptical cylinder it varies considerably with both the x and s coordinate. Although the axially-stiff laminate doesn't completely mitigate the effect of ellipticity on the axial strain at midspan, the increased percentage of fibers in the axial direction controls the degree of spatial variation for the axial strain there. To be noted, the degree of orthotropy has little if any influence on the shear strain distribution with x and s.

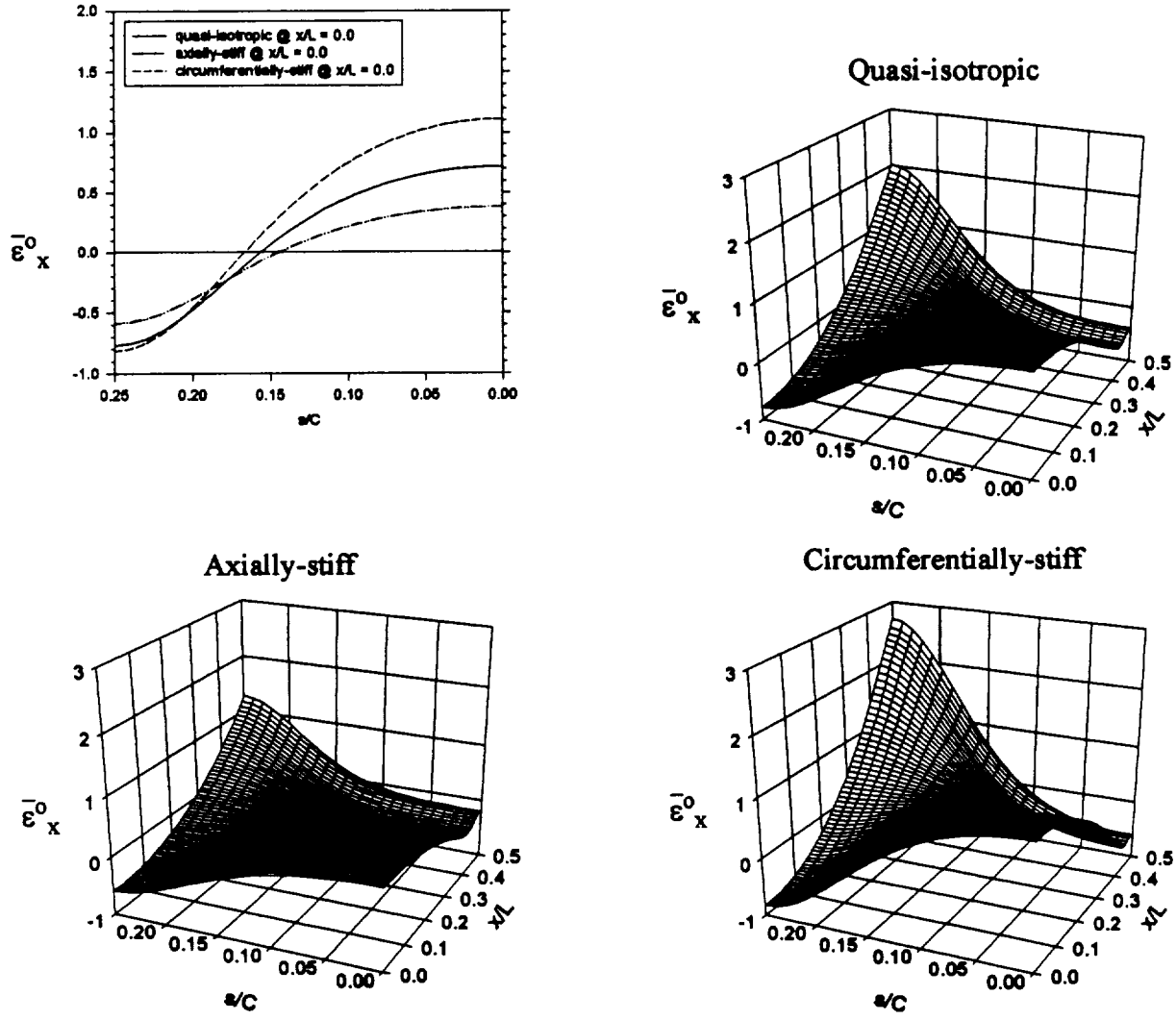

Figure 4-5. Influence of orthotropy on the axial strain.

As seen in fig. 4-6, in the midspan region the axial curvature is similar for all orthotropies, namely zero. In the boundary region, however, the variation with s of the axial curvature depends on the orthotropy. Recall that the behavior of the axial curvature at the boundary is due to the clamped boundary conditions imposed on the cylinder ends, and that the elliptical shape forces a reversal in curvature at the boundary as s/C changes from 0 to 0.25. The orthotropy affects the degree of the reversal in curvature at the boundary. Comparatively, at the boundary, the axial curvature for the axially-stiff laminate varies least with the s coordinate, and it varies the most for the circumferentially-stiff laminate. Therefore, the percentage of fibers in the axial direction controls the degree of reversal of the curvature at the boundary. Interestingly, the axially-stiff elliptical cylinder evaluated using a linear analysis instead of a nonlinear analysis does not show this reversal of curvature.

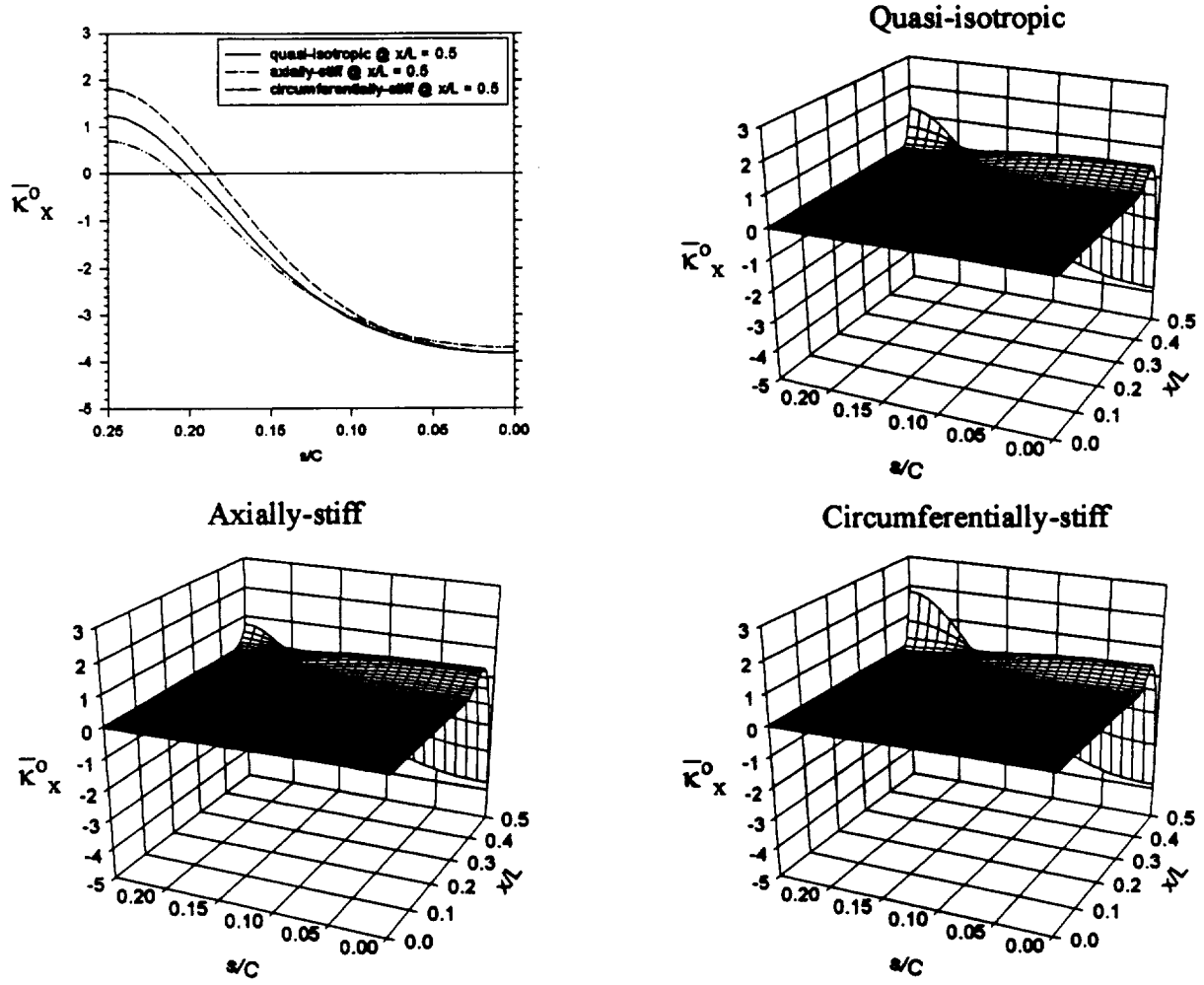

Figure 4-6. Influence of orthotropy on the axial curvature.

As seen in fig. 4-7, the overall behavior of the twist curvature is similar for all orthotropies. However, the magnitude of the local extreme in the twist curvature, and its location with x and s, changes with the degree of orthotropy. The twist curvature for the circumferentially-stiff laminate has a minimum value of -0.3796 located at x/L=0.4758 and s/C=0.1458, the twist curvature for the quasi-isotropic laminate has a minimum value of -0.3920 located at x/L=0.4678 and s/C=0.1458, and the twist curvature for the axially-stiff laminate has a minimum value of -0.4285 located at x/L=0.4678 and s/C=0.1563. Therefore, as the percentage of fibers in the axial direction

increases, the magnitude of the local minimum value of the twist curvature increases and shifts toward the side of the cylinder, and as the percentage of fibers in the circumferential direction increases, the magnitude of the local minimum value of the twist curvature decreases and shifts toward the clamped boundary. The circumferential curvature does not depend on the degree of othotropy.

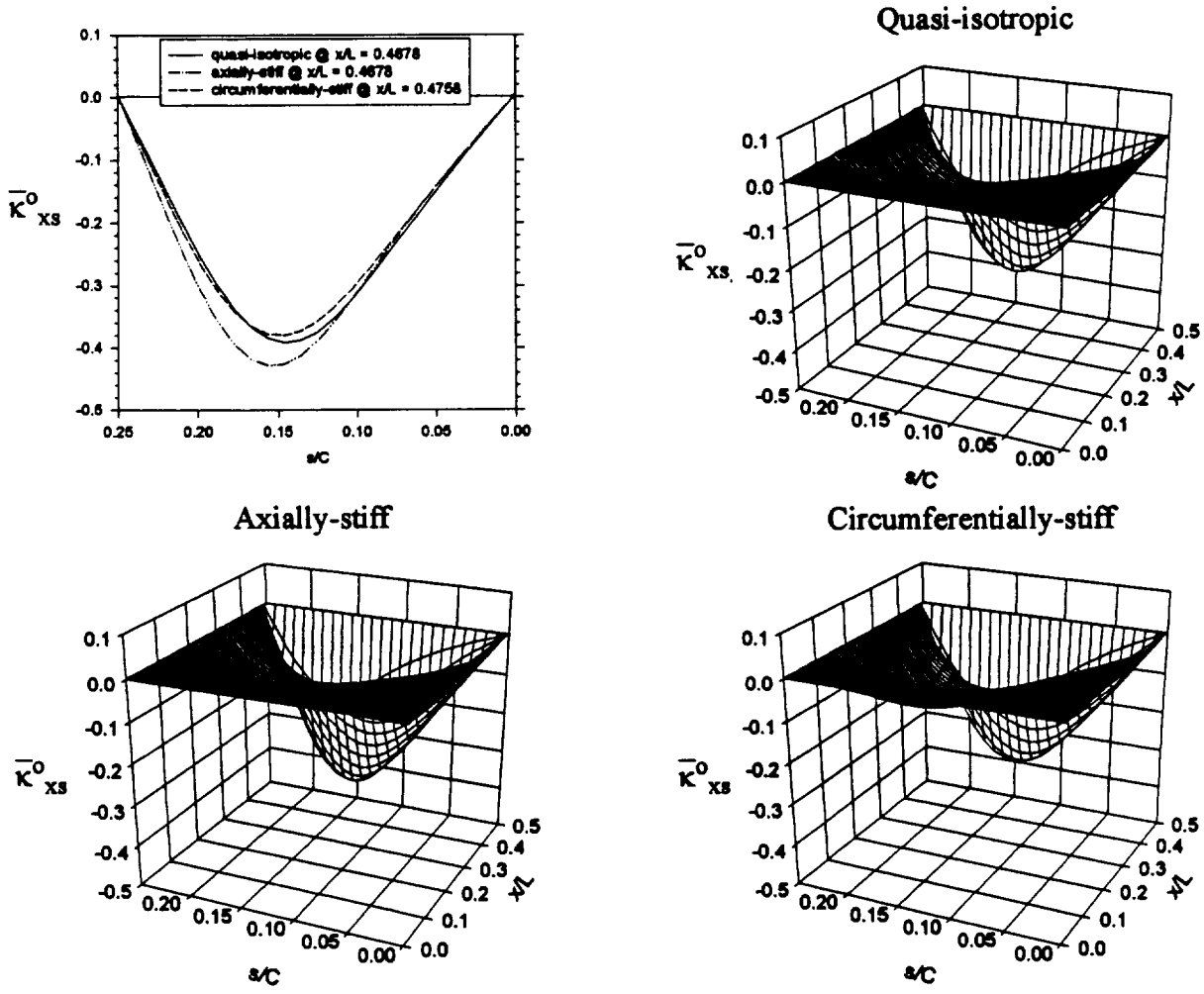

Figure 4-7. Influence of orthotropy on the twist curvature.

4.3 Force and Moment Resultants

As seen in fig. 4-8, the boundary region for the circumferential force resultant differs among the circumferentially-stiff, axially-stiff, and quasi-isotropic laminates. At the clamped boundary, the circumferential force resultant for the quasi-isotropic laminate varies more with the s coordinate than for the axially-stiff laminate, but it varies less than the circumferential force resultant for the circumferentially-stiff laminate. Therefore, as the percentage of fibers in the axial direction increases, the variation with the s coordinate of the circumferential force resultant at the boundary decreases.

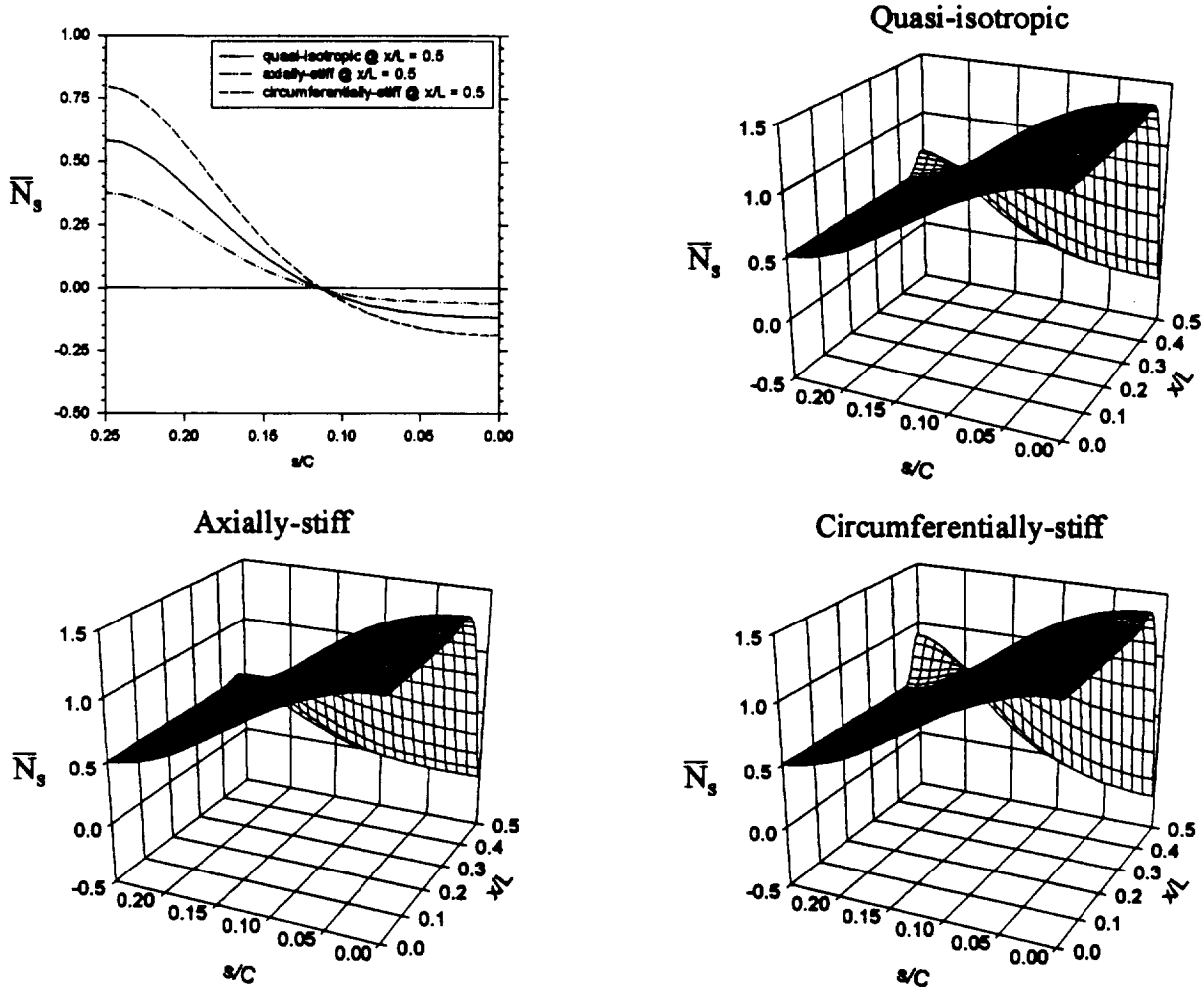

Figure 4-8. Influence of orthotropy on the circumferential force resultant.

The circumferential moment resultant, as seen in fig. 4-9, also differs among the circumferentially-stiff, axially-stiff, and quasi-isotropic laminates. The variations with s along x/L=0 and 0.5 are examined for a closer look at these differences. The circumferential moment resultant is not large in magnitude at the midspan, but there are differences among the orthotropies. The circumferential moment resultant for the circumferentially-stiff laminate is significantly greater in magnitude at the side of the cylinder, changes sharply between s/C=0.20 and 0.15, then flattens out at the crown to a magnitude greater than those for the axially-stiff and quasi-isotropic lami-

nates. Along the clamped boundary the circumferential moment resultant for the circumferentially-stiff laminate is greater in magnitude at the side and the crown than for the other two laminates. The axial and twist moment resultants have results similar to the circumferential moment resultant in that the magnitude at the side and crown, and at the midspan and clamped boundary depend to some degree on orthotropy.

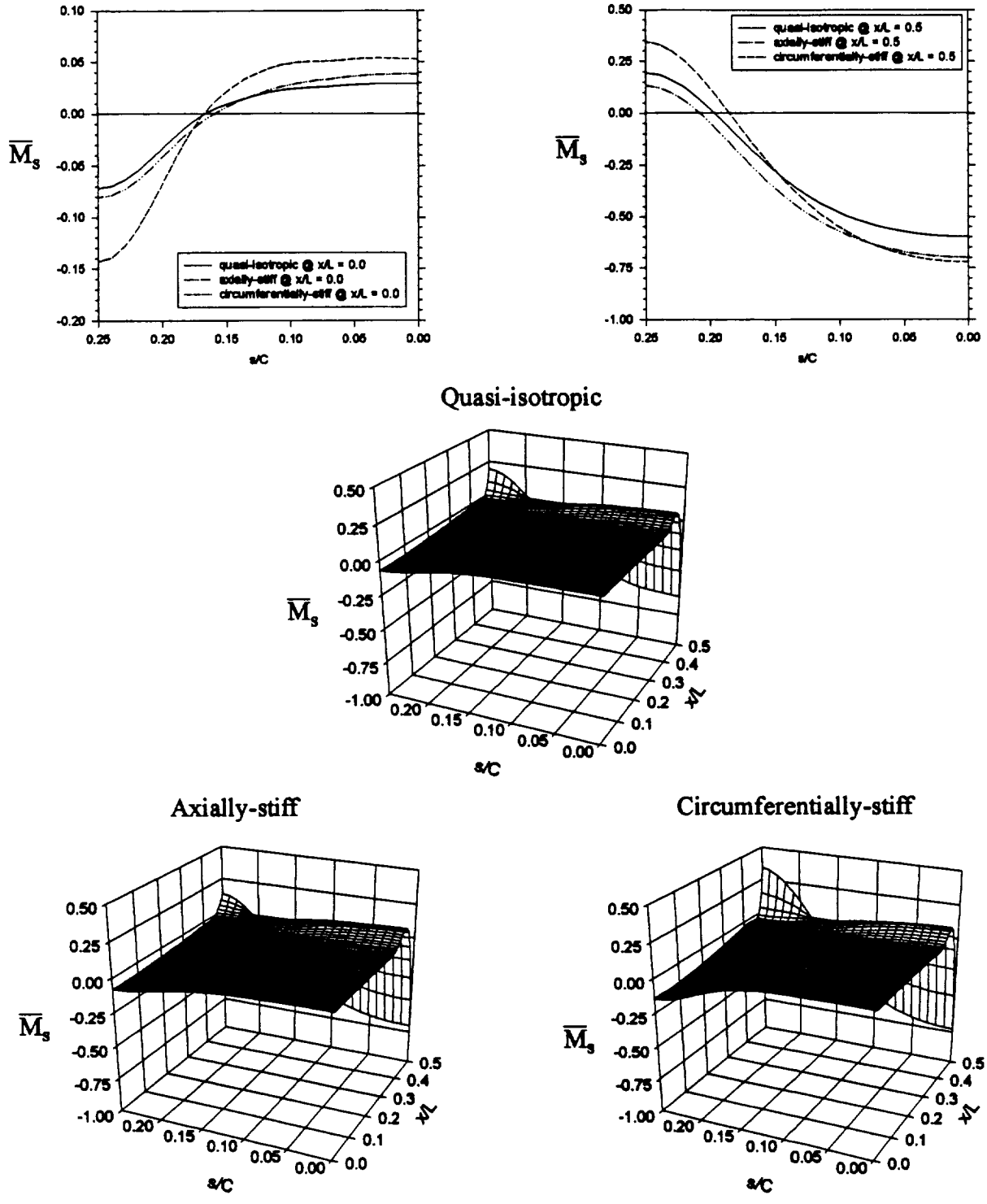

Figure 4-9. Influence of orthotropy on the circumferential moment resultant.

As seen in fig. 4-10, in the midspan region the circumferential transverse shear force resultant is similar for all three orthotropies, namely, almost zero. In the region of the clamped boundary, however, the variation of the force resultant depends on the orthotropy. Recall that the axial and circumferential transverse shear force resultants enforce the w^o=0 condition at the boundary of the cylinder, and with the elliptical geometry they are forced to a change sign at the boundary because the cylinder moves outward at the crown and keel, and inwards at the sides. The orthotropy affects the degree of the sign reversal of the circumferential transverse shear force resultant at the boundary. Comparatively, the force resultant for the axially-stiff laminate varies least with the *s* coordinate at the boundary and that for the circumferentially-stiff varies most. In general, the percentage of fibers in the axial direction controls the degree of the sign reversal of the circumferential transverse shear force resultant at the boundary.

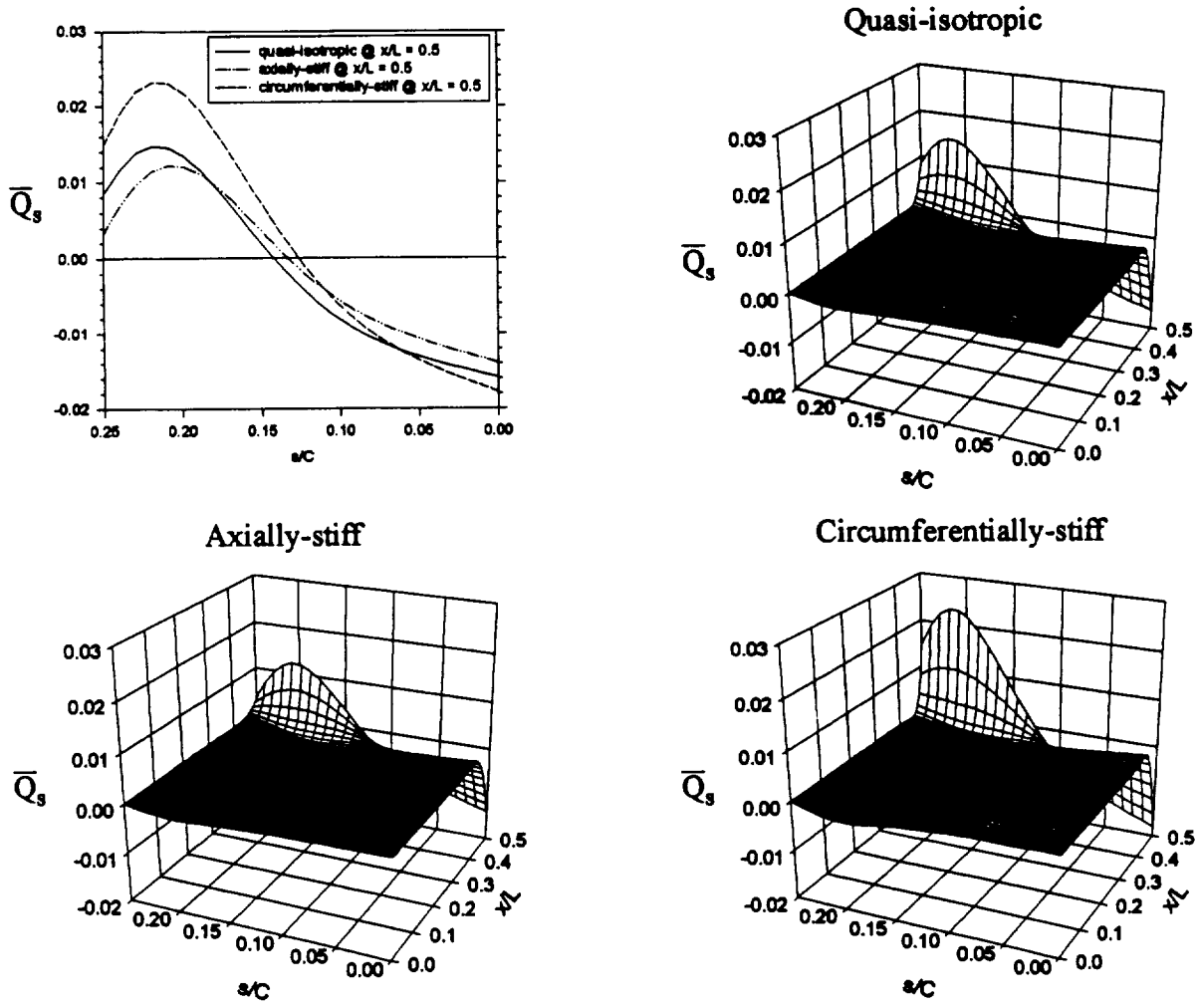

Figure 4-10. Influence of orthotropy on the circumferential transverse shear force resultant, Q_s.

As seen in fig. 4-11, in the midspan region the axial transverse shear force resultant is similar for all orthotropies, being close to zero there in all cases, but in the clamped boundary region the variation of the force resultant depends on the orthotropy. Again the boundary conditions on w^o combined with the elliptical geometry force a change of sign in the force resultant, the location of this sign change depending on the orthotropy. Furthermore in the side region of the cylinder, the force resultant for the circumferentially-stiff laminate is greatest in magnitude and that for the

axially-stiff laminate is smallest in magnitude. In the crown region of the cylinder, this trend reverses. The force resultant for the circumferentially-stiff laminate is smallest in magnitude and that for the axially-stiff laminate is greatest.

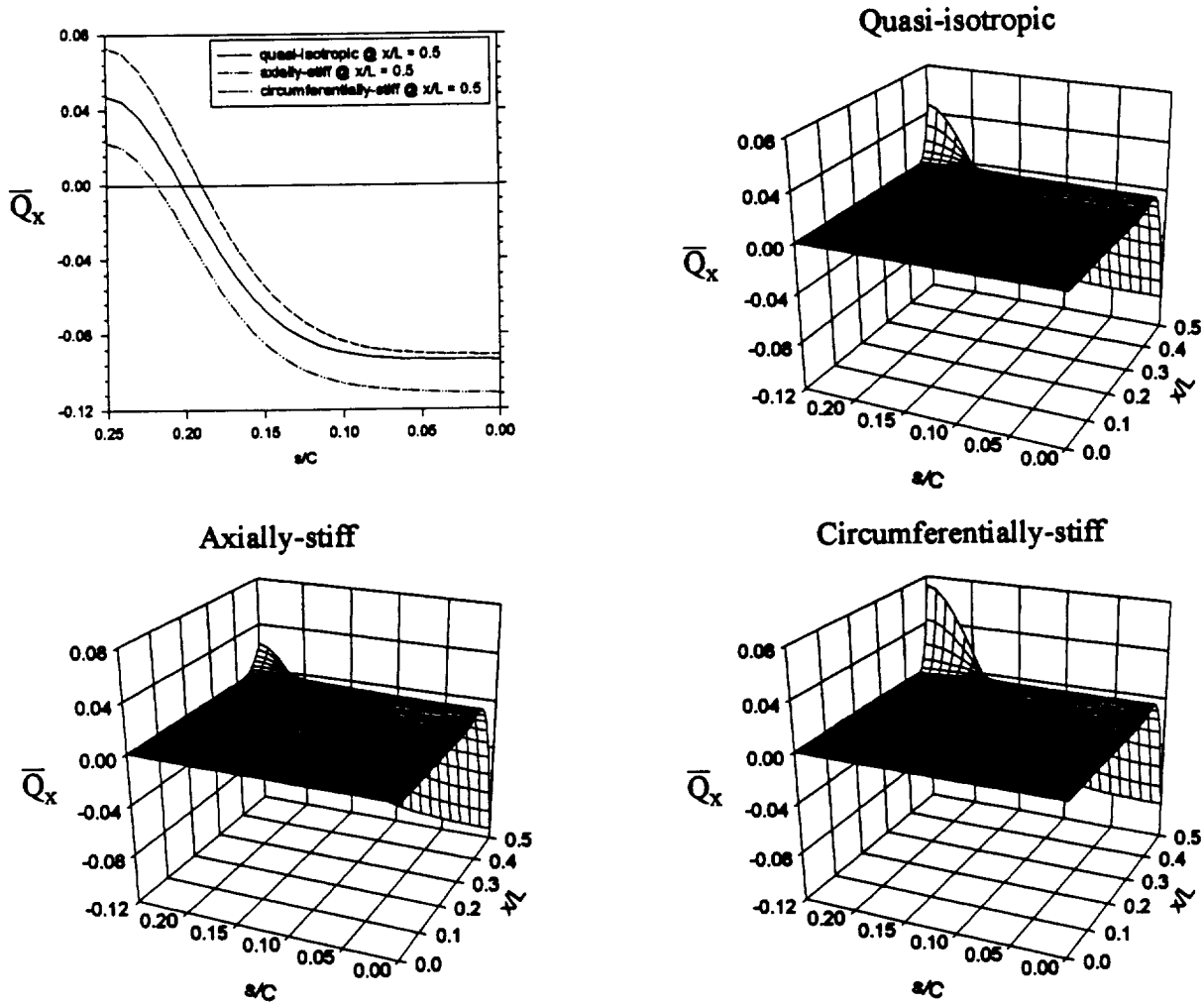

Figure 4-11. Influence of orthotropy on the axial transverse shear force resultant, Q_x.

As seen in fig. 4-12, in the midspan region the circumferential transverse force resultant is similar for all orthotropies, but in the boundary region of the cylinder it varies. The orthotropy affects the location of the sign reversal and the peak-to-peak variations of the circumferential transverse force resultant at the boundary. In general, as the percentage of fibers along the axial

direction increases, the variation of the circumferential transverse force resultant with the s coordinate decreases at the boundary.

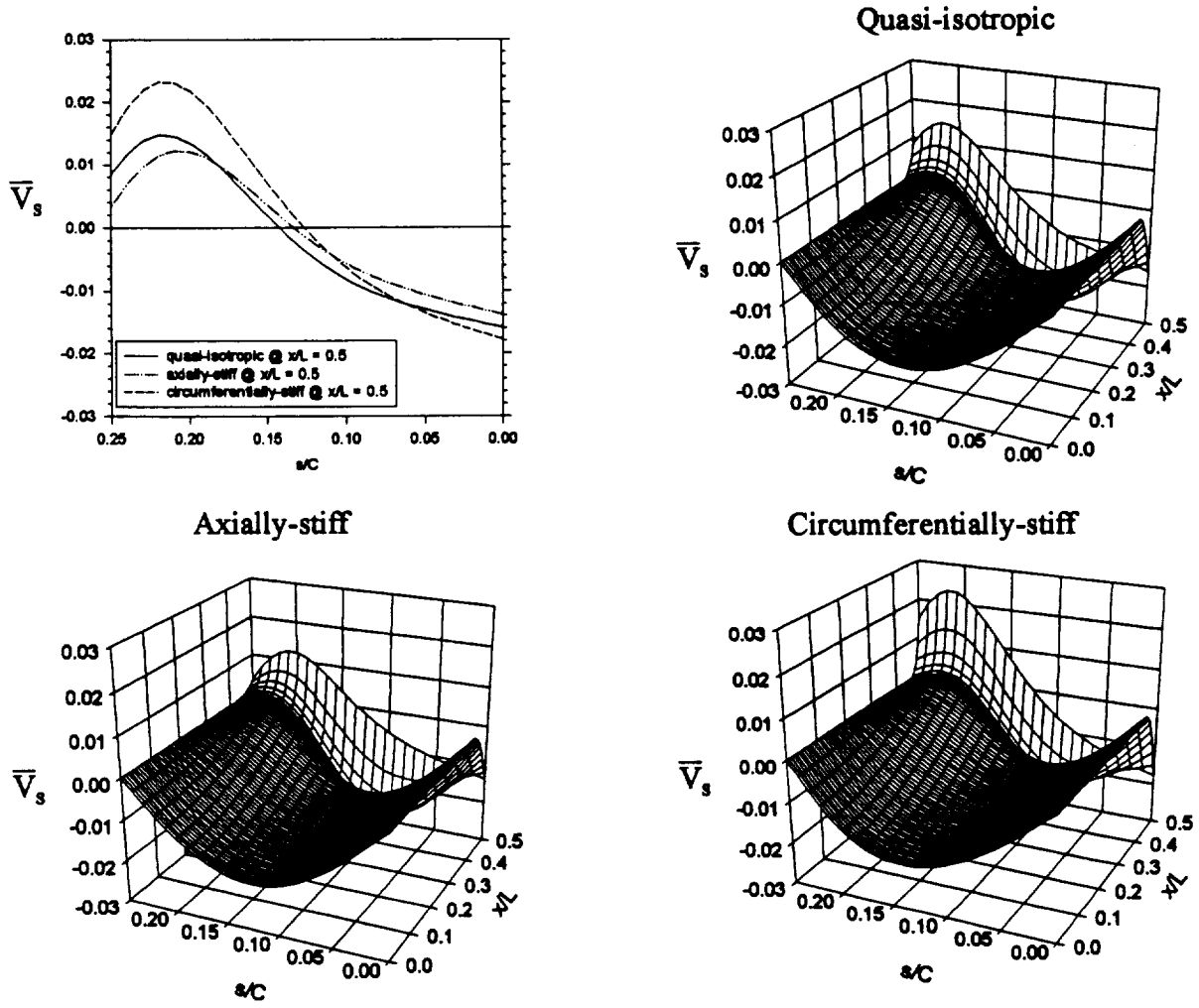

Figure 4-12. Influence of orthotropy on the circumferential transverse force resultant, V_s.

As seen in fig. 4-13, in the midspan region the axial transverse force resultant is similar for all orthotropies, being very close to zero, but in the boundary region it varies, depending on the orthotropy. Again, the boundary conditions on w^o and the elliptical geometry force a change of sign in the axial transverse force resultant at the boundary. The orthotropy affects the location of the sign reversal and the peak-to-peak variation of the axial transverse force resultant at the

boundary. In the side region of the cylinder, the force resultant for the circumferentially-stiff laminate is greatest in magnitude, and for the axially-stiff laminate it is smallest in magnitude. In the crown region of the cylinder, these characteristics reverse such that the force resultant for the circumferentially-stiff laminate is smallest in magnitude, and for the axially-stiff laminate it is greatest in magnitude.

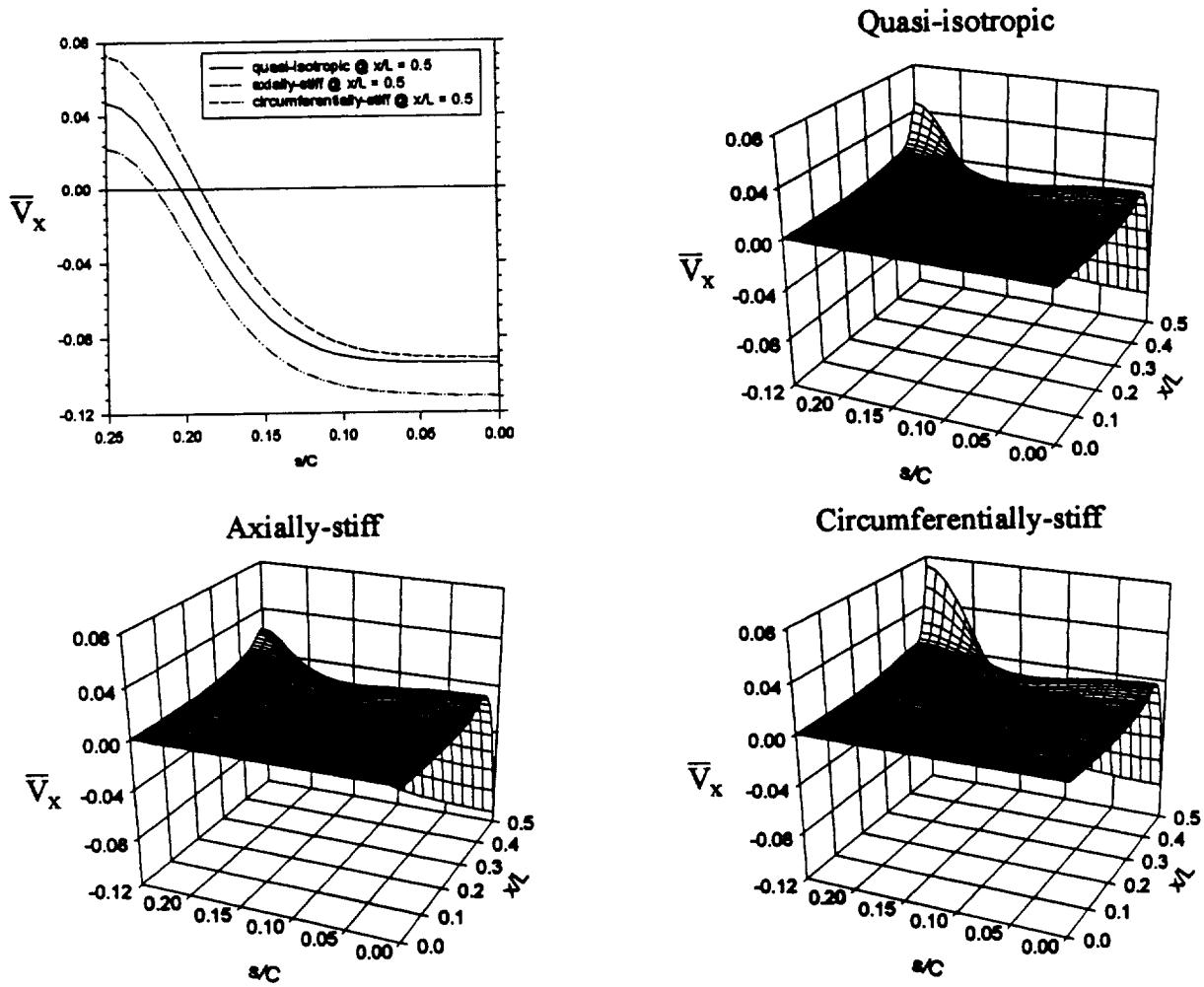

Figure 4-13. Influence of orthotropy on the axial transverse force resultant, V_x.

4.4 Summary of the Effects of Orthotropy

The effects of orthotropy seen in this section included several key issues. The axially-stiff, circumferentially-stiff, and quasi-isotropic laminates resulted in an overall difference in magnitude for the axial, circumferential, and normal displacements. In fact, the axially-stiff elliptical cylinder evaluated using nonlinear analysis contracts axially in response to internal pressure, whereas, for the other two cases there is axial extension. For some responses, orthotropy mitigates the effect of ellipticity. For example, the circumferential strain behaves like that of a circular cylinder in the midspan region of the circumferentially-stiff laminate. For the axially-stiff laminate, the axial strain displays less spatial variation with both x and s compared to the axial strains for the circumferentially-stiff and quasi-isotropic laminates. The variation with s at the clamped boundary of the axial curvature, the circumferential force and moment resultants, and the transverse force resultants depends significantly on orthotropy. Compared to the circumferentially-stiff and quasi-isotropic laminates, for these responses the axially-stiff laminate does not generally exhibit as much variation with s.

This chapter has presented a through discussion of the character of the response to internal pressure of elliptical cylinders with three different levels of orthotropy. A complete catalogue of all the geometrically nonlinear responses of the three cylinders is presented in Appendix A, along with a comparison of the responses as predicted by the finite element code STAGS [6]. The latter comparison is for the purpose of verifying the present analysis. As noted in Appendix A, by the nature of finite element analysis, many of the important responses are not computed exactly at the ends of the cylinder, the location where many responses assume a maximum or minimum value. For this reason there appears to be a lack of agreement between STAGS predictions and the predictions of the present analysis near the ends of the cylinder. This issue becomes important when

failure is studied, as it is in the next chapter. Whereas the present analysis may predict failure to occur at the exact ends of the cylinder due to a certain pressure level, STAGS would predict failure to occur slightly inwards of the ends at a different pressure level. However, STAGS is not used here to study failure so the issue never arises.

Also by way of a catalogue, Appendix B provides a listing of the axial displacement Δ for each of the cases discussed here. Recall, Δ is determined by eq. 1.4.

Chapter 5 Failure Analysis

In the past several chapters the influences of geometry and orthotropy on the responses of elliptical and circular cylinders constructed with quasi-isotropic, axially-stiff, and circumferentially-stiff laminates have been evaluated. Both geometrically linear and nonlinear analyses have been used. In this chapter, an evaluation of failure using the maximum stress and Hashin [7] failure criteria is presented for elliptical cylinders by considering geometrically linear and nonlinear analyses and quasi-isotropic, axially-stiff, and circumferentially-stiff laminates. The failure criteria are used to assess the mode of failure (e.g., tensile or compressive fiber or matrix modes), the location of failure, and the pressure at failure.

5.1 Failure Criteria

The maximum stress and Hashin failure criteria are three-dimensional theories that are based on one-dimensional uniaxial and shear failure stresses. The one-dimensional failure stresses are denoted as follows:

σ_A^+ = tensile failure stress in the fiber direction

σ_A^- = compressive failure stress in the fiber direction (absolute value)

σ_T^+ = tensile failure stress transverse to the fiber direction

σ_T^- = compressive failure stress transverse to the fiber direction (absolute value)

τ_T = transverse failure shear stress

τ_A = axial failure shear stress

For graphite-epoxy typical values of the failure stresses are [2]:

$$\begin{aligned} \sigma_A^+ &= 200,000 \text{ psi} \\ \sigma_A^- &= 180,000 \text{ psi} \\ \sigma_T^+ &= 7250 \text{ psi} \\ \sigma_T^- &= 29,000 \text{ psi} \\ \tau_A &= 14,500 \text{ psi} \\ \tau_T &= 14,500 \text{ psi} \end{aligned} \tag{5.1}$$

The maximum stress and Hashin failure criteria are linear and quadratic in the stresses, respectively. For the maximum stress criterion, failure is assumed to occur when any one of the stresses in the principal material coordinate system equals the respective failure stress level. For the Hashin criterion, the stresses in the principal material coordinate system and the failure stresses are combined quadratically to form a number of expressions and the material is assumed to fail when any one of the expressions terms reaches unity. Alternatively, the maximum stress criterion can be formatted so that failure is assumed to occur when the ratio of any one of the stresses in the principal material system divided by the respective failure stress level reaches unity. Therefore, these two criteria can be put on a somewhat similar basis.

5.1.1 Maximum Stress Theory

For the maximum stress criterion, there are three modes of failure: tensile, compressive, and shear. There is assumed to be no interaction between modes of failure or between the stresses in principal material coordinate system. For example, tensile failure occurs when either σ_{11} or σ_{22} reaches the respective failure value, but σ_{22} doesn't interact with σ_{11} to cause tensile failure, say, when both are 90% of their failure value. The shear failure mode is independent of sign, such that a negative or a positive shear stress is equally capable of causing shear failure. The failure modes of the maximum stress theory are denoted as follows:

Tensile Modes (σ_{11}, $\sigma_{22} > 0$):

$$\sigma_{11} < \sigma_A^+ \qquad \sigma_{22} < \sigma_T^+ \tag{5.2}$$

Compressive Modes (σ_{11}, $\sigma_{22} < 0$):

$$-\sigma_{11} < \sigma_A^- \qquad -\sigma_{22} < \sigma_T^- \tag{5.3}$$

Shear Modes:

$$|\sigma_{23}| < \tau_T \qquad |\sigma_{13}| < \tau_A \qquad |\sigma_{12}| < \tau_A \tag{5.4}$$

For the purpose of computation, the following is a more convenient form for the maximum stress criterion:

Tensile Modes (σ_{11}, $\sigma_{22} > 0$):

$$\frac{\sigma_{11}}{\sigma_A^+} < 1 \qquad \frac{\sigma_{22}}{\sigma_T^+} < 1 \tag{5.5}$$

Compressive Modes (σ_{11}, $\sigma_{22} < 0$):

$$\frac{-\sigma_{11}}{\sigma_A^-} < 1 \qquad \frac{-\sigma_{22}}{\sigma_T^-} < 1 \tag{5.6}$$

Shear Modes:

$$\frac{|\sigma_{23}|}{\tau_T} < 1 \qquad \frac{|\sigma_{13}|}{\tau_A} < 1 \qquad \frac{|\sigma_{12}|}{\tau_A} < 1 \tag{5.7}$$

With this form of the failure criterion, the cylinder is assumed to be safe from failure if all seven of the left hand sides of eqs. 5.5-5.7 are less than unity, and failure is assumed to occur when any one of the seven left hand sides equals unity.

5.1.2 Hashin Theory

For the Hashin criterion, there are four modes of failure: tensile fiber, compressive fiber, tensile matrix, and compressive matrix. The Hashin theory is written in terms of quadratic stress

polynomials such that the interaction between the stresses represents an average stress state. The four modes of the Hashin criterion are denoted as follows:

Tensile Fiber Mode: $\sigma_{11} > 0$

$$\left(\frac{\sigma_{11}}{\sigma_A^+}\right)^2 + \frac{1}{\tau_A^2}(\sigma_{12}^2 + \sigma_{13}^2) < 1 \tag{5.8}$$

Compressive Fiber Mode: $\sigma_{11} < 0$

$$\frac{-\sigma_{11}}{\sigma_A^-} < 1 \tag{5.9}$$

Tensile Matrix Mode: $(\sigma_{22} + \sigma_{33}) > 0$

$$\frac{1}{(\sigma_T^+)^2}(\sigma_{22} + \sigma_{33})^2 + \frac{1}{\tau_T^2}(\sigma_{23}^2 - \sigma_{22}\sigma_{33}) + \frac{1}{\tau_A^2}(\sigma_{12}^2 + \sigma_{13}^2) < 1 \tag{5.10}$$

Compressive Matrix Mode: $(\sigma_{22} + \sigma_{33}) < 0$

$$\frac{1}{\sigma_T^-}\left[\left(\frac{\sigma_T^-}{2\tau_T}\right)^2 - 1\right](\sigma_{22} + \sigma_{33}) + \frac{1}{4\tau_T^2}(\sigma_{22} + \sigma_{33})^2 + \frac{1}{\tau_T^2}(\sigma_{23}^2 - \sigma_{22}\sigma_{33}) + \frac{1}{\tau_A^2}(\sigma_{12}^2 + \sigma_{13}^2) < 1 \tag{5.11}$$

However, since σ_{33} is assumed to be negligible for the present analysis of the elliptical cylinders, the Hashin failure criterion simplifies as follows:

Tensile Fiber Mode: $\sigma_{11} > 0$

$$\left(\frac{\sigma_{11}}{\sigma_A^+}\right)^2 + \frac{1}{\tau_A^2}(\sigma_{12}^2 + \sigma_{13}^2) < 1 \tag{5.12}$$

Compressive Fiber Mode: $\sigma_{11} < 0$

$$\frac{-\sigma_{11}}{\sigma_A^-} < 1 \tag{5.13}$$

Tensile Matrix Mode: $\sigma_{22} > 0$

$$\left(\frac{\sigma_{22}}{\sigma_T^+}\right)^2 + \left(\frac{\sigma_{23}}{\tau_T}\right)^2 + \frac{1}{\tau_A^2}(\sigma_{12}^2 + \sigma_{13}^2) < 1 \tag{5.14}$$

Compressive Matrix Mode: $\sigma_{22} < 0$

$$\frac{\sigma_{22}}{\sigma_T^-}\left[\left(\frac{\sigma_T^-}{2\tau_T}\right)^2 - 1\right] + \left(\frac{\sigma_{22}}{2\tau_T}\right)^2 + \left(\frac{\sigma_{23}}{\tau_T}\right)^2 + \frac{1}{\tau_A^2}(\sigma_{12}^2 + \sigma_{13}^2) < 1 \tag{5.15}$$

Hence, the cylinder is assumed to be safe from failure when all four left hand sides of eqs. 5.12-5.15 are less than unity, and failure is assumed to have occurred when any one of the four left hand sides equals unity.

5.2 Determination of Stresses

In order to make use of either failure criterion, computation of the inplane and interlaminar shear stresses in the principal material coordinate system, which is shown in fig. 5-1, are necessary. Note the coordinate ξ_3 coincides with the through-thickness coordinate ζ, where ζ varies from $-H/2 \leq \zeta \leq H/2$ and is zero at the wall midsurface, or reference surface. The normal and shear stresses in the (ξ_1,ξ_2) plane $(\sigma_1, \sigma_2, \sigma_{12})$ are termed inplane stresses. The shear stresses trans-

verse, or perpendicular, to the (ξ_1,ξ_2) plane $(\sigma_{13}, \sigma_{23})$ are called interlaminar stresses. (Actually due to the complementary nature of shear stresses, σ_{13} and σ_{23} also act parallel to the 1-2 plane)

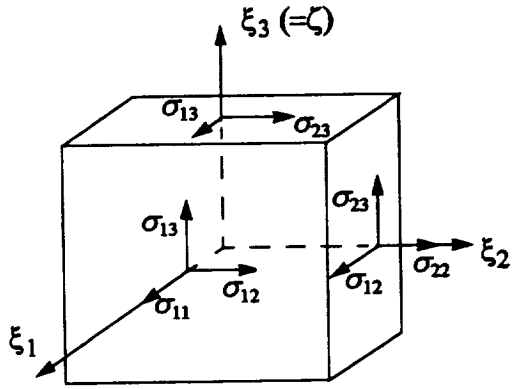

Figure 5-1. Inplane and interlaminar stresses in principal material direction.

5.2.1 Inplane Stresses

The inplane stresses can be written in terms of reference surface strains and curvatures, which are, as seen in previous chapters, a direct result of the semi-analytical solution. These stresses vary through the thickness of the cylinder wall and the inplane stresses in the k^{th} layer are given by

$$\begin{bmatrix}\sigma_x\\ \sigma_s\\ \tau_{xs}\end{bmatrix}^k = \begin{bmatrix}\bar{Q}_{11}\ \bar{Q}_{12}\ \bar{Q}_{16}\\ \bar{Q}_{12}\ \bar{Q}_{22}\ \bar{Q}_{26}\\ \bar{Q}_{16}\ \bar{Q}_{26}\ \bar{Q}_{66}\end{bmatrix}^k \begin{bmatrix}\varepsilon_x\\ \varepsilon_s\\ \gamma_{xs}\end{bmatrix}^k = \begin{bmatrix}\bar{Q}_{11}\ \bar{Q}_{12}\ \bar{Q}_{16}\\ \bar{Q}_{12}\ \bar{Q}_{22}\ \bar{Q}_{26}\\ \bar{Q}_{16}\ \bar{Q}_{26}\ \bar{Q}_{66}\end{bmatrix}^k \begin{bmatrix}\varepsilon_x^o + \zeta\kappa_x^o\\ \varepsilon_s^o + \zeta\kappa_s^o\\ \gamma_{xs}^o + \zeta\kappa_{xs}^o\end{bmatrix}, \tag{5.16}$$

where $[\bar{Q}_{ij}]^k$ is the transformed reduced stiffness matrix of the k^{th} layer, and eq. 1.6 has been employed to compute the strains in the k^{th} layer. The stresses in principal material coordinate system can be obtained by transformation, namely

$$\begin{bmatrix}\sigma_1\\ \sigma_2\\ \sigma_{12}\end{bmatrix}^k = \begin{bmatrix} cos^2\theta_k & sin^2\theta_k & 2cos\theta_k sin\theta_k \\ sin^2\theta_k & cos^2\theta_k & -2cos\theta_k sin\theta_k \\ -cos\theta_k sin\theta_k & cos\theta_k sin\theta_k & (cos^2\theta_k - sin^2\theta_k)\end{bmatrix}\begin{bmatrix}\sigma_x\\ \sigma_s\\ \tau_{xs}\end{bmatrix}^k, \tag{5.17}$$

where θ_k is the fiber angle of the k^{th} layer with respect to the axial direction of the cylinder.

5.2.2 Interlaminar Stresses

For the geometrically linear case, the interlaminar stresses in the layers, τ_{rs} and τ_{rx}, can be evaluated by using the equilibrium equations of linear elasticity written in a cylinder coordinate system, namely,

$$\begin{aligned}\frac{\partial\sigma_r}{\partial r} + \frac{\partial\tau_{rs}}{\partial s} + \frac{\partial\tau_{rx}}{\partial x} + \frac{\sigma_r - \sigma_s}{r} &= 0\\ \frac{\partial\sigma_s}{\partial s} + \frac{\partial\tau_{rs}}{\partial r} + \frac{\partial\tau_{xs}}{\partial x} + \frac{2}{r}\tau_{rs} &= 0\\ \frac{\partial\sigma_x}{\partial x} + \frac{\partial\tau_{rx}}{\partial r} + \frac{\partial\tau_{xs}}{\partial s} + \frac{1}{r}\tau_{rx} &= 0,\end{aligned} \tag{5.18}$$

where the r, x, and s coordinates are shown in detail in fig. 5-2. In fig. 5-2 both r-s and r-x cylinder wall cross sections are shown. The radius of curvature of an arbitrary point within the wall is r and, recall, the radius of curvature of the wall midsurface is $R(s)$. (The equilibrium equations of linear elasticity are used because, as will be shown, the contributions of the interlaminar stresses to either failure criteria considered are quite small. It therefore was concluded that the interlaminar stresses were not causing failure. The nonlinear equations of equilibrium are very complex

and could not be treated in the manner of the section to follow to compute τ_{rs} and τ_{rx} as a function of r.)

Figure 5-2. Geometry of a section of the cylinder wall.

In order to determine τ_{rx}, eq. 5.18c is rewritten as follows:

$$\frac{\partial \tau_{rx}}{\partial r} + \frac{1}{r}\tau_{rx} = \frac{1}{r}\frac{\partial}{\partial r}(r\tau_{rx}) = -\left(\frac{\partial \sigma_x}{\partial x} + \frac{\partial \tau_{xs}}{\partial s}\right) . \tag{5.19}$$

Defining

$$r = R(s) + \zeta , \tag{5.20}$$

it follows that

$$\frac{\partial}{\partial r} = \frac{\partial}{\partial \zeta} \tag{5.21}$$

so eq. 5.19 becomes

$$\frac{\partial}{\partial \zeta}[(R(s) + \zeta)\tau_{rx}] = -\left(\frac{\partial \sigma_x}{\partial x} + \frac{\partial \tau_{xs}}{\partial s}\right)(R(s) + \zeta). \tag{5.22}$$

Before $\frac{\partial}{\partial \zeta}[(R(s) + \zeta)\tau_{rx}]$ can be integrated with respect to ζ to obtain τ_{rx}, σ_x and τ_{xs} need to be written explicitly in terms of ζ, namely, from eq. 5.16, as

$$\begin{aligned} \sigma_x &= \bar{Q}_{11}(\varepsilon_x^o + \zeta\kappa_x^o) + \bar{Q}_{12}(\varepsilon_s^o + \zeta\kappa_s^o) + \bar{Q}_{16}(\gamma_{xs}^o + \zeta\kappa_{xs}^o) = \sigma_x^\varepsilon + \zeta\sigma_x^\kappa \\ \tau_{xs} &= \bar{Q}_{16}(\varepsilon_x^o + \zeta\kappa_x^o) + \bar{Q}_{26}(\varepsilon_s^o + \zeta\kappa_s^o) + \bar{Q}_{66}(\gamma_{xs}^o + \zeta\kappa_{xs}^o) = \tau_{xs}^\varepsilon + \zeta\tau_{xs}^\kappa \end{aligned} \tag{5.23}$$

where,

$$\begin{aligned}
\sigma_x^{\varepsilon} &= \bar{Q}_{11}\varepsilon_x^o + \bar{Q}_{12}\varepsilon_s^o + \bar{Q}_{16}\gamma_{xs}^o \\
\sigma_x^{\kappa} &= \bar{Q}_{11}\kappa_x^o + \bar{Q}_{12}\kappa_s^o + \bar{Q}_{16}\kappa_{xs}^o \\
\tau_{xs}^{\varepsilon} &= \bar{Q}_{16}\varepsilon_x^o + \bar{Q}_{26}\varepsilon_s^o + \bar{Q}_{66}\gamma_{xs}^o \\
\tau_{xs}^{\kappa} &= \bar{Q}_{16}\kappa_x^o + \bar{Q}_{26}\kappa_s^o + \bar{Q}_{66}\kappa_{xs}^o.
\end{aligned} \tag{5.24}$$

Within a layer these quantities do not vary with the thickness coordinate, ζ. Equation 5.22 can now be written as,

$$\begin{aligned}
\frac{\partial}{\partial\zeta}[(R(s)+\zeta)\tau_{rx}] &= -\left(\frac{\partial\sigma_x^{\varepsilon}}{\partial x} + \zeta\frac{\partial\sigma_x^{\kappa}}{\partial x} + \frac{\partial\tau_{xs}^{\varepsilon}}{\partial s} + \zeta\frac{\partial\tau_{xs}^{\kappa}}{\partial s}\right)(R(s)+\zeta) \\
&= -\left\{\left(\frac{\partial\sigma_x^{\varepsilon}}{\partial x} + \frac{\partial\tau_{xs}^{\varepsilon}}{\partial s}\right)(R(s)+\zeta) + \left(\frac{\partial\sigma_x^{\kappa}}{\partial x} + \frac{\partial\tau_{xs}^{\kappa}}{\partial s}\right)(R(s)\zeta+\zeta^2)\right\}.
\end{aligned} \tag{5.25}$$

Equation 5.25 can be integrated with respect to ζ to obtain

$$(R(s)+\zeta)\tau_{rx} = \hat{h}_x(x,s) - \left\{\left(\frac{\partial\sigma_x^{\varepsilon}}{\partial x} + \frac{\partial\tau_{xs}^{\varepsilon}}{\partial s}\right)\left(R(s)\zeta + \frac{\zeta^2}{2}\right) + \left(\frac{\partial\sigma_x^{\kappa}}{\partial x} + \frac{\partial\tau_{xs}^{\kappa}}{\partial s}\right)\left(R(s)\frac{\zeta^2}{2} + \frac{\zeta^3}{3}\right)\right\}, \tag{5.26}$$

where $\hat{h}_x(x,s)$ is an unknown but to-be-determined function of integration. Dividing eq. 5.26 by $(R(s)+\zeta)$ yields

$$\tau_{rx} = \frac{\hat{h}_x(x,s)}{R(s)+\zeta} - \left\{\left(\frac{\partial\sigma_x^{\varepsilon}}{\partial x} + \frac{\partial\tau_{xs}^{\varepsilon}}{\partial s}\right)\left[\frac{\left(R(s)+\frac{\zeta}{2}\right)\zeta}{(R(s)+\zeta)}\right] + \left(\frac{\partial\sigma_x^{\kappa}}{\partial x} + \frac{\partial\tau_{xs}^{\kappa}}{\partial s}\right)\left[\frac{\left(R(s)+\frac{2}{3}\zeta\right)\frac{\zeta^2}{2}}{(R(s)+\zeta)}\right]\right\}. \tag{5.27}$$

The terms in square brackets in eq. 5.27 can be simplified. In general, for thin-walled cylinders ζ is small when compared to $R(s)$. This can be shown as follows:

$$\frac{\zeta}{R(s)} < \frac{\zeta_{MAX}}{R_{MIN}} = \frac{1}{2e^2}\left(\frac{H}{a}\right) = \frac{1}{2(0.7)^2}\left(\frac{0.0495}{5}\right) = 0.0101 \ll 1 \tag{5.28}$$

where the numbers for a nine-layer elliptical cylinder have been used. Therefore,

$$\frac{\zeta}{R(s)} \ll 1. \tag{5.29}$$

Thus, for example, the denominator of the terms in eq. 5.27 are

$$(R(s) + \zeta) = R(s)\left(1 + \frac{\zeta}{R(s)}\right) \approx R(s). \tag{5.30}$$

Using similar arguments on other terms in eq. 5.27, it is concluded that

$$\frac{\left(R(s) + \frac{\zeta}{2}\right)}{(R(s) + \zeta)} \approx 1 \qquad \frac{\left(R(s) + \frac{2}{3}\zeta\right)}{(R(s) + \zeta)} \approx 1. \tag{5.31}$$

Therefore, eq. 5.27 can be reduced to

$$\begin{aligned} \tau_{rx} &= \frac{\hat{h}_x(x, s)}{R(s)} - \left\{\left(\frac{\partial \sigma_x^{\varepsilon}}{\partial x} + \frac{\partial \tau_{xs}^{\varepsilon}}{\partial s}\right)\zeta + \left(\frac{\partial \sigma_x^{\kappa}}{\partial x} + \frac{\partial \tau_{xs}^{\kappa}}{\partial s}\right)\frac{\zeta^2}{2}\right\} \\ &= h_x(x, s) - \left\{f_x(x, s)\zeta + g_x(x, s)\frac{\zeta^2}{2}\right\}, \end{aligned} \tag{5.32}$$

where $f_x(x,s)$ and $g_x(x,s)$ are known for each layer at a given value of x and s. The unknown function of integration term has been redefined to be $h_x(x,s)$. The function $h_x^{(k)}(x,s)$ for the k^{th} layer can be determined by utilizing the condition that

$$\tau_{rx} = 0 \text{ at } \zeta = -\frac{H}{2} \qquad \left(\text{i. e., } \tau_{rx}^{(1)} = 0 \text{ at } \zeta = -\frac{H}{2}\right) \tag{5.33}$$

and the continuity condition

$$\tau_{rx}^{(k-1)} = \tau_{rx}^{(k)}, \tag{5.34}$$

where k denotes the layer number. These conditions translate into, respectively,

$$\tau_{rx}^{(1)} = 0 = h_x^{(1)}(x, s) - \left\{f_x^{(1)}(x, s)\left(-\frac{H}{2}\right) + g_x^{(1)}(x, s)\frac{1}{2}\left(-\frac{H}{2}\right)^2\right\} \tag{5.35}$$

or

$$h_x^{(1)}(x, s) = \left\{ f_x^{(1)}(x, s)\left(-\frac{H}{2}\right) + g_x^{(1)}(x, s)\frac{1}{2}\left(-\frac{H}{2}\right)^2 \right\} \tag{5.36}$$

and

$$h_x^{(k-1)}(x, s) - \left\{ f_x^{(k-1)}(x, s)\zeta_k + g_x^{(k-1)}(x, s)\frac{\zeta_k^2}{2} \right\} = h_x^{(k)}(x, s) - \left\{ f_x^{(k)}(x, s)\zeta_k + g_x^{(k)}(x, s)\frac{\zeta_k^2}{2} \right\} \tag{5.37}$$

or

$$h_x^{(k)}(x, s) = h_x^{(k-1)}(x, s) + (f_x^{(k)}(x, s) - f_x^{(k-1)}(x, s))\zeta_k + (g_x^{(k)}(x, s) - g_x^{(k-1)}(x, s))\frac{\zeta_k^2}{2}, \tag{5.38}$$

for $k = 2, 3, ..., n$, where n is the total number of layers. The quantity ζ_k is the interfacial location between the k^{th} and $(k\text{-}1)^{st}$ layers.

In order to determine τ_{rs}, eq. 5.18b is rewritten as follows:

$$\frac{\partial \tau_{rs}}{\partial r} + \frac{2}{r}\tau_{rs} = \frac{1}{r^2}\left[\frac{\partial}{\partial r}(r^2 \tau_{rs})\right] = -\left(\frac{\partial \sigma_s}{\partial s} + \frac{\partial \tau_{xs}}{\partial x}\right). \tag{5.39}$$

Using eq. 5.20 and eq. 5.21, eq. 5.39 becomes

$$\frac{\partial}{\partial \zeta}[(R(s) + \zeta)^2 \tau_{rs}] = -\left(\frac{\partial \sigma_s}{\partial s} + \frac{\partial \tau_{xs}}{\partial x}\right)(R(s) + \zeta)^2 . \tag{5.40}$$

Before $\frac{\partial}{\partial \zeta}[(R(s) + \zeta)^2 \tau_{rs}]$ can be integrated with respect to ζ to obtain τ_{rs}, σ_s needs to be written explicitly in terms of ζ, namely, from eq. 5.16, as

$$\sigma_s = \bar{Q}_{12}(\varepsilon_x^o + \zeta\kappa_x^o) + \bar{Q}_{22}(\varepsilon_s^o + \zeta\kappa_s^o) + \bar{Q}_{26}(\gamma_{xs}^o + \zeta\kappa_{xs}^o) = \sigma_s^\varepsilon + \zeta\sigma_s^\kappa \tag{5.41}$$

where,

$$\sigma_s^{\varepsilon} = \bar{Q}_{12}\varepsilon_x^o + \bar{Q}_{22}\varepsilon_s^o + \bar{Q}_{26}\gamma_{xs}^o$$
$$\sigma_s^{\kappa} = \bar{Q}_{12}\kappa_x^o + \bar{Q}_{22}\kappa_s^o + \bar{Q}_{26}\kappa_{xs}^o. \tag{5.42}$$

Within a layer these quantities do not vary with the thickness coordinate, ζ. Equation 5.40 can now be written as,

$$\frac{\partial}{\partial\zeta}[(R(s)+\zeta)^2\tau_{rs}] = -\left(\frac{\partial\sigma_s^{\varepsilon}}{\partial s} + \zeta\frac{\partial\sigma_s^{\kappa}}{\partial s} + \frac{\partial\tau_{xs}^{\varepsilon}}{\partial x} + \zeta\frac{\partial\tau_{xs}^{\kappa}}{\partial x}\right)(R(s)+\zeta)^2$$
$$= -\left\{\left(\frac{\partial\sigma_s^{\varepsilon}}{\partial s} + \frac{\partial\tau_{xs}^{\varepsilon}}{\partial x}\right)(R(s)+\zeta)^2 + \left(\frac{\partial\sigma_s^{\kappa}}{\partial s} + \frac{\partial\tau_{xs}^{\kappa}}{\partial x}\right)\zeta(R(s)+\zeta)^2\right\}. \tag{5.43}$$

Equation 5.43 can be integrated with respect to ζ to obtain

$$(R(s)+\zeta)^2\tau_{rs} = \hat{h}_s(x,s) -$$
$$\left\{\left(\frac{\partial\sigma_x^{\varepsilon}}{\partial x} + \frac{\partial\tau_{xs}^{\varepsilon}}{\partial s}\right)\left(\zeta R^2(s) + \zeta^2 R(s) + \frac{\zeta^3}{3}\right) + \left(\frac{\partial\sigma_x^{\kappa}}{\partial x} + \frac{\partial\tau_{xs}^{\kappa}}{\partial s}\right)\left(\frac{\zeta^2}{2}R^2(s) + \frac{2}{3}\zeta^3 R(s) + \frac{\zeta^4}{4}\right)\right\}, \tag{5.44}$$

where $\hat{h}_s(x,s)$ is another function of integration. Dividing eq. 5.44 by $(R(s)+\zeta)^2$ yields

$$\tau_{rs} = \frac{\hat{h}_s(x,s)}{(R(s)+\zeta)^2} -$$
$$\left\{\left(\frac{\partial\sigma_x^{\varepsilon}}{\partial x} + \frac{\partial\tau_{xs}^{\varepsilon}}{\partial s}\right)\left[\frac{\left(R^2(s) + \zeta R(s) + \frac{\zeta^2}{3}\right)\zeta}{(R(s)+\zeta)^2}\right] + \left(\frac{\partial\sigma_x^{\kappa}}{\partial x} + \frac{\partial\tau_{xs}^{\kappa}}{\partial s}\right)\left[\frac{\left(R^2(s) + \frac{4}{3}\zeta R(s) + \frac{\zeta^2}{2}\right)\frac{\zeta^2}{2}}{(R(s)+\zeta)^2}\right]\right\}. \tag{5.45}$$

The terms in square brackets in eq. 5.45 can be simplified due to eq. 5.29. The numerator term in the first square bracket in eq. 5.45 can be written as follows:

$$\left(R^2(s) + \zeta R(s) + \frac{\zeta^2}{3}\right) = R^2(s)\left(1 + \frac{\zeta}{R(s)} + \frac{1}{3}\left(\frac{\zeta}{R(s)}\right)^2\right) \approx R^2(s) \tag{5.46}$$

so

$$\frac{\left(R^2(s) + \zeta R(s) + \frac{\zeta^2}{3}\right)\zeta}{(R(s) + \zeta)^2} \approx \zeta \tag{5.47}$$

Similarly

$$\frac{\left(R^2(s) + \frac{4}{3}\zeta R(s) + \frac{\zeta^2}{2}\right)\frac{\zeta^2}{2}}{(R(s) + \zeta)^2} \approx \frac{\zeta^2}{2}. \tag{5.48}$$

Therefore, eq. 5.45 can be reduced to

$$\begin{aligned} \tau_{rs} &= \frac{\hat{h}_s(x, s)}{(R(s) + \zeta)^2} - \left\{\left(\frac{\partial \sigma_x^s}{\partial x} + \frac{\partial \tau_{xs}^s}{\partial s}\right)\zeta + \left(\frac{\partial \sigma_x^\kappa}{\partial x} + \frac{\partial \tau_{xs}^\kappa}{\partial s}\right)\frac{\zeta^2}{2}\right\} \\ &= h_s(x, s) - \left\{f_s(x, s)\zeta + g_s(x, s)\frac{\zeta^2}{2}\right\} \end{aligned} \tag{5.49}$$

where $f_s(x,s)$ and $g_s(x,s)$ are known for each layer at a given value of x and s. The unknown function of integration term has been redefined to be $h_s(x,s)$. The function $h_s^{(k)}(x,s)$ can be determined utilizing the condition that

$$\tau_{rs} = 0 \text{ at } \zeta = -\frac{H}{2} \qquad \left(\text{i. e., } \tau_{rs}^{(1)} = 0 \text{ at } \zeta = -\frac{H}{2}\right) \tag{5.50}$$

and the continuity condition,

$$\tau_{rs}^{(k-1)} = \tau_{rs}^{(k)}, \tag{5.51}$$

where k denotes the layer number. These conditions translate into, respectively,

$$\tau_{rs}^{(1)} = 0 = h_s^{(1)}(x, s) - \left\{f_s^{(1)}(x, s)\left(-\frac{H}{2}\right) + g_s^{(1)}(x, s)\frac{1}{2}\left(-\frac{H}{2}\right)^2\right\} \tag{5.52}$$

or

$$h_s^{(1)}(x, s) = \left\{f_s^{(1)}(x, s)\left(-\frac{H}{2}\right) + g_s^{(1)}(x, s)\frac{1}{2}\left(-\frac{H}{2}\right)^2\right\} \tag{5.53}$$

and

$$h_s^{(k-1)}(x,s) - \left\{ f_s^{(k-1)}(x,s)\zeta_k + g_s^{(k-1)}(x,s)\frac{\zeta_k^2}{2} \right\} = h_s^{(k)}(x,s) - \left\{ f_s^{(k)}(x,s)\zeta_k + g_s^{(k)}(x,s)\frac{\zeta_k^2}{2} \right\} \tag{5.54}$$

or

$$h_s^{(k)}(x,s) = h_s^{(k-1)}(x,s) + (f_s^{(k)}(x,s) - f_s^{(k-1)}(x,s))\zeta_k + (g_s^{(k)}(x,s) - g_s^{(k-1)}(x,s))\frac{\zeta_k^2}{2}, \tag{5.55}$$

for $k = 2, 3, \ldots, n$.

The interlaminar stresses in principal material coordinate system can be obtained by transformation, namely,

$$\begin{bmatrix} \sigma_{23} \\ \sigma_{13} \end{bmatrix}^k = \begin{bmatrix} \cos\theta_k & -\sin\theta_k \\ \sin\theta_k & \cos\theta_k \end{bmatrix} \begin{bmatrix} \tau_{rs} \\ \tau_{rx} \end{bmatrix}^k. \tag{5.56}$$

It should be noted that the schemes just described for computing the interlaminar stresses do not allow for enforcement of the conditions that the interlaminar shear stresses must be zero at the outer radial location, just as they are at the inner radial location. That is, the conditions

$$\tau_{rx}^{(n)} = \tau_{rs}^{(n)} = 0 \text{ at } \zeta = +\frac{H}{2} \tag{5.57}$$

cannot be explicitly enforced as there are not enough functions of integration $h_x^{(k)}(x,s)$ and $h_s^{(k)}(x,s)$ to allow enforcement. There is, therefore, no guarantee that the conditions of eq. 5.57 will be satisfied. As will be seen, they are not exactly satisfied.

5.3 Character of Interlaminar Stresses

The interlaminar stresses for aluminum and composite circular and elliptical internally pressurized cylinders are illustrated in figs. 5-3 - 5-6 to convey the character of the distribution through the thickness, and to provide some insight into the magnitude of these stresses. These stresses, τ_{rx} and τ_{rs}, or in alternate notation $\tau_{x\zeta}$ and $\tau_{s\zeta}$, are compared at the axial and circumferential locations where the magnitudes of the transverse shear force resultants, Q_x and Q_s, given by eq. 2.7, are maximum. Generally that location is x/L=0.5 and s/C=0 with the exception of the aluminum elliptical cylinder, where the location is x/L=0.5 and s/C=0.15625. These locations are at the end of the cylinder where the condition w=0 is enforced. A review of fig. 2-7, for example, shows the character of $\overline{Q}_x$ and $\overline{Q}_s$ for both circular and elliptical cylinders. Of course the circular cylinder is axisymmetric so the location s/C=0 is not unique.

For the aluminum circular cylinder, fig. 5-3, there is no interlaminar stress τ_{rs}. Note that at ζ=+$H/2$, the shear stress τ_{rx} is not quite zero. As just mentioned, this is due to the lack of enough unknown functions of integration to uniquely specify the shear stress at both ζ=+$H/2$ and ζ=-$H/2$.

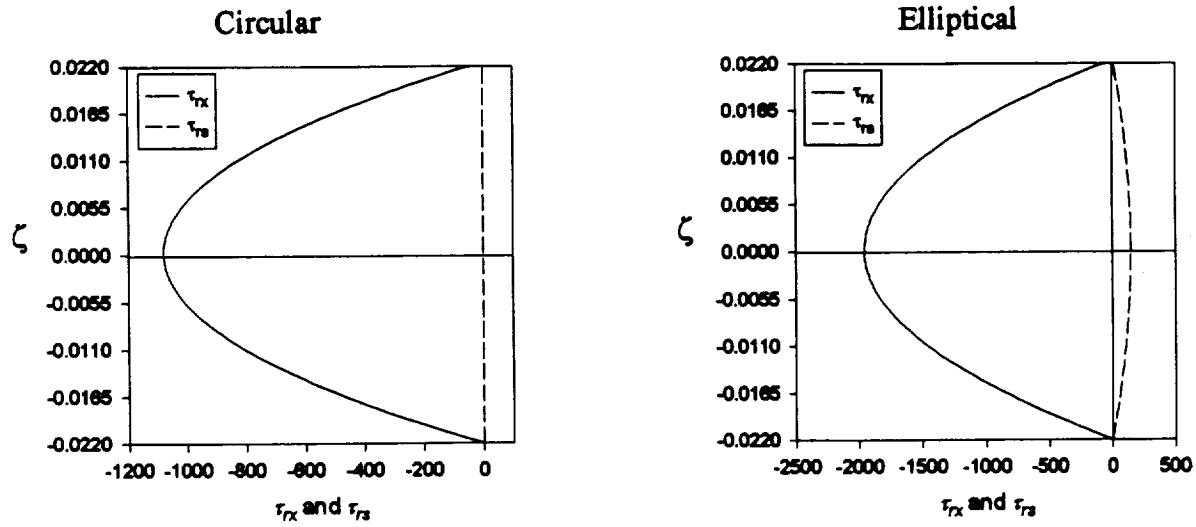

Figure 5-3. Interlaminar shear stresses for an aluminum circular and elliptical cylinders, p_o=100 psi, x/L=0.5, s/C=0.0, except for τ_{rs} for the elliptical cylinder where s/C=0.15625

For the quasi-isotropic cylinder, and the other composite cases, the distributions of the shear stresses are piecewise parabolic, as can be seen from the form of eqs. 5.32 and 5.49. The interlaminar stress τ_{rx} is larger than interlaminar shear stress τ_{rs} and it generally peaks at or near ζ=0. The interlaminar shear stress τ_{rs} generally peaks between the +45° and -45° layers and has a lower value near ζ=0. Note that τ_{rx} is not zero at ζ=+*H*/2 and this is felt to be responsible for the lack of symmetry, with respect to ζ=0, of the distribution of the interlaminar shear stresses.

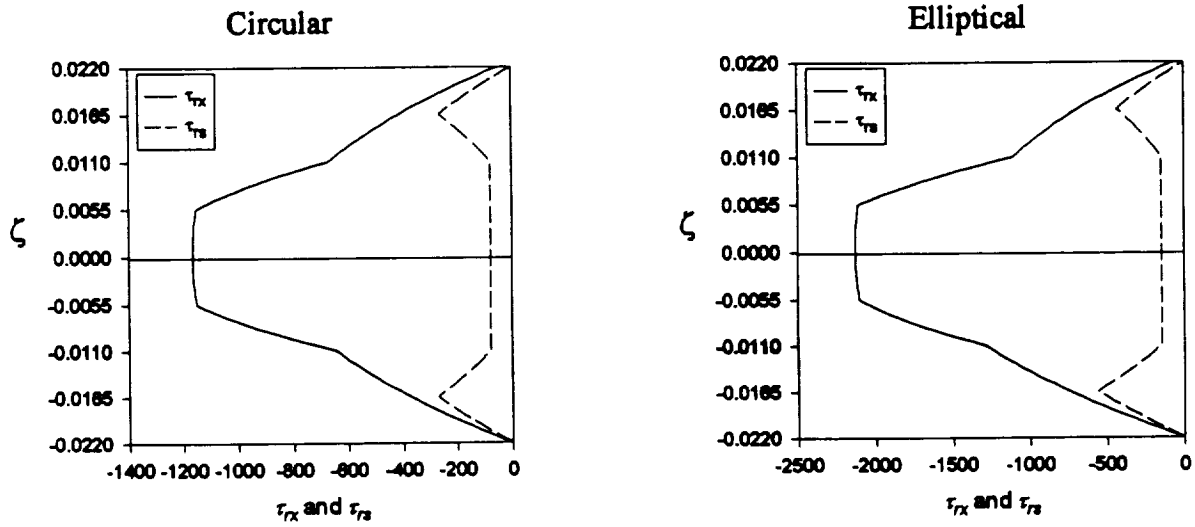

Figure 5-4. Interlaminar shear stresses for a quasi-isotropic circular and elliptical cylinders, p_o=100 psi, x/L=0.5, s/C=0.0

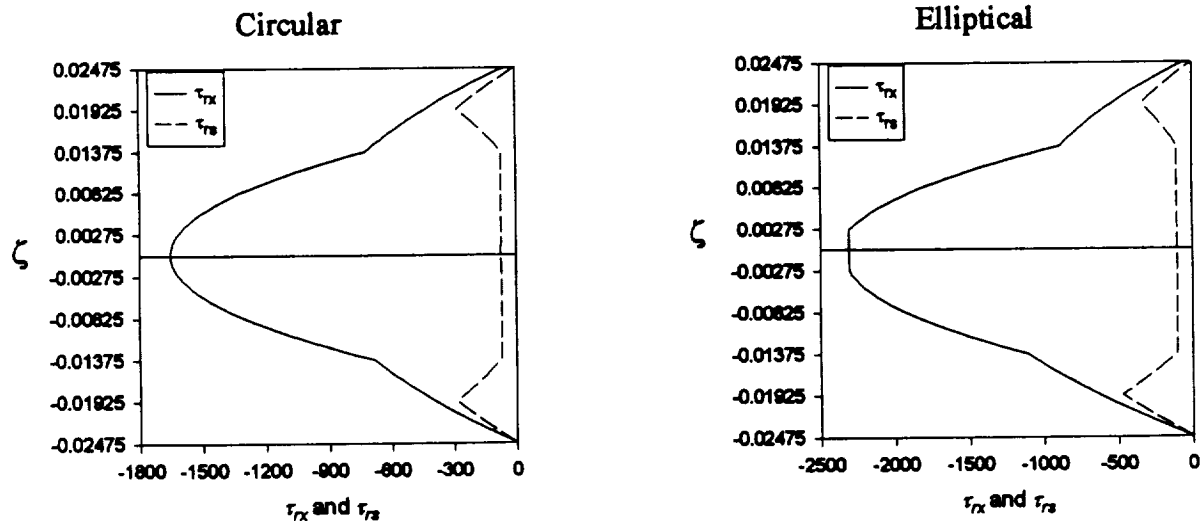

Figure 5-5. Interlaminar shear stresses for an axially-stiff circular and elliptical cylinders, p_o=100 psi, x/L=0.5, s/C=0.0

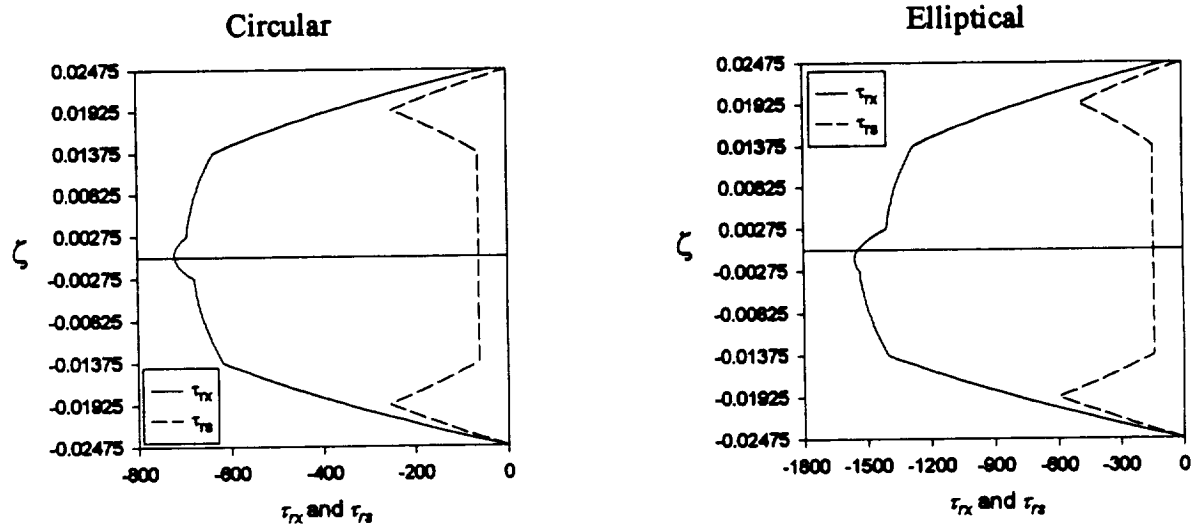

Figure 5-6. Interlaminar shear stresses for a circumferentially-stiff circular and elliptical cylinders, p_o=100 psi, x/L=0.5, s/C=0.0

5.4 Interlaminar Shear Stress Validation

As a check on the interlaminar stress calculations, the integrals of the interlaminar stresses given by eq. 2.7 were compared with the transverse shear stress resultants, Q_x and Q_s, as given by the derivatives of the moments in eq. 2.6. Table 5-1 shows the comparison for the condition of maximum Q_x and the maximum Q_s. In the table the values have been normalized by the quantity p_oR, as has been done earlier, and the x and s location of the maximum value are indicated, along with the percent error in the integral calculations.

The aluminum circular cylinder does not have a circumferential transverse shear force resultant and the circumferential interlaminar shear stress integrated through the thickness reflects zero response. The integrated axial interlaminar shear stress compared with the axial transverse shear force resultant gives a small error of 3.2%. The aluminum elliptical cylinder shows similar

results for $\int \bar{\tau}_{rx} d\zeta$ and $\overline{Q}_x$, but $\int \bar{\tau}_{rs} d\zeta$ and $\overline{Q}_s$ show a slightly larger error of 7.1%. The composite cylinders also resulted in small differences between the transverse shear force resultants and the integrated interlaminar shear stress. The average error between $\int \bar{\tau}_{rx} d\zeta$ and $\overline{Q}_x$ is 3.5% for the circular composite cylinder and 2.5% for the elliptical composite cylinder. The average error between $\int \bar{\tau}_{rs} d\zeta$ and $\overline{Q}_s$ for both the circular and elliptical composite cylinders is 0.0%. These errors are felt to be minimal.

This chapter has introduced the Hashin and maximum failure criteria, discussed the approach for computing the inplane stresses, and presented a method for computing the interlaminar shear stresses that contribute to the failure criteria. The integral of the interlaminar shear stresses through the thickness were compared to the transverse shear stress resultant to verify the derivation of the interlaminar shear stresses. The difference between the integrated interlaminar shear stresses and the transverse shear stress resultant was considered to be negligible.

Table 5-1. Linear interlaminar shear stress comparison

		Aluminum	Quasi-isotropic	Axially-stiff	Circumferen-tially-stiff
Circular	$\overline{Q}_x$	0.06203	0.06035	0.08843	0.05050
	$\int \bar{\tau}_{rx} d\zeta$	0.06402	0.06252	0.09092	0.05247
	% Error	3.2	3.6	2.8	3.9
	Location (x/L,s/C)	(0.5,0.0)	(0.5,0.0)	(0.5,0.0)	(0.5,0.0)
	$\overline{Q}_s$	0	0.01010	0.01084	0.00970
	$\int \bar{\tau}_{rs} d\zeta$	0	0.01010	0.01085	0.00970
	% Error	0	0.0	0.0	0.0
	Location (x/L,s/C)	(0.5,0.0)	(0.5,0.0)	(0.5,0.0)	(0.5,0.0)
Elliptical	$\overline{Q}_x$	0.11291	0.11104	0.12662	0.10889
	$\int \bar{\tau}_{rx} d\zeta$	0.11564	0.11406	0.12921	0.11216
	% Error	2.4	2.7	2.0	3.0
	Location (x/L,s/C)	(0.5,0.0)	(0.5,0.0)	(0.5,0.0)	(0.5,0.0)
	$\overline{Q}_s$	0.00820	0.01894	0.01593	0.02138
	$\int \bar{\tau}_{rs} d\zeta$	0.00878	0.01895	0.01593	0.02140
	% Error	7.1	0.0	0.0	0.0
	Location (x/L,s/C)	(0.5,0.15625)	(0.5,0.0)	(0.5,0.0)	(0.5,0.0)

Chapter 6 Failure Predictions

Utilizing the approaches for computing the inplane and interlaminar shear stresses discussed in the previous chapter, this chapter will present a discussion of failure of internally pressurized elliptical cylinders. The Hashin and maximum stress failure criteria and geometrically linear and nonlinear analyses will be considered to predict the location and mode of failure.

6.1 Failure Predictions for the Geometrically Linear Theory

The Hashin and maximum stress failure criteria were implemented in a FORTRAN code using the stresses obtained for the geometrically linear analysis. The FORTRAN code computed the stresses in the principal material coordinate system at an internal pressure of 100 psi, then combined them as prescribed in eqs. 5.5-5.7 for the maximum stress criterion and eqs. 5.12-5.15 for the Hashin criterion. For the maximum stress criterion, the seven left-hand sides in the criterion were then computed as a function of axial, circumferential, and through-thickness location. The left-hand side that was the maximum was then singled out. For all cylinders, the maximum left-hand side value was below unity, which implied that for an internal pressure of 100 psi failure had not yet occurred. An internal pressure at which each cylinder would begin to fail, or the failure pressure, was predicted by linearly extrapolating, namely, multiplying the maximum left-hand side of the equation by a variable p_f, such that,

$$(LHS_{\max})p_f = 1 \,. \tag{6.1}$$

It follows, then, that the failure pressure was given by

$$p_f = \frac{1}{LHS_{\max}} p_o \,. \tag{6.2}$$

where p_o is 100 psi. The particular left-hand side which was maximum identified the failure mode.

For the Hashin criterion, the four left-hand sides in the criterion were computed as a function of axial, circumferential, and through-thickness location. The left-hand side that was the maximum was then singled out. Again, for all cylinders the maximum left-hand side value was below unity. For the tensile modes of failure, the failure pressure was predicted by linearly extrapolating, namely, multiplying the maximum left-hand side of the equation by the square of a variable p_f, such that,

$$(LHS_{\max}) p_f^2 = 1 \,. \tag{6.3}$$

It follows, then, that the failure pressure was given by

$$p_f = \sqrt{\frac{1}{LHS_{\max}}}\, p_o \,, \tag{6.4}$$

where p_o is 100 psi. In the case of compressive matrix failure, failure pressure was determined by eq. 6.4 if $\left[\left(\frac{\sigma_T^-}{2\tau_T}\right)^2 - 1\right] = 0$. If $\left[\left(\frac{\sigma_T^-}{2\tau_T}\right)^2 - 1\right] \neq 0$, then the failure pressure was determined by

$$p_f = \left(\frac{-b \pm \sqrt{4a + b^2}}{2a}\right) p_o \tag{6.5}$$

where

$$\begin{aligned} a &= \left(\frac{\sigma_{22}}{2\tau_T}\right)^2 + \left(\frac{\sigma_{23}}{\tau_T}\right)^2 + \frac{1}{\tau_A^2}(\sigma_{12}^2 + \sigma_{13}^2) \\ b &= \frac{\sigma_{22}}{\sigma_T^-}\left[\left(\frac{\sigma_T^-}{2\tau_T}\right)^2 - 1\right]. \end{aligned} \tag{6.6}$$

For compressive fiber failure, eq. 6.2 was applied. The particular left-hand side which was maximum identified the failure mode.

Table 6-1 shows the failure pressure and location for axially-stiff, quasi-isotropic, circumferentially-stiff elliptical cylinders as predicted by the Hashin criterion. Recall, the axially-stiff and circumferentially-stiff cylinders are nine layers thick and have a total thickness of H=0.0495 in., and the quasi-isotropic cylinder is eight layers with a total thickness H=0.044 in. The location of failure through the thickness is specified both by indicating the value of the ζ coordinate, and by indicating the layer number and interface number for that layer. The footnote in the table explains the layer and interface numbering scheme. The circumferential location is denoted by the value of s/C. Also shown in table 6-1 are the values of the stress components at the location of failure when the pressure equals the failure pressure. Note that in each case failure occurs at the ends of the cylinders. This is due to effects associated with the clamped end conditions. It is important to realize that there are two ends of the cylinder and the s/C location noted is the crown location. There is a companion circumferential location in the keel where the failure conditions are satisfied at exactly the same pressure. As can be seen, in all cases σ_2 is generally close to the failure level of 7250 psi at the failure pressure (see eq. 5.1). In each case failure is attributed mainly to tension in the matrix, or σ_2. For the quasi-isotropic and axially-stiff laminates failure occurs at the inner radius and thus the interlaminar shear stresses do not contribute to failure of these cylinders. As failure occurs in layer seven of the circumferentially-stiff laminate, near the outer radius, the interlaminar shear stresses could contribute to the failure, but, in fact, are an order of magnitude less than inplane stress σ_2, and therefore have little bearing on the failure predictions. In general, the interlaminar shear stresses are always an order of magnitude less than the inplane stresses. Therefore, the interlaminar shear stresses can be computed from the geometri-

cally linear equilibrium equations, as has been done in the preceding sections, with little effect on the failure predictions for the geometrically nonlinear theory. Note that for the circumferentially-stiff laminate failure occurs exactly at the two side locations, $s/C=\pm 0.25$, simultaneously.

Table 6-1. Failure pressure and location for elliptical graphite-epoxy cylinders, geometrically linear analysis, Hashin failure criterion

	p_f (psi)	*loc**	ζ	s/C**	σ_1 (psi)	σ_2 (psi)	τ_{12} (psi)	τ_{13} (psi)	τ_{23} (psi)
Axially-stiff	130.4	1/1 (+45)	-0.0248	-0.07	16200	6980	-3950	0	0
Quasi-isotropic	130.9	1/1 (+45)	-0.0220	-0.07	13200	6990	-3880	0	0
Circumferentially-stiff	106.7	7/2 (90)	0.0138	±0.25	2180	7250	-4.28	82.5	-663

* Location is given as layer number/interface, where 1 is the innermost layer and 1 denotes the inner and 2 the outer interface. The fiber direction of the layer is shown in parenthesis.
** All failures occur at the ends of the cylinders: $s/C=0$ is crown, $s/C=\pm 0.25$ are sides, C=circumference, s=arclength measure (see fig. 1-2)

As a comparison to the Hashin criterion, table 6-2 shows the failure pressure and location for the three elliptical cylinders as predicted by the maximum stress criterion. Again the failure mode is predicted to be due to σ_2 at the ends of the cylinders. The table shows the values of the stresses at the location of failure when the pressure equals the failure pressure. Note that σ_2 equals its failure value (see eq. 5.1). Any deviation from an exact σ_2=7250 psi is due to round off and other numerical anomalies that result from all the algorithms involved in the calculations. By comparing tables 6-1 and 6-2 it is seen that the Hashin and maximum stress criteria both predict similar scenarios, namely failure due to matrix cracking caused by high values of σ_2 at very similar, if not identical, locations.

Table 6-2. Failure pressure and location for elliptical graphite-epoxy cylinders, geometrically linear analysis, maximum stress failure criterion

	p_f (psi)	loc*	ζ	s/C**	σ_1 (psi)	σ_2 (psi)	τ_{12} (psi)	τ_{13} (psi)	τ_{23} (psi)
Axially-stiff	135.6	1/1 (+45)	-0.0248	-0.07	16800	7260	-4110	0	0
Quasi-isotropic	135.6	1/1 (+45)	-0.0220	-0.08	6790	7260	-3840	0	0
Circumfer-entially-stiff	106.8	7/2 (90)	0.0138	±0.25	2180	7250	-4.28	82.6	-663

* Location is given as layer number/interface, where 1 is the innermost layer and 1 denotes the inner and 2 the outer interface. The fiber direction of the layer is shown in parenthesis.
** All failures occur at the ends of the cylinders: s/C=0 is crown, s/C=±0.25 are sides, C=circumference, s=arclength measure (see fig. 1-2)

Since all the failures in table 6-1 and 6-2 are matrix cracking failures, these can be considered first ply, or initial, failures. Catastrophic failure of the cylinder is not expected. Increased pressure capacity beyond the pressure levels in the tables is highly likely. However, when fibers begin to fail, failure of the cylinder is more likely. Failure of fibers in tension will lead to increased tension in the surrounding fibers. Failure of fibers in compression could lead to crushing and deterioration of the material in the surrounding region. For either situation, there could be a sudden cascading effect which would lead to catastrophic failure. Because of this, the pressures required to produce first fiber failure were computed. Table 6-3 and 6-4 show these pressures. These pressures were computed by ignoring all failures except fiber failure. For the Hashin criterion, this means either eq. 5.12 or 5.13 governs failure, while for the maximum stress criterion, this means the first of either eq. 5.5 or 5.6 governs. First fiber failures are predicted to be fiber compression failure in all cases. The location is again at the ends of the cylinders. Fiber crushing is predicted to occur at the outer radius, due to high bending effects. The predicted fiber failure

pressures are about twice as high as the predicted matrix cracking pressures. The Hashin and maximum stress criteria predict identical results because for the fiber compression failure mode, the Hashin criterion (eq. 5.13) and the maximum stress condition (the first of eq. 5.6) are identical equations. It is interesting to note that at the locations where the fibers fail by compression, the matrix is also in compression and near or beyond its failure level and the shear stress τ_{12} is more than one-half its failure level. Interlaminar stress does not play a role because of their small magnitudes.

A comment is in order regarding failure due to internal pressure. By the nature of pressure, a matrix crack in the inner layer will allow the pressure to reach the faces of the crack and perhaps force them apart further than if, for example, a bladder was used inside the cylinder to contain the pressure. In fact with a crack in the first layer and no bladder, the pressure reaches the second layer from within. This pressure could act to separate the second layer from the inner layer. With a bladder this would not happen, since the mechanics of force equilibrium around the crack would be different with a bladder, the bladder still reacting to the pressure force despite the matrix crack. It is not clear what the first matrix crack means in the presence of a bladder when compared to the case of no bladder. It is felt that with no bladder the first matrix crack has the potential for triggering failure, whereas with a bladder it is felt the first matrix crack could well be inconsequential.

Table 6-3. First fiber failure pressure and location for elliptical graphite-epoxy cylinders, geometrically linear analysis, Hashin failure criterion

	p_f (psi)	loc*	ζ	s/C**	σ_1 (psi)	σ_2 (psi)	τ_{12} (psi)	τ_{13} (psi)	τ_{23} (psi)
Axially-stiff	242.1	9/2 (+45)	0.0248	-0.08	-180000	-5860	7800	-91.0	81.3
Quasi-isotropic	228.8	8/2 (+45)	0.0220	-0.07	-180000	-7070	8400	-112	95.9
Circumfer-entially-stiff	227.5	9/2 (+45)	0.0248	-0.06	-180000	-8710	9240	-109	91.7

* Location is given as layer number/interface, where 1 is the innermost layer and 1 denotes the inner and 2 the outer interface. The fiber direction of the layer is shown in parenthesis.
** All failures occur at the ends of the cylinders: s/C=0 is crown, s/C=±0.25 are sides, C=circumference, s=arclength measure (see fig. 1-2)

Table 6-4. First fiber failure pressure and location for elliptical graphite-epoxy cylinders, geometrically linear analysis, maximum stress failure criterion

	p_f (psi)	loc*	ζ	s/C**	σ_1 (psi)	σ_2 (psi)	τ_{12} (psi)	τ_{13} (psi)	τ_{23} (psi)
Axially-stiff	242.1	9/2 (+45)	0.0248	-0.08	-180000	-5860	7800	-91.0	81.3
Quasi-isotropic	228.8	8/2 (+45)	0.0220	-0.07	-180000	-7070	8400	-112	95.9
Circumfer-entially-stiff	227.5	9/2 (+45)	0.0248	-0.06	-180000	-8710	9240	-109	91.7

* Location is given as layer number/interface, where 1 is the innermost layer and 1 denotes the inner and 2 the outer interface. The fiber direction of the layer is shown in parenthesis.
** All failures occur at the ends of the cylinders: s/C=0 is crown, s/C=±0.25 are sides, C=circumference, s=arclength measure (see fig. 1-2)

It was seen in chapter 3 that geometric nonlinearities have an influence on the response of elliptical cylinders subjected to internal pressure. An important issue is how the inclusion of geo-

metric nonlinearities influences the predictions of failure. To that end, the next section addresses the prediction of failure when geometrically nonlinear analyses are used.

6.2 Failure Predictions from the Geometrically Nonlinear Theory

To compute the failure pressure using the geometrically nonlinear analysis, iteration must be used, each iteration using a different internal pressure. The first step in the iteration process follows the failure analysis for the geometrically linear case, namely, the analysis is conducted for a pressure of p_o=100 psi. Then, considering the maximum stress criterion as an example, the seven left-hand sides of the failure criterion are computed, and using p_o=100 psi the failure pressure is computed using eq. 6.2. The geometrically nonlinear analysis is then conducted using this predicted failure pressure, i.e., now p_o is the failure pressure predicted from the first step. The seven left-hand sides are again computed and eq. 6.2 is used to compute a new failure pressure. If this failure pressure prediction is within 10% of the first iteration's failure pressure prediction, the iteration process is considered converged. If the second failure pressure prediction is not with 10% of the first prediction, the geometrically nonlinear analysis is repeated using the second failure pressure prediction as p_o and the failure predictions made again using eq. 6.2. A similar iteration procedure is used for the Hashin criterion based on eq. 6.2, 6.4, or 6.5 and the four left-hand sides in that criterion.

Tables 6-5 through 6-8 represent the geometrically nonlinear case counterpart to tables 6-1 through 6-4, which were computed using geometrically linear analysis. Table 6-5 shows the failure pressure and location for axially-stiff, quasi-isotropic, and circumferentially-stiff elliptical cylinders as predicted by the Hashin failure criterion. Also shown are the values of the stress components at the location of failure when the pressure equals the failure pressure. Note that in each

case failure occurs at the ends of the cylinders. As can be seen, in all cases σ_2 is generally near the failure level of 7250 psi at the failure pressure and, therefore, in each case failure is attributed mainly to tension in the matrix, or σ_2. For the quasi-isotropic and axially-stiff laminates failure occurs at the inner radius and thus again the interlaminar shear stresses do not contribute to this failure of the cylinder. As failure occurs in layer seven of the circumferentially-stiff laminate, near the outer radius, the interlaminar shear stresses could contribute to the initial failure, but, in fact, are an order of magnitude less than inplane stress σ_2, and therefore again have little bearing on the failure predictions. Comparing tables 6-1 and 6-5, it is seen than nonlinearities are predicted to have minimal influence on the failure predictions. The failure pressure levels for the axially-stiff and quasi-isotropic cylinders are predicted to be slightly greater for the nonlinear analysis, and the *s/C* locations of failure are predicted to be somewhat farther away from the crown, i.e., the *s/C*=0 location. On the other hand, compared to the geometrically linear case, the geometrically nonlinear analysis for the circumferentially-stiff case predicts a slightly lower failure pressure but the same *s/C* location.

Table 6-5. Failure pressure and location for elliptical graphite-epoxy cylinders, geometrically nonlinear analysis, Hashin failure criterion

	p_f (psi)	*loc**	ζ	*s/C***	σ_1 (psi)	σ_2 (psi)	τ_{12} (psi)	τ_{13} (psi)	τ_{23} (psi)
Axially-stiff	135.3	1/1 (+45)	-0.0248	-0.09	13100	6990	-3870	0	0
Quasi-isotropic	134.1	1/1 (+45)	-0.0220	-0.10	4540	7020	-3650	0	0
Circumfer-entially-stiff	104.9	7/2 (+90)	0.0138	±0.25	2170	7230	-6.04	105	-803

* Location is given as layer number/interface, where 1 is the innermost layer and 1 denotes the inner and 2 the outer interface. The fiber direction of the layer is shown in parenthesis.
** All failures occur at the ends of the cylinders: s/C=0 is crown, s/C=±0.25 are sides, C=circumference, s=arclength measure (see fig. 1-2)

As a comparison to the Hashin criterion, table 6-6 shows the failure pressure and location for the three elliptical cylinders as predicted by the maximum stress criterion and the geometrically nonlinear analysis. Again the failure mode is predicted to be due to σ_2 at the ends of the cylinders. The table shows the values of the stresses at the location of failure when the pressure equals the failure pressure. Note that σ_2 equals its failure value. By comparing tables 6-5 and 6-6 it is seen that the Hashin and maximum stress criteria both predict similar scenarios, namely failure due to matrix cracking caused by high values of σ_2 at very similar, in not identical, locations. Furthermore, by comparing tables 6-2 and 6-6, it is seen that according to the maximum stress criterion, geometric nonlinearities predict slightly increased failure pressures for the axially-stiff and quasi-isotropic cases, with the failures occurring somewhat farther away from the s/C=0 location. For the circumferentially-stiff case, the nonlinear analysis predicts the same s/C location and a slightly lower failure pressure. This relationship between linear and nonlinear analyses for the

maximum stress criterion is identical to the relationship between linear and nonlinear analyses for the Hashin criterion.

Table 6-6. Failure pressure and location for elliptical graphite-epoxy cylinders, geometrically nonlinear analysis, maximum stress failure criterion

	p_f (psi)	loc*	ζ	s/C**	σ_1 (psi)	σ_2 (psi)	τ_{12} (psi)	τ_{13} (psi)	τ_{23} (psi)
Axially-stiff	140.3	1/1 (+45)	-0.0248	-0.10	7990	7250	-3860	0	0
Quasi-isotropic	138.6	1/1 (+45)	-0.0220	-0.10	4700	7250	-3780	0	0
Circumfer-entially-stiff	105.0	7/2 (90)	0.0138	±0.25	2170	7250	-6.05	105	-804

* Location is given as layer number/interface, where 1 is the innermost layer and 1 denotes the inner and 2 the outer interface. The fiber direction of the layer is shown in parenthesis.
** All failures occur at the ends of the cylinders: s/C=0 is crown, s/C=±0.25 are sides, C=circumference, s=arclength measure (see fig. 1-2)

The pressure required to produce first fiber failure for the geometrically nonlinear cases are shown in tables 6-7 and 6-8. Using the Hashin failure criterion, first fiber failures are predicted to be fiber compression failure in all cases except for the circumferentially-stiff laminate. The location is again at the ends of the cylinders. Except for the circumferentially-stiff laminate, failure is predicted to occur at the outer radius, again due to high bending effects. Note that for these two cases of high fiber compressive stresses, the matrix is in a high compressive state and the shear stress τ_{12} is about one-half its failure level. Also for these two cases, compared to the geometrically linear case of table 6-3, geometric nonlinearities lead to somewhat higher first fiber failure pressures, and failure locations further away from s/C=0. The failure pressures for these two first fiber failure cases are about a factor of two greater than the matrix failure pressures of table 6-5, as in the linear case.

The prediction for the first fiber failure for the circumferentially-stiff case in table 6-7 is quite interesting. The Hashin criterion and the nonlinear analysis predict first fiber failure to be tensile in the outer layer at the sides of the cylinder, whereas, according to table 6-3, the linear analysis predicted fiber compressive failure in the outer layer at the crown of the cylinder. For the nonlinear analysis of table 6-7, both σ_2 and τ_{12} are larger in magnitude than in table 6-3. Since the Hashin criterion uses a combination of stresses, it appears that the high tensile σ_1 and high values of σ_2 and τ_{12} for the geometrically nonlinear case combine to produce fiber tensile failure as opposed to fiber compressive failure, and the location of failure is different. If the variation of curvature with circumferential location at the end of the cylinder, particularly the sign change from side to crown (see fig. A-15) is examined, it can be seen why the failure in the outer layer could be tensile in the cylinder sides or compressive in the crown. For the circumferentially-stiff geometrically nonlinear case, in addition to the failure mode changing relative to the linear case, the failure pressure is higher. Also, the first fiber failure pressure predicted by the nonlinear analysis is, as has been the case, about a factor of two greater than for the first matrix failure predicted by the nonlinear analysis.

Table 6-7. First Fiber failure pressure and location for elliptical graphite-epoxy cylinders, geometrically nonlinear analysis, Hashin failure criterion

	p_f (psi)	loc*	ζ	s/C**	σ_1 (psi)	σ_2 (psi)	τ_{12} (psi)	τ_{13} (psi)	τ_{23} (psi)
Axially-stiff	269.8	9/2 (+45)	0.0248	-0.11	-180000	-5070	7400	-1590	1580
Quasi-isotropic	260.6	8/2 (+45)	0.0220	-0.10	-180000	-5600	7660	-1460	1460
Circumfer-entially-stiff	248.0	9/2 (+45)	0.0248	0.24	153000	12100	-10187	-84.9	117

* Location is given as layer number/interface, where 1 is the innermost layer and 1 denotes the inner and 2 the outer interface. The fiber direction of the layer is shown in parenthesis.
** All failures occur at the ends of the cylinders: s/C=0 is crown, s/C=±0.25 are sides, C=circumference, s=arclength measure (see fig. 1-2)

As seen in table 6-8, the geometrically nonlinear analysis and the maximum stress criterion predict first fiber failure to be compressive for all three laminates. Compared to the analog geometrically linear analysis, table 6-4, the predicted failure locations are further away from the s/C=0 location and the pressure levels are higher. Also compared to the geometrically nonlinear maximum stress criterion analysis for matrix failure, table 6-6, the first fiber failure pressure for the axially-stiff and quasi-isotropic laminates are about factor of two higher, for the circumferentially-stiff laminate, the factor is about 2.5.

Table 6-8. First Fiber failure pressure and location for elliptical graphite-epoxy cylinders, geometrically nonlinear analysis, maximum stress failure criterion

	p_f (psi)	loc*	ζ	s/C**	σ_1 (psi)	σ_2 (psi)	τ_{12} (psi)	τ_{13} (psi)	τ_{23} (psi)
Axially-stiff	269.8	9/2 (+45)	0.0248	-0.11	-180000	-5070	7400	-1590	1580
Quasi-isotropic	260.6	8/2 (+45)	0.0220	-0.10	-180000	-5600	7660	-1460	1460
Circumfer-entially-stiff	266.0	9/2 (+45)	0.0248	-0.09	-180000	-6380	8060	-877	865

* Location is given as layer number/interface, where 1 is the innermost layer and 1 denotes the inner and 2 the outer interface. The fiber direction of the layer is shown in parenthesis.
** All failures occur at the ends of the cylinders: s/C=0 is crown, s/C=±0.25 are sides, C=circumference, s=arclength measure (see fig. 1-2)

Tables 6-9 and 6-10 summarize the key results just discussed. Table 6-9 shows the failure pressure, location, and mode of failure for both the Hashin and maximum stress failure criteria for the cylinders. Results for both linear and nonlinear analysis have been included. As has been discussed, the differences in failure pressure and location of failure between linear and nonlinear analysis are quite small. In each case failure is due to tension in the matrix. In a general sense, both the axially-stiff and quasi-isotropic laminates are predicted to experience the first matrix crack at around 130-140 psi in the first layer (a +45° layer) at the inner radial location at s/C ≈ -0.10. The circumferentially-stiff laminate is predicted to experience the first matrix crack at around 105 psi in the seventh layer (a 90° layer) at the outer radial location at s/C = ±0.25. Whether failure is due to bending or inplane effect is examined by evaluating the part of the stress that is contributed by bending effects and comparing it with the part contributed by inplane effects. The ratio $\sigma_\kappa/\sigma_\varepsilon$ is the ratio of these two parts and the table shows that both the axially-stiff and the quasi-isotropic laminates are predicted to fail due to bending effects. On the other hand,

the circumferentially-stiff laminate is predicted to fail due to inplane effects. The bending effects at the end are induced by the conditions of w=0 and $\frac{\partial w}{\partial x}$ =0 there, while inplane effects are induced by the condition v=0 there and the inplane stress resultants caused by the internal pressure. Note that for the axially-stiff and quasi-isotropic cases, geometric nonlinearities reduce bending effects relative to inplane effects, whereas for the circumferentially-stiff case the reverse is true.

Table 6-9. Failure pressure, location, and mode for elliptical graphite-epoxy cylinders, geometrically linear and nonlinear analyses, two failure criteria

		Axially-Stiff		Quasi-Isotropic		Circumferentially-Stiff	
		Hashin	Max σ	Hashin	Max σ	Hashin	Max σ
linear	p_f, psi	130	136	131	136	107	107
	loc*	1/1 (+45)	1/1 (+45)	1/1 (+45)	1/1 (+45)	7/2 (90)	7/2 (90)
	ζ	-0.0248	-0.0248	-0.0220	-0.0220	0.0138	0.0138
	s/C**	-0.07	-0.07	-0.07	-0.08	±0.25	±0.25
	mode $\sigma_\kappa/\sigma_\varepsilon$	$+\sigma_2$ 3.3/1	$+\sigma_2$ 3.3/1	$+\sigma_2$ 4/1	$+\sigma_2$ 2.86/1	$+\sigma_2$ 0.33/1	$+\sigma_2$ 0.33/1
nonlinear	p_f, psi	135	140	134	139	105	105
	loc	1/1 (+45)	1/1 (+45)	1/1 (+45)	1/1 (+45)	7/2 (90)	7/2 (90)
	ζ	-0.0248	-0.0248	-0.0220	-0.0220	0.0138	0.0138
	s/C**	-0.09	-0.10	-0.10	-0.10	±0.25	±0.25
	mode $\sigma_\kappa/\sigma_\varepsilon$	$+\sigma_2$ 2.7/1	$+\sigma_2$ 2.3/1	$+\sigma_2$ 2.2/1	$+\sigma_2$ 2.2/1	$+\sigma_2$ 0.38/1	$+\sigma_2$ 0.38/1

* Location is given as layer number/interface, where 1 is the innermost layer and 1 denotes the inner and 2 the outer interface. The fiber direction of the layer is shown in parenthesis.
** All failures occur at the ends of the cylinders: s/C=0 is crown, s/C=±0.25 are sides, C=circumference, s=arclength measure (see fig. 1-2)

Table 6-10 shows the failure pressure and location of failure for the Hashin failure criterion and examines matrix (as seen in table 6-9) and fiber failure. Results for both linear and nonlinear analysis have been included. The most notable difference between first fiber and matrix failure is the increase in failure pressure from 105-135 psi to 227-270 psi. This indicates that as the pressure increases the matrix will fail long before the first fiber failure pressure is reached. Also, from matrix failure to first fiber failure, the location of failure shifts dramatically from the inside to the outside of the cylinder for the axially-stiff and quasi-isotropic laminates, and from the outer 90° layer to the outer +45° layer for the circumferentially-stiff laminate. Geometric nonlinearities have a somewhat stronger influence on first fiber failure pressure as compared to matrix failure, causing increases in failure pressure around 10%, as opposed to 2% for matrix failure pressures. Based on the nonlinear analysis, the axially-stiff laminate fibers fail at 270 psi in the ninth layer, the outer +45° layer, on the outer interface at s/C = -0.11. The quasi-isotropic laminate fibers fail at 261 psi in the eighth layer, the outer +45° layer, on the outer interface at s/C = -0.10. The circumferentially-stiff laminate fibers fail at 248 psi in the ninth layer, the outer +45° layer, on the outer interface at s/C = 0.24.

Table 6-10. Failure pressure, location, and mode for elliptical graphite-epoxy cylinders, geometrically linear and nonlinear analyses, two failure modes, Hashin failure criterion

		Axially-Stiff		Quasi-Isotropic		Circumferentially-Stiff	
		Matrix	Fiber	Matrix	Fiber	Matrix	Fiber
linear	p_f, psi	130	242	131	229	107	227
	loc*	1/1 (+45)	9/2 (+45)	1/1 (+45)	8/2 (+45)	7/2 (90)	9/2 (+45)
	ζ	-0.0248	0.0248	-0.0220	0.0220	0.0138	0.0248
	s/C**	-0.07	-0.08	-0.07	-0.07	±0.25	-0.06
	mode $\sigma_\kappa/\sigma_\varepsilon$	$+\sigma_2$ 3.3/1	$-\sigma_1$ 1.25/1	$+\sigma_2$ 4/1	$-\sigma_1$ 1.3/1	$+\sigma_2$ 0.33/1	$-\sigma_1$ 1.25/1
nonlinear	p_f, psi	135	270	134	261	105	248
	loc*	1/1 (+45)	9/2 (+45)	1/1 (+45)	8/2 (+45)	7/2 (90)	9/2 (+45)
	ζ	-0.0248	0.0248	-0.0220	0.0220	0.0138	0.0248
	s/C**	-0.09	-0.11	-0.10	-0.10	±0.25	0.24
	mode $\sigma_\kappa/\sigma_\varepsilon$	$+\sigma_2$ 2.7/1	$-\sigma_1$ 1.2/1	$+\sigma_2$ 2.2/1	$-\sigma_1$ 1.2/1	$+\sigma_2$ 0.38/1	$+\sigma_1$ 0.59/1

* Location is given as layer number/interface, where 1 is the innermost layer and 1 denotes the inner and 2 the outer interface. The fiber direction of the layer is shown in parenthesis.
** All failures occur at the ends of the cylinders: s/C=0 is crown, s/C=±0.25 are sides, C=circumference, s=arclength measure (see fig. 1-2)

6.3 An Alternative View of Failure Predictions

With composite materials there is often scatter in the results of tests designed to determine failure stresses. Considering the failure stress of a composite material to be exactly a certain level is somewhat unrealistic. The scatter is due to small unpredictable irregularities in the microstructure of composites and possible anomalies in the manufacturing process. As a result, the location with the highest stress may not fail first. A slightly lower stress at another location, coupled with a microstructural irregularity, could lead to lower failure stress levels. To that end, the geometri-

cally nonlinear failure analysis was used to compute the locations within the ellipse where the seven left-hand sides in the Hashin failure criterion were within 20% of the failure level, i.e., the left-hand sides were in the range 0.80 to 1.00, with 1.00 corresponding to the cases discussed in table 6-5.

Figures 6-1 through 6-3 show the locations of the maximum left-hand side and all values within 20% of the maximum value for the Hashin failure criterion for the axially-stiff, quasi-isotropic, and circumferentially-stiff laminates. The axially-stiff, quasi-isotropic, and circumferentially-stiff laminates were evaluated using nonlinear analysis at failure pressure, p_f. In each figure a greatly distorted view of the crown section of the cylinder wall through the thickness from $-H/2 \leq \zeta \leq H/2$, around the circumference from $-0.25 \leq s/C \leq 0.25$, and at $x/L=0.5$ provides a visual display of the points within 20% of failure. Each figure includes a table which lists in descending order the location of the points, and stresses at those points at the failure pressure.

Figure 6-1 shows all points within 20% of the maximum left-hand side value for the axially-stiff laminate, which has a thickness, H, of 0.0495 in. As indicated in previous tables, the maximum left-hand side value, or initial failure point, is located at the first layer, a +45° layer, at the inner radial location of the cylinder at $s/C=-0.09$. Considering points where the left-hand side is less than 1.00, the points are dispersed circumferentially on both sides of the initial failure point, but remain in the first layer at the inner radial location. Eventually, the points reach to both sides of the interface between the first and second layers. An alternative interpretation of the spatial distribution of the points is that if the pressure is increased beyond the value to predict failure at point 1, point 2 will be the next location of failure. Further increases in pressure would lead to failure at points 3, 4, 5, etc. With this interpretation, then, it is felt that the geometric distribution of points would represent the progression of damage as the pressure increases beyond the value

necessary to have the Hashin criteria to equal 1.00. If this is the case, then, matrix cracking will accumulate in layer 1 at the inner radial location (ζ=-0.02475) in the range $-0.16 \leq s/C \leq 0$. There will also be cracking in layer 2 at the interface between the 1st and 2nd layers (ζ=-0.01925). All these failures would be due to high values of σ_2.

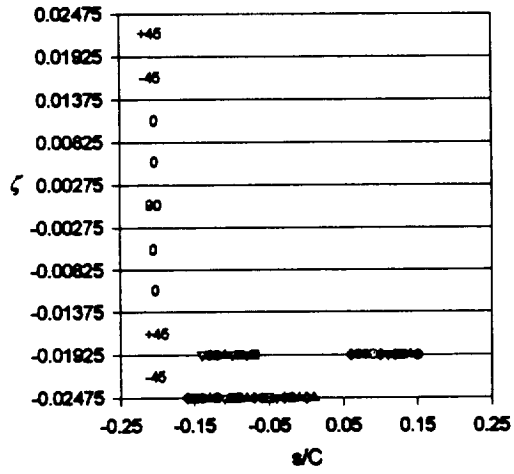

	loc	ζ	s/C	σ_1	σ_2	τ_{12}	τ_{13}	τ_{23}
1	1/1 (+45)	-0.02475	-0.090	13100	6990	-3870	0	0
2	1/1 (+45)	-0.02475	-0.100	7700	6990	-3730	0	0
3	1/1 (+45)	-0.02475	-0.080	18500	6950	-4000	0	0
4	1/1 (+45)	-0.02475	-0.110	2430	6950	-3570	0	0
5	1/1 (+45)	-0.02475	-0.070	23900	6870	-4110	0	0
6	1/1 (+45)	-0.02475	-0.060	29300	6770	-4200	0	0
7	1/1 (+45)	-0.02475	-0.120	-2710	6860	-3380	0	0
8	1/1 (+45)	-0.02475	-0.050	34700	6640	-4280	0	0
9	1/1 (+45)	-0.02475	-0.130	-7590	6710	-3170	0	0
10	1/1 (+45)	-0.02475	-0.040	39900	6490	-4340	0	0
11	1/1 (+45)	-0.02475	-0.030	45100	6320	-4390	0	0
12	1/1 (+45)	-0.02475	-0.140	-12100	6490	-2950	0	0
13	1/1 (+45)	-0.02475	-0.020	50100	6120	-4430	0	0
14	1/1 (+45)	-0.02475	-0.150	-16100	6220	-2700	0	0
15	1/1 (+45)	-0.02475	-0.010	54900	5900	-4450	0	0
16	2/1 (-45)	-0.01925	0.110	-7030	6050	2850	-133	-775
17	2/1 (-45)	-0.01925	0.100	-2500	6020	2960	-135	-812

Figure 6-1. Points within 20% of failure pressure, Hashin criterion, axially-stiff laminate, nonlinear analysis, x/L=0.5

18	2/1 (-45)	-0.01925	0.120	-11300	6040	2740	-132	-728
19	2/1 (-45)	-0.01925	0.090	2210	5940	3050	-135	-841
20	2/1 (-45)	-0.01925	0.130	-15300	5980	2600	-129	-671
21	1/2 (+45)	-0.01925	-0.110	-8310	5930	-2770	-954	119
22	1/2 (+45)	-0.01925	-0.100	-3660	5910	-2880	-966	122
23	1/1 (+45)	-0.02475	0.000	59600	5670	-4460	0	0
24	1/2 (+45)	-0.01925	-0.120	-12700	5910	-2630	-938	113
25	2/1 (-45)	-0.01925	0.080	7050	5850	3130	-136	-865
26	1/2 (+45)	-0.01925	-0.090	1180	5860	-2990	-972	125
27	2/1 (-45)	-0.01925	0.140	-18700	5870	2460	-124	-599
28	1/2 (+45)	-0.01925	-0.080	6140	5780	-3070	-975	127
29	1/1 (+45)	-0.02475	-0.160	-19600	5870	-2440	0	0
30	1/2 (+45)	-0.01925	-0.130	-16800	5840	-2490	-911	107
31	2/1 (-45)	-0.01925	0.070	12000	5720	3210	-136	-883
32	1/2 (+45)	-0.01925	-0.070	11100	5660	-3150	-976	129
33	1/1 (+45)	-0.02475	0.010	64200	5420	-4460	0	0
34	1/2 (+45)	-0.01925	-0.140	-20300	5720	-2330	-871	100
35	2/1 (-45)	-0.01925	0.060	17000	5580	3270	-136	-899
36	2/1 (-45)	-0.01925	0.150	-21600	5700	2290	-118	-514

Figure 6-1. Points within 20% of failure pressure, Hashin criterion, axially-stiff laminate, nonlinear analysis, x/L=0.5

Figure 6-2 shows all points within 20% of the maximum left-hand side value for the quasi-isotropic laminate, which has a thickness, H, of 0.044 in. As indicated in previous tables, the initial failure point is located in the first layer at the inner radial location of the cylinder at s/C=-0.100. Considering points where the left-hand side is less than 1.00, the points are dispersed circumferentially on both sides of the initial failure point but remain in the first layer at the inner radial location. Eventually the points reach to both sides of the interface between the first and second layers, and the outer radial location of the eighth layer. An alternative interpretation of the spatial distribution of the points is that matrix cracking will accumulate in layer 1 at the inner radial location (ζ=-0.02220) in the range $-0.16 \leq s/C \leq 0$. There will also be cracking in layers 1 and 2 at the interface between these layers (ζ=-0.0165). Some cracking will also occur in layer 8 at the outer location (ζ=0.0220). All these failures would be due to high values of σ_2.

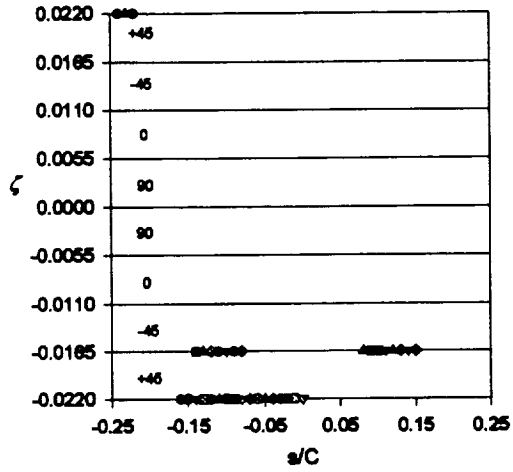

	loc	ζ	s/C	σ_1	σ_2	τ_{12}	τ_{13}	τ_{23}
1	1/1 (+45)	-0.0220	-0.100	4540	7020	-3650	0	0
2	1/1 (+45)	-0.0220	-0.090	9800	7000	-3790	0	0
3	1/1 (+45)	-0.0220	-0.110	-567	7000	-3510	0	0
4	1/1 (+45)	-0.0220	-0.080	15200	6930	-3900	0	0
5	1/1 (+45)	-0.0220	-0.120	-5470	6910	-3330	0	0
6	1/1 (+45)	-0.0220	-0.070	20500	6830	-3990	0	0
7	1/1 (+45)	-0.0220	-0.060	26000	6710	-4080	0	0
8	1/1 (+45)	-0.0220	-0.130	-10100	6780	-3150	0	0
9	1/1 (+45)	-0.0220	-0.050	31500	6550	-4150	0	0
10	1/1 (+45)	-0.0220	-0.140	-14200	6580	-2930	0	0
11	1/1 (+45)	-0.0220	-0.040	36800	6380	-4200	0	0
12	1/1 (+45)	-0.0220	-0.030	42200	6180	-4250	0	0
13	1/1 (+45)	-0.0220	-0.150	-17900	6330	-2700	0	0
14	1/1 (+45)	-0.0220	-0.020	47500	5970	-4280	0	0
15	2/1 (-45)	-0.0165	0.120	-14800	6040	2640	-154	-844
16	2/1 (-45)	-0.0165	0.110	-10900	6010	2740	-157	-902
17	2/1 (-45)	-0.0165	0.130	-18200	6020	2550	-150	-771
18	1/1 (+45)	-0.0220	-0.160	-20700	6000	-2470	0	0
19	1/1 (+45)	-0.0220	-0.010	52600	5730	-4300	0	0
20	2/1 (-45)	-0.0165	0.100	-6760	5930	2810	-159	-946
21	8/2 (+45)	0.0220	-0.230	32100	5810	-3790	-14.6	-3.36
22	2/1 (-45)	-0.0165	0.140	-21100	5960	2440	-142	-679
23	1/2 (+45)	-0.0165	-0.120	-16400	5870	-2520	-1060	130
24	8/2 (+45)	0.0220	-0.240	45000	5680	-4080	-15.4	6.02
25	1/2 (+45)	-0.0165	-0.110	-12500	5860	-2620	-1090	136

Figure 6-2. Points within 20% of failure pressure, Hashin criterion, quasi-isotropic laminate, nonlinear analysis, x/L=0.5

26	2/1 (-45)	-0.0165	0.090	-2340	5830	2870	-159	-980
27	1/2 (+45)	-0.0165	-0.130	-19900	5850	-2410	-1020	121
28	1/2 (+45)	-0.0165	-0.100	-8190	5810	-2700	-1100	141
29	2/1 (-45)	-0.0165	0.150	-23200	5830	2310	-132	-567
30	8/2 (+45)	0.0220	-0.220	17400	5680	-3330	-11.5	-12.6
31	1/2 (+45)	-0.0165	-0.090	-3630	5720	-2790	-1120	144
32	1/2 (+45)	-0.0165	-0.140	-22900	5770	-2290	-964	109
33	2/1 (-45)	-0.0165	0.080	2290	5700	2930	-159	-1010
34	1/1 (+45)	-0.0220	0.000	57600	5480	-4310	0	0
35	1/2 (+45)	-0.0165	-0.080	1150	5600	-2850	-1120	148

Figure 6-2. Points within 20% of failure pressure, Hashin criterion, quasi-isotropic laminate, nonlinear analysis, x/L=0.5

Figure 6-3 shows all points within 20% of the maximum left-hand side value for the circumferentially-stiff laminate, which has a thickness, H, of 0.0495 in. As indicated in previous tables, the initial failure points are located at the outer interface in the seventh layer, a 90° layer, at $s/C=\pm 0.25$. Considering points where the left-hand side is less than 1.00, the points are located at the outer interface of the seventh layer and inward of $s/C=\pm 0.25$. The points are also located at the inner and outer interfaces of other layers, and inward of $s/C=\pm 0.25$. An alternative interpretation of the spatial distribution of the points is that as pressure increases matrix cracking will accumulate in layer 7 at the outer interface location ($\zeta=0.01375$) in the ranges $-0.25 \leq s/C \leq -0.22$ and $0.22 \leq s/C \leq 0.25$. There will also be cracking in layer 6 at the interface between layers 6 and 7 ($\zeta=0.00825$). Some cracking will also occur in layer 8 at the interface between layers 8 and 9 ($\zeta=0.01925$), and at the outer radial location in layer 9 ($\zeta=0.02475$). All these failures would be due to high values of σ_2.

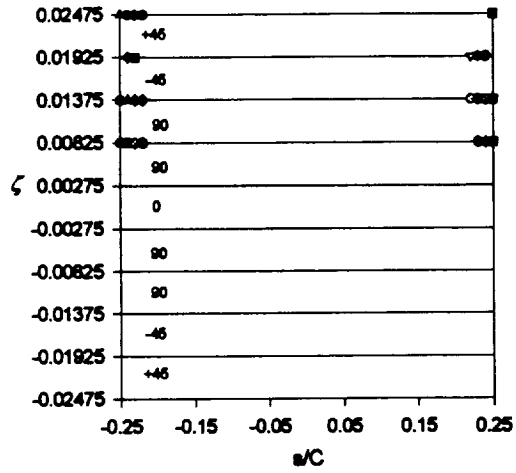

	loc	ζ	s/C	σ_1	σ_2	τ_{12}	τ_{13}	τ_{23}
1	7/2 (90)	0.01375	-0.250	2170	7230	-6.04	105	-803
2	7/2 (90)	0.01375	0.250	2170	7230	-6.04	105	-803
3	7/2 (90)	0.01375	-0.240	2140	7130	547	33.2	-783
4	7/2 (90)	0.01375	0.240	2130	7100	-559	169	-760
5	7/2 (90)	0.01375	-0.230	2030	6770	1080	-40.4	-702
6	7/2 (90)	0.01375	0.230	2010	6710	-1090	221	-658
7	6/2 (90)	0.00825	-0.250	1940	6450	-6.04	105	-866
8	6/2 (90)	0.00825	0.250	1940	6450	-6.04	105	-866
9	7/1 (90)	0.00825	-0.250	1940	6450	-6.04	105	-866
10	7/1 (90)	0.00825	0.250	1940	6450	-6.04	105	-866
11	9/2 (+45)	0.02475	-0.230	42300	6070	-4190	2.88	-22.6
12	9/2 (+45)	0.02475	-0.240	52400	6020	-4440	7.46	-17.8
13	6/2 (90)	0.00825	-0.240	1910	6350	547	31.9	-844
14	7/1 (90)	0.00825	-0.240	1910	6350	547	31.9	-844
15	6/2 (90)	0.00825	0.240	1900	6330	-559	171	-819
16	7/1 (90)	0.00825	0.240	1900	6330	-559	171	-819
17	7/2 (90)	0.01375	-0.220	1860	6200	1570	-111	-571
18	9/2 (+45)	0.02475	-0.220	30800	5900	-3810	-0.861	-26.0
19	7/2 (90)	0.01375	0.220	1830	6100	-1580	259	-508
20	9/2 (+45)	0.02475	-0.250	60500	5720	-4510	12.6	-12.2
21	9/2 (+45)	0.02475	0.250	60500	5720	-4510	12.6	-12.2
22	6/2 (90)	0.00825	-0.230	1810	6060	1080	-43.4	-759
23	7/1 (90)	0.00825	-0.230	1810	6060	1080	-43.4	-759
24	6/2 (90)	0.00825	0.230	1800	6020	-1090	225	-710
25	7/1 (90)	0.00825	0.230	1800	6020	-1090	225	-710

Figure 6-3. Points within 20% of failure pressure, Hashin criterion, circumferentially-stiff laminate, nonlinear analysis, x/L=0.5

26	9/1 (+45)	0.01925	-0.230	37400	5610	-3840	394	-124
27	7/2 (90)	0.01375	-0.250	4260	5920	-3.72	57.0	-433
28	7/2 (90)	0.01375	0.250	4260	5920	-3.72	57.0	-433
29	9/1 (+45)	0.01925	-0.240	47100	5510	-4050	495	-127
30	8/2 (-45)	0.01925	0.230	36700	5560	3780	87.8	550
31	8/2 (-45)	0.01925	0.240	46600	5480	4020	108	577
32	7/2 (90)	0.01375	0.240	4250	5830	-556	78.0	-415
33	7/2 (90)	0.01375	-0.240	4210	5830	548	32.5	-421

Figure 6-3. Points within 20% of failure pressure, Hashin criterion, circumferentially-stiff laminate, nonlinear analysis, x/L=0.5

This chapter has presented a comprehensive discussion of failure of internally pressurized elliptical cylinders. The Hashin and maximum stress failure criteria, geometrically linear and non-linear analyses, and first matrix failure and first fiber failure were considered. Additionally, the concept of an accumulation of matrix cracks was introduced. It was shown that for the first matrix failure there was not much difference between the predictions of the two failure criteria or between linear and nonlinear analyses. However, the predicted pressure to cause first fiber failure was about a factor of two higher than the predicted pressure to cause matrix failure. Additionally, considering nonlinear analysis, the Hashin prediction of first fiber failure for the circumferentially-stiff laminate was quite different than the prediction of the maximum stress criterion. The mode and location differed significantly, and the pressure levels were somewhat different. The next chapter summarizes this entire study, presents conclusions, and provides ideas for future work.

Chapter 7 Conclusions and Future Work

This chapter summarizes this entire study, presents conclusions, and provides ideas for future work.

7.1 Summary

Using numerical results, a thorough explanation was given of the effects of cylinder geometry, specifically, circular vs. elliptical cross sections, and geometric nonlinearities on cylinder responses. Also, the effects of orthotropy were studied using quasi-isotropic, axially-stiff, and circumferentially-stiff graphite-epoxy laminates. Displacements, reference surface strains and curvatures, and force and moment resultants were used to define cylinder responses. The Hashin failure theory and the maximum stress theory were used to assess the pressure capacity of elliptical composite cylinders. Interlaminar shear stresses were considered in the assessment of pressure capacity by integrating the geometrically linear equilibrium equations of elasticity in polar coordinates through the thickness at the cylinder wall. These interlaminar shear stresses together with the inplane (intralaminar) stresses were used in the failure theories. Failure pressure levels, failure location, and failure modes were studied.

7.2 Conclusions

The effects of elliptical geometry as discussed in chapter 2 include several key issues. For instance, responses for the elliptical case vary with both the x and s coordinate. This variation is

seen in every elliptical response, either over the entire domain, or at the boundary. For the elliptical cylinder:

- axial responses are compressive at certain locations for axial displacement, axial strain, and the axial force resultant, despite the axial tensile effect of the internal pressure on the cylinder end plates
- the circumferential displacement and shear force resultant are not zero, whereas, both of these responses are zero for the circular cylinder
- the normal displacement can be negative
- the shear strain is as large, or larger, than axial and circumferential strain, whereas, it is zero for the circular cylinder
- the circumferential and twist curvatures are not zero at the midspan, whereas, both of these responses are zero at the midspan for the circular cylinder
- an ellipticity of 0.7 causes a change in sign of the response at the boundary for axial curvature, all moment resultants, and the shear force resultants as s varies from $s/C = 0$ to $s/C = 0.25$. It is felt less severe ellipses, e.g., an ellipticity of 0.90, may not experience these sign reversals.

The differences between the geometrically linear and nonlinear analyses considered here are strictly due to the nonlinear terms in the strain-displacement equations. Chapter 3 examines the differences between linear and nonlinear analyses created by these nonlinear terms. The effects of geometric nonlinearities seen in this chapter include several key issues. Between linear and nonlinear analyses:

- a smaller axial end displacement, Δ, is required to satisfy axial equilibrium
- the axial displacement displays an overall difference in magnitude

•the circumferential displacement has a shift of the location of the extreme value

•the normal displacement flattens at the crown of the cylinder.

Aside from the displacements, differences between linear and nonlinear analyses, if any exist, seem to split into two categories: those due to flattening of the crown of the cylinder, and those; involving a change in magnitude of the behavior at the boundary. Flattening of the crown of the cylinder is seen in:

•the circumferential strain

•the circumferential curvature

•the circumferential force resultant.

The change of the behavior at the boundary is seen in:

•the axial curvature

•the axial and circumferential transverse shear force resultants, $\overline{Q}_s$ and $\overline{Q}_x$.

The moment resultants show both behaviors, a flattening in the crown and a change of magnitude at the boundary. Also, two definitions of the transverse force resultants, $\overline{V}_s$ and $\overline{V}_x$, are introduced for the nonlinear case. There are significant differences between the circumferential transverse shear force resultant, $\overline{Q}_s$, and the circumferential transverse force resultant, $\overline{V}_s$.

In chapter 4 the focus is shifted from the influence of elliptical geometry and geometric nonlinearities to the influence of material orthotropy. Each laminate has a different response to internal pressure due to the percentages of fibers in the axial and circumferential directions. The axially-stiff, circumferentially-stiff, and quasi-isotropic laminates result in an overall difference in magnitude for the axial, circumferential, and normal displacements. In fact, the axially-stiff elliptical cylinder evaluated using nonlinear analysis contracts axially in response to internal pressure,

whereas, for the other two cases there is axial extension. For some responses orthotropy mitigates the effect of ellipticity. For example:

- the circumferential strain behaves like that of a circular cylinder in the midspan region of the circumferentially-stiff laminate, namely being independent of circumferential location
- for the axially-stiff laminate, the axial strain displays less spatial variation with both x and s compared to the axial strains for the circumferentially-stiff and quasi-isotropic laminates.

The variation with s at the clamped boundary depends significantly on orthotropy for:

- the axial curvature
- the circumferential force resultant
- the circumferential moment resultant
- the transverse force resultants.

Compared to the circumferentially-stiff and quasi-isotropic laminates, for these responses, the axially-stiff laminate does not generally exhibit as much variation with s.

In chapter 5, an evaluation of material failure using the maximum stress and Hashin failure criteria is presented for elliptical cylinders by considering geometrically linear and nonlinear analyses and quasi-isotropic, axially-stiff, and circumferentially-stiff laminates. Also, the approach is discussed for computing the inplane stresses, and a method is presented for computing the interlaminar shear stresses that contribute to the failure criteria. The integral of the interlaminar shear stresses through the thickness are compared to the transverse shear stress resultant to verify the derivation of the interlaminar shear stresses. The difference between the integrated interlaminar shear stresses and the transverse shear stress resultant is considered to be negligible.

In chapter 6, the Hashin and maximum stress failure criteria and geometrically linear and nonlinear analyses are considered in order to predict the location of failure, mode of failure, and the pressure at failure. First matrix failure and first fiber failure are considered. Additionally, the concept of an accumulation of matrix cracks is introduced. Catastrophic failure is not expected at initial failure due to matrix cracking. Catastrophic failure due to fiber failure is more likely. For the geometrically linear analysis:

- the Hashin and maximum stress criteria both predict failure due to matrix cracks due to high values of σ_2 at very similar, if not identical, pressure levels and locations
- first fiber failure is predicted to be fiber compression for all cases at identical locations for the Hashin and maximum stress criteria
- pressures for first fiber failure are about twice as high as for matrix cracking pressures
- the contributions of the interlaminar shear stresses to failure were small.

For the geometrically nonlinear analysis:

- the Hashin and maximum stress criteria both predict failure due to matrix cracks due to high values of σ_2 at very similar, if not identical, pressure levels and locations
- slightly higher failure pressures at locations somewhat farther from the crown are predicted for the quasi-isotropic and axially-stiff laminates compared to the geometrically linear case
- slightly lower failure pressures but identical locations are predicted for the circumferentially-stiff laminate compared to the geometrically linear case
- first fiber failure for the Hashin criterion is predicted to be fiber compression for the axially-stiff and quasi-isotropic laminates at pressures higher than first fiber failure for the geometrically linear case

- first fiber failure for the Hashin criterion is predicted to be fiber tension for the circumferentially-stiff laminate at a higher pressure and different location than first fiber failure for the geometrically linear case
- first fiber failure for the maximum stress criterion is predicted to be fiber compression for all cases at higher pressures at locations farther away from $s/C = 0$ than first fiber failure predicted using a geometrically linear analyses.

For all cases, axially-stiff and quasi-isotropic laminates are predicted to fail due to bending effects and the circumferentially-stiff laminate is predicted to fail due to inplane effects. The differences in the predictions of the two failure criteria as expressed in the last three bulleted points is considered significant.

7.3 Future Work

7.3.1 Numerical

Future work will focus on a progressive failure analysis. This will mean moving beyond the first ply failure analysis and reaching the point of having a significant number of fibers fail. Since the initial failure will take place at certain circumferential, i.e., s/C, locations and not others, degraded material properties are to be incorporated only in the affected locations. This will make the analysis much more difficult than if material properties of the cylinder are the same at all locations. Therefore the finite element program STAGS will be used to study the progressive failure analysis. This will involve doing a sequence of analyses, each with a different distribution of material properties, the distributions reflecting the progressive degradation of material properties as the pressure increases.

7.3.2 Experimental

For the experimental phase of the work, existing elliptical cylinders will be prepared for pressure testing in the Structural Mechanics Branch of the NASA-Langley Research Center. This will involve C-scanning the cylinders for any material imperfections, then scanning the geometry to determine the exact shape of the cylinders. End fittings will have to be attached and strain gages mounted. The end fittings will be ones specially-designed for pressure testing. Testing to bursting failure will then take place.

References

1. Meyers, C.A., "An Analytical and Experimental Investigation of the Response of Elliptical Composite Cylinders." Diss. Virginia Tech, 1996.

2. Hyer, M.W., *Stress Analysis of Fiber-Reinforced Composite Materials*. WCB/McGraw-Hill, New York, 1998.

3. Marguerre, K., "Stability of the cylindrical shell of variable curvature," NASA TM 1302, 1951.

4. Wolfram, S., *Mathematica: A System for Doing Mathematics by Computer*. Addison-Wesley Publishing Co., Redwood City, CA, 1991.

5. IMSL MATH/Library User's manual, pp. 660-671, IMSL, Houston TX, 1987.

6. Brogan, F.A., Rankin, C.C., and Cabiness, H.D., "STAGS Users Manual," Lockheed Palo Alto Research Laboratory Report LMSC PO32594, 1994.

7. Hashin, Z., "Failure Criteria for Unidirectional Fiber Composites," *Journal of Applied Mechanics*, Vol. 47, 1980, pp. 329-334.

Appendix A Comparison between Present and STAGS Results

In this appendix the displacement, strain, and stress resultant responses are shown for eight and nine layer graphite-epoxy cylinders with semi-major diameters of 5 in., ellipticities of 0.7, and lengths of 12.5 in. These responses are computed with the semi-analytical solution of the present study and with the finite element code STAGS [A-1]. Only geometrically nonlinear analyses are considered. The material and geometric properties of a layer of graphite-epoxy are taken to be

$$\begin{aligned} E_1 &= 18.85 \text{ Msi} \qquad E_2 = 1.407 \text{ Msi} \\ G_{12} &= 0.725 \text{ Msi} \qquad \nu_{12} = 0.300 \qquad h = 0.0055 \text{ in.} \end{aligned} \tag{A.1}$$

where h is the thickness of a single layer. The laminates considered are: quasi-isotropic, $[\pm 45/0/90]_S$; axially-stiff, $[\pm 45/0_2/90_{\frac{1}{2}}]_S$; circumferentially-stiff, $[\pm 45/90_2/0_{\frac{1}{2}}]_S$, where 0 degrees is in the axial direction.

The mesh for the semi-analytical solution has 125 finite-difference nodes in the axial direction and 100 nodes around the circumference for a total of 12,500 nodes. In the axial direction the distance between nodes is adjusted by the finite-difference scheme according to the magnitude of the axial gradients in the response quantities. In the circumferential direction the distance between nodes is 0.2718 in. The STAGS mesh has 41 nodes in the axial direction and 97 nodes around the circumference, for a total of 3997 nodes and 3840 elements. The nodes are equispaced in both directions and the length of the element is 0.3125 in. in the axial direction and 0.2803 in. in the circumferential direction. Essentially, the mesh is finer in the present solution

than for the STAGS solution. The difference in the mesh between the present and STAGS solution is most significant in the axial direction, as is apparent in figs. A-1 - A-18.

For the STAGS solution the displacements are computed at the nodes. The strains, curvatures, force resultants, moment resultants, and shear force resultants are computed at the Gauss points, which are located at the center of the element. Therefore, for the STAGS solutions there are no results for the ends of the cylinder, which is where failure is predicted to occur. By increasing the number of points in the axial direction, the Gauss points can approach the ends of the cylinder, but they can never reach the ends. For this reason, a failure prediction using STAGS results will not agree with a failure prediction using the present analysis. For a given failure criterion, STAGS will be nonconservative.

References

A-1. Brogan, F.A., Rankin, C.C., and Cabiness, H.D., "STAGS Users Manual," Lockheed Palo Alto Research Laboratory Report LMSC PO32594, 1994.

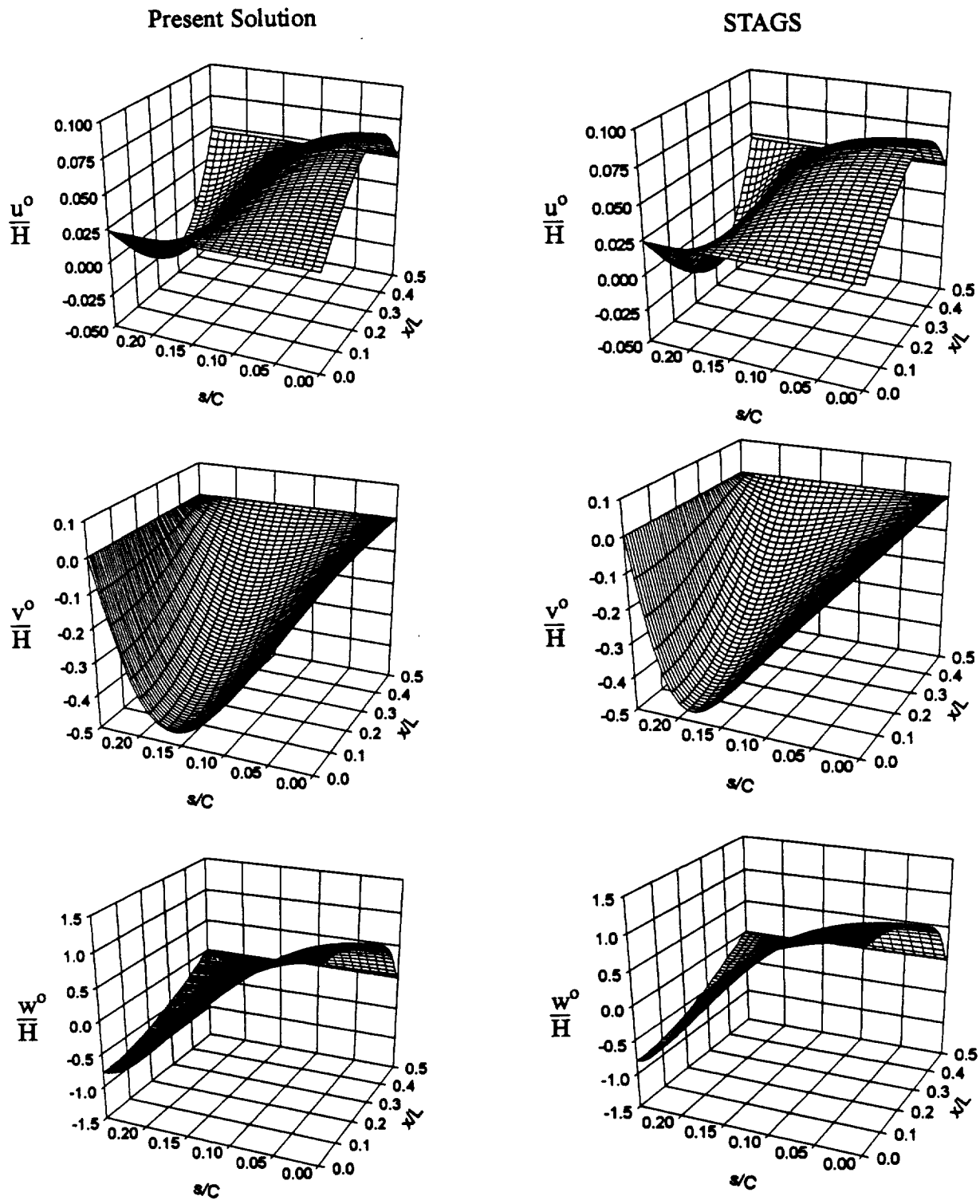

Figure A-1 Comparison between present solution and STAGS for a quasi-isotropic elliptical cylinder, e=0.7, p_o=100 psi: displacements

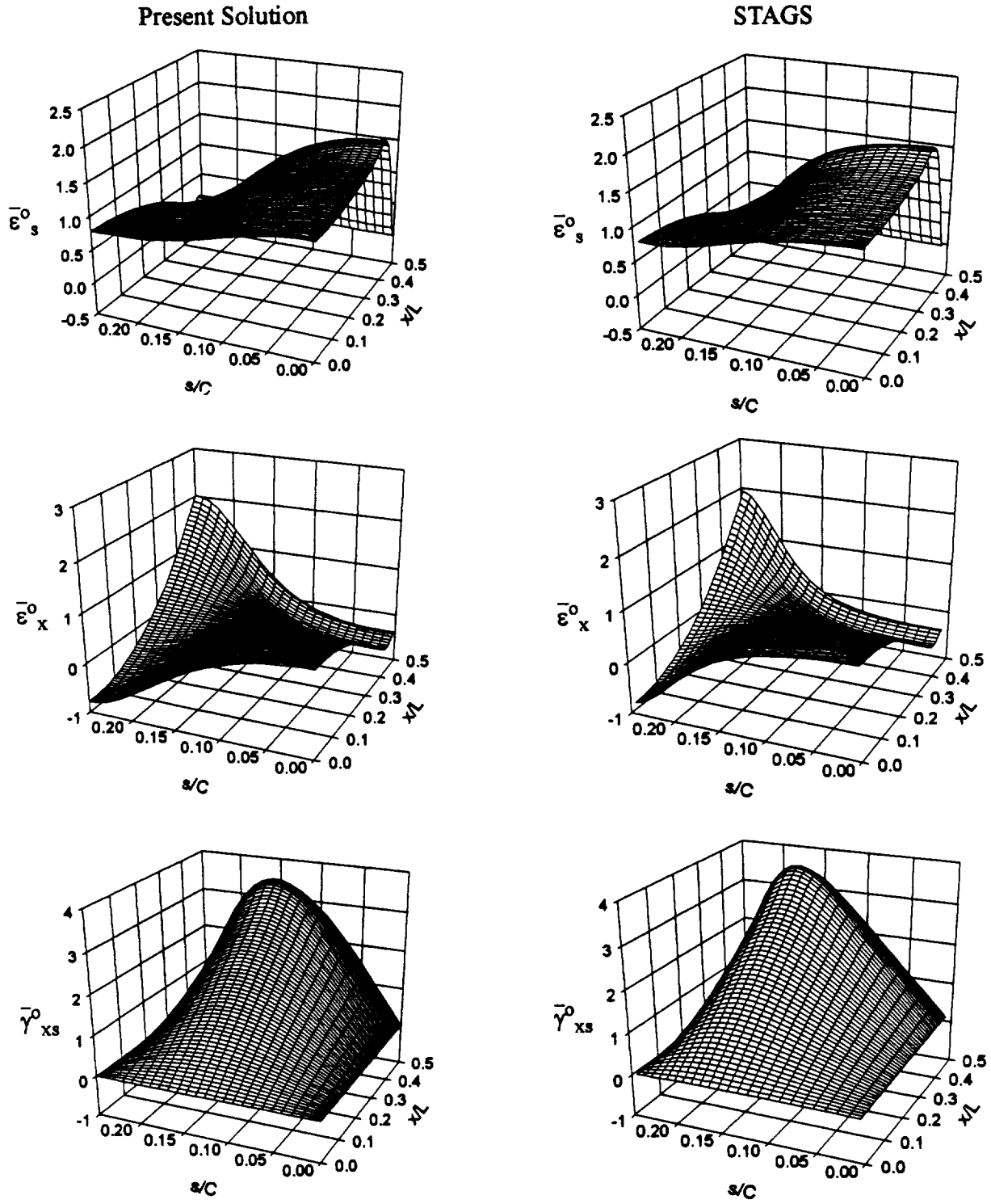

Figure A-2 Comparison between present solution and STAGS for a quasi-isotropic elliptical cylinder, e=0.7, p_o=100 psi: reference surface strains

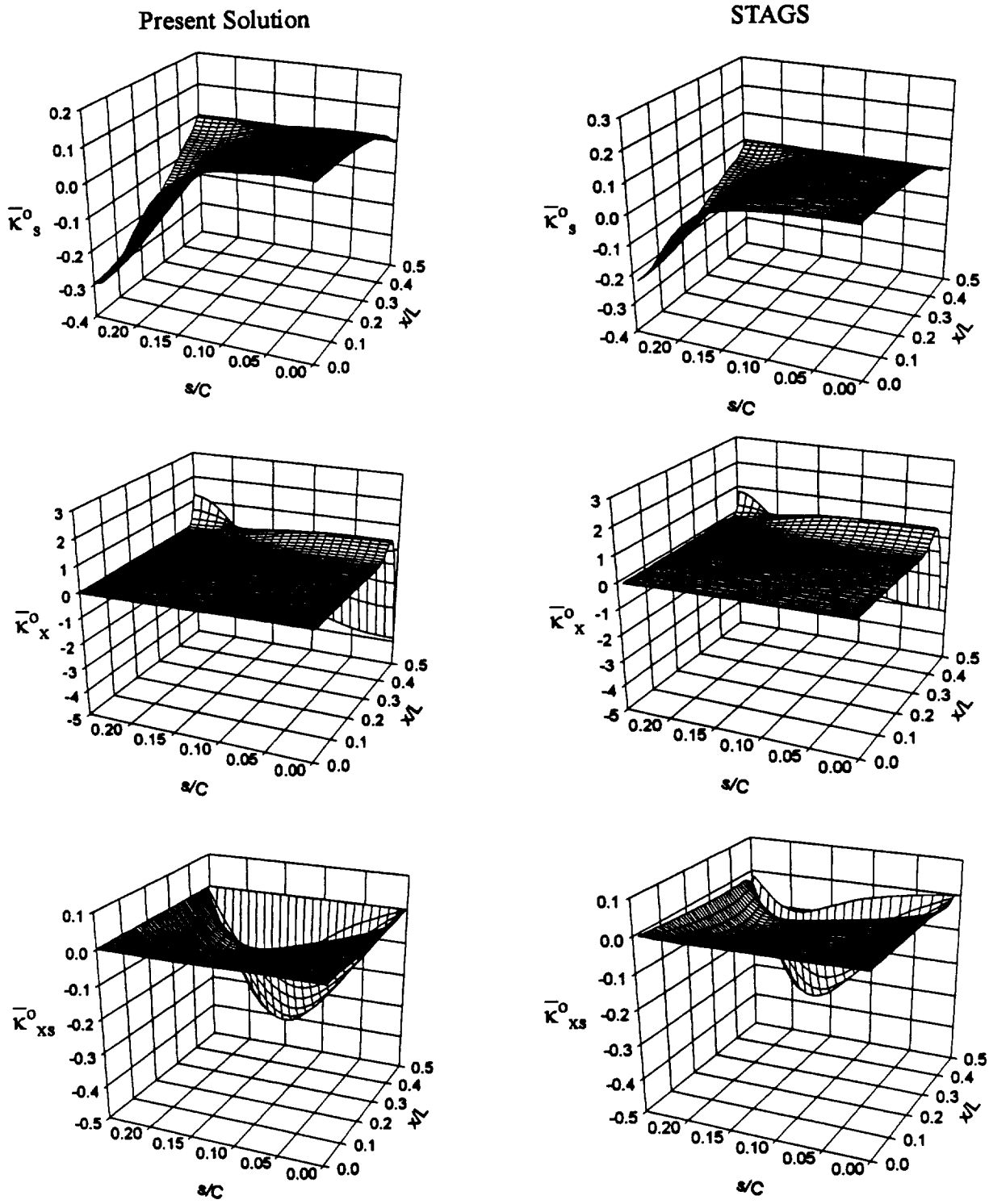

Figure A-3 Comparison between present solution and STAGS for a quasi-isotropic elliptical cylinder, e=0.7, p_o=100 psi: reference surface curvatures

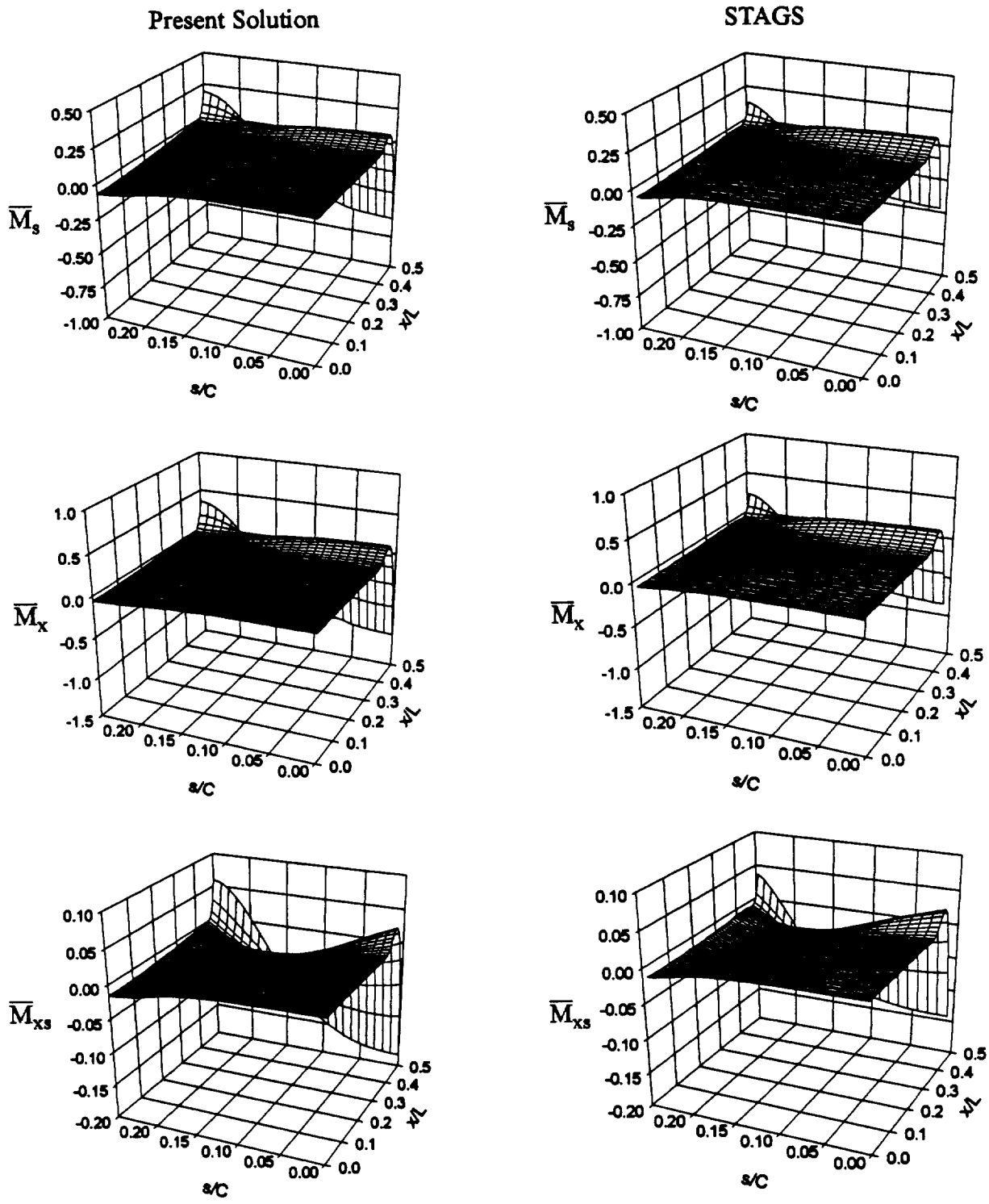

Figure A-4 Comparison between present solution and STAGS for a quasi-isotropic elliptical cylinder, e=0.7, p_o=100 psi: moment resultants

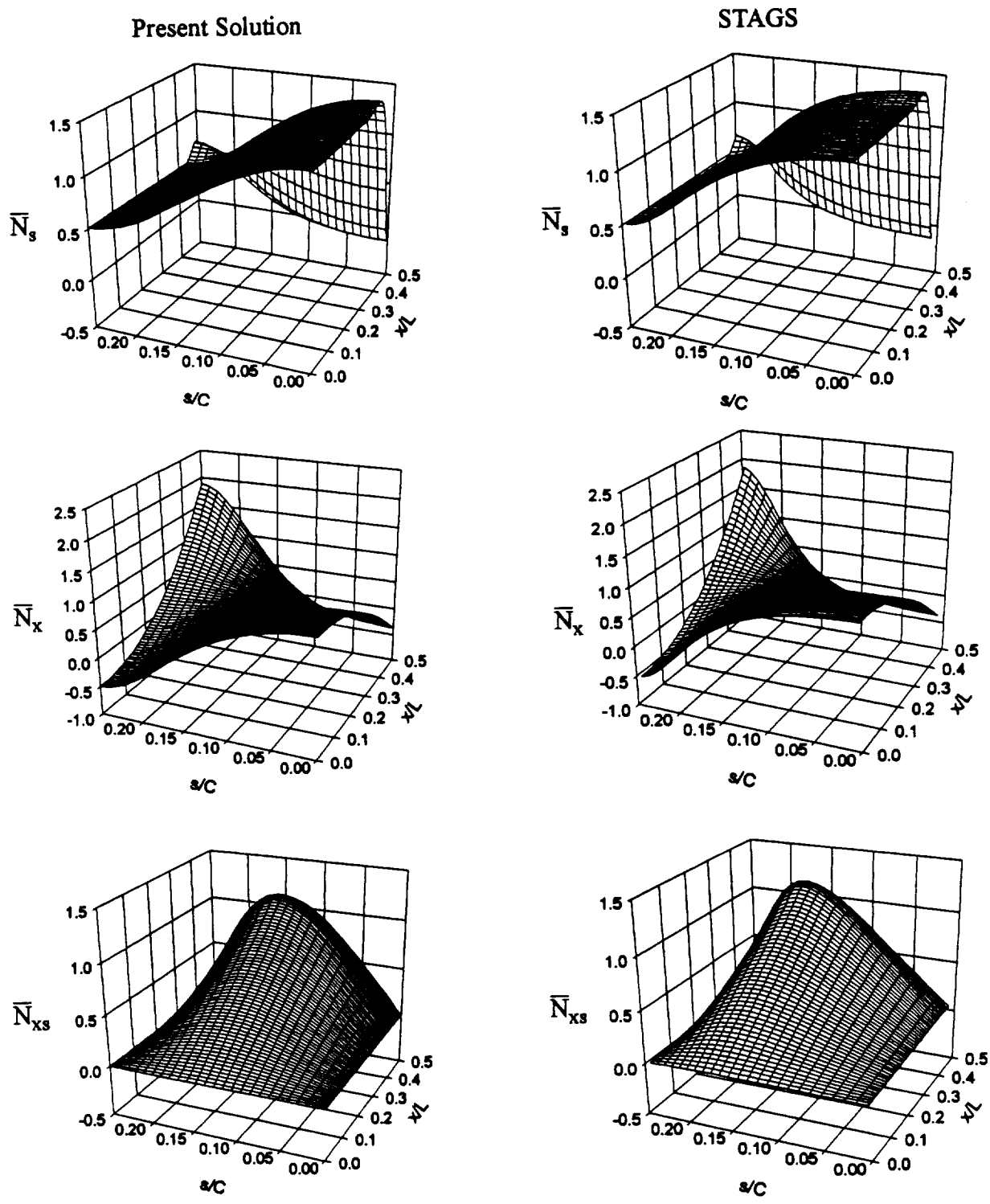

Figure A-5 Comparison between present solution and STAGS for a quasi-isotropic elliptical cylinder, e=0.7, p_o=100 psi: force resultants

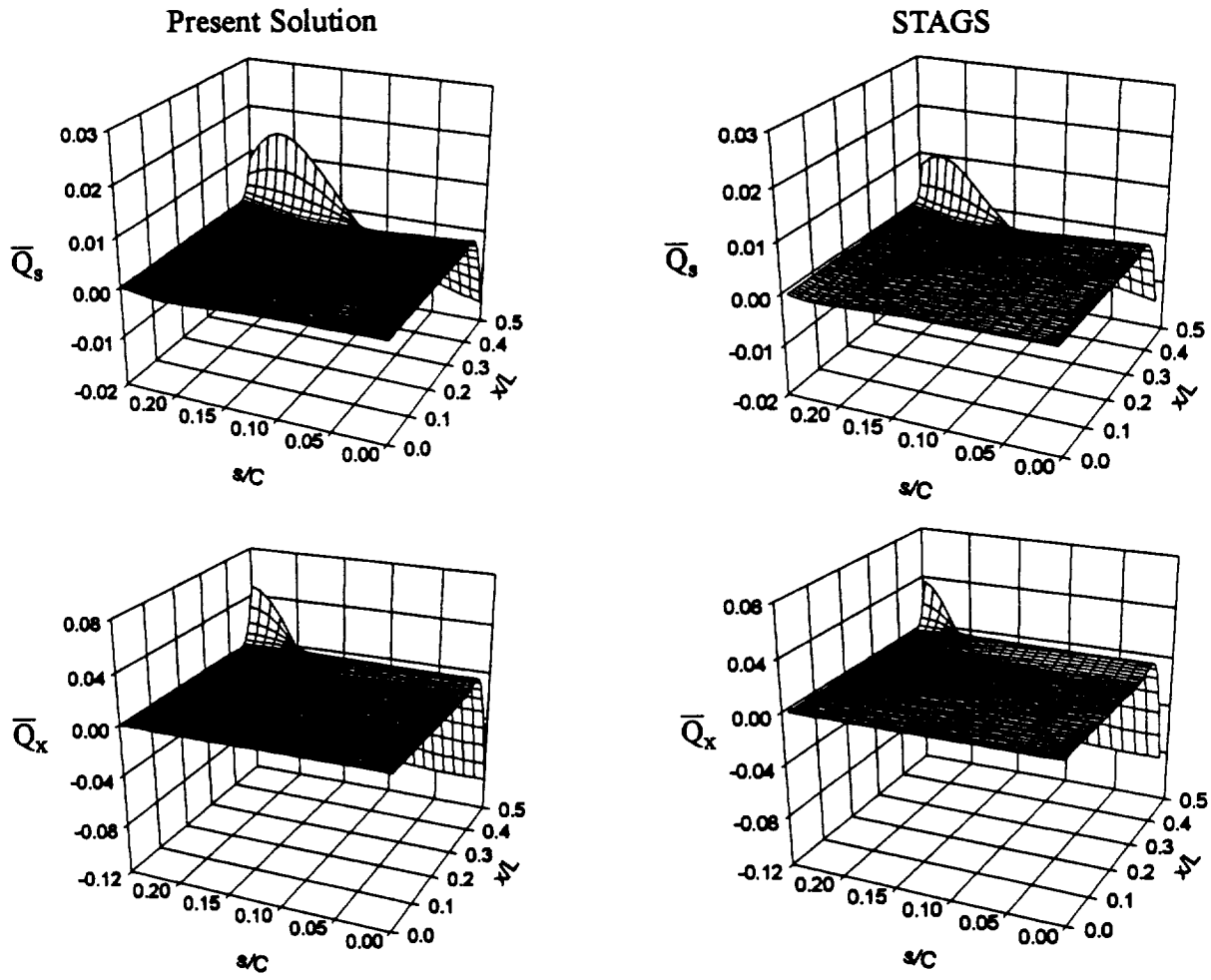

Figure A-6 Comparison between present solution and STAGS for a quasi-isotropic elliptical cylinder, e=0.7, p_o=100 psi: transverse shear force resultants

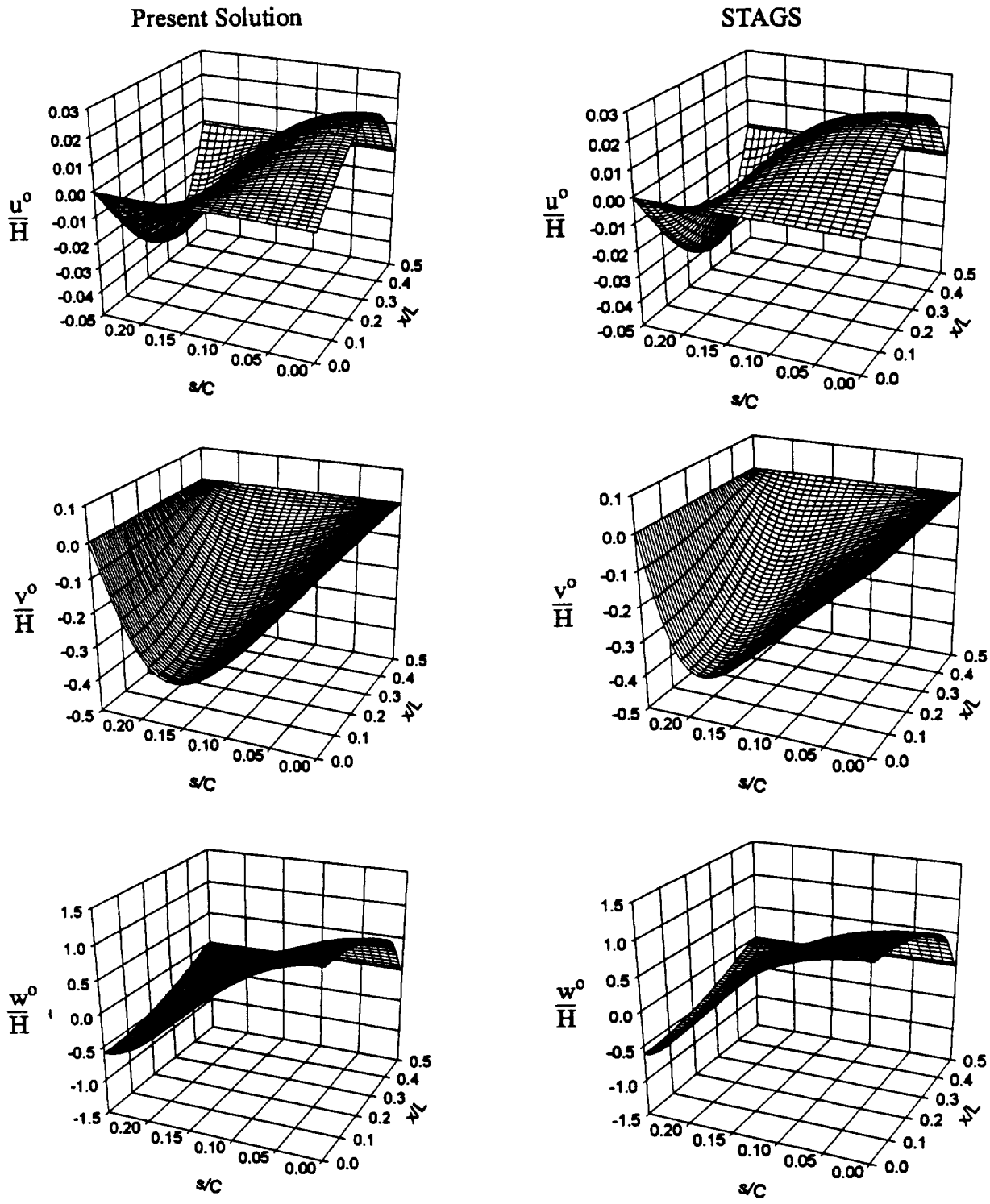

Figure A-7 Comparison between present solution and STAGS for an axially-stiff elliptical cylinder, e=0.7, p_o=100 psi: displacements

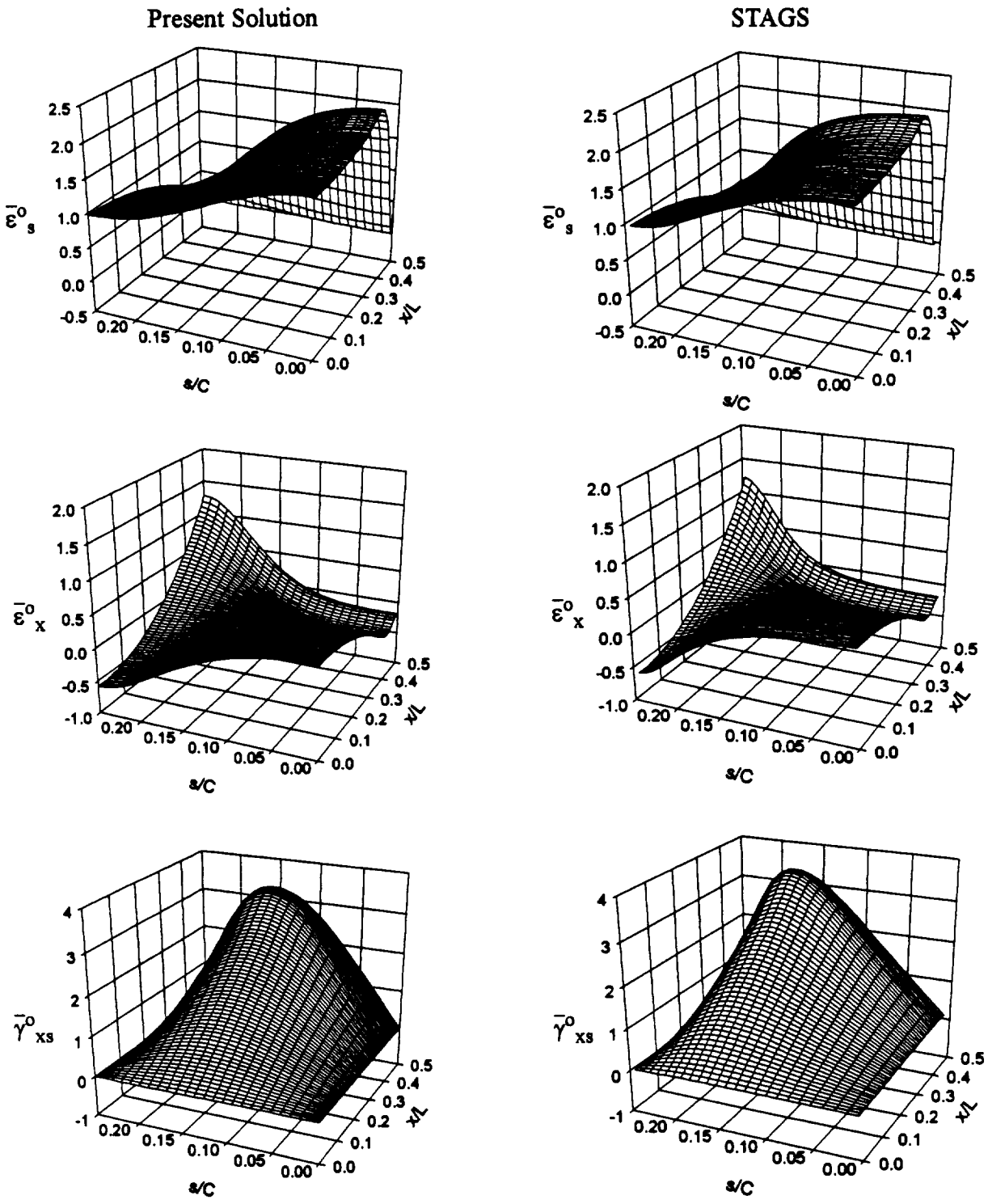

Figure A-8 Comparison between present solution and STAGS for an axially-stiff elliptical cylinder, e=0.7, p_o=100 psi: reference surface strains

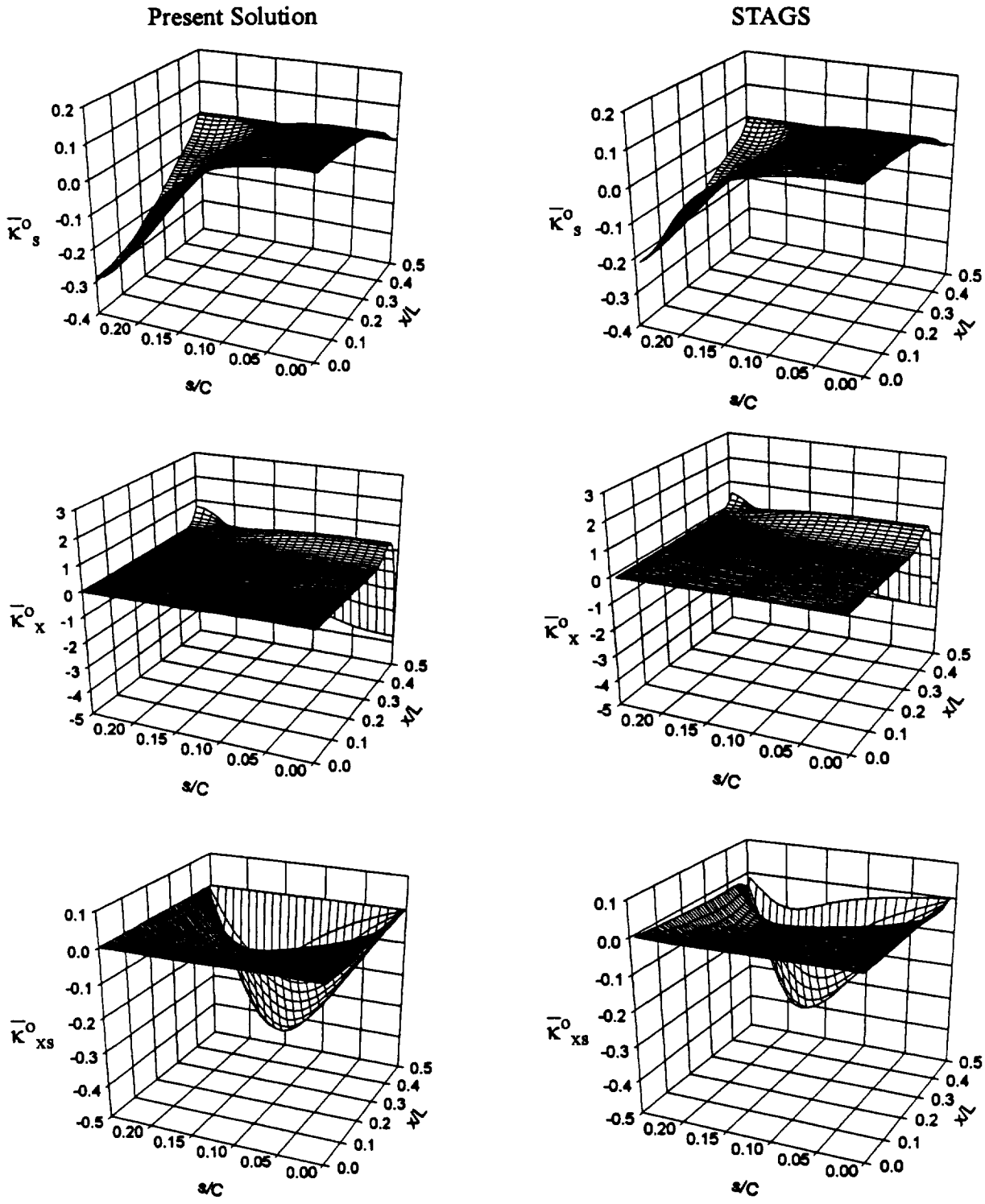

Figure A-9 Comparison between present solution and STAGS for an axially-stiff elliptical cylinder, e=0.7, p_o=100 psi: reference surface curvatures

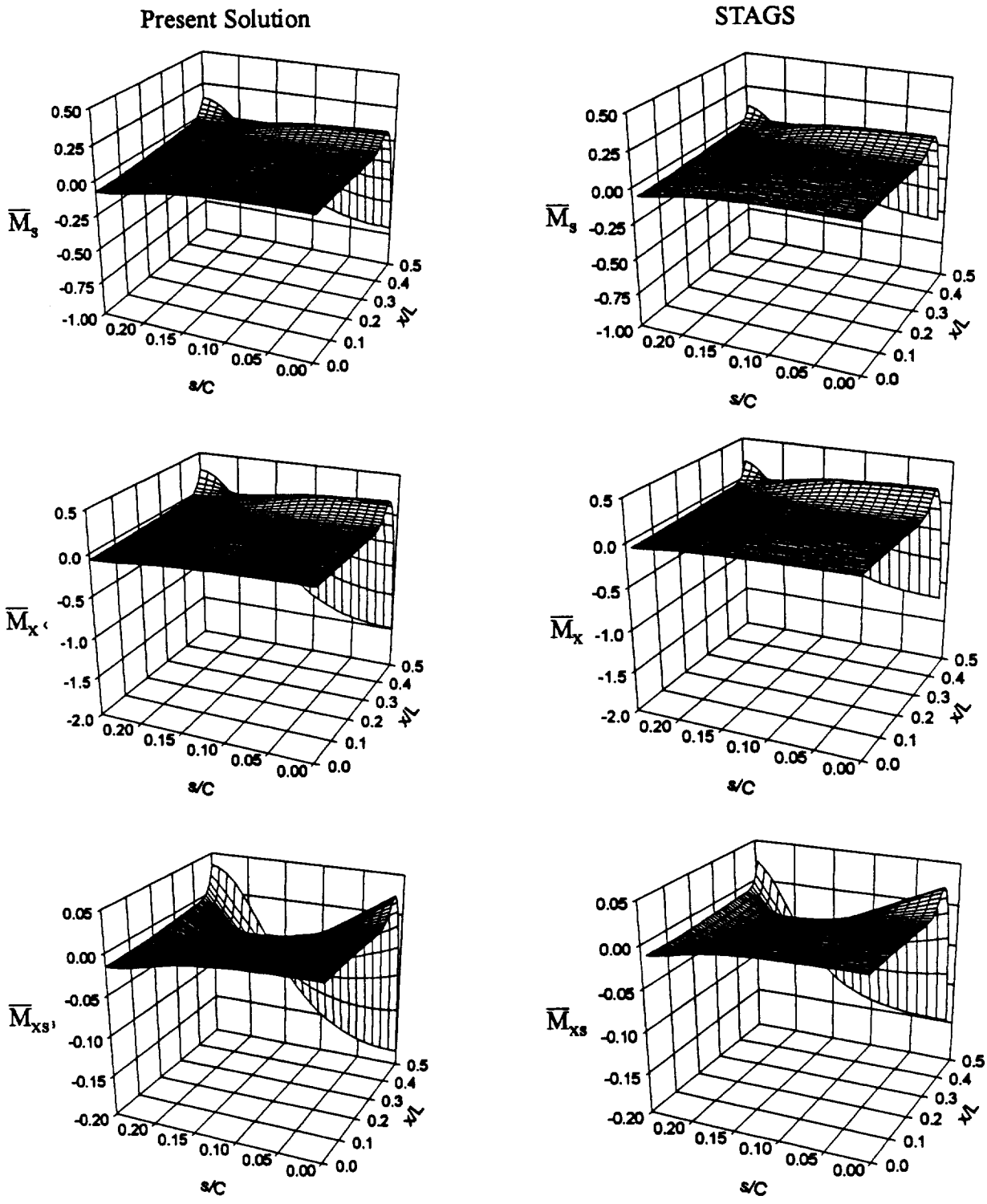

Figure A-10 Comparison between present solution and STAGS for an axially-stiff elliptical cylinder, e=0.7, p_o=100 psi: moment resultants

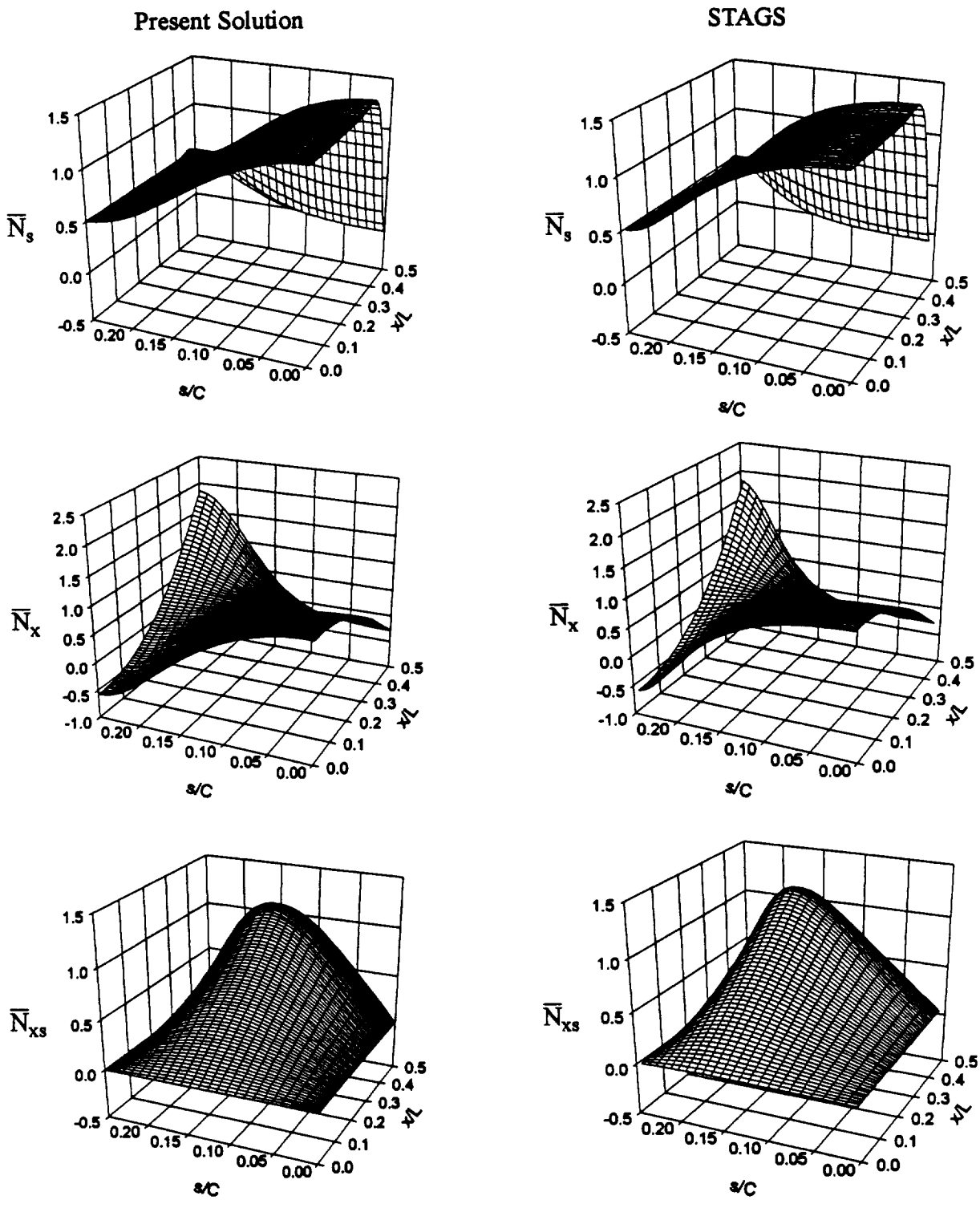

Figure A-11 Comparison between present solution and STAGS for an axially-stiff elliptical cylinder, e=0.7, p_o=100 psi: force resultants

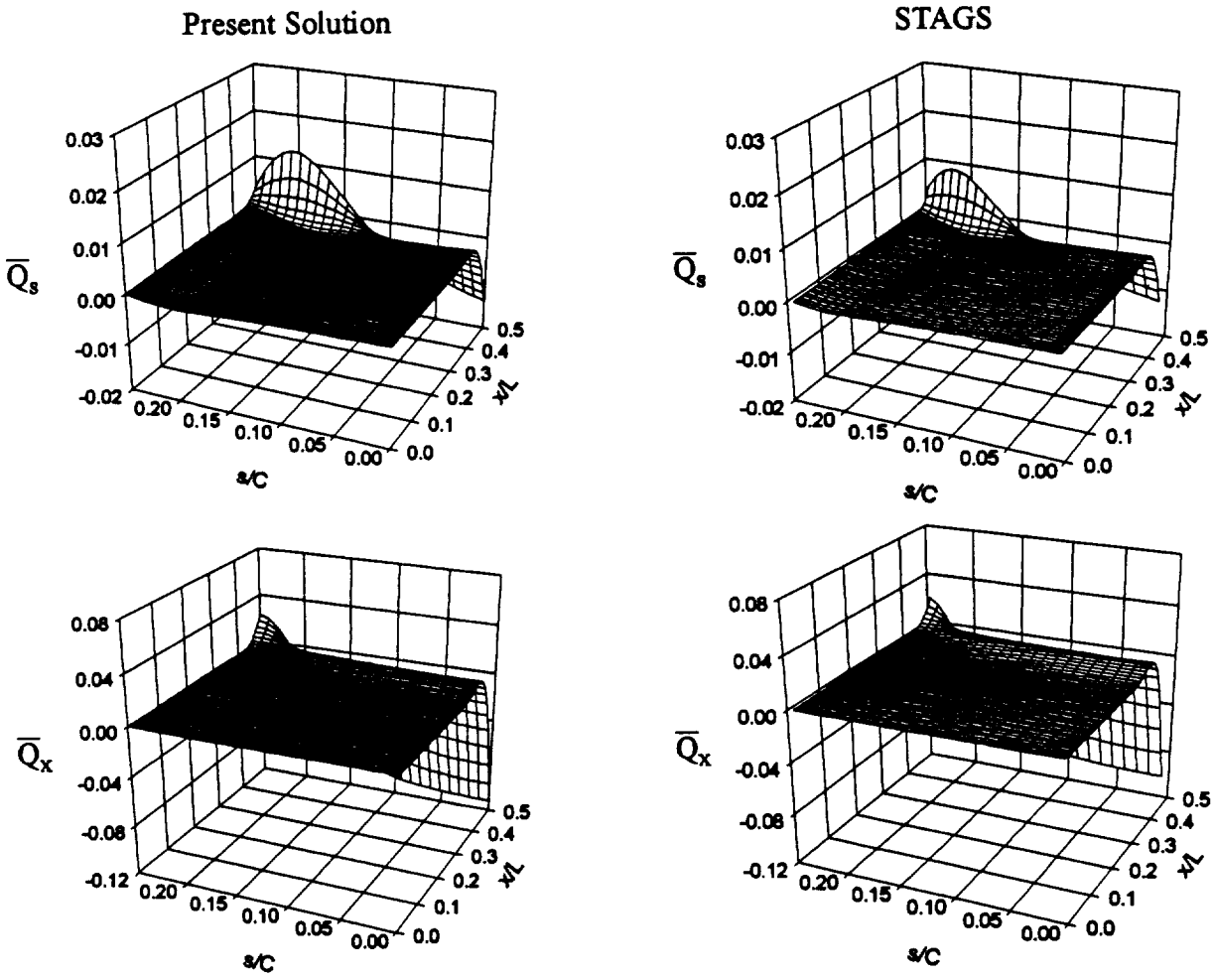

Figure A-12 Comparison between present solution and STAGS for an axially-stiff elliptical cylinder, e=0.7, p_o=100 psi: transverse shear force resultants

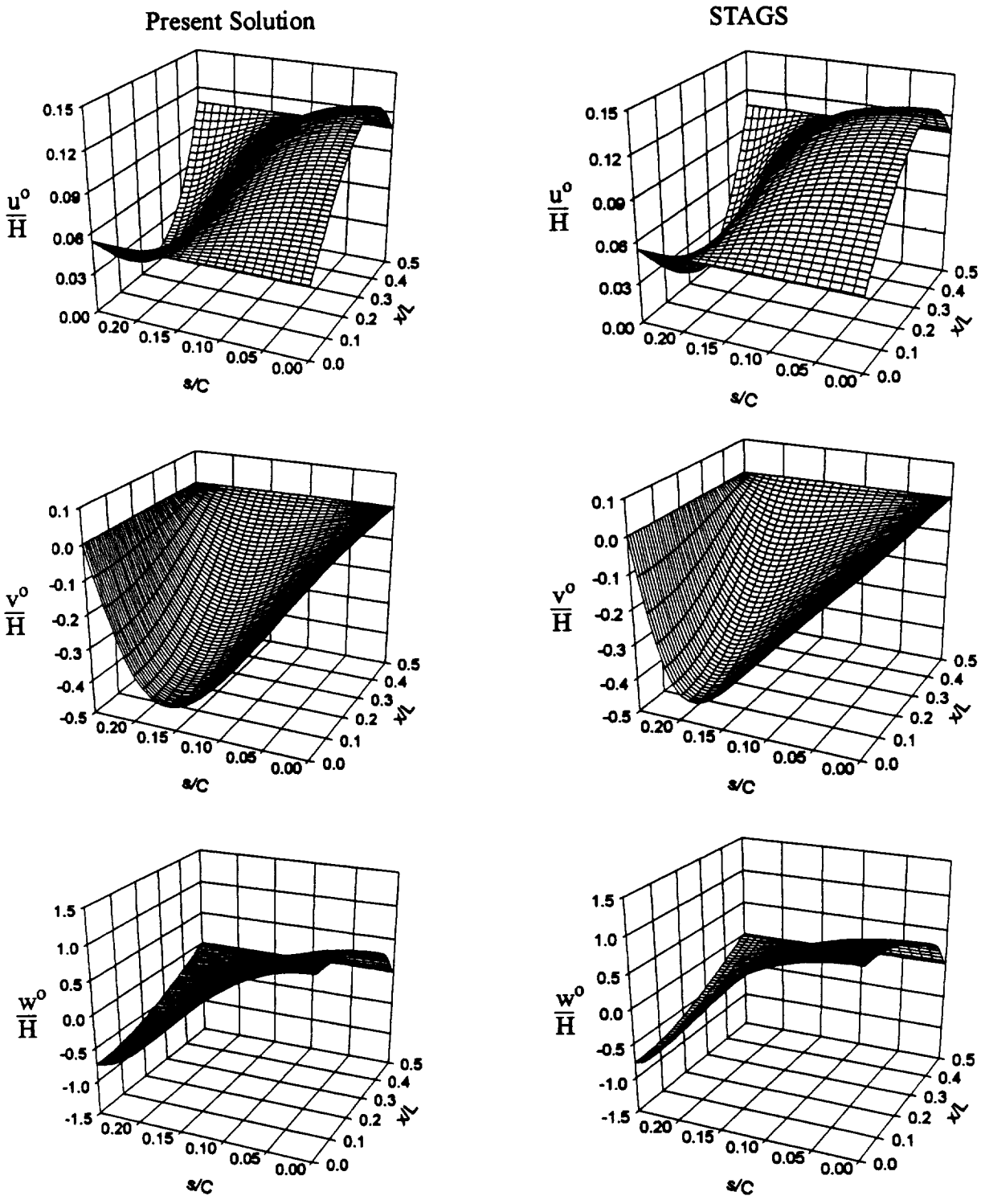

Figure A-13 Comparison between present solution and STAGS for an circumferentially-stiff elliptical cylinder, e=0.7, p_o=100 psi: displacements

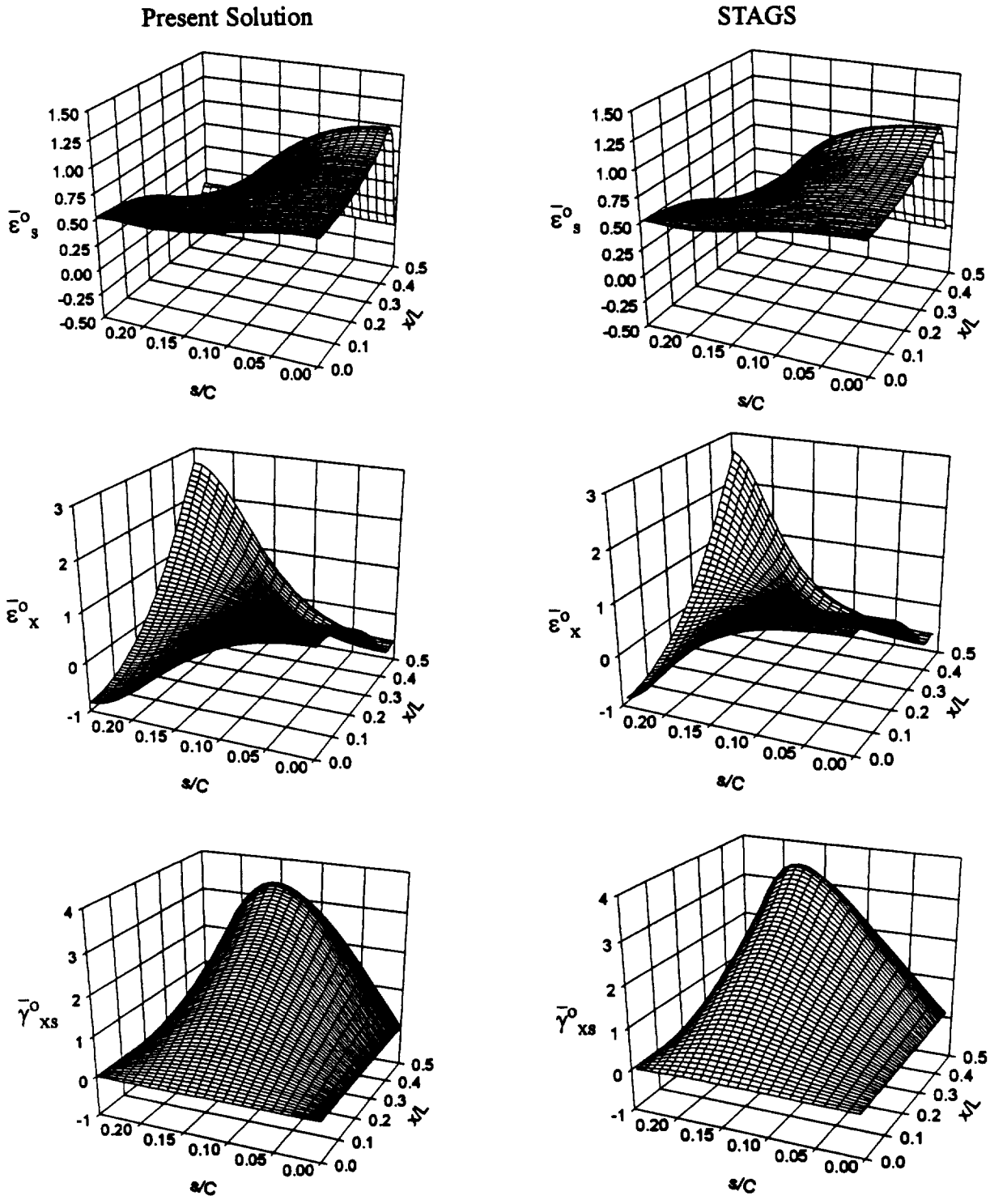

Figure A-14 Comparison between present solution and STAGS for an circumferentially-stiff elliptical cylinder, e=0.7, p_o=100 psi: reference surface strains

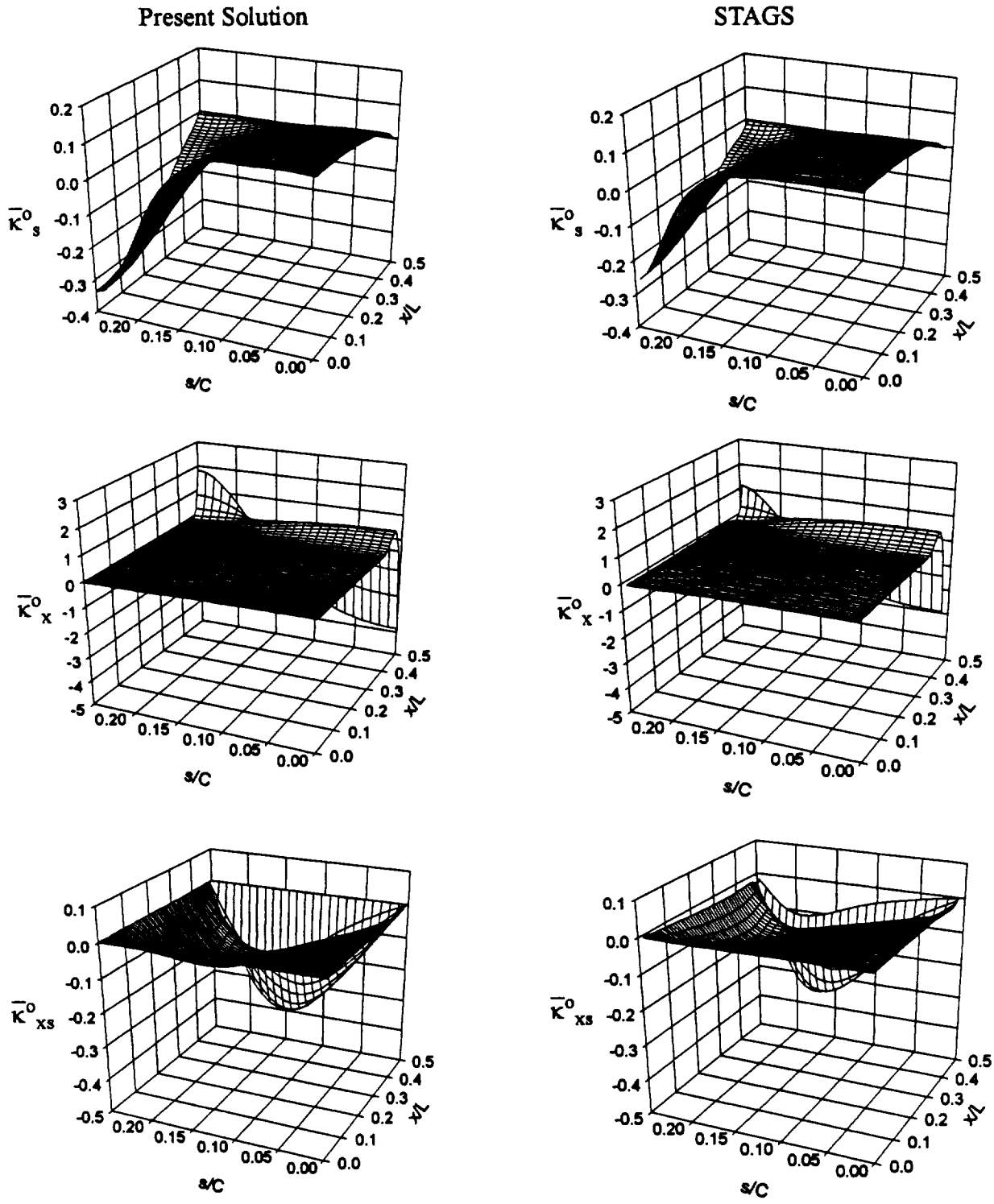

Figure A-15 Comparison between present solution and STAGS for an circumferentially-stiff elliptical cylinder, e=0.7, p_o=100 psi: reference surface curvatures

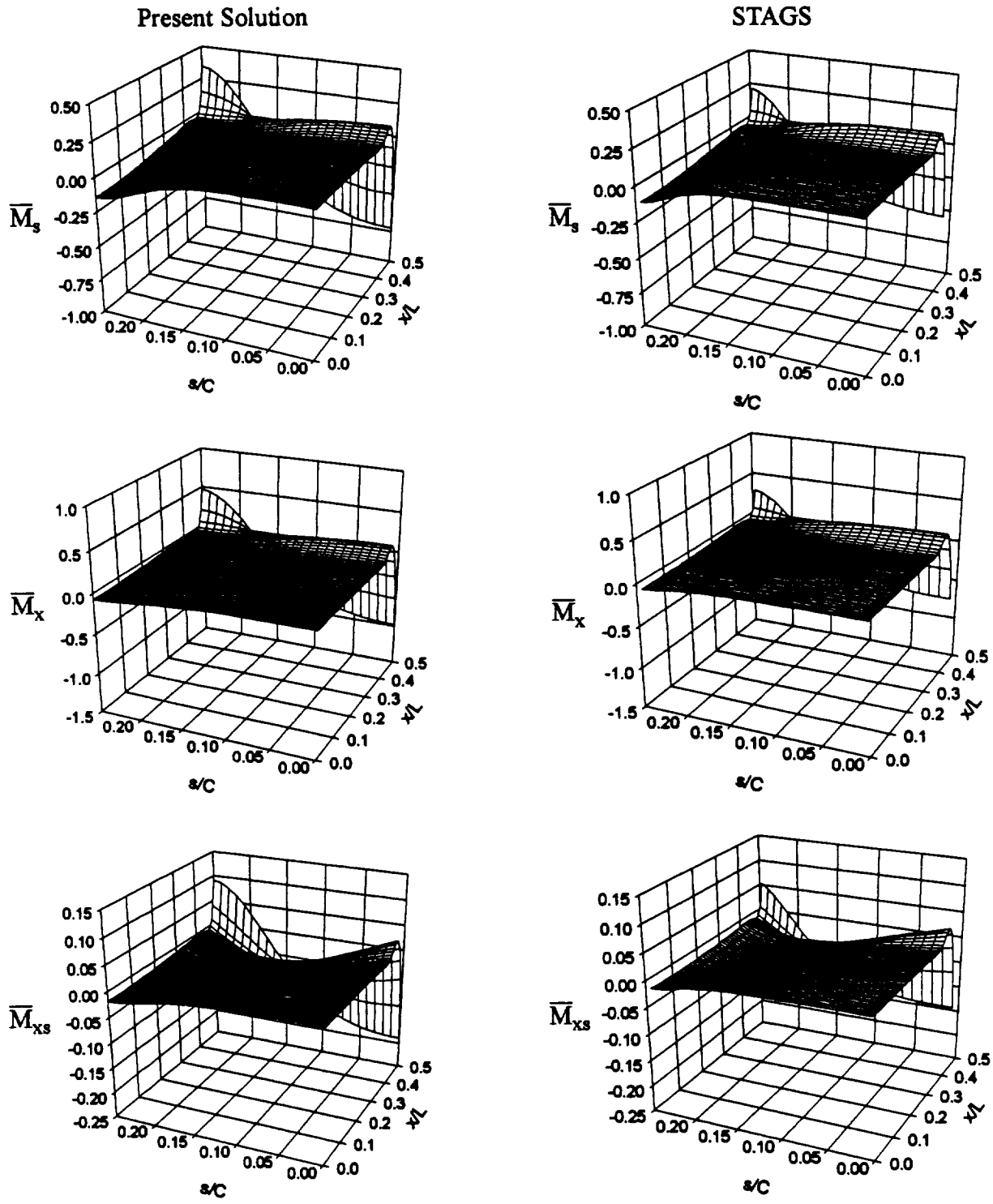

Figure A-16 Comparison between present solution and STAGS for an circumferentially-stiff elliptical cylinder, e=0.7, p_o=100 psi: moment resultants

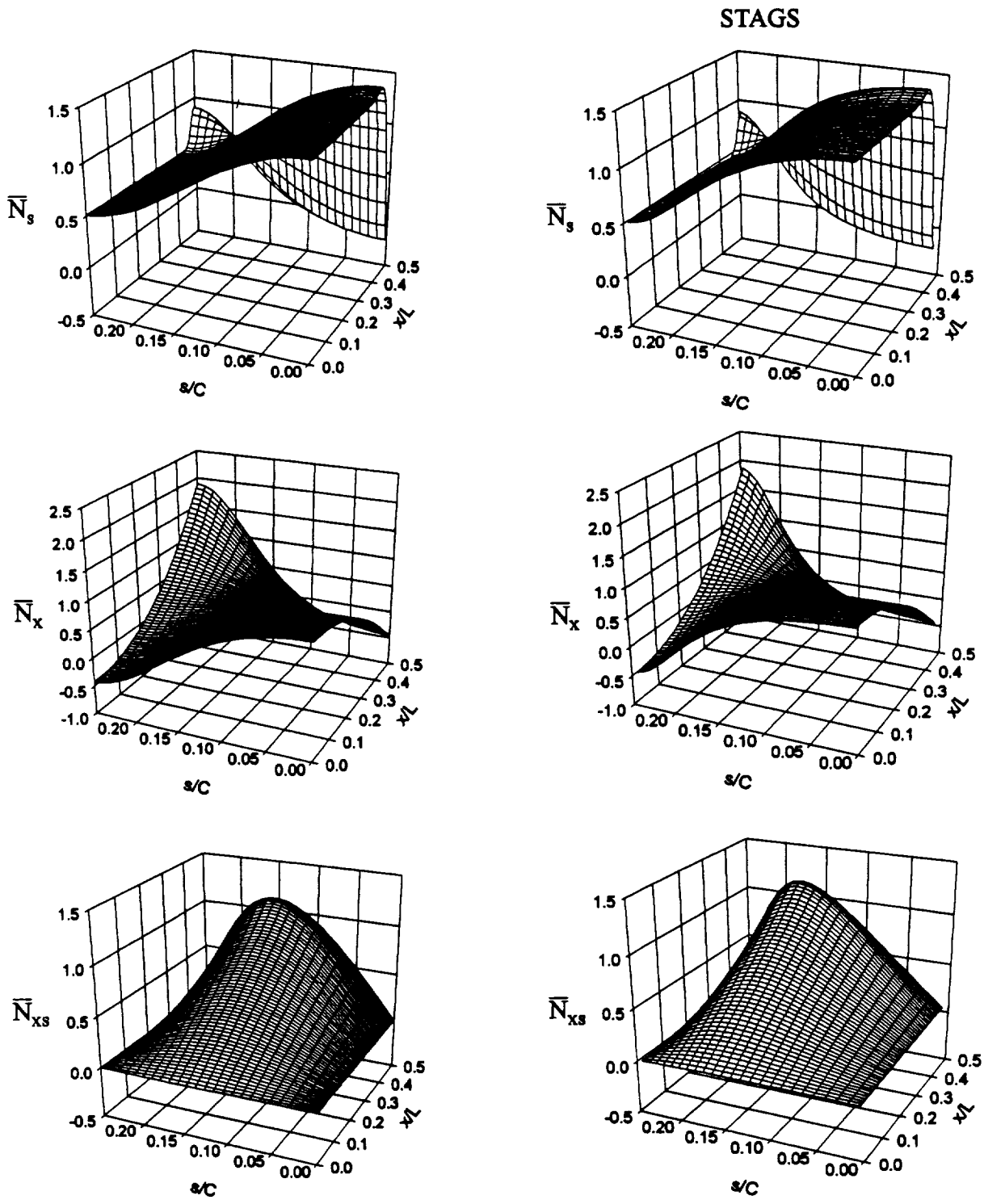

Figure A-17 Comparison between present solution and STAGS for an circumferentially-stiff elliptical cylinder, e=0.7, p_o=100 psi: force resultants

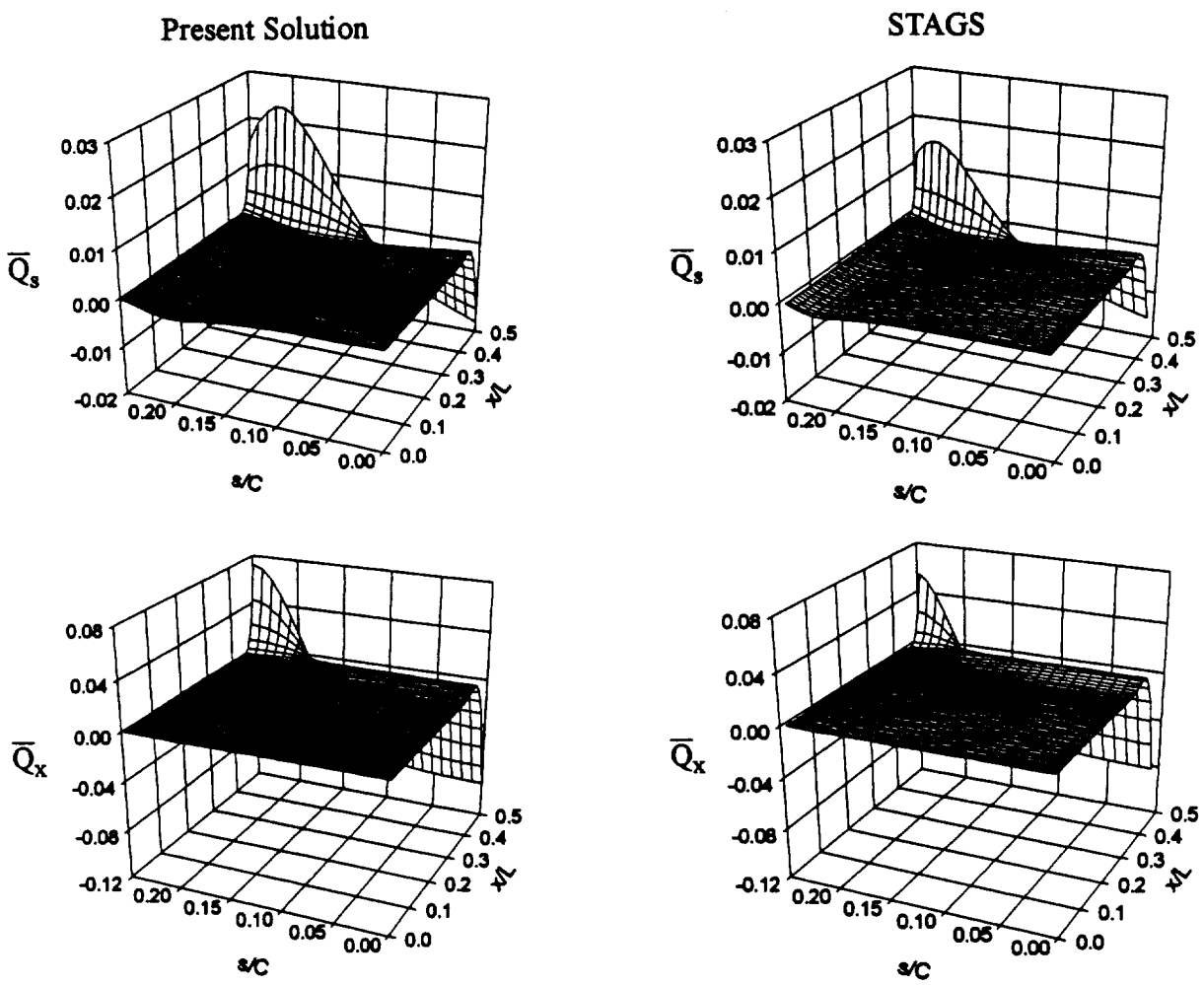

Figure A-18 Comparison between present solution and STAGS for an circumferentially-stiff elliptical cylinder, e=0.7, p_o=100 psi: transverse shear force resultants

Appendix B Axial Displacement Required for each Pressure

Due to the assumed rigid end plates, clamped-clamped boundary conditions are applied to each end of the cylinder, with the exception of allowing the end at $x = +L/2$ end to expand uniformly in the axial direction with displacement Δ. The end at $x = -L/2$ cannot move axially in order to restrict axial rigid body translation. Formally, the boundary conditions at the ends of the cylinder ($x = \pm L/2$) are as follows:

$$\begin{aligned} &\text{i)}\ u^o = 0\ @\ x = -\frac{L}{2},\ u^o = \Delta\ @\ x = +\frac{L}{2} \\ &\text{ii)}\ v^o = 0 \\ &\text{iii)}\ w^o = 0 \\ &\text{iv)}\ \frac{\partial w^o}{\partial x} = 0. \end{aligned} \tag{B.1}$$

The end displacement Δ is determined by enforcing axial equilibrium of the end enclosure at $x = +L/2$, namely,

$$\int_0^C N_x ds = p_o \pi ab, \tag{B.2}$$

where N_x is the axial force resultant within the cylinder, C is the circumference of the cylinder reference surface, and the cross-sectional area of the ellipse is πab. Physically, eq. B.2 states that the net axial force due to the internal pressure times the cross-sectional area of the end enclosure must be balanced by the net axial force due to the axial force resultant.

Tables B-1 and B-2 show the end displacements Δ used for various internal pressure values for the quasi-isotropic, axially-stiff, and circumferentially-stiff laminates evaluated using lin-

ear and nonlinear analyses, respectively. Since table B-1 shows the end displacements for each laminate evaluated using linear analysis, only one internal pressure value is needed. The end displacement can be determined for any other internal pressure by linearly extrapolating. The circumferentially-stiff laminate requires the largest end displacement Δ to satisfy axial equilibrium, whereas the axially-stiff laminate requires the smallest end displacement Δ. This can be explained by considering the percentage of fibers along the axial direction. The circumferentially-stiff laminate has fewer fibers in the axial direction than the quasi-isotropic and axially-stiff laminates. Therefore, the circumferentially-stiff laminate provides less resistance to expansion in the axial direction.

Table B-1. End displacement required to satisfy axial equilibrium corresponding to an internal pressure evaluated using linear analysis

	Quasi-isotropic	Axially-stiff	Circumferentially-stiff
Pressure (psi)	100	100	100
Δ (in.)	0.002391	0.000326	0.005627

For the nonlinear analyses, the end displacements cannot be obtained through linear extrapolation, as seen in table B-2. In the nonlinear case, linearly extrapolating overestimates the end displacement Δ necessary to satisfy axial equilibrium. Therefore, for each pressure used the end displacement Δ must be determined. Again, the circumferentially-stiff laminate requires the largest end displacement Δ to satisfy axial equilibrium.

Table B-2. End displacement required to satisfy axial equilibrium corresponding to an internal pressure evaluated using nonlinear analysis

	Quasi-isotropic	Axially-stiff	Circumferentially-stiff
Pressure (psi)	100	100	100
Δ (in.)	0.002039	-0.000061	0.005349
Pressure (psi)	130	130	240
Δ (in.)	0.002536	0.000208	0.012180
Pressure (psi)	250	250	
Δ (in.)	0.004137	0.001240	

In general, the end displacement Δ required for the nonlinear case is smaller than for the linear case. The most significant difference is seen with the axially-stiff laminate for 100 psi. The axially-stiff laminate evaluated using linear analysis extends 0.000326 in. but contracts -0.000061 in. when evaluated using nonlinear analysis. Recalling the definition of axial reference surface strain,

$$\varepsilon_x^o = \frac{\partial u^o}{\partial x} + \underline{\frac{1}{2}\left(\frac{\partial w^o}{\partial x}\right)^2}, \tag{B.3}$$

the difference in the axial displacements between the linear and nonlinear case exist in the underlined term. With the addition of the underlined term for the nonlinear case, the end displacement is more sensitive to outward or inward wall deflection caused by the internal pressure.

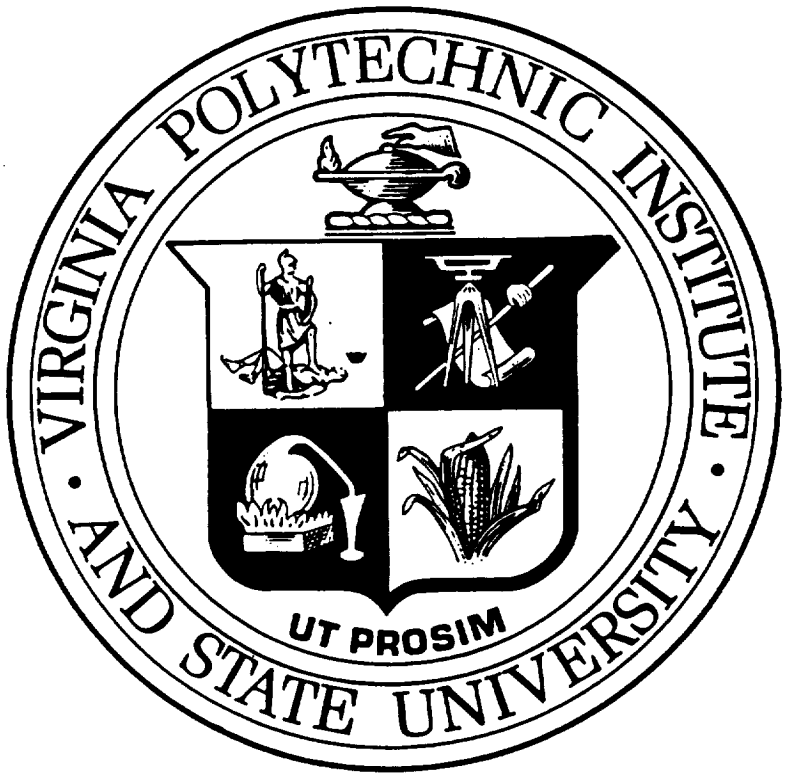

Manufacturing Distortions of Curved Composite Panels

T. T. OCHINERO and M. W. HYER

ABSTRACT

This paper briefly discusses the influences of through-thickness thermal expansion, a misaligned ply, and a resin-rich slightly thicker ply on the deformations of a curved composite laminate during cool down from the cure temperature. Both two-dimensional and three-dimensional level finite-element analyses are used. The deformations are categorized as to radial and tangential deformations and twist, and for each of the three influences these deformations are quantified. An additional outcome of the study is an indication of the level of analysis needed to study each of these three influences.

INTRODUCTION

When manufacturing flat and curved composite panels, the intention is to produce panels with specific geometric properties, i.e., length, width, radius of curvature, etc. Often, upon completion of the various stages of the manufacturing, and after the panel has cooled to room temperature and has been removed from the tool, hot press, or autoclave, the dimensions of the panel are not as intended. Focusing on curved panels, the lack of the proper radius of curvature and the presence of twist in the panel are among some of the problems. This lack of dimensional fidelity can be thought of, and are often spoken of, as a manufacturing distortion or warpage. Distortion can be a serious problem because it means that panels must be forced to fit onto existing frames or stiffeners arrangements, or forced to fit with other panels to make up a complete structure. This forcing to achieve a fit can lead to unwanted stresses that lead to fatigue or other stress-related problems and, in the case of production-level quantities, a lack of quality control.

T. Thomas Ochinero and M. W. Hyer
Department of Engineering Science and Mechanics
Virginia Polytechnic Institute and State University, Blacksburg, VA 24061.

The goals of this paper are to: (1) categorize the types of distortions that can occur; (2) illustrate that there are inherent, or natural, deformations that occur due to the thermal expansion behavior of composite materials and a curved geometry, and occur in so-called perfect panels; (3) quantify the levels of distortions predicted as a function of the level of refinement of the analysis tool. The paper will lead the reader through the mechanisms and considerations that account for some of the manufacturing distortions of curved composite panels. A very specific problem will be considered, namely, a four-layer graphite-epoxy panel with a 150 in. radius of curvature, a 60° opening angle, and a 150 in. length. The 150 in. radius and 60° opening angle lead to an arc length of approximately 150 in. The specific lay-up is nominally $[\pm\theta^\circ]_S$, with θ varying from 0° to 90°. The radius to thickness ratio R/H is 600. The angle θ is measured relative to the axial direction, values of θ between 0° and 30° corresponding to axially stiff panels and values between 60° and 90° corresponding to circumferentially stiff panels. Manufacturing distortions are predicted using two-dimensional and three-dimensional ABAQUS models of the panel, the latter to capture the influences of through-thickness effects, assuming there are any. The two-dimensional ABAQUS models were constructed of 392 S8R5 8-noded shell elements. The three-dimensional ABAQUS models were constructed of 1568 C3D20 20-noded solid brick elements.

It is assumed the manufacturing process can be divided into three stages. Stage one is the room-temperature lay-up stage. In this stage the prepreg material is applied to a tool, either by hand or by an automated process. At this stage there can be variations in ply thickness, both within a ply and from ply to ply; there can be ply waviness, i.e., the fibers are not straight within a layer, rather they form either long or short wavelength 'S' patterns; there may be gaps in the prepreg; uneven resin distribution; and broken fibers. In addition, a given ply alignment may be slightly different than the intended alignment. All of these effects, particularly the latter, can lead to unwanted changes in the geometry of the panel. Stage two consists of consolidation and curing of the laminate at elevated temperatures and pressures. During this time a number of influences are possible. Temperature gradients along the length or circumference can lead to different curing conditions in different regions of the panel. These different curing conditions can result in spatially nonuniform mechanical and thermal expansion properties. As resin bleed, and therefore ply thickness and fiber volume fraction, depend on compaction pressure, variations in pressure from location to location can lead to spatially nonuniform ply properties, both in the lengthwise and circumferential directions, and also in the thickness direction. It is also possible that during this second stage ply shifts cause fiber misalignments. If a panel is consolidated and cured in multiple steps, such as with a sandwich panel, for example, other problems can occur during this stage. The third stage in the process is cooling and removal from the tool. Though most of the factors which cause distortions have occurred before this stage, it is during this third stage that the factors become evident. There can be actual failures of the

material during cooling, and closed sections can become bound on the tools, thereby requiring force to remove them.

Of all these influences, three will be considered here. The first will be that of the inherent difference in through-thickness thermal expansion of composite material relative to the inplane thermal expansion. This effect is responsible for spring-in and spring-out. The second influence will be that of ply misalignment, and the third will be that of a slightly thicker ply. The first influence cannot be avoided; the second and third ones can.

For purposes of discussion, it is convenient to define warpage metrics that will be used to describe and compare the deformation of the panel. Figure 1 shows the three primary warpage metrics that will be repeatedly utilized throughout the rest of this paper. For consistency, the displacement data presented here will be of a corner of the panel. Radial gap, ΔR, is defined as the radial displacement of the corner node, measured in inches. A positive radial gap corresponds to a spring-out of the panel. Tangential gap, ΔT, is defined as the circumferential displacement of the corner node, measured in inches. A positive gap corresponds to an increase in panel arc length. Finally, twist, ϕ, measured in degrees, is the angle that the two originally parallel sides make after the thermal load is applied.

BASELINE

It is useful to consider the radial and tangential gaps and the twist of a $[\pm\theta^\circ]_S$ laminate due to a -300° F temperature change, representing cool-down from curing, as predicted by classic two-dimensional analysis employing the plane-stress and Kirchhoff assumptions. This would perhaps be the analysis level initially used to study manufacturing distortions. As a baseline, consider that all plys are oriented as intended, and all ply thicknesses are uniform and identical, i.e., the curved panel is perfect. In Fig. 2 the solid line with the circles shows the relationship between radial gap and θ. The horizontal axis in Fig. 2 is the angle θ as it is varied from 0° to 90°. The vertical axis is the radial gap. As can be seen, for small values of θ, the panel is predicted to exhibit slight spring-in (approx. 0.1 in.), while for θ greater than 48°, minimal spring-out is predicted. Focusing on the solid line with circles in Fig. 3, the tangential gap varies from a circumferential contraction of -0.3 in. at θ = 0° to no gap at θ = 48° and finally to a small expansion for θ greater than 48°. For this perfect baseline case and the two-dimensional analysis, for all θ, the tangential gap and the accompanying radial gap are due simply to the circumferential coefficient of thermal expansion of the $[\pm\theta^\circ]_S$ laminate which can be computed quite readily from classical lamination theory [1]. For the baseline case, as shown in Fig. 4, it is predicted that no twist develops for any value of θ.

Radial Gap

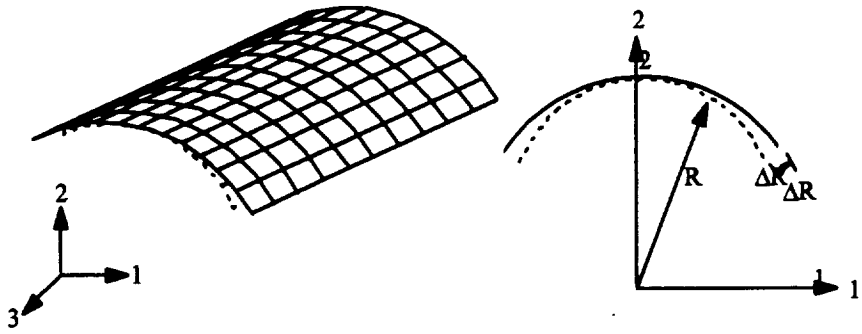

Tangential Gap

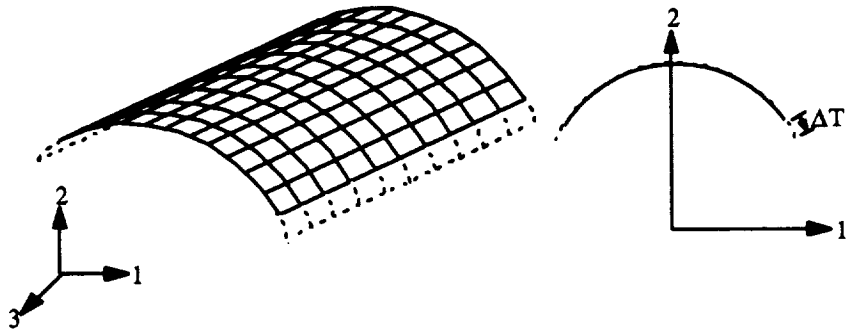

Twist

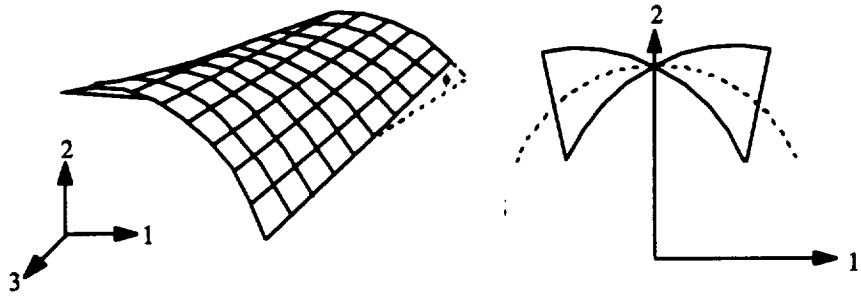

Figure 1 -W

EFFECT OF THROUGH-THICKNESS THERMAL EXPANSION

With fiber-reinforced composite materials, the through-thickness thermal expansion coefficient is considerably larger than the thermal expansion coefficient in the fiber direction. As a result, a curved laminated panel can have a circumferential coefficient of thermal expansion that is smaller than coefficient in the thickness direction. When the temperature is changed, this can result in thermally-induced circumferential stresses that lead to a net thermally-induced circumferential moment which is directly responsible for spring-in or spring-out, depending on the sign of the moment [2,3]. To account for the effect of the differences between circumferential and through-thickness thermal expansion coefficients, something other than a classic two-dimensional analysis must be used. Here a fully three-dimensional finite-element model was used. Note that two-dimensional models do not require information regarding the through-thickness thermal expansion coefficient, or any other out-of-plane property for that matter. In addition, with two-dimensional analyses three of the six stress components are equated to zero, and the displacements are assumed to vary in specific manners as a function of the laminate thickness coordinate. None of these restrictions are present in a three-dimensional model. In Fig. 2, the dashed line with circles illustrates the predicted radial gap of the perfect panel as a function θ using a three-dimensional analysis. Note that at small values of θ, a condition that results in similar values for the through-thickness and circumferential thermal expansion coefficients, there is not much difference between the spring-in predictions of the two-dimensional model and the predictions of the three-dimensional model. However, for increasing θ, a condition which leads to larger values of the through-thickness thermal expansion coefficient than circumferential thermal expansion coefficients, the predictions of the two analyses diverge. For θ greater than 48 °, the two-dimensional analysis predicts spring-out and the three-dimensional analysis predicts spring-in. (That the spring-in prediction of the three-dimensional analysis appears to be independent of θ is the result of certain effects dominating for one range of θ and other effects dominating for other ranges of θ. This is opposed to one effect being present in the three-dimensional analysis that is absent in the two-dimensional analysis and dominating for the entire range of θ.) The tangential gap, in Fig. 3, is not significantly influenced by three-dimensional effects, as evidenced by the closeness of the solid and dashed lines with circles for all θ. Interestingly, the three-dimensional model predicts a slight twisting, even for perfect laminates.

EFFECTS OF PLY MISALIGNMENT

As mentioned, a misaligned ply can occur during the manufacturing of a composite panel. Opinions vary, but common tolerances for this process are believed to be around ±3-5°. Here, two-dimensional and three-dimensional finite element analyses were conducted assuming a 1° ply misalignment on the inner layer, assuming all other layers have been oriented perfectly. Hence the lamination arrangement considered was $[\theta+1/-\theta/-\theta/\theta]_T$. Figure 2 illustrates the influence of this misalignment on the radial gap. The solid line with the triangles shows the results from the two-dimensional analysis and the dashed line with the triangles shows the results of the three-dimensional analysis. It can immediately be noted that the magnitudes of displacement associated with the ply misalignment tend to overshadow any of the small displacements associated with the perfect cases, either with or without through-thickness thermal expansion effects. Both two-dimensional and three-dimensional analyses predicts a maximum radial gap to occur when θ is about 30° and the gap is on the order of 1 in. For θ greater than 60°, the influence of the misaligned ply is not as strong. It should be noted that a positive radial gap due to a misaligned ply does not necessarily signify spring-out for this case. Accompanying this radial gap is twist, which results in negative displacements at other corners of the curved panel. It can be seen in the figure that a two-dimensional analysis fairly well represents the radial gap effects. At $\theta = 90°$ there is disagreement because of the through-thickness thermal expansion effect. The tangential gap, shown in Fig. 3, is also influenced by ply misalignment. In relation to the tangential gap for the perfect case, at $\theta = 30°$ there is about 0.2 inch more tangential gap, or about twice as much as the perfect case. It should be emphasized that overcoming an unwanted tangential gap in a curved panel is much more difficult than overcoming an unwanted radial gap. To overcome an unwanted tangential gap, the laminate must be stretched or compressed in the circumferential direction, essentially overcoming inplane stiffness A_{22}. (For compression, buckling could be an issue.) To overcome a radial gap requires bending the laminate in the circumferential direction. This is resisted by the bending stiffness D_{22}. Bending a thin laminate requires less force than stretching it. Finally, Fig. 4 illustrates the twist that results from a misaligned inner ply. The misalignment effect is most extreme for $\theta = 0°$ and 90° and crosses zero at θ just less than 45°. The predictions of the two-dimensional analysis are very close to the predictions of the three-dimensional model, indicating that a two-dimensional model is quite sufficient to reflect twisting effects, as was the case for both radial and tangential gaps. For all three measures of distortion, the effect of a misaligned ply tend to be much more severe than the effects of through-thickness thermal expansion.

EFFECT OF PLY THICKNESS VARIATION

During the curing of the laminate, the resin liquefies and flows out of the laminate to be absorbed by the bleeder material covering the outside surface of the laminate. One of the results of this bleeding process can be a geometrically unsymmetric laminate due to variations in ply thickness from one ply to the next. Specifically, if the curved panel is fabricated on a tool, then it is possible the plys nearest the tool do not bleed as much as the plys away from the tool and in contact with the bleeder material. Here it is assumed the inner ply is 1% thicker than the other three. It is further assumed that the increased thickness is due to excess resin, so the material properties of the thicker ply are slightly different than the other plys. Once again, two-dimensional and three-dimensional finite element analyses were used to compare results. Figure 2 shows the variation in radial gap vs. θ due to the inner ply being 1% thicker due to excess resin. The solid and dashed lines with X's represent the variations based on two-dimensional and three-dimensional analyses, respectively. It is seen that for all θ the radial gap is negative, the largest radial gap occurring at $\theta = 30°$. Compared to the misaligned ply case, the thicker ply doesn't produce as large a maximum deviation of radial gap relative to the baseline case. For θ greater than 60° the influences of the thicker ply are not as great as for smaller values of θ. The tangential gap, shown in Fig. 3, is different enough relative to the baseline case that it could cause misfit problems. Averaged over θ, the thicker ply causes about the same deviation of the radial and tangential gaps relative to the baseline case as the misaligned ply. In contrast, the twist due to the thicker ply, shown in Fig. 4, is nowhere as severe as the twist due to a misaligned ply, though the twist is much more than the baseline case. Overall, for the radial and tangential gaps and the twist, the two-dimensional model and the three-dimensional model agree reasonably well.

CONCLUSIONS

From the study it can be concluded that for the situation considered here, the misaligned ply causes the most severe distortion of a curved panel. Obviously this is based on using a 1° misalignment and a 1% thicker ply, somewhat arbitrary numbers. Of less importance is the influence of the through-thickness thermal expansion. It should be noted, however, that as laminate thickness increases, for a fixed radius, the through-thickness thermal expansion effect becomes more pronounced. Furthermore, it appears that a two-dimensional model adequately represents the effects of a misaligned ply and a thick ply, but a three-dimensional model is needed to evaluate through-thickness thermal expansion effects.

ACKNOWLEDGMENTS

The work discussed was supported by the NASA-Virginia Tech Composites Program, grant NAG-1-1895 from the NASA Langley Research Center, with additional financial support from the Virginia Space Grant Consortium. Technical discussions with the grant monitor, Dr. James H. Starnes Jr., at the NASA Langley Research Center are greatly appreciated.

REFERENCES

1 - Hyer, M.W., Stress Analysis of Fiber-Reinforced Composite Materials, WCB/McGraw-Hill, 1998, New York

2 - Jain, L.K. and Mai, Y-.W, 'Stresses and Deformations Induced during Manufacture. Part I: Theoretical Analysis of Composite Cylinders and Shells,' *J. Composite Materials*, vol. 31, no. 7, pp. 672-695, 1997

3 - Jain, L.K., Lutton, B.G., and Mai, Y-.W, 'Stresses and Deformations Induced during Manufacture. Part II: A Study of the Spring-In Phenomenon,' *J. Composite Materials*, vol. 31, no. 7, pp. 696-719, 1997

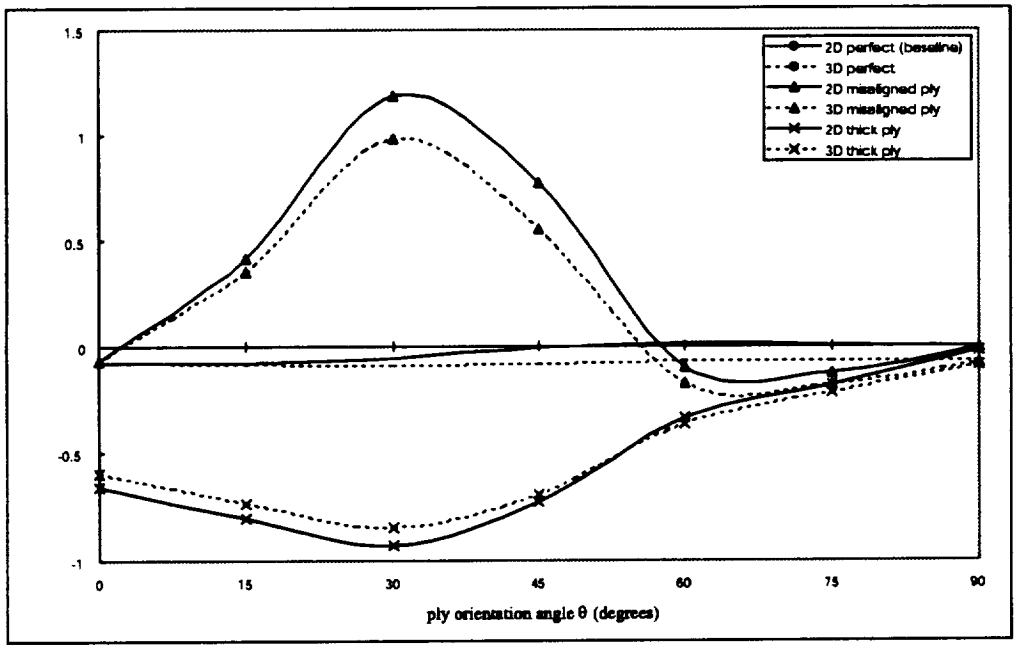

Figure 2 - Radial Gap due to Cool-Down from Curing

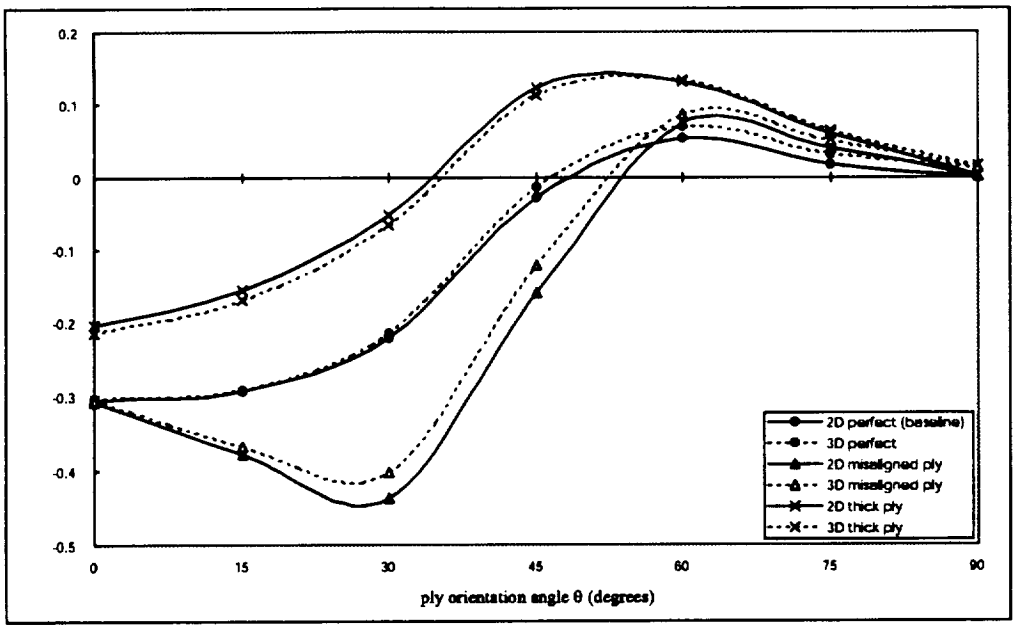

Figure 3 - Tangential Gap due to Cool-Down from Curing

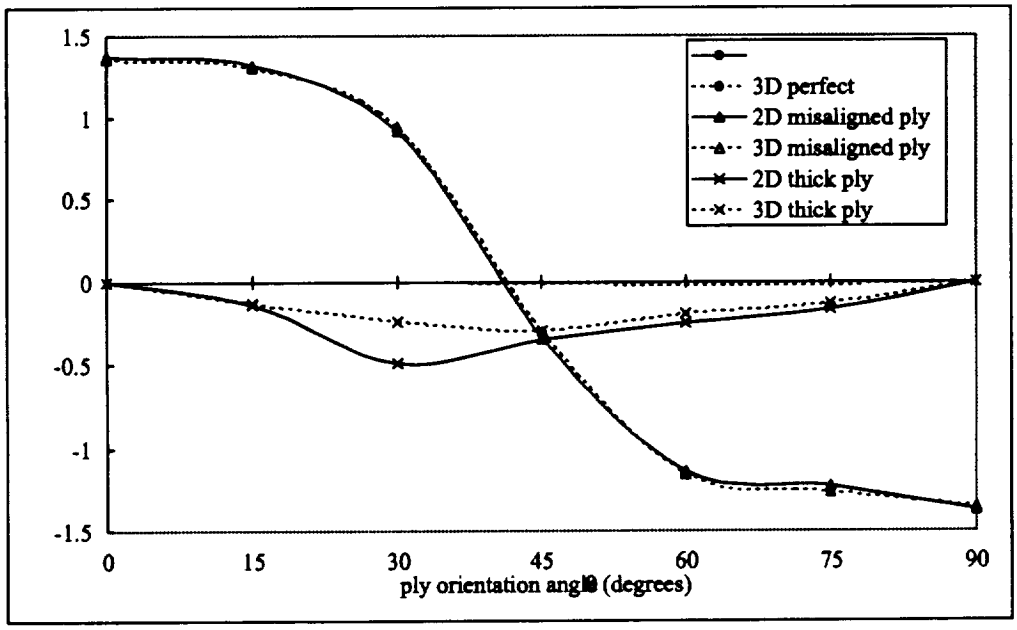

Figure 4 - Twist due to Cool-Down from Curing